CHARACTERISING DEMIXED POLYMER SURFACES TO STIMULATE MESENCHYMAL STROMAL CELL ACTIVITY AND INFLUENCE TISSUE DEVELOPMENT DURING OSTEOCHONDRAL REGENERATION

Shane B. Walsh

2015

Submitted for Doctorate of Philosophy (Ph.D.) to Newcastle University

AUTHOR'S DECLARATION

This candidate confirms that the work submitted here is his own and that appropriate credit has been made to the work of others

. _____ .

ACKNOWLEDGEMENTS

I would like to acknowledge the combined efforts of the whole Tissue Engineering Centre team. In particularly Kathleen Wright, Matt Benning and Deepak Kalaskar for helping to establish protocols and develop ideas, your expertise and patience has help refine my skills and added new ones to my repertoire. Technician Sharron Watson for discussing, testing ideas and providing years of insights into all things histological and microscope related troubleshooting. Kate Rennie, Kenny Rankin and Prof. John Robinson, for your helpful diplomacy. Debbie Wilde thanks for every meeting, events, travel arraignments and general life organisation.Dr. Mark 'Chief' Birch, thank you sincerely for not only your continued guidance through scientific, academic and ecumenical matters but also for your calm demeanour, friendly ear and open door policy. You were not only a PI but also the wise old elder of the project.

Prof. Kenny 'Commander' Dalgarno thank you for over seeing mechanical engineering operations and maintaining a well-stocked lab with an excellent array of instruments. You were the most involved professor I've ever worked with, thank you for all your help.

Prof. Andrew 'Admiral' McCaskie group lead and co-founder of the ARUK tissue engineering centre. Your guidance and navigation with the big picture project, helped develop this group to far greater heights.

The collective work of our collaborators in York University, thanks to the efforts Dr Paul Genever and his team (particularly Charlotte Knight), from whom I benefited from the use of immortalized TERT_MSC cell line. Saving me countless days/week and most importantly weekends from doing laborious tissue culture. Prof. Cosimo De Bari and the Aberdeen University team (Anke Roelofs) for all your help and knowledge on all things chondrogenic.

My humble thanks to all the staff of the Institute of Cellular Medicine, Newcastle University with special thanks to all the members past and present of the Muscuoskeletal Research Group (MRG) laboratory. Your inspiration, education, inclusion, comradery, support and stimulation helped get me through. I will never forget my time at the MRG and know the MRG will never for get me, your welcome.

ABSTRACT

Osteoarthritis (OA) is defined clinically as the world's leading cause of joint disease. Better understanding of the disease aetiology, contributing factors and improved imaging technologies has changed how we can treat this disease. Early intervention and long-term implant integration has inspired a new generation of biomaterials, able to influence local biological events *in situ*. The response of cells to their physical environment is known to regulate their proliferation, phenotype, gene expression and differentiation. To rebuild tissue with the appropriate structural and cellular organisation, temporal and spatial cues are required, possibly in combination with biomolecules and/or biomolecular motifs, to control musculoskeletal and adult mesenchymal stromal cell (MSC) phenotype and subsequent differentiation.

Work presented here identifies a simple, adjustable and efficient technique for the investigation of how controlled chemical and distinct topographical surfaces can be used to influence MSC differentiation.

Thin films of polymers were spread onto glass substrate by spin coating. Using a combination of immiscible polymers, Polystyrene (PS) and Poly (methyl methacrylate) (PMMA), phase separation generates a landscape of opposing structures. This is further accentuated by the addition of small quantities of water to produce pores. Low concentration polymer solutions (3%w/v) were demixed at various ratios (v/v) and spin coated at speeds > 8,000rpm under humid conditions. Polymer surfaces were evaluated for topography, pattern and chemistry using; atomic force microscopy (AFM), scanning electron microscopy (SEM) and X-ray photon spectroscopy (XPS). Biological response was evaluated using immunofluorescence, histological staining, and qPCR. Primary adult human mesenchymal stem cells (huMSC) were isolated the marrow of bone fragments. Multipotent cell populations were characterized by flow cytometry and tri-lineage differentiation. Immobilized proteins and other biomolecules functionalised the surfaces using zero length crosslinking, restrictively bound to discreet areas of the bi-phasic surfaces. Lineage specific growth factors (BMP-2, TGF-β and KRTGN) were immobilized on the surfaces and evaluated for their ability to influence MSC phenotype.

A range of demixed polymer ratios, concentrations and solvents were evaluated and these combinations produced a variety of distinct surfaces. A selection of surfaces (PS:PMMA [(i)40:60,(ii)50:50,(iii)60:40] at 3%w/v in toluene) were chosen for further characterization based upon the reproducibility of their fabrication. Different ratios

created opposing raised PMMA and low lying PS islands [(i) 8 μm^2,(ii) 8-12 μm^2,(iii)12-15 μm^2]. Saturated humid conditions induced breath figure patterns producing average crater-like features, *caldera*, of (i) 0.5 μm, (ii) 0.7 μm,(iii)1 μm in height. Variations in these crater-like structures and their distribution were observed to differ between demixed polymer ratios and this concurrently altered cell adherence profiles. Short-term (24h and 72h) effects displayed concentrated cell focal adhesion plaque interaction with the raised *caldera*, altered polymer demixed ratios consequently influence cell morphology. Changes in surface topography between surface *i* to *ii* altered cell morphology from polygonal to multipolar and hyperbolae shapes, in turn changing cell F-actin cytoskeleton. Long-term effects found higher commitment to a more chondrogenic lineage, with RNA expression levels elevated for SOX9 and ACAN. Effects were not isolated to individual cell behaviour but displayed mass cell condensation and aggregation. Histological analysis displayed altered ECM deposition of cell clusters.

Immobilized large biomolecules to the polymer surface, using a fluorescein isothiocyanate labelled albumin (AL-FITC) identified restricted immobilization to opposing polymer chemistry. Functionalized surfaces with immobilized phosphatase enzyme illustrated the retention of bioactivity of a protein for up to 12 days. Growth factor immobilization showed slight phenotypic change to direct cell lineage commitment but this was not significant (I-BMP2 and I-TGF-β).

Surface fabrication methods described in this thesis identify a simple reproducible method for evaluation of cell response to their physical environment. Polymer demixing generates chemically distinct surfaces with additional adaptability for downstream processing of these surfaces with covalent crosslinking. Simple modification of the fabrication conditions by introducing humidity greatly enhanced the topographical features adding an altered height dynamic to these textured surfaces. Micro- and nano- topographical features influenced cell adhesion and cell morphology. This in turn resulted in altered gene expression and indicated potential for phenotype change. Surfaces of high caldera elevation and dispersion were associated with enhanced chondrogenic lineage expression by primary MSCs. Additionally, cell-cell interactions were influenced on these surfaces, promoting cell aggregation, condensation and localised matrix deposition.

Demixed polymer blends provided tuneable topographies for the stimulation of multipotent cells through identified contact with distinct Caldera positioning. Utilizing the individual polymer chemistries of these topographies, biomolecules were able to be restrictively bound and retain bioactivity, but tailored surfaces immobilized with tissue specific growth factor only displayed slight lineage effects in the work presented here but is an area worthy of further study.

TABLE OF CONTENTS

LIST OF FIGURES AND TABLES

ABBREVIATIONS

TE	Tissue Engineering
RM	Regenerative Medicine
MSC	Mesenchymal Stromal Cell
ACI	Autologous Chondrocyte Implantation
ECM	Extracellular Matrix
SDS-PAGE	Sodium Dodecyl Sulphate - Polymer Acrylamide Gel Electrophoresis
PS	Polystyrene
PMMA	Poly Meth(Methyl acrylate)
PCL	Polycaprolactone
PEG	Polyethylene glycol
PLGA	Poly(lactic-co-glycolic acid)
PTFE	Polytetrafluoroethylene (Teflon)
DCM	Dichloromethane
THF	Tetrahydrofuran
HMDS	Hexamethyldisilazane
Eth.	Ethanol, absolute
EDTA	Ethylene Diamine Tetra Acetic Acid
BF	Brightfield (microscopy)
SEM	Scanning Electron Microscopy
AFM	Atomic Force Microscopy
XPS	X-Ray Photon Spectroscopy
qPCR	Quantitative Polymerase Chain Reaction
DAPI	4',6-diamidino-2-phenylindole
Al-FITC	Albumin, Fluorescein Isothiocyanate
SDF-1	Stromal Derived Factor 1
KRTGN	Kartogenin
BMP	Bone Morphogenetic Protein
TGF	Transforming Growth Factor
ROCK	Rho Kinase signalling pathways
TRP	Transient Receptor Potential family of intracellular cation channels
Pg.	Page
O/N	Overnight

CHAPTER 1. INTRODUCTION

1.1. Background on Tissue Repair and Regeneration

1.1.1. *Tissue Regeneration in Nature*

The physiological response of tissue to injury is a highly conserved process throughout evolution and between different species. Nature provides spectacularly effective examples of tissue and organ regeneration, and the most striking of these mysterious abilities are found in the invertebrates *Planaria maculata* and *Hydra,* that are known to regenerate the whole animal body from tiny body parts[6,7]. While larger species like the Japanese salamander retain the ability to regenerate whole limbs throughout their life[8], similar appendage regeneration is observed in young lizards[9] being able to regrow a tail as part of a predatory-prey defence mechanism. Limited natural regenerative capacity has been observed in the mouse, a phenomena that is shared with humans and highlights the relatively deficient understanding of *Homo sapien* regeneration[10]. While all animals retain some form of regenerative capacity to maintain tissue (therefore survival), mammals have little or no natural renewal in whole tissue groups like; cardiac muscle, spinal cord and major appendages.

A rapidly growing area of research called regenerative medicine is beginning to uncover abilities and techniques to selectively inhibit or enhance precise steps of healing and regeneration, these may be transferable between tissues. Although the specific dynamics of regenerative medicine still remain elusive, one thing is certain, that the tissue for reconstitution must be competent at both the cellular and molecular level. Tissue plasticity is lost during maturation, for example, childrens' ability to regrow lost fingertips is not recapitulated in adults[11]. This is strongly suspected to result from the pivotal role genes play in regeneration, highlighted by classical findings of Takahashi and Yamanaka, 2006. renewed pluripotency of mature mammalian cells by inducing reprograming with four key factors (Oct3/4, Sox2, c-Myc and Nanog), designated induced pluripotent stem cells (IPS cells)[12]. The molecular mechanisms underpinning the inverse relationship between age and regeneration is not fully understood, ageing skeletal muscle tissue was observed to respond positively to blood-based factors of younger animals[13], suggesting involvement of soluble signalling effectors[14]. Within a tissue the mechanisms that stimulate cell-based regeneration are believed to be involved either stem cells or progenitor cells (a cell population devoid of age related decline i.e. the ability to self- renew). Stem or progenitor cell regeneration involves the maintenance of a self- renewing reservoir of undifferentiated cells to be available and present in or close to the tissue.

To develop a successful next-generation therapy it is necessary to understand a tissues endogenous regenerative capacity, identifying its mediators and the relative

stem cells and/or progenitor subpopulations necessary, is crucial to deciphering regenerative therapies in the future treatment of injured tissue and degenerative disease.

1.1.2. ***Regenerative Medicine and Tissue Engineering***

Original observations made by Ross G. Harrison in 1907, noted altered embryonic cell development to nerve fibres, when cultured on top of silk fibres adapted and alining with the culture fibres. This *in vitro* cell manipulation lead to interest for tissue regeneration. Both fields of Tissue Engineering (TE) and Regenerative Medicine (RM) strive to capitolise on this knowledge but are hindered due to the limitations of human regeneration. To distinguish between the two; RM is defined as use of "human cells, tissue or organs, to restore or establish normal function"[15].; and Langer and Vacanti defined TE as "interdisciplinary fields that applies the principles of engineering and life sciences toward the development of biological substitutes that restore, maintain, or improve tissue or whole organ function"[16]. Either, the manipulation of native tissue repair systems like stem / progenitor cell populations or fabrication of biomimetic structures from natural or synthetic materials with cells, was the commencement in the engineering of tissue.

It was the discovery and characterisation of stem cells that greatly improved the range of possibilities for cell therapies due to their multi-lineage capabilities. Furthermore, the identification of adult stem cells enabled autologous replacement of tissue(s); devoid of immunogenic complication or allogeneic complications[17].Although since the breakthrough of stem cells in the 1960's it has slowly come to light that the cells alone were not enough to regenerate a fully functioning tissue in humans. Major difficulties were discovered when delivering the stem cell population to a specific site, large population numbers were required, cell migrated from site and uncertainty surrounded lineage differentiation[18,19].

Tissue engineering aims to solve these difficulties, since its rudimentory inception in the late 1930's by Alexisios Carrel, to providing a 3D environment for the cell populations. An impregnated scaffold with identified multipotent cells, physically tenable for surgical implantation or cell-free but highly specialised material and structure, can potentially provide a rapid functional repair and enhance capacity for full tissue regeneration. Using novel biomimetic materials suitable mechanical and biological properties can be provided, with adaptability to incorporate lineage specific factors and/or induce migration of native stem cell populations. Since its conception in the early 1990's tissue engineering has represented an evolutionary leap in tissue grafting, establishing autografts as the paramount procedure for implantation[16].

1.2. Bone and Cartilage Biology

1.2.1. ***Bone***

1.2.1.1. Formation

Bone is a specialist type of connective tissue that is continuely reinforced with minerals since its formation and is designed to withstand mechanical forces in the support of the skeleton and protection of vital organs. During development there are two distinct modes of bone formation (osteogenesis), both of which derive bone tissue through differentiation of osteoblasts from pre-existing mesenchymal stromal cell precursors via activation of transcriptional factors, which include RUNX2 and Osterix. 1) Intramembranous ossification; is the direct differentiation of mesenchymal tissue into bone (typically observed in the formation of the skull) [20]. 2) Endochondral ossification; is a two-step process where mesenchymal cells differentiate into cartilage, and at a later stage the cartilage is slowly calcified and replaced by bone[21].

1.2.1.2. Structure

The collagen fibril constitutes the first major component of bone and is the main three-dimensional matrix into and onto which mineralization occurs. The second major component is the bone minerals, this mainly consists of a carbonated apatite called calcium hydroxyapatite (Ca_5 (PO_4. CO_3)$_3$ OH)[20]. The protein fibril networks are reinforced by the hardened crystalline minerals, providing great tensile strength, but these matrices can also act as major reservoirs for calcium and phosphate, necessary for a wide variety of metabolic functions[22].

A different arrangement of these components varies throughout the skeleton, based on the bones function, adapting the bone density to bulk mechanical demands. Each arrangement can differ through organisation, orientation, and substructures provide superior hierarchical levels of structure and function. Mineralized collagen fibrils can be found arranged parallel, perpendicular, or juxtaposed to each other, depending on their position in the overall bone and can give rise to cylindrical columns (Osteons) in cortical bone (Figure 1). Design of the hollow cortical bone supports heavy load-bearing forces but can encase a highly porous cancellous bone marrow. The arrangement of compact and spongy bone combine to form the whole bone, this in turn fits succinctly with neighbouring bones to form the skeleton[22].

These collective arrangements form the hierarchical levels of bone, ranging in scale from nanometers to millimeters, with major implications from individual cell adhesion up to the full mechanical properties of load bearing and movement.

1.2.1.3. Cell Development, Homeostasis and Repair

Bone is continually remodelling throughout life with resident cell types that include; osteoblasts, bone forming cells that synthesize bone ECM that when encased in this matrix become known as osteocytes. Osteocytes have low metabolic activity levels and are incapable of mitotic division, but can readily communicate[23] during bone remodelling with osteoclasts and osteoblasts[22]. The bone destructive osteoclasts can dissolve both the inorganic and protein portions of the bone matrix. They are regulated by the balance of RANKL and its soluble decoy receptor, osteoprotegerin, and believed to derive from the same precursors as macrophages[20,24]. Bone resorption is essential to the homeostasis of bone remodelling, but when unbalanced can result in disease, such as age related bone loss (osteoporosis)[25].

Osteocytes are found in circular rings within the cylindrical osteons, where at the centre is a hollow central canal (Haversian canal). Perpendicular to these canals are Volkmann's canals, which interconnect osteons together (Figure 1). It is through these networks that the passage of nutrients and waste can pass in and out of bone, as well as, the migration of cells. The haematopoietic progenitor cells of the blood system are housed in the bone marrow along with multipotent mesenchymal stromal cells[26]. Bone matrix is routinely turned over for mineral use and remodelled depending on structural demands or growth and this is orchestrated through a verity mechanosensory mechanisms[22]. Resident cells sense the changes in the whole bone, localised architecture and even nano-scale breaks to fibril matrix. Osteocyte changes are pivotal in the recruitment of osteoclasts during a bone remodelling event, before osteoblast and osteocytes reconstruct an area in a specific response to changes[22].

In terms of repair the bony tissue retains a high level of self-healing capacity, provided the fractured bone fragments remain relatively close. Repair of a whole bone is possible but the regeneration of finer hierarchical structures will not be identical. None the less, this is an effective tissue reconstruction in an adult, limited only by areas of heavily mineralized bone at injury site, a fracture callus. It is undetermined if this healing capacity is reserved by the bony tissue alone or through associated effects due to the high levels of MSCs in close proximity[27,28] and/or their secretion of trophic factors[29].

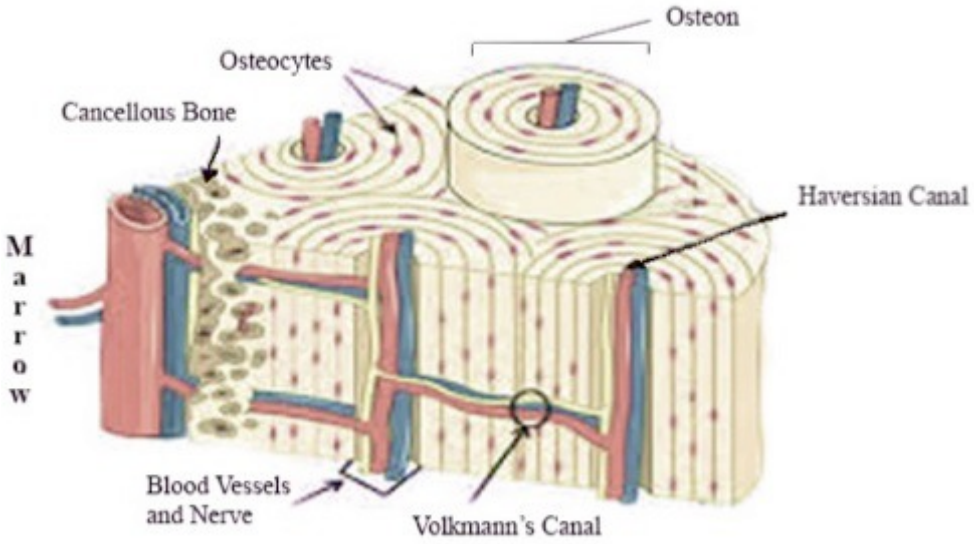

Figure 1. Structural Composition of Bone adapted from Westone[1]

1.2.2. ***Cartilage***

1.2.2.1. Formation

Chondrocytes are the resident specialized cellular component of articular cartilage, derived from similar mesenchymal precursor stem cells as bone but expresses transcriptional factors including SOX9 and specialized matrix proteins like colagen type II, COL2. They are sparsely distributed and are limited in engaging in cell-to-cell contact due to a dense encapsulating extracellular matrix (ECM)[30]. Adult articular cartilage can undergo remodeling through anabolic and catabolic processes mediated by the chondrocytes, these specialized cells maintain metabolic homeostasis of the ECM[31]. The extracellular matrix is a highly hydrated structure consisting of fibrillar and extra fibrillar components; the fibrillar components of the ECM consists mainly of collagen, a tightly wound triple helix assembly of repeat units of Gly-X-Y (glycine and typically proline and hydroxyproline dependant on the collagen type) a combination of collagen subtypes are present namely types II, IX, XI[32]. This collagen network of fibers provides the characteristic tensile strength to cartilage. The water content of articular cartilage is 80% of the total weight of the structure, and plays a major role in the impact resistance and the mechanical property of the tissue[33]. The interwoven arrangement of fibers with viscoelastic aggrecan prevents the excessive expansion of the tissue and maintains a stiff construct[34]. The non-fibrillar components are formed from polyanionic aggregates. These aggregates are derived from highly sulfated aggrecan monomers, attached to hyaluronic acid with the addition of common linker proteins[35]. The remainder of the collagen construct is formed by non-aggregating proteoglycans (PG), which exert pivotal functional roles in aiding matrix cohesion and chondrocyte function. Recognized PGs include decorin, fibromodulin and biglycan[36].

1.2.2.2. Structure

The anatomy of articular cartilage consists of three main areas, known as; 1) The superficial zone nearest the articular surface, where cells are small, numerous and parallel with surface; 2) The intermediate zone, where cells are sparse and surrounded with heavy ECM deposition; 3) The deep zone nearest the hardened calcified tide mark, beneath which is bone, has numerous hypertrophic cells vertically stacked in pillar-like structures perpendicular to the bone.

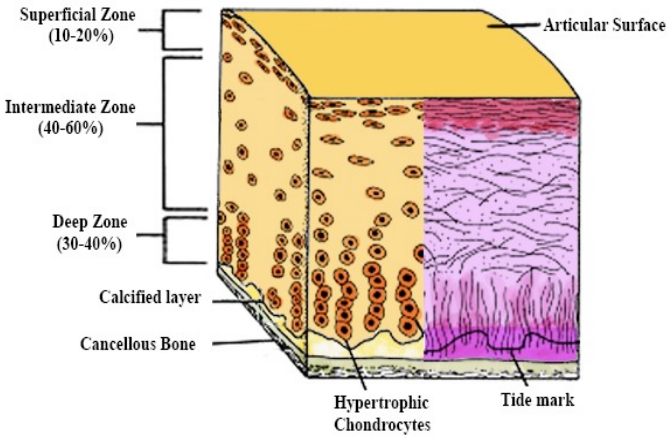

Figure 2. Structural composition of Articular Cartilage (adapted from Sophia Fox *et al.*[4])

1.2.2.3. Tissue Homeostasis and Repair

In order for articular cartilage to exert its biomechanical properties, this three-dimensional fibrous arrangement with immobilized PG is essential. Articular cartilage is defined as avascular, alymphatic and aneural this as a result translates into poor regenerative capabilities. This tissue does not self-regulate or repair like bone. As a result, interventional surgery is increasingly necessary in maintaining the morphological and physiological integrity of this tissue, and hence functional abilities of the joint of bone and cartilage

1.3. Musculoskeletal Disease

The musculoskeletal system is a network of interconnected and interdependent systems comprised of muscles, bones and joints that provides form, support, stability, and movement to the body. Often damage to one system has knock-on effects possibly resulting in long-term disabilities and loss of patient's quality of life. Musculoskeletal conditions of the joints, bones and muscles, include pain along with rarer systemic autoimmune diseases such as lupus, collectively these affect over ten million people the UK and Ireland. Osteoarthritis (OA) is the most common musculoskeletal condition and in the UK increased by 16% between 1990 and 2010[37], this statistic is set to increase due to increased obesity and an aging population. Osteoarthritis is a chronic condition that gradually worsens over time

1.3.1. *Osteoarthritis*

OA is a degenerative joint disease resulting from degradation of the articular cartilage, which can lead to bone-to-bone contact and as a result comprises a multitude of associated osteoarthritic complications most commonly observed by x-ray (e.g. joint space narrowing, osteophytosis and sacroiliac joint dysfunction). The amalgamation of this factors result in chronic pain and loss of mobility, where it commonly presents in the clinic. Monitoring the rate of cartilage degradation is still the best method of assessing the disease progression, several different techniques are available but one established method to grading by the International Cartilage Repair Society (ICRS) scores[38,39].

The pathological progression of OA is generally divided into three broad stages, which classify the pathophysiological mechanisms of the disease. Stage I involves the proteolytic breakdown of the cartilage matrix by metalloproteinase[40]. The resulting damage propagates an increase in water content with a reduction in the matrix-associated molecules. In stage II, the native cell population of cartilage, chondrocytes, attempt to compensate for such effects increasing their metabolic activity. The consequence of such activity induces fibrillation and decreased health of cells and the neighbouring cartilage. By-products from this elevated metabolic activity are subsequently released into the surrounding synovial fluid. During stage III, chondrocytes fail to maintain their level of activity resulting in the breakdown of cartilage tissue. In addition, synovial inflammation occurs as a consequence of cellular phagocytosis stimulating the production of proteases and pro-inflammatory cytokines[41]. Advanced cases of OA will present macroscopically with distinct pathological characteristics including eburnation of the subchondral bone plate and subchondral cyst formation.

1.3.1.1. Clinical Overview

A clinical diagnosis of OA is a long-standing debate amongst clinicians and one set to continue due to the multifaceted characteristics of the disease. One aspect agreed upon is the growing frequency of the disease in society, annually 1 in 5 people consults a GP about a musculoskeletal condition; this is attributable to an aging population with higher life expectancy, excessive and repetitive loading of joints in obese people or high performance athletes. In addition, other risk factors include; genetic and hereditary factors, as well as gender prevalence (females), previous joint injury due to trauma, physical joint abnormalities and related OA induced by associated disease (gout, rheumatoid arthritis). OA affects over 8.75 million people (>45yrs) in the UK; 5 million of these are female compared to 3.75 million men (ARUK statistics, 2013). In England alone, 7.3 million people have sought treatment for osteoarthritis (33% of the population >45yrs), with surgery performed for over 77,000 total knee replacements and 66,000 total hip replacements in England and Wales during 2011[42]. The rate of hip replacement increased by over 25% between 2000 and 2009 and total knee replacement was even higher, observed across the Common-wealth countries[43]. Globally it is believed to affect 10% of men and 18% of women over the age of 60 (WHO, 2010) and this is predicted to increase in the future.

1.3.1.2. Financial Burden

The disease incurs substantial economic costs to the UK economy, with hip and knee replacements estimated to exceed £850 million in 2010 and arthroscopic surgery for OA to be £1.34 million. Not only are the direct costs of treating this disease high but the indirect costs are substantial, the losses due to decreased economic production has been estimated at over £3.2 billion, and costs of £43 million for community services and £215 million on social services[44].

1.4. In the Clinic – Current Treatments for OA

1.4.1. *Non-Surgical treatments for OA*

Early detection of OA is problematic as patients exhibit few symptoms pre-degradation of cartilage and typically defer consultation until pain is felt, allowing the disease to develop in the joint. Confirmation of the disease without intervention relies on radiographic imaging detection (e.g. magnetic resonance imaging), which is difficult as limited ability to detect cartilage on the articulating surface[45].

Any natural regeneration in cartilage as result of trauma commonly causes the formation of scar tissue. This is the initial phase of wound healing in all mammals[10]; isolating a wound from exposure to prevent infection, inter-compartmental seepage and re-establishing a framework for tissue function[46,47]. Formation of scar tissue limits the future remodelling of the tissue due to the dense matrix formed and renders the restoration and regeneration of functional cartilage as negligible.

A number of therapy plans presently exist for the treatment of OA patients. Several promote the self-management of OA through light exercise and physiotherapy, but more advanced OA when presented in the clinic will require pain management. Medicating pain with analgesics, anti-inflammatory and even corticosteroid injections, are very effective but should be used in moderation due to the known dampening of drug effect and development of dependency, sustained by prolonged periods of use. Other therapies to be considered include; electrotherapy and thermotherapy for pain relief, joint supports and bracing for the joint, corrective footwear and insoles, and other assistive devices (e.g. walking sticks, etc).

1.4.2. *Surgical approaches to treat OA*

1.4.2.1. End Stage Disease Intervention

People with chronic arthritis, whether as a result of aggressive disease development in young patients or late stage maturation in elderly, once all medicinal therapy options have been exhausted surgery is the only end stage option to restoration joint mobility. Surgery is invasive but total joint replacement surgery has proven to be one of the most successful procedures, heralded as the 'Operation of the century'[48]. While this focused greatest success on restoring joint mobility and improving the quality of life to an incapacitated patient. Greatest benefit has predominantly been in an elderly population or severely damaged joints post trauma, today young patients presenting for total joint replacement require restoration of joint for high function and physically demanding longevity. Greater knowledge of the disease has helped identify disease

earlier and younger patients in early stages of disease are with an interventional treatment, having to manage degradation of joint until deemed suitable for surgical intervention. This can be a very long and painful period for the patient(s), effecting life style and overall health.

Although invasive surgery offers a number of options (Osteotomy: the correction of deformity for improved load dispersion, Arthrodesis: joint fusion, that stabilizes the joint and eliminates pain but severely restricts motion, arthroplasty: remodelling/replacing of damaged tissue to repair joint surface)[49]. There are significant risk of complication to major surgery including; deep vein thrombosis[50], stroke, and cardiac complications[51]. As well as post operative complications; infections[52], nerve damage, vascular injury, limb inequality[53], loosing[54], dislocation[55] and revision surgery[51].

The uses of titanium and related alloys (Co-Cr, stainless steel) in orthopaedic implants are based on the mechanical properties alone and unveiled a number of biological complications. At a cellular level, hard materials like titanium presents problems as they are 'overly' adhesive and with new enhanced and complex coated-implants (e.g. plasma coated Hydroxyapatite) the native MSCs within bone marrow are encouraged to form large aggregated osteogenic masses around the implant. Elevated quantity of adhesion rather than quality of adhesion tends to initially lead to soft tissue encapsulation of the implants, enabling micromotion and potentially early implant failure[56]. Eventual mineral deposition ensues around the implant increasing tensile strength at that localised area of the bone, transferred strain is placed on distal areas of the bone and the subsequent associated joints. This is referred to as stress shielding and results in reduced bone density (osteopenia)[57]. This also depletes the natural reservoir of progenitor cells used to maintain this continually remodelling tissue, altering the delicate homeostasis of native MSC population and the over all balance of the bone marrow niche[58].

Orthopaedic implants, in particularly for whole joint replacement, must be of a hardened material like alloys but at the interface between implant and body, there is a pressing need to adapt materials with an applied engineered purpose[59] for an instantaneous recovery of tissue function. The enhancement of the topographical interface shows potential in playing an integral role in communicating an alternative cell response, as cells are responsiveness to architectural (spatial), mechanical and chemical cues. A number of studies have shown that topographical features at micro- and nano-scale can control cell proliferation, migration, self-renewal and differentiation[60-62].

1.4.2.2. Earlier Disease Intervention

A number of methods have been developed to treat the disease such as; injections of Hyaluronic acid[63], mosaicplasty, autologous chondrocyte implantation (ACI)[64,65], arthroscopic debridement[49] and various bone marrow stimulation techniques (subchondral abrasion, microfracture[66]); all have drawbacks and none are perfect[67,68].

The use of chondrocytes has been established as a cell therapy for a number of years in ACI and MACI procedures. These are labour intensive procedures entailing; surgical intervention for extraction of a healthy chondrocyte biopsy, *in vitro* culture expansion (>3weeks) and second intervention for implantation. Quite frequently after this protracted and expensive process is performed a fibrocartilage repair is formed with limited cartilage function. Recapitulation of a dynamic and challenging three-dimensional tissue with end stage differentiated cells may be beyond the chondrocytes capabilities, regardless of population potency. There is a need to improve organisation and durability of the repaired tissue. The use of MSCs would be advantageous to the treatment, as trophic support and providing greater plasticity to the repair process.

In vivo bone marrow MSCs are highly motile cells in the response to damaged tissue, with the ability to cross multiple tissue barriers, secrete immunomodulatory factors at the site of injury and differentiate into multiple lineages of the mesoderm (osteogenic, chondrogenic, adipogenic and neuronal)[26,69]. These multipotent stromal cells appear ideal candidates for tissue repair of osteochondral lesions and prove effective in proof of concept by intra-articular injection in a caprine model in 2003[70]. In a randomised study for treatment of OA (72 patients) autologous MSCs were locally administered to the joint, for comparison with standard ACI, after 12 months patients reported improved pain-relief and improved mobility[71,72]. The study concluded that MSCs are as good as ACI with less donor cell morbidity and cheaper[72]. Since this work in 2010 different studies have cast doubt on the ability of chondrocytes[73] and MSCs to treat full thickness articular cartilage lesions and large variations have been seen between patients, in particularly relating to age[74-76] These applications using MSCs are still part of a two-step procedure with mass culture expansion of multipotent cells *in vitro,* and therefore there remains the potential for spontaneous differentiation, phenotypic and genetic modification.

Several studies have shown that the *in vitro* cell culture duration and degree of population expansion has an evident impact on MSCs morphology, potency, viability, and migratory properties[77]. Furthermore, other studies have shown that freshly isolated MSC show superior mobility compared to culture expanded MSCs[78] and this helped

identify different MSC subtypes, like classical MSC and multipotent adult progenitor cells as they have different migration potential[79].

An additional note, as there is a requirement for anti-inflammatory drugs post surgery as well as in the treatment of inflammatory diseases (e.g. Rheumatoid Arthritis), cell-based therapies could be used, for example the immunomodulatory properties of MSCs (or identifying immunomodulatory subpopulations of MSCs), acting as long term *in situ* protection in the joint milieu[28,80].

Moreover, recent observations suggest the paracrine effects of MSCs extend beyond immunosuppression and suggests a method of action for tissue repair, mediated by secreted factors stimulating the native tissue cells at injury sites, and these soluble factors may enhance cellular repair or may be sufficient to induce desired repair alone[28,81].

1.4.3. ***Biomaterials for Musculoskeletal Tissue Repair***

1.4.3.1. Materials presently used in treatment interventions

There are limitations of current biomaterials in orthopaedics, for example titanium, as the metal implant can satisfy structural demands for biomechanical movement of the joint, but clearly fails to adapt, remodel and grow with the person. This focus on physical performance over biological function has knock on effects (e.g. stress shielding) and satisfying the needs of the joint structure, function and tissue will enhance long-term integration and adaption to the needs of the living skeleton.

The perfect orthopaedic implant material does not currently exist because bone is architecturally distinct, continuously remodelling, and a biologically complex tissue. It has a hierarchical structure with great load bearing ability based on highly organized micro-/nano-scale components and the replication of this would be a colossal undertaking for even modern manufacturing to imitate[82]. A novel approach to provide better continuity between implant and bone is the use of new 'smart-materials', which can engage the innate tissue repair cascade.

A select few are mentioned here as there is a vast number currently under investigation and found in a variety of conformations, including; solid structures, porous foams, hydrogels, fibres (electrospun), comprised of a range of different materials, e.g. composites of calcium phosphate, ceramic, bioglass, polymers[83].

Some of the most explored organic materials include several collagens[84,85], tropoelastin[86], and silk[87]. Where as naturally derived elements like calcium,

phosphorous and silca have formed innovative systems such as phosphate glasses, silica-based glasses and different apatite combinations like hydroxyapatite and tri-calcium phosphate[88,89]. These materials have limitations due to scale-up (poor process ability), induction of highly porous structures and brittleness. Artificial materials include pure metal elements like titanium (Ti), composite alloys cobalt chromium (Co-Cr) and several polymers. While other synthetic materials lack active biocompatibility, like polymers, they can have remarkable characteristics and advantages including environmental responsiveness[90] to pH, temperature[91], ionic change, and can even have unnatural attributes like superelastistiy or quasi-plastic deformation shape-memory[92].

Building from the original success observed with ACI (1989)[93] the next generation matrix-assisted autologous chondrocyte implantation (MACI) aimed to improve patient outcomes. But cell-free strategies are now emerging, partly in combination with the success of other surgical techniques like microfracturing (1999)[94] and its modern day equivalent nanofracture® [95]. These approaches have evolved into combination processes of microfrature and a collagen I/III membrane implantation (Chondro-Gide®), to give a one step technique called autologous matrix-induced chondrogenesis (AMIC). Orthopaedics is continually exploring more possibilities that combine native tissue repair by progenitor/stem cell populations[96] within an implanted scaffold that recruits and encourages tissue repair.

1.4.3.2. Enhanced Scaffold Approaches

More recent tissue engineering strategies attempt to apply physiologically relevant biophysical and biomolecular cues to provide a platform to improve orthopedic constructs before implantation[97]. The incorporation of these two approaches into regenerative medicine aims; for the materials to directly recruit native MSCs or specialised progenitor cells into the implant scaffold (chemoattractant, e.g. stromal-derived factor-1, SDF-1[98]) and/or pre-load the scaffold with biomolecules (e.g. BMP-2 and TGF-ß) and other multifactorial stimuli to direct cell growth (scaffold architecture and surface topography).

One landmark TE implant, with notable success, was INFUSE by Medtronic (2002); a simple fusion device of bovine type I collagen sponge soaked in rhBMP-2[99]. Since then the field has uncovered potential for autologous cells to reconstitute ECM and even differentiate without the requirement of growth factors. In 2007 M. Dalby *et al.* published in *Nature Materials*, the influence of nanopit topographies in producing bone mineral formation without the presence of osteogenic media (hBMP-2 & ascorbic acid)[61], claiming equal if not better osteogenesis than chemically induced controls[100].

The physical nature of these scaffolds has a profound effect on triggering stem cell fate and tissue development[101].

Advancement of TE implants for certain tissue repair would greatly benefit from scaffolds and biomaterials being devoid of biomolecule components such as growth factors, cytokines and even peptides because this would; lower production costs, extend product life for 'off the shelf' use, and ease regulatory approval and surgical acceptance[99].

1.4.3.3. Limitations in the use of Biological Agents

Use of animal materials like whole ECM grafts (xenografts), partial grafts (decellularized matrices) and their constituent elements (proteins) has several drawbacks including; source, animal ethics, regulatory issues, purification, processing quality, reproducibility and immunological response control.

The *in vitro* expansion of cells for re-implantation requires multiple patient interventions, prolonged time and is expensive as a result. There is also biological (phenotypic) risk for modification of cells during amplification, with increased possibility of contamination. Associated risks involve delivery of unwanted cells, heterogeneous cocultures, resulting in ineffective repair. This cell 'farming' also risks simple mix-up in the delivery of the donor cells to recipient patient[102].

Cell-free devices have an increased clinical interest due to ease of medical device regulation approval, mass production potential and 'off the shelf' convenience. But performance of the final product in a uniform and global manner cannot be guaranteed, due to the large variation between patients.

1.4.4. ***Scaffold and the Cells***

A scaffold with and without cells differs in the possible applications and can offer alternative benefits. Smart-material scaffolds without cells can recruit an endogenous cell population, accessing native tissue repair and tissue specific progenitor cell subpopulations. A nude scaffold can recruit cell specific populations through the correct use of immobilized chemoattractants (e.g. SDF-1 activates CXCR4 receptors on MSCs[98]). Contrastingly, a scaffold pre-loaded with a known multipotent cell population can introduce a constructive cell population to an isolated, avascular tissue and provide the necessary elements for tissue regeneration. A negative aspect of pre-loading the scaffold with cells is the requirement of multiple interventions, like ACI & MACI, it is

cells in procedures like this can benefit from improved implant incorporation and low immune response, but the potential for karyotypic abnormalities to arise during *in vitro* culture expansion remains a concern[103,104]. This being said the most encouraging results have been seen with pre-loaded scaffolds[105].

This relatively young healthcare sector has learnt the hard way that products that work experimentally (*in vitro* or *in vivo*) won't necessarily translate into commercial success. The ground-breaking TE products needed to overcome several obstacles and issues in the scale-up, shelf-life, distribution and quality control. A fundamental philosophy evolving from this is to stop attempting to fabricate the complete complex organic tissue *ex vivo* and instead utilise key signalling pathways to unlock a cells, tissue and indeed the body's innate regenerative capacity through synthetic materials more adaptable for manufacture engineering.

In fact, growing evidence has illustrated that fragments of ECM proteins possess bioactive stimulation for cell proliferation, angiogenesis and differentiation[106]. Development of pseudo organic surfaces by the addition of ECM protein-motifs (e.g. peptides R: arginine; G: glycine; D: aspartic acid. RGD-motifs[107]) to the surface can greatly enhance the apparent biocompatibility of the structure without inhibiting the structural integrity of the implant. Careful balancing of these ligands, motifs and other mediating factors can orchestrate successful recruitment, organisation and stimulation of a progenitor population. A proof of concept study by Lee *et al.* showed the successful reconstitution of articular cartilage in a rabbit model using a composite poly-ε-caprolactone and hydroxyapatite structural scaffold including a collagen hydrogel with and without TGF-β3. None of these scaffolds were preloaded with cells but was still successful in recruiting endogenous stem and progenitor cells to regenerate tissue. The TGF- β3 loaded implants showed superior induction with added benefit of recruiting not only bone marrow MSCs but also related progenitor/stem populations from synovium, adipose (fat pad) and suspected vasculature cells[108].

Using a fabricated scaffold enables it to be tailored to regulate cell activity. Therefore we need to better understand how cells are influenced by material chemistry, topography and physical properties. Future TE applications can incorporate sophisticated textures and patterning of polymers to alter adhesion-motifs and possibly encase growth factors upon or within scaffolds to aid regeneration of a heterogeneous tissue[109].

1.4.5. *The Industry of Tissue Engineering & Regenerative Medicine*

The Industry to-date has gained some public confidence for the use of stem cells in the clinic, partly due to a hand full of high-profile successes. Several patients have regained full urinary function through TE bladder implants[110] and a 30 year old Colombian female receiving a TE tracheal segment, maintain the use of her left lung[111]. In the USA today >50million people have benefited from various forms of artificial tissue therapy. Engineered tissue is possible in numerous forms, from suspended aggregates (Cartilcel) or thin sheets of cells (Apligraf) to even thick constructs of complex tissue (Vascugel) but there is a long way to go to before achieving the ultimate engineering goal of engineering an entire functioning organ.

1.4.5.1. Origins

Throughout this field TE constructs often take designs from nature, for example during the early development of some orthopaedic applications material was quite literally taken from natural sources. Demineralized bone matrix, the proteinaceous husk of bone devoid of cells or mineral[112], was used as an implant in soft tissue and remarkably induced bone formation in surrounding muscle[113]. Mechanisms underlying this observation elucidated the role of specific proteins (growth factors) known as Bone Morphogenic Proteins (BMP). These findings accelerated discoveries of many other growth factors and even the use of animal tissue as scaffold support systems (xenografts); decellularized pig small intestine submucosa are to this day commonly used in reconstructive surgery wound healing (Oasis Wound Matrix™) and equine pericardium (the fibrous double-layer conical sac that surrounds heart) can substitute for the cranial dura mater layer following brain surgery (DurADAPT_Pegasus™).

Product evolution extends right up to the break-through success of a Columbian patient's autologous cell re-population of a decellularized allograft trachea, previously mentioned[111], which was devoid of immunological complications thanks to the presence of the patient's own cells.

Interest in autologous implants has risen as they avoid the mounting regulatory concerns for the use of animal material in human implants but by the same extent using allogeneic tissue material sources will inevitably encounter the same limitations as traditional tissue/organ transplantation… demand for donor tissue. Incorporation of the most basic biological elements required for tissue repair in a suitable, adaptable and abundant material source would be the pinnacle pursuit of biomaterial-engineering[114].

1.4.5.2. Commercial Stem Cell Therapeutics in Tissue Engineering

Since its inception the commercial industry surrounding translation of stem cell therapies, has suffered staggered growth, first reported in 1995 the TE industry was 70 companies with 3,300 employees, just before the turn of the century the industry suffered a 'dark period' (restrictions on stem cell research caused private investment and funding to be pulled), it did not recover until 2002-2003. The industry rebound and was reportedly 'back on track' by 2008, using the revamped titles of "Tissue engineering" and "Regenerative Medicine". The industry showed sales in excess of US$240 million in the US alone with global markets being considerably bigger estimated at >8% of global healthcare spending[99]. TE and RM are collectively referred to as Stem cell therapeutics in the wider healthcare industry. Between 2007 and 2011 this industry under went a competitive growth spurt, total sector activity (spending by companies on TE or stem cell products or services) grew 1.5-fold to ~$3.6 billion, sales and services topped $2.8 billion and constituted 202 companies employed >13,810 personnel[80]. Of the 2011 stem cell therapeutic activities analysed, 50% of commercial TE products were for Orthopaedic applications (>$1.7 billion)[80].

1.4.5.3. Clinical Trials

The resurgence of commercial growth in tissue engineering has vastly improved since the industries 'dark period' but also more recently from the current global recession (circa 2008-2009). Renewed confidence continues to grow today in the industry with 116 clinical studies completed in 2014 alone for stem cell therapeutics [Clinicaltrails.gov], almost half of these (57) were published and the rest (59) remain private[56]. Mesenchymal stromal cells were the dominant cell type used (35%), other types included; haematopoietic stem/progenitor cells, bone marrow mononuclear cells and even two embryonic stem cell cases. Of these studies 71% showed a general positive result with evidence of efficacy with no safety or feasibility issues[56].

1.4.5.4. Problems to overcome

It was observed amongst the most dominant cells studied, MSCs, were majority administered by intravenous injection and it became clear that a large proportion of MSCs when injected via this route became trapped in the lungs upon first passage[115-117] and relocated to other organs including the liver or spleen[116,118] Similarly arterial injections used as targeted delivery of MSCs for ischemic heart conditions, were retained by the glomeruli for a number of days[118], later it was found direct injection into myocardium improved retention[116,118]. It has also been noted that the *in vitro* expansion

of MSCs results in a shorter lifespan of cells after *in vivo* administration. Intravenously infused MSC home to the lungs from where they are cleared of within 24h[117].

One possible explanation for this could be the use of tissue culture plastic during *in vitro* expansion of MSC populations. Crude selection of adherent cells to flat plastic isolates for specific cohort of cells, dramatically increases the expression of adhesion molecules and inevitably affects the phenotype of those cells[27]. While these effects do not appear to hinder regenerative or immunomodulatory capacity of cells, delivery of cells intravenously or through unstructured systems may not be sufficient in retaining the cells, and fail to capitalise on their regenerative capabilities. A growing belief in the future of scaffold design is for tissue specific tailoring of implants to favour regenerative attributes of the target tissue for sustained and functional repair.

Therefore, future design strategies for tissue repair using stem cell therapeutics could possibly combine delivery of cells (stem / progenitor populations) with appropriate structural scaffolds, capable of the mechanical demands of injured tissue site and comprise sustained architectural, topographical and chemical design for directed therapy within biocompatible/biodegradable material(s).

1.5. Alternative Stimuli to Influence Cell Behaviour

The traditional belief that only exogenous soluble molecular mediators (e.g. transcription factors and growth factors) can be used to influence stem cell fate, has been altered by the growing knowledge of the diverse array of unassuming environmental factors that influence cells like; magnetic field [119] electrical fields (electro-magnetic)[120] and mechanical stimulation[121]. In particularly there is increasing evidence for the physical environment with different mechanisms including material elasticity, shear forces, mechanical forces and nano-/micro-scale geometries all playing a role.

Once a damaged tissue site has been stimulated and recruitment of appropriate regenerative cells has occurred, the orchestrated repair must be meticulously regulated. Cells in a heightened state of activity require appropriate structures to be present to undergo a successful regenerative program. The cells undergoing morphogenesis are not only directed by soluble mediators, but also take instruction from patterns and architecture of the ECM. One such set of genes identified in mammals is the Hox genes, and take instruction from topographical cues during morphogenesis to regulate positional memory of organ recapitulation[122].

1.5.1.1. Hierarchical Control of Stem Cell Fate by Topographical Features

The ability to engineer artificial ECMs that through physical as well as molecular interactions enable directed control of stem cell behaviour might further extend our capabilities to engineer functional tissue substitutes *in situ*. By controlling the nanotopography, mechanical properties and mechanical loading environment of tissue engineering scaffolds, we may further improve the regulation of stem cell fate in bioartificial systems[123].

The remarkable process of morphogenesis, the process in which cells self-organise into complex tissues and organs is well understood from developmental embryology. A substantial number of genes and chemical cues that mediate this process have been identified, but they are not enough to explain how singular cells create tissues to form organs in a three-dimensional space (e.g. induced cardiac muscle can rhythmically contract *in vitro* but this does not form four synchronised chambers and valves of the heart). Studies have revealed that it is here where the physical ECM architecture, mechanics and topography contribute to tissue development and homeostasis throughout adulthood.

Although the whole process in its entirety remains unclear, formation of complete structure relies on the ability of the constituent cells to generate mechanical forces

within their cytoskeleton and to transmit them between cells and across the ECM. The mechanical linkage between the cytoskeleton of neighbouring cells occurs primarily at apical adheren junctions (transmembrane cadherin proteins)[124] with studies suggesting that two cadherin proteins (α-catenin and β-catenin) mediate part of the mechanical linkage[125]. Intracellular microfilaments (actin and myosin bundles) form the contractile cytoskeleton, spanning from the nucleus to cell cortex, transmembrane integrin receptors and cadherins at the cytoplasmic interface feeding back through these links[126]. Once initiated, morphogenic movements develop ECM patterns and organ specific determination of cell fate, orchestrated through complex mechanochemical processes of which chemical cues manifest largely through changes in the physical microenvironment. An example is observed by the compaction of mesenchymal cells in the condensing dental mesenchyme that induces production of collagen VI structures, which stabilises condensed tissue form and physically induces cell lineage specific differentiation during murine tooth formation[127].

This environmental sensing extends far beyond the ability of cells to identify specific ECM ligands; the adhesive interface detects the surrounding matrix topography[128,129], rigidity[130,131] and anisotropy[132,133]. However, none of these mechanisms are necessarily linear and complex integrated systems can inter-relate to induce a wide variety of responses to environmental changes. The ECM can also act as a biochemical signal store, for example latent TGF-β from integrin bound TGF-β-binding protein 1, working independently from the elasticity of the matrix may dissociate in response to mechanical stimulus or in concert with cell cytoskeletal tension to direct development, remodelling and differentiation[134,135]. Counter intuitively, cells can sense changes in physical forces, whether it be an externally applied force or internal alteration in cell contractility, without the presence of chemical cues[136]. They can transduce these signals to change internal biochemistry or gene expression[137], a process called mechanotransduction[138,139]. The intracellular signals responding to these multifaceted mechano-sensations all feed back into, altered cytoskeletal systems, and this feed back loop appears to be integral in morphogenesis and homeostasis of adult tissue.

1.5.1.2. The Determining Intercellular Mechanisms of Repair

Cells ability to self-organisation, communication and form complex tissues is through cell-cell and cell-ECM interactions. Understanding these intricate communications, will enable an implant to artificially stimulate and unlock their abilities. These pathways have the ability to form vastly complex tissues as it was during early development, e.g. tubular networks within the kidney[140] or neural connection of the optical fibre from the

retina to the visual cortex of the brain[141]. But understanding these communications is still poorly understood. More investigation into the 'transduction' of these communications provides an insight by which the surface molecules can be balanced for a controlled response. Focus on the intercellular adhesion networks carry substantial impact on cellular functions, more over, coordination of cell-matrix and cell- cell adhesion profiles are crucial in morphogenesis therefore directing both form and function[142].

Integrins are the major cell surface receptors for cell-ECM interactions, comprised of two transmembrane proteins (alpha and beta) with many subunit variants and these can be used in an array of different integrin combinations. Integrins and cadherins share common cytoskeletal linkages and signalling pathways, the overlapping features elicit a dynamic array of cell responses and on multiple levels. Interactions with a neighbouring cell might lead to conformational changes, and even alterations in gene expression, and this can be modulated by the presence of an adhesion molecule(s) or other proteins in the ECM that are involved in regulating adhesion[143].

Cells are exposed to a number of complex molecular stimuli, providing chemotactic directions[141] but organisation and boundary formation are mostly affected by cell-cell interactions, the majority of which are regulated through cadherins (the family of transmembrane glycoproteins). The cadherins regulate cell-cell adhesion through Ca^{2+} dependant extracellular cytosolic domains and intracellular domains connect to the actin cytoskeleton through catenins[144]. They are believed to play important roles in sorting different cell types throughout morphogenesis, histogenesis, regeneration and cell motility[145,146].

Cadherins and integrins coordinate a cells response through altered physical linkages, orchestrating initial tissue development but also subsequent tissue repair, forming of complex biological tissues. It is not yet fully understood how cadherin and integrin adhesions interact to definitively affect signalling cascades as a response dynamic microenvironments. But the importance of adhesions, cell–ECM interactions (integrin-based) and cell–cell contact (cadherin-dependent), are emerging as integral mediators in the functional development of a tissue and provide a coherent picture into the integrated network of pathways rather than distinct cascades[142].

Biomaterials, devoid of defined molecular recognition sites, display how simple chemistry manipulation can provide inadvertent cell-instructive stimuli. The use of different functional groups in one study altered surface hydrophilicity with changed the conformation of fibronectin, and in turn altered integrin binding that significantly unregulated osteoblastic differentiation[147]. This use of ionic chemical moieties mimic observations made *in vivo* as many glycoproteins involved in bone mineralisation

display several negatively charged amino acids; aspartic acid residues within osteopontin (BSP-I) and glutamic acid sequences in bone sialoprotein (BSP-II)[148]. The absolute method of action is unknown, whether chemical modifications act directly on cells or modified protein deposition and orientated accumulation altered local cell attachment sites and/or including cell-cell interaction signals.

1.5.2. *Understanding Cell Response to Basic Biomaterial Environments*

Polymers enable adaptable *in vitro* investigation of cell response, as they are a cheap and abundant material with an almost infinite number of conformations and adaptable combinations. This immense adaptability is a powerful tool for the investigation of cellular response to individual adherence components, tuneable to systematically probe independent and collated mechanisms of MSC. Inert polymers materials can be devoid of chemical stimuli for cells, furthermore insoluble polymers[149] can withstand vigorous chemical and mechanical downstream processes to strip it of all organic material. Alternatively, multiple crosslinking domains maybe presented for the adherence and specific orientation of different molecules (e.g. RGD-motiffs or growth factors). Some polymers can also degrade in changing conditions (environmentally responsive)[150].

Numerous parameters; pressure, thermal casting, pH, solvent evaporation, and photo-activation, can be controlled for monomer polymerisation and in an array of fabrication methods, such as; static casting, moled casting, spin coating[151], polymer embossing[132], lithography[152], electrospinning[153] and 3D-printing[154] can be applied to the polymer. For example: spin coating of a liquid polymer(s) over a solid surface provides an efficient technique for low quantities of materials to be spread across a solid substrate. Thin polymers films minimise elasticity forces of the material and can help focus/refine the effect of individual parameters, like topography.

Polymers provide a powerful tool kit in the scientific investigation of the topographical influence on cell adhesion, mechanics, organisation and ultimately cell fate. The creation of micro- and nano- scale topographies has offered unique opportunities to understand mechanisms of cell response to the physical environment, morphological effects, individual cell cytoskeletal conformation, cellular tension and integrin interaction at the nanoscale[155].

It is necessary to breakdown the process of an individual cells response to mechanical and chemical signals at the molecular level, if we are to understand how all environmental forces regulate and guide appropriate tissue development. Identifying the simplest possible chemistry, topography and architectural features to influence tissue behaviour is intrinsic to developing the next generation of therapeutics[127,137,155].

AIMS & OBJECTIVES OF THIS THESIS

The aims of this research were to investigate whether novel surfaces could be efficiently and reproducably fabricated using a combination of established techniques for polymer surface generation, to produce textured patterned surfaces adaptable to biological modifications. Thus enabling the investigation whether these could be used to subsequently influence or direct stem cell behaviour *in vitro*.

The specific objectives to achieve these goals were:

1. Create distinct and adjustable topographies to investigate the influence physical surfaces have on mesenchymal stromal cell adherence, growth and development.
2. To refine a spin coating method to prepare a systematic series of polymer surfaces with controlled chemistry and topographical features, using a simple and reproducible fabrication approach.
3. To investigate the downstream modification of these novel polymer surfaces for discrete immobilization of biologically active molecules.
4. To isolate adult human MSCs from bone fragments and demonstrate their capablities to differentiate into three distinct cell types.
5. To investigate the MSC response to the different defined polymer surfaces and determine the relative importance of topographical features in determining the cell activity.

On completion of this research, substantially more will be understood regarding the potiential for modified textured polymer surfaces to influence a native progenitor cell population for tissue engineering applications.

CHAPTER 2. MATERIALS AND METHODS

2.1. Cleaning and Treatment of Substrate

2.1.1. *Piranha Cleaning*

Preparation of the substrate before spin coating requires the glass substrate to be completely clean. Piranha cleaning strips the glass of any physical particles and even organic contaminants including oils. The highly effective action of piranha cleaning is due to a combining of acid with alkaline [Sulphuric acid (H_2SO_4): Hydrogen Peroxide (H_2O_2)]. These two highly corrosive reagents when combined react violently in an exothermic reaction striping the glass substrate of any contaminants. Piranha cleaning was only allowed to react for 10mintues before being quelled in excess water (add acid solution to water not the reverse). Longer reaction times would lead to corrosive etching of the glass. The acid and base were added together in equal measure, at a ratio of [1:1].

Warning: Piranha is a highly corrosive, exothermic reaction, and attacks all organic materials. Under no circumstances is it to come in contact with eyes or skin. Do not breathe the vapours. All work to be performed in a fumehood with full personal protective wear and equipment. A neutralization basin (1L) of water is used to quench the reaction, fully submerge reaction in case of emergency.
Piranha violently reacts with most plastics. PTFE (Teflon) is the only safe plastic to use with Piranha. You must do Piranha processing in glass containers using PTFE or stainless steel tools.

Reagents and Equipment:
Circular cover slips, borosilicate glass (13 mm, no.631-0150; 22 mm, no.631-0159. VWR, UK)
Sulphuric Acid (96 %), H_2SO_4 (Sigma Aldrich, H1009)
Hydrogen Peroxide (30 %), H_2O_2 (Fisher scientific, 12933634)

2.1.2. ***Plasma Cleaning***

Treatment of the substrate (glass cover slips; 13 / 22 mm in diameter) by bombarding the surface with low energy electrons while in a vacuum, strips the outer surface clean of any contaminants, this is known as plasma cleaning. This is a superior technique commonly used in the removal of contaminant layers from semiconductors and treatment of glassware in optical devices[156].

We applied plasma treatment to the glass surfaces for 60 seconds in a negative atmosphere (vacuum). Substrate surfaces were found to be extremely hydrophilic after treatment.

Equipment

Vacuum Plasma Cleaner (MTI corporation, PDC-32G)

2.1.3. ***Silanization Treatment***

To optimize the adherence of the demixed polymer film to the substrate, a fine layer of silanization was applied to the glass surface after cleaning. Silanization applies self-assembling organo-functional alkoxysilane molecules to a substrate surface, like Mica, metal and glass, because they provide hydroxyl groups, which attack and displace the alkoxy groups of silane to forming covalent –Si-O-Si- bond.

3-(Trimethoxysilyl) propyl methacrylate was selected to covalently link polymer to substrate as it displays methoxy groups $–OCH_3$ available for adherence to PMMA.

Reagents

3-(Trimethoxysilyl) propyl methacrylate (Sigma Aldrich, M6514)

Ethanol, absolute (Fisher scientific, BP2818-4)

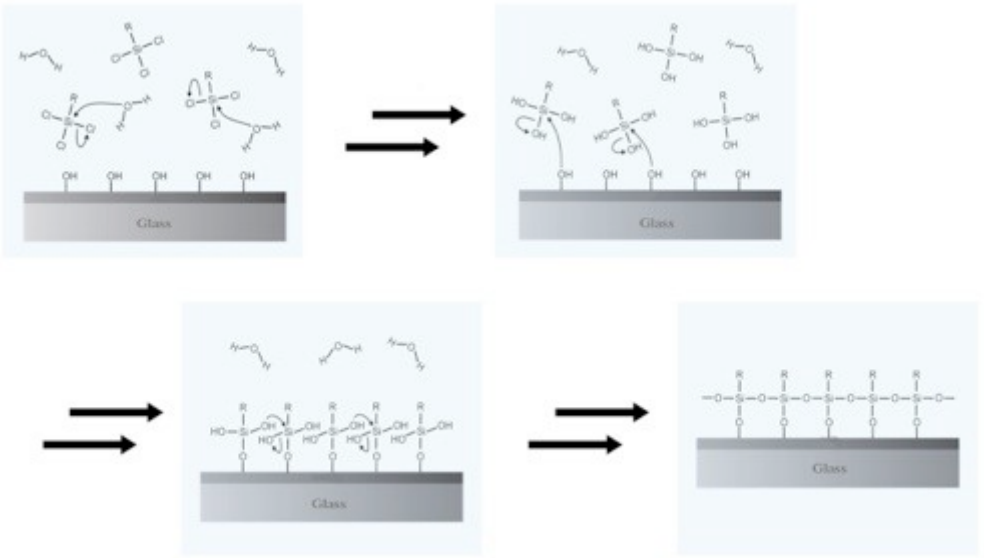

Figure 3. Self-assembly and organisation of silanization layer when coated onto the glass substrate. Silicone silanization self-orientates to present methoxy groups for ploymer to bind with (2%v/v silanization reacts O/N @RT).

2.2. Polymers

Two polymers: Polystyrene (PS) M_w ~ 250,000 and Poly(methyl methacrylate) (PMMA) M_w ~ 550,000 were used in this study. Both polymers were separately dissolved in clean glass vials by the organic solvent Toluene, anhydrase 99.5% (179418, Sigma Aldrich, UK). Environmental surfactants like oxygen and water (moisture) were limited by the use of nitrogen balloons. Pellet forms of the polymer took longer time to dissolve but this was accelerated by vigorous agitation, ~12 h.

The strong immiscible nature of each polymer causes desired phase separation when forced together on a solid substrate. For this reason homo-polymers were only added together in the desired ratios (v/v) minutes before use [10:90 / 25:75 / 40:60 / 50:50 and vice versa]. Structural formulas see Figure 17 (pg. 79).

Reagents and Equipment:

Polystyrene, atactic (Alfa Aesar, no.44537)

Poly(methyl methacrylate) (Alfa Aesar, no.43982)

2.3. Imaging

2.3.1. *Microscopy*

A combination of two upright fluorescent microscopes were used throughout the course of this research (DMLD, Leica, UK) and (Leica DM4000B, Leica, UK) both providing bright field, DIC, phase contrast and fluorescence microscopy. Images were obtained with SPOT advance and DFC 310 FX cameras, driven by Spot-advance software and Leica AF software, respectfully. A full-range of dry objectives (2.5X, 5X, 10X, 20X and 40X) were used including a 100X Oil objective. Fluorescent filter sets for UV/Dapi, Alexa480/FITC, Rhodamine and Texas Red were available.

The microscopy imaging software allowed for basic adjustment of images (scale bars, overlay images, etc.) but detailed morphometric analysis was preformed with either ImageJ or Fiji software.

Reagents and Equipment:

Fluorescent microscope 1 (DMLD, Leica, UK)

Fluorescent microscope 2 (DM4000B, Leica, UK)

SPOT advanced (Diagnostic Instruments Inc., Michigan, USA)

2.3.2. *Cell Fixation*

At the end of the experimental culture period cells were embedded in a formalin-saline to; terminate cellular growth, preserve biological structure and for long-term storage. A variety of methods were employed including; 10% Formalin, 4% Paraformaldehyde and absolute Methanol fixing and additional paraffin-wax embedding was performed as and when stated.

Formalin fixation was commonly performed before wax embedding and excess formalin was washed away with 70% ethanol.

Paraformaldehyde (4% w/v) was used at 37ºC to increase cross-linking and maintain biological structural integrity. Excess paraformaldehyde was washed away with a weak detergent solution to expose epitopes, further details explained below.

Glutaraldehyde[157] fixing is from the Formalin family but is far smaller molecule, providing high quality cross-linking of proteins for electron microscopy.

Methanol (absolute) was used at -20ºC given strong alcohols are good coagulant fixatives. Alcohol evaporates enabling rapid drying of sample and aids clear histological staining.

Due to the indiscriminate masking effects in of most formalin-fixed tissue an antigen retrieval step is required to maximize antibody binding. This is due to the formation of methylene bridges during fixation, which cross-link proteins and can therefore mask antigenic sites. Heat induces epitopes retrieval (HIER) and is one of the most common damasking methods, although in this particular case proteolysis was best in the liberation of extracellular epitopes. We utilized a combination of dilute detergents to liberate the desired epitopes of interest.

Reagents

Formalin (Sigma Aldrich, HT501128)

Paraformaldehyde (Sigma Aldrich, P6148)

Glutaraldehyde (Fisher Scientific, 119980250)

Methanol, absolute (Fisher Scientific, 10675112)

2.3.3. *Fluorescence microscopy*

At end of culture period adherent cells were washed once with Hank's balanced salt solution (HBSS) to remove culture medium and any excess protein in solution. A weak solution of paraformaldehyde was used to fix cells, preheating the solution to 37ºC to increase the cross-linking efficiency. Multiple, vigorous wash steps with a dilute detergent in PBS (0.1% Tween 20), limits the entire embedding of samples in formaldehyde. A sandwich antibody technique identified specific mature Vinculin sites with primary rabbit-anti-Vinc and this was fluorescently labelled by secondary mouse-anti-rabbit FITC antibody, blocking with 3% goat serum increased specificity. Complementary staining of F-actin by Rhodamine phalloidin was preformed in conjunction with secondary antibody and was enhanced by additional wash steps with 0.1% Triton x-100 to increase permeability of cellular membrane. Staining of nuclei was achieved by the presence of DAPI (4',6-diamidino-2-phenylindole) in the Vectorshield mounting media; this oil immersion media protects the fluorescent samples from accelerated degradation.
Complete protocol can be found in the appendix pg.XXXVII.

Reagents and Equipment:
Primary antibody [Anti-Vinc, produced by Rabbit] (V4139, Sigma)
Secondary antibody [Anti-Rabbit IgG with FITC, produced by Mouse] (Sigma)
Goat serum (G9023, Sigma Aldrich)
Rhodamine Phalloidin (P1951, Sigma Aldrich)
VectorShield® with DAPI (H-1200, Vectorlabs)
Tween 20 (P1379, Sigma Aldrich)
Triton X-100 (X100, Sigma Aldrich)

2.3.4. *Scanning electron microscopy*

A high intensity electron beam is focused onto the surface of a sample and the interaction of the electrons with the sample can be detected using a photon detector. This combined with the position of the beam can produce an image. Scanning electron microscopy (SEM) can be performed in high or low vacuum and in either wet or dry conditions, but best results are seen under high vacuum on dry samples that have been coated in a very fine layer of metal (i.e. Gold) to enhance electron reflection and hence improve detection image.
Samples devoid of cells were cleaned with compressed nitrogen (N_2) to remove all dust particles and then mounted and gold coated.

At the end of the designated culture period (typically 24-48 h) cells were terminated by aldehyde fixation. The surfaces were washed once with HBSS and twice more with sterile PBS before a 2%(w/v) Glutaraldehyde solution was added and left to incubate @4ºC, 1 h. Samples were washed repeatedly (x3) in PBS to remove any excess glutaraldehyde before dehydrating in a series of alcohol wash-steps. The samples underwent i) chemical or ii) critical point drying; once dehydrated (100% Eth.) surfaces were i) chemically dried by bring samples up through increasing concentrations of hexamethyldisilazane (HMDS) [20,40,60,80 and 100%] and once in 100% HMDS are left to evaporate for 12 h (O/N) in fumehood; ii) mounted into vertical stainless-steel tower chamber and separated by 1.5mm bevelled washers. Critical point CO_2 drying was performed at ~1,200 psi and ~35ºC, where liquid CO_2 replaces water. When the process is released the shift in temperature through the critical point with decreasing pressure changes liquid CO_2 into vapour. Low temperatures without surface tension effects maintain biological integrity and morphological structure.
All slides were mounted onto aluminium stubs with carbon adhesive tabs/tape and gold coated before being placed in a high vacuum gold coating chamber (Polaron). Samples were analysed using a Scanning electron microscope Stereoscan 240 (Cambridge Instruments Ltd., UK) with digital images collected by Orion6.60.6 software.

<u>Reagents and Equipment:</u>
Hexamethyldisilazane (Sigma Aldrich, 440191)
Automatic Sputter Coater, Au (Polaron, E5200)
Electron microscope (Cambridge, Stereoscan 240)

2.3.5. *Atomic Force Microscopy*

Surface topographies were observed in greater detail using atomic force microscopy (AFM). The AFM operates by physical interaction of a cantilever tip coming into contact with the test surface. Adhesion forces between tip and surface are detected by the deflection of a laser reflecting of the back of the cantilever head. Thus, the cantilever tip can be used to image with atomic resolution and its ability to image surfaces under liquids gives greater accuracy and is more conducive to biological conditions.

Different scanning settings were explored (contact/tapping mode, wet/dry, etc.) and best images were found to come from immersed scanning contact mode. Where sample surfaces were submerged under ultrapure water, in specialised water contact chamber. Contact mode gently lets the probe touch the polymer surfaces in a controlled manner by a scanner. The probes were typically made from, silicon or silicon nitride, piezoelectric material that can move the probe very precisely in the x, y, and z axes. The cantilever probes also have a sharp integrated tip. The amalgamation of the sharp tips, the very sensitive optical lever, and the highly accurate movements by the scanner, in combined with the controlled probe-sample forces allow for extremely high-resolution images.

AFM images were captured using Agilent technologies (S500 MAC mode III, USA) and Picoview 1.8.2 software for [80 / 40 / 20 / 10 μm^2] areas at 1.2lines/s; 612 pts/line resolution. Data visualisation and analysis was preformed on Gwyddion 2.38 (Sourceforce.net, Czech Republic)

A detailed account of the AFM setting used for these experiments can be found in the appendix pg. XXIV

Materials and Equipment:

Atomic Force Microscope (S500 MAC mode III, Agilent Technologies, USA)

Picoview software (version 1.8.2)

Gwyddion software (version 2.38)

Sharp right-angle tipped tweezers

Ultrapure water

2.4. Cell Culture

2.4.1. *Media, Supplements and Passaging*

The maintenance of cell populations dissociated from the parental tissue (primary cells) or immortalised cell lines, requires assimulated culture conditions to native *in vivo* conditions; incubator is slightly hypoxic and at body temperature (5% CO_2 and 37ºC). Specific adherent cultures grown here were cultured in nutrient rich media on suitable sterile plastic. All activities with the cells were preformed under aseptic conditions to minimise infection from bacteria or fungi. Cell populations were regularly passaged using enzymatic means to avoid monolayer cultures becoming over confluent and to assist health propigation of the culture.

The nutrient medium for MSCs was a modified adaptation to basic Dulbecco's modified eagle's medium with low glucose (DMEM-LG), sodium bicarbonate and without glutamine, was used as a basal media. Additional to the medium was Glutamax (1X); a more stable form of L-glutamine for long-stay cell culture (≥ 1month) and a combination of Penicillin/Streptomycin (P/S) antibiotics to minimise infection, working concentration 1X (P=100 units/ml and S=100 µm/ml).

Occasionally fibroblast-like growth factor beta (β-FGF) was used intermittently to assist proliferation but was dropped after initial year, due to the selective nature of FGF responsive cells during cell expansion.

Passaging cell: Remove and discard the spent cell culture media from flask. Wash with sterile PBS twice before removing all fluid. Add approprate volume of trypsin (enzyme) to the cells according surface area of the flask (20µl per cm^2). Heat the flask to 37ºC to accelerate enzyme action (~2 mins), gently striking the flask on the sode can help physically dislodge the cells. Once cells are in suspention netrilise the enzyme action by adding an equal volume of medium (containing FBS) as trypsin. Spin down cells into pellet using a centrifuge (200xg; 5 mins) and carefully remove supernatent. Resuspend in fresh media and dispence into new larger/multiple flasks. Incubate at 5%CO_2 37ºC.

<u>Reagents</u>

DMEM-LG (Sigma Aldrich, D5546)

1% Penicillin/Streptomycin solution, 100X (Invitrogen-Gibco, 15140)

1% GlutaMax 100X solution (Invitrogen-Gibco, 35050) 10%

Foetal Bovine serum (Sigma Aldrich, F9665)

[Verified from a countries to be free of bovine spongiform encephalopathy (BSE)]

0.05% Trypsin-EDTA (1x) (Invitrogen-Gibco, 25300-054)

2.4.2. *Isolation of Primary Human Bone Marrow Stromal Cells from Bone Fragments*

The primary mesenchymal stromal cells were sourced from the discarded tissue waste of elective orthopaedic surgeries for total knee and hip replacements (TKR / THR), restricting cell selection to geriatric patients in the advanced stages of OA[158]. These were preformed at the Freeman Hospital, Newcastle upon Tyne following informed consent from the patients and following all local and national ethical guidelines and practice. Extraction of MSCs were excavated from interior trabecular spongy bone and gently washed in a buffer containing ethylenediaminetetraacetic acid (EDTA) to aid detachment and separation of the cells. Mincing with surgical pliers exposed greater areas of the cancellous bone, this was then filtered through a 50 μm sieve and the cell suspension is then carefully pored above an equal measure of Ficoll™. The density gradient separation occurs when the biphasic solution are forced together by centrifuging at high speed (700 g, 40 mins). The contents of the tube were separated out into different fractions (*bottom to top*) red blood cells, granulocytes, mononuclear cells and plasma. The mononuclear cells (MNCs) were extracted and additional wash and spin steps were performed to get a purified pellet (Solution A). This pellet was re- suspended in culture medium and spread over plastic for MSCs to adhere too, with each media change the selection for plastic-adherent cells was refined and self re-newel capasity of MSCs enables them to proliferate and become the dominant population over time.

Primary isolates underwent feeding every 2-3 days and passaged on average every week after initial first passage after ~2 weeks (seeding ~5000 cells/cm^2). Bone samples should be used within 24 h of harvesting (if kept at 4°C) and within 4 h (if kept at room temperature). Adherent mesenchymal stromal cells should not be used past passage 6 *in vitro*[159,160].

Bone fragments obtained included; the femoral hips and femoral condyles but intermittently bone marrow aspirates accompanied THR. Aspirates recovered from the marrow of the gluteal tuberosity of femur require less mechanical breakdown of cortical bone and more wash steps due to the blood rich nature of the marrow.

Other enrichment techniques were explored including a commercially available spin column, coated with a Haematopoietic binding cocktail (RosetteSep® Human Mesenchymal Stem Cell Enrichment Cocktail). But was discontinued as excessive processing of a small population was counter productive.

Please find detailed protocol(s) in appendix pg. XXVIII.

Note: All cell culture procedures are preformed within Class II Laminar flow hood All surfaces are sterilized with 70% Ethanol.

Name	Contents
Wash Solution A	DPBS (with $Ca^{++}$and Mg^{++}) & 1%P/S
Wash Buffer	5mM EDTA, 0.2% bovine serum albumin (BSA), in Solution A.
Cell Culture Media	DMEM (with low glucose and without L-glutamine), batch tested 10/20% FBS, 1% P/S, 1% Glutamax optional: β-FGF (8 ng/ml)

Table 1. Itemised solutions and buffers for primary cell isolation and nutrient cell propegation medium for sustand cell growth.

2.5. Cytotoxicity testing

2.5.1. *MTT cell proliferation assay*

Measurement of cell viability and proliferation was readily achieved through a quantitative colorimetric assay, identifying mitochondrial succinate dehydrogenase activity in living cells. The Thiazolyl Blue Tetralian Bromide (MTT), yellow colour in solution, is directly degraded by dehydrogenase in the mitochondria of living cells and converts the yellow coloured tetrazolium salt (insoluble) into blue/purple coloured formazan (soluble)[161].

The intensity of the blue/purple colour formed can be quantified by specific absorbance wavelength at 570 nm and measured using a spectrophotometer plate reader (Tecan sunrise). Using a standard curve plot of known cell numbers vs absorbance, we can calculate the cell number of other unknown samples.

Reagents and Equipment:

96-well plate_Flat bottom (Costar 3596)

Platereader (TECAN sunrise®)

DMEM (same as culture medium) or PBS

MTT reagent – 3-(4,5-dimethythiazol-2-yl)-2,5-diphenyltetrazolium bromide (Sigma M2128-1g)

Absolute isopropanol (Propan-2-ol, Fisher Ltd. P/7507/17)

2.6. Differentiation of Primary Mesenchymal Stromal Cells

2.6.1. Induced Differentiation of Primary MSCs into Adipogenic, Osteogenic and Chondrogenic Lineages

Cultures of suspected pluripotent mesenchymal stromal cells (MSCs) were isolated from bone marrow fragments within 24 h of surgery. Mononuclear cells were separated from the diverse complex of stromal cells found in bone by isolating for plastic-adherent, fibroblast-like cells[162] during prolonged tissue culture expansion. This helped in achieving a more homogeneous population.

Multipotency evaluation or differentiation experiments were initially preformed in 8-well chamber slides; one well for every lineage, except for chondrogenesis[163-165], which has two as to access difference of monolayer culture and micro-mass differentiation. Control chambers of identical numbers of cells are seeded and cultured in standard media mirrors each chamber[166].
Similar seeding densities were used for larger differentiation experiments on glass slides and polymer topographies. Identical protocols were followed for stimuli where stated and histological staining.

	Adipogenic	Osteogenic	Chondrogenic	Micro-mass	
Expt.				O	Patient:
Ctrl				O	Date:

Monolayer – 10,000 cells per well
Micro-mass – 200,000cells per well
Incubate @ 37°C, 5%CO_2 for 14 days
Change media every 3 days

2.6.2. ***Chondrogenesis***

- Seed cells in monolayer (10,000) or micro-mass (200,000) per surface
- Wells were filled with 500 µl of serum-free media and incubated over night
- At Day 1; media changed for Chondrogenic medium and incubate for 14 days
- Media changed every 3 days
- Expt. terminated and fixed with 4% Paraformaldehyde
- Histological staining with Alcian Blue, Safranin O and Masson's trichrome. Identified presence of proteoglycans, collagen and overall tissue definition, respectively.

Note: adhered micro-mass was seeded as droplet of ~10 µl and left to adhere overnight. Suspended Micro-mass culture were also preform, please see 'Alternative Chondrogenic Differientiation *in vitro* Techniques' Appendix pg. XXXIV.

Chondrogenic Medium

Conc.	Volumes (per 50ml)	Reagent	* Only to be added on the day of use
1%	500µl	GlutaMax	
1%	500µl	P/S	
100 nM	5µl	Dexamethasone	
50 µg/ml	83µl	Ascorbic Acid-2-phosphate	* (1.7 µl per ml)
40 µg/ml	20µl	Proline	
1x	50µl	ITS + L premix	* (10 µl per ml)
10 ng/ml	500µl	TGFβ3 ★	* (10 µl per ml)
	47.9ml	DMEM (low glucose)	

Reagents and Equipment:

Trypsin (Gibco, 25300-054)

PolyPropylene tubes, 15 ml (Starlab, E1415-0200)

Filter-sterilise (0.22 µm pore size)

Serum-free Medium:

DMEM - low glucose, without L-Glutamine (Sigma D5546)

1% Glutamax (Gibco, 35050)

1% P/S (Gibco, 15140)

Additions:

Ascorbic acid (Fluka Biochemika 49752)

Insulin, Transferrin, and Sodium selenite, human (ITS+L premix) (Sigma I3146)

Dexamethasone (Sigma D4902)

Growth factor stimuli ★

TGF-β3 (Gibco PHG9305) @10 g/ml final concentration

Kartogenin (Cambridge Bioscience, CAY11826) @10 ng/ml final concentration

2.6.3. ***Osteogenesis***

- Seed MSCs at 10,000 cells/surface (monolayer)
- Well was filled with 1ml of standard media and incubated O/N to allow cells to adhere.
- Medium was replaced the next day for Osteogenic media and incubated for 14 days
- Media was changed every 3 days
- Expt. terminated and fixed with 4% Paraformaldehyde
- Histological staining with Fast blue RR and Alizarin Red-S. Identified presence of alkaline phosphatase and calcium deposition, respectively.
- Additional tests with alkaline phosphatase substrate quantified ALP levels by spectroscopy .

Osteogenic Media

Conc.	Volumes (per 50ml)	Reagent	* Only to be added on the day of use
1%	500 µl	GlutaMax	
1%	500 µl	P/S	
10%	5 ml	FBS	
50 µg/ml	83 µl	Ascorbic Acid-2-phosphate	* (1.7 µl per ml)
10nM	0.5 µl	Dexamethasone	
5mM	250 µl	B-glycerol phosphate	
100 ng/ml	500 µl	hBMP-2 ★	* (10 µl per ml)
	43.2 ml	DMEM (low glucose)	

2.6.4. ***Adipogenesis***

- Seed MSCs at 10,000 cells/surface (monolayer)
- Well was filled with 1ml of standard media and incubated O/N to allow cells to adhere.
- Confluent monolayers of cells were treated in rotation of induction (I) and maintenance (M) media every 3 days.
- Change media every 3 days, for (I) and 2 days for (M) alternating between both A minimum of 3 Induction cycles were required, approx. 14 day incubation, experiment terminated and fixed with ice-cold Methanol
- Histological staining with Oil Red O. Identified the presence of fat vacuoles in the cytoplasm of differentiated cells

Adipogenic Induction Media (I)

Conc.	Volumes (per 50ml)	Reagent
1%	500 µl	P/S
10%	5 ml	FBS
10 µg/ml	50 µl	Insulin (human)
1 µM	50 µl	Dexamethasone
0.5 mM	250 µl	Isobuthylmethylxanthine (IBMX)
60 µM	3 µl	Indomethacin ★
20 nM	37.5 µl	Insulin-like growth factor 1 (IGF1)
2 µM	5 µl	Rosiglitazone
	44.1 ml	DMEM (low glucose)

Adipogenic Maintenance media (M)

Conc.	Volumes (50ml)	Reagent
1%	500 µl	P/S
10%	5 ml	FBS
10 µg/ml	50 µl	Insulin (human)
20 nM	37.5 µl	Insulin-like growth factor 1 (IGF1)
	44.5 ml	DMEM

2.6.5. ***Staining of Differentiated MSC Populations***

	Stain	Concentration	Volume	Incubation
Adipogenic	Oil O Red	0.3%	50-100 µl	@RT 60min
Chondrogenic	Alcian Blue	1%	50 µl	@RT 30min
Osteogenic	ALP +	-	500 µl	@ 37°C 15min
	Alizarin Red S	2%	50 µl	@RT 2min

General Considerations

- All procedures involving formaldehyde must be performed in a Laminar flow cabin / fume hood.
- Samples should never dry for more than 30 seconds throughout whole process.
- Gently add and remove all reagents to the sample to avoid cell removal. Example: drip reagents down walls of the culture chamber.

Fixing Cells

- Remove cultures from incubator and place in a fume hood.
- Remove media from the wells, always from the control first.
- Gently rinse the plate with 2 mL of sterile DPBS.
- Remove the DBPS and add 500uL 4% Paraformaldehyde. Incubate 20-30 minutes @ RT.

2.6.5.1. Adipogenic_Oil Red O

- After cells are fixed. Remove 4% Paraformaldehyde
- During this time prepare Oil Red O working solution (a)
  a) Make a 3:2 dilution of 0.5% Stock solution in upH_2O
  [0.5%stk (500 mg in 100 ml Isopro)]
  Note: this working solution is only stable for 2hr
- Remove all Paraformaldehyde from well and wash twice with PBS
- Add 500 µl 60% isopropanol to each well and leave for 5 min
- Remove Isopropanol and add 100ul Oil Red O working solution (ensure this layer doesn't evaporate)
- Incubate @ RT for 60 min
- Remove stain and well with room temperature tap water

Optional: stain cell nuclei by adding 200 µl Hematoxylin stain to well for 1min @RT

2.6.5.2. Chondrogenic_Alcian Blue 8GS

- After cells are fixed. Remove 4% Paraformaldehyde
- Replace with 1% Alcian Blue, ~50 µl per well and incubate @RT for 30 min
- Remove access stain and wash with 3% Acetic Acid (2-3 min)
- Remove and rinse with uH_2O x2
- Rinse well in 95% Ethanol (3 min)
- Replace with 100% Ethanol (3 min)
- Finally wash with uH_2O

2.6.5.3. Osteogenic_ALP & Alizarin Red S

Alkaline Phosphatase assay (ALP) [p-nitrophenol]

- After cells are fixed. Remove 4% Paraformaldehyde
- Add 500 µl 0.1M Tris buffer @ pH = 8.3, to alkalinise the sample
- Empty well and replace with 500µl Alkaline phosphatase yellow (pNPP) Liquid substrate.
- Incubate for 15 min @37°C
- Transfer into a 96 well plate, placing 100 µl of liquid into each well
- Read on plate reader @405 nm [Tecum Sunrise™ plate reader]

Optional: Utilizing the fluorescent Dapi to count nuclei, hence cells, per well. One can calculate amount of p-nitrophenol in absorbance in correlation to number of cells present.

Alizarin Red S[169]

After cells are fixed. Remove 4% Paraformaldehyde

Add pre-filtered 2% Alizarin Red S. ~50 µl per well and incubate @RT 2 min

Add 500 µl Acetone in the fume hood and incubate @RT for <10 min

(dehydrate) Rinse well with tap water

Chamber slides: Remove chamber walls and any excess glue

Glass slides: Load samples onto microscope slides

Apply mounting media (with Dapi) and carefully place cover clip over samples

Gently apply pressure to remove air bubbles and seal with nail varnish around the periphery

Note: evaluation of Safranin O for Chondrogensis (stains Col II) and Von Kossa for Osteogenesis (stains mineralized phosphate) were assessed and found inferior to the selected.

2.7. *Phenotyping MSC Cell Populations by Flow Cytometry*

Flow cytometry is a powerful technique for the high through put characterization of cells and quantification of cell attributes (e.g. surface markers). Every cell in the mammalian body displays surface markers distinct to the cell type, or lack of markers for definitive phenotypes. The population of cells of interest can be stained with specific antibodies for cell-surface molecules and usually concurrently for multiple antibodies, before being quantified by flow cytometer simultaneously. Cells are focused into a single-file stream by hydrodynamic fluidics, where individual cells past an observation area for analyse by detectors and one if not several excitation lasers. Two main methods of light scattering techniques are utilised; forward scattering (detects cell size) and side scatter (detection of complex cellular components). Careful selection of multiple fluorophores of different wavelengths coupled to antibody probes, enables an array of markers to be checked in unison.

No one specific phenotypic marker exists for MSCs, this is believed to be due to their naive multipotent state. Therefore detection of MSC markers is a complex of several positive and negative cell surface markers, established by the international society for cellular therapies 2006[170].

Cells were passaged and when in suspension separated into four tubes, 100,000 cells per tube. Tubes were spun down to form cell pellets and the supernatant removed. The appropriate antibodies are added to each tube, except DAPI, gentle mixed and incubated at 4ºC in the dark for 15 mins. Wash cells with 200 µl of wash buffer and spun down again, Resuspend cells in 400µl of FACS buffer and keep in the dark until needed. DAPI is added just before going to the cytometer. Setup BD FACSCanto II flow cytometer and run auotmated cleaning program before loading each tube separately and in numerical order, with wash steps in between samples. Obtain results on the BD instrument acquisition software and followed by analysis on BD Divia software.

After passaging experiment does not need to be sterile.

Tubes

1. Unstained cells– Negative control group to account for any auto-fluorescence
2. Isotypic control stain – The characteristics of the primary cell antibodies have no specificity for the target antigen. They bind none-specifically to the cells and cause fluorescence, providing negative control and help to differentiate non-speific Ig signal from specific antibody signal.
3. Antibodies stain 1 – Antibodies against all three positive markers (CD73, CD90, CD105) and all four negative haematopoietic markers (CD14, CD19, CD34, CD45).
4. Antibodies stain 2 – Antibody against Class II human leuocyte antigen HLA-DR.

Antibody	Fluorophore	Product number*
CD14 (φ1)	FITC§	345784
CD19	FITC	345776
CD34	FITC	555821
CD45 (leukocyte common antigen, Ly-5)	FITC	345808
CD73 (ecto-5'-nucleotidase)	PE	550257
CD90 (Thy-1)	PerCP-Cy 5.5	561557
CD105	APC	562408
HLA-DR	APC-H7	641411
Isotype		
Mouse IgG1, ctrl (specific for dansyl)	FITC§	555742
Mouse IgG1, k	FITC	555748
Mouse IgG1, k	PE	555749
Mouse IgG1, k	PerCP-Cy 5.5	552834
Mouse IgG1, k	APC	555751
Mouse IgG2a, k (specific for TNP)	APC-H7	560897

Table 1. Details of MSC of target antibodies and their coupled fluorophores, with respective isotopic controls listed below. (*Product catalogue of BD sciences)

2.8. *Reverse Transcription for First Strand cDNA Synthesis*

Whole DNA and RNA constructs were extracted from lysis cells using two different methods; Trizol™ and Cell-to-cDNA™ II kit, the later proving most effective due to low cell number. Purification steps were required achieved by; chloroform washing and multiple centrifugation steps for Trizol and enzyme digestion of DNA for cell-to-cDNA using DNase©. Both methods result in complete RNA isolates, ready for reverse transcription to compliment DNA (cDNA).

Nanodrop determined concentration of total RNA solutions. 1 µg of total RNA was combined with non-specific primers (Oligo dT12-18), and dNTP mix (10 mM of dATP, dGTP, dCTP and dTTP at neutral pH) and heated at 65ºC_5 mins opens RNA strands and enables binding of primer. First strand cDNA synthesis can occur using a thermo- cycler set to amplification program (50ºC_50 mins, 70ºC_15 mins, 4ºC_END) with the presence of first-strand buffer, Dithiothreitol (0.1M DTT) to stabilise enzymatic activity and the transcriptase enzyme (SuperScript III). On completion samples were stored at -20ºC (short term) or -80ºC (long term).

[Note: throughout protocol samples, reagents and sterile tips were kept on ice]

Reagents and Equipment:

Cell-to-cDNA™ II kit (AM1722 Ambion, Life Technologies, UK)
Trizol™ (15596-026, Thermo, Life Technologies, UK)
Oligo$(dT)_{12-18}$ (18418-012, Thermo, Life Technologies, UK)
Deoxynucleotide mix, dNTP (D7295, Sigma Aldrich, UK)
Water, molecular grade (W4502, Sigma Aldrich, UK)
Superscript III Reverse Transcription Kit (Invitrogen, 18080-044)
- 5X first strand buffer
- Dithiothreitol (0.1M DTT
- RNase Inhibitor

Microcentrifuge (75002477, Thermo Scientific or MSE Micro Centaur)
Thermo-cycler (PTC-200, MJ Research)

2.9. *Quantitative Real-Time PCR (qPCR)*

The polymerase chain reaction (PCR) is one of the most powerful technologies in molecular biology, use of real-time PCR enables the precise quantification of amplicons and the cycle (Ct) they occurs at. The expression Ct obtained for a gene of interest was compared with a house-keeping gene, called Comparative quantification.

Once reverse transcribed to cDNA each sample undergoes dilutions, 1:20 dilution of cDNA with water makes template stock. A sample of this was diluted 1:10 in the quantification PCR, giving an overall dilution of 1:200. Individual wells of each sample measured for the specific genes of interest and house-keeping gene, TaqMan assisted PCR reactions assisted primer and cDNA mix, (discussed in detail in Chapter. 3). The PCR amplification cycles were preformed under the conditions: 94ºC_4 mins, then 50 cycles at 94ºC_25 s, 53ºC_30 s, 72ºC_45 s and final extension at 72ºC_10 mins. Replicates of each sample (triplicates) aided accuracy and were compared to Human glyceraldehyde 3-phosphate dehydrogenase (GAPDH) housekeeping gene as an internal control. Higher than normal (40) PCR cycles (50) were used for gene detection due to low RNA yields and sample purity. Statistical significance between groups was assessed by two-way analysis of variance (ANOVA) with Sidak's and/or Tukey's multiple comparison post-hoc tests.
Technical controls were always run simultaneously on each plate; empty wells containing only water (same water used to dilute samples) acted as negative controls for the machine, and other wells contained almost complete experimental cocktail except for the Taqman enzyme, to helped identify faluse positives.

<u>Materials and Equipment</u>

Real-Time PCR (ABI PRISM 7900HT, Applied Biosystems, Foster City, CA, USA)
Taqman® Master Mix (4371357, Life Technologies, Thermo-Scientific, Germany)
SDS Software 2.3 - Absolute Quantification (Applied Biosystems, CA, USA)

CHAPTER 3. FABRICATING SIMPLE ADJUSTABLE SURFACE TOPOGRAPHIES WITH DISTINCT FEATURES AND CHEMISTRY COMBINATIONS

3.1. INTRODUCTION

Many scientists have strived to use material sciences to emulate the *in vivo* environment of a tissue. Recent research from the past decade has highlighted the strong rational for tailored nanotopographies to influence individual cells and how their physical environment can significantly influence cell fate and tissue development. Replicating the *in vivo* environment to which cells are exposed to can provide biomimicking milieus for advanced *in vitro* platform to understand and elucidate fundamental mechanisms of cellular development, physiology and pathology[171,172].

Several techniques have been utilised to evaluate and create *in vitro* environments to study bio-physical stimuli including; chemical etching, physical deposition, nanoimprint, electron lithography[172] and phase-separation[173]. Polymer-demixing is an economic and effective technique used to induce phase separation and generate micro-/nano-textured polymer films[61,129] A well-established method for phase separation of immiscible polymer blends in a common solvent, is obtained by spin-coating[3,174-179]. High interfacial tensions between immiscible polymers greatly influences the resulting surface attributes such as; water contact angle, spreading coefficient, and surface adhesion[178,180]. Intense external forces such as centripetal force (spin coating) can stretch the polymer body across the substrate to exacerbate tessellated patterns and generate raised, divergent micro-landscapes. Of the numerous demixed polymer combinations investigated, polystyrene and poly(methyl methacrylate) [PS-PMMA], are the most widely established immiscible polymer blends for thin film investigation[175,176,181-184] These established and characterised polymers were used here to investigate topographical influence on MSCs as a proof of concept only.

Recent studies have shown porous polymer films to have applications as improved *in vitro* surfaces and can even stimulate differentiation[61,123,185,186]. Of numerous methods and applications for fabricating porous polymer films, none have attracted more attention due to their simplicity then breath figure patterning (BFP). Use of breath figure pattern during polymer film fabrication can form ordered hexagonal lattice or honeycomb patterns.

In this chapter, the novel combination of demixed phase separation by spin coating and breath figure patterning as a single step process. We investigate surfaces for stable reproducible micro-/nano-topograpical pattern fabrication and quantify pronounced topographical features size, separation and chemical composition.

3.2. Aim

Develop a variety of demixed polymer surfaces of controlled chemical and distinct topographical features, using a simple and reproducible fabrication approach.

3.3. Objectives

Devise a simple and reproducible spin coating protocol for the efficient, economical and effective fabrication of thin polymer films

Enable modification and adaptation of the spin coating process to induce breath figure patterns on polymer surfaces

Evaluate hydrophobicity of polymer films and the topographical features of fabricated surfaces according to area, height, degree of separation and feature dispersion

Determine the defined chemical composition of each polymer surface

Identify potential polymer film candidates for biological evaluation with cells

3.4. Materials and Methods

3.4.1. *Polymers*

Two established polymers appear repeatedly in the literature of this period, polystyrene and poly (methyl methacrylate), and were established as dependable polymers for generating distinct topographical patterns. Building from this knowledge the work presented here utilised these two central polymers to expand on surface topographies and the specific influence on biological activity. The polymers both individually and in different ratio combinations were evaluated with several different solvents, in keeping with the literature, to create novel topographical surfaces for investigation. The main solvents used in this study were chloroform, dioxane, tetrahydrofuran and toluene. The latter three of these solvents were of greatest interest; rapidly dissolving both polymers, exhibiting high evaporation rates and being hydrophilic (anhydrous solvents). The water miscibility proved essential for stable breath figure pattern induction and the hydrophilic nature of Dioxane and Toluene were identified as the most suitable.

The spin coating technique was optimized by varying; the volumes added, concentration of polymer, acceleration rate and top speed of the spin coating machine. The surfaces generated were assessed, in the first instance, by brightfield microscopy to determine suitable uniform spread of the polymer, minimizing edge effects and low chuck patterning (Figure 4.) It was found that low concentrations of polymer (1-3% wt.) were most suitable for creating a fine layer over the glass substrate. Higher concentrations of polymer incurred more complex spin coating profiles as greater viscosity (the resistance forces of a fluid tending to flow, due to the magnitude of internal friction from constituent units/area. i.e. polymer/solvent) played greater role in spin dynamics. Lower polymer concentration also assisted the rapid spreading of the material before complete evaporation of solvent before the spin cycle finished. Considerable time was spent obtaining the optimal uniform spread, as consistent border or ‘edge effect’ appeared, displayed in appendix pg.XXVII. We minimized the depth of the edge effects to micrometres. And chuck patterns were rectified through removal of conductive area by use of a rubber buffer layer, Figure 5_rubber bung.

3.4.2. ***Surface Preparation & Characterisation Techniques***

3.4.2.1. Silanization

To address polymer-substrate detachment a mild treatment with silane, *3-(trimethoxysilyl)propyl methacrylate,* was applied to create a mono layer across the glass substrate. Gentle treatment with a 2% silane solution immediately after vigorous acidic cleaning (Piranha), provided a suitable thin silane coating. Cover slips were kept submerged for storage, to preventing an oxidised layer forming at the surface. Absolute ethanol was used to keep the glass submerged as it was also used as diluent for silane. Cover slips were nitrogen dried directly before spin coating with liquid polymer. The silane presents carboxyl groups at the surface of glass for the covalent binding of PS and PMMA.

3.4.2.2. Plasma Cleaning

The excitation of gaseous atoms with high voltages causes the release of electrons, ions and radicals. These bombard surfaces of the material 'sputtering', stripping it of all impurities including organic components, but if left long enough will induce etching and heating. A side effect of the cleaning process is the reduction of surface energy i.e. plasma cleaning of most surfaces greatly increases hydrophilicity. This is typically proportionate to the alternating voltage, plasma gas used (e.g. nitrogen, oxygen) and the length of time left exposed.

Plasma cleaning has the added benefit of assisting solvent removal in a vaccum, crucial in the design of medical device fabrication process.

3.4.2.3. Water Contact Angle

A simple technique that quantifies the wettability of a material uses the contact angle of a liquid drop on the surface. First described by Thomas Young in 1805[187], the unique contact angle of a liquid drop on a surface is determined by the mechanical equilibrium of interfacial tensions between solid/liquid/vapor. Contact angle is the tangent (θ) determined by the Young-Laplace equation where droplet shape at liquid-vapor interface and solid/surface is baseline[188].

Static water contact angles of all demixed polymer surfaces, solitary polymer controls and bare glass controls were measured by CAM101 (KSV instruments Ltd., Finland). A steel screw syringe dispensed identical droplets, assisted by droplet silhouette software and a 'one-touch' syringe plunger dispensed on the surface. Ultrapure water droplets were used and dispensed in triplicate to provide six independent measurements (left θ , right θ), mean values are presented for each surface.

PMMA is an exception, known to have unstable hydrophilization properties[189]. PMMA initially increases in hydrophobicity after plasma treatment but recovers to a stable θ ~70º once washed in solution.

3.4.2.4. Optical Microscopy

Simple transmission microscopy enabled fast and efficient inspection of topographical differences between each polymer surface. Brightfield (BF) images were taken with an upright light microscope (DMLB 3000, Leica Ltd.) and digital images were captured and processed using advanced SPOT™ (Diagnostic Instruments Inc.).

3.4.2.5. Scanning Electron Microscopy

Detailed surface imaging was captured through high-powered scanning electron microscope (Stereoscan 240; Cambridge Instruments Ltd., UK), described previously. Surfaces were cleaned, dried and gold coated in a vacuum to enhance electron detection and give high-resolution images. Once spin coated polymer surfaces were cleaned/dehydrated by a series of ascending ethanol washes (20, 40, 60, 80 and 100%) and left to dry in a sealed container until gold coating.

All slides were mounted as noted in Chapter.2 Materials & Methods.

3.4.3. *Image J Surface Topography Analysis*

Both SEM and BF images were processed using Image J to identify, isolate and quantify the topographical pattern. Identifying the phase-separated regions of either polymer was determined due to opposing topographical patterns induced from breath figure patterns. Opposing polymer characteristics to water droplets results in the formation of distinctly different condensation patterns, when spin coated over a ridged substrate in combination with rapidly evaporating solvent, the polymerization of both polymers casts the pattern into a solid topography. Isolating these two distinct patterns is quantifiable by morphology.

Image J software (1.49i; National Institute of Health, USA) strips back images to greyscale basic 8-bit images and thresholds for features within.

IMAGE J analysis

Shape Descriptor

(macro)

>Image J 'Open' image (.jpeg / .tiff)

> *Analyse >> 'Set Scale'* (use image scale bar to equate pixel-micron ratio)

>Crop image to remove scale bar

(Insure all cropped images are of same dimensions 230x200μm)

>Image >> Adjust >>Brightness/Contrast

>Image >> Type >> 8-bit or optional: Process>FTT>> Band filter (flattens image)

>Image >>Adjust >>Threshold

>Analyse >>Analyse particles ;

PMMA Size: ≤ 10 – infinity ; Circularity: 0.6-1.0 ; Overlay Mask applied

PS Size: 0 – ≤ 200 ; Circularity: 0.0-0.5 ; Overlay Mask applied

>Results >Summarised and Entire

>Results Entire >Distribution graphs >>Area ; Circularity. ; Perimeter (Bin: 50)

SEM images were converted into basic 8-bit binary images, which reduces the image to two, 'bi', tone images. Where it is easier to threshold/identify pronounced features on the surface. Specifically isolating caldera shapes required additional parameter restrictions, where the distinct morphology of the caldera was utilised, namely circularity between 0.4 and 1, where one is a perfect circle.

The evaluation of the caldera was based on the degrees of separation from each other in relation to the number found per field of view, referred to as the theoretical nearest neighbour distance. This is calculated using each caldera's ultimate eroded point (UEP), essentially the centre point of the caldera. This was then used to calculate the distribution distances of the UEPs using the formula: 0.5*sqrt(area/n)[190]. The measured nearest neighbour distances were statistically compared to get the theoretical (median). Homogeneity of the variance was achieved by preforming an F-test, which informs the use of either a Student's T-test or a Welch Test for the final statistical evaluation. Across all surfaces homogeneity of variance was not found and so statistical analysis was preformed using Welch test while the confidence interval were set at 95%.

3.4.4. *Atomic Force Microscopy*

Surface topographies were observed in greater detail using atomic force microscopy. AFM images were captured using Agilent technologies (S500 MAC mode III, USA) and Picoview 1.8.2 software for [80 / 40 / 20 / 10μm^2] areas at 1.2lines/s; 612 pts/line resolution. Data visualisation and analysis was preformed on Gwyddion 2.38 (Sourceforce.net, Czech Republic)

For more details, see Chapter.2 Materials & Methods.

3.4.5. *X-Ray Photoelectron Spectroscopy*

XPS spetra were taken on a K-Alpha™ 128-channel detector (Thermo Scientific) spectrometer with micro-focussed monochromated Al Kα source (1486.6 eV) X-rays operated at 150W. The Monoatomic Ar ion and Polyatomic Gas-Cluster Ion Beam (GCIB) source enabled detailed depth profiling of the polymer surfaces. Spectrometer was calibrated to internationally accepted standards in accordance with (ISO TC\201 SC7). Depth profiles were concurrently collected and enabled analysis of polymer films down to the glass substrate and elements identified using Kratos element library. Duplicates of each surface were taken and database of reference spectra for PS and PMMA polymers were utilised.

3.4.6. *Spin Coating and Optimisation*

Spin coating is a simple, rapid and reproducible technique for the fabrication of thin polymer films. With a basic spin coater liquid polymer was dispersed across the surface of the substrate, static dispensing technique was employed to carefully deposit polymer before rotation. Dispersion of the fluid across the entire surface was ensured before commencing the rotation. Minimal time between deposition and commencement of the rotation was desirable to minimize differential evaporation times between each sample. Once rotation commences the most influential parameter of the spin coating technique is in play, rotational speed (rpm), whether it be direct acceleration to the desired speed or staggered acceleration depends principally on the viscosity of the material being spread Figure 4_B.

Greater control was obtained by staggered acceleration where an initial lower speed step was preformed before increasing to final higher speed. This initial lower-speed ran for ≥4 seconds giving enough time for the fluid to slowly spread out over the substrate before the high-speed step discards excess fluid and defines the film thickness. The rotational speed (rpm) affects the intensity of centrifugal forces applied to the fluid, pushing radially out from the centre spot. Countering this is the resistance of the liquid viscosity, gravity and air turbulence directly above fluid[191]. The latter parameters should all stay the same making speed the key variable factor.

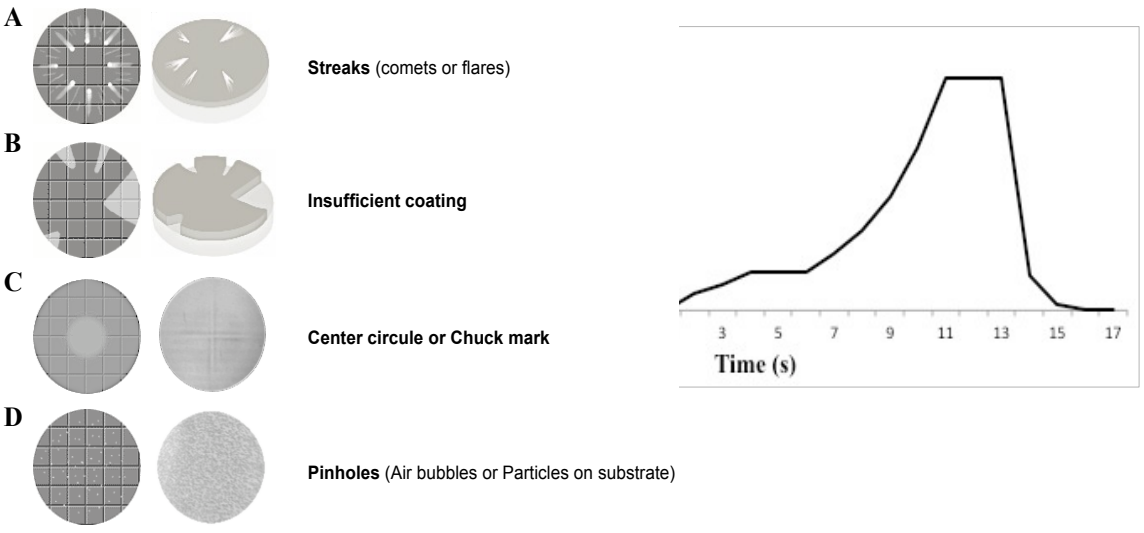

Figure 4. Spin Coating parameters of; dispersion malfunctions [A-D] and graph plot of rotational acceleration *(right)*

3.4.7. *Modifications for Humidity Chamber*

Simple modifications were made to the spin coater; a doughnut shaped aluminium plate was fabricated to fit beneath the metal spin coating chamber (Figure 5_A). The plate was fitted with four evenly dispersed holes drilled into the plate, pointing towards the centre of the circle. Four 30W heating cartridges (220V, RS no.724-1999) were fitted and bound into the holes with thermal adhesive epoxy (Electrolube, RS no.155-8320). Each heating element was fitted with K-type thermocouple (-50ºC→+1100°C, RS no. 621-2158), which feed back into a digital electronic controller (TLK 39, Tecnologic Ltd., Italy) enabling stable, prolonged temperature control.

The internal spin coating chamber was fitted with a dual thermometer/hygrometer probe (FB61272.Fisherbrand, UK), providing a digital readout of humidity changes within the chamber (Figure 5_B).

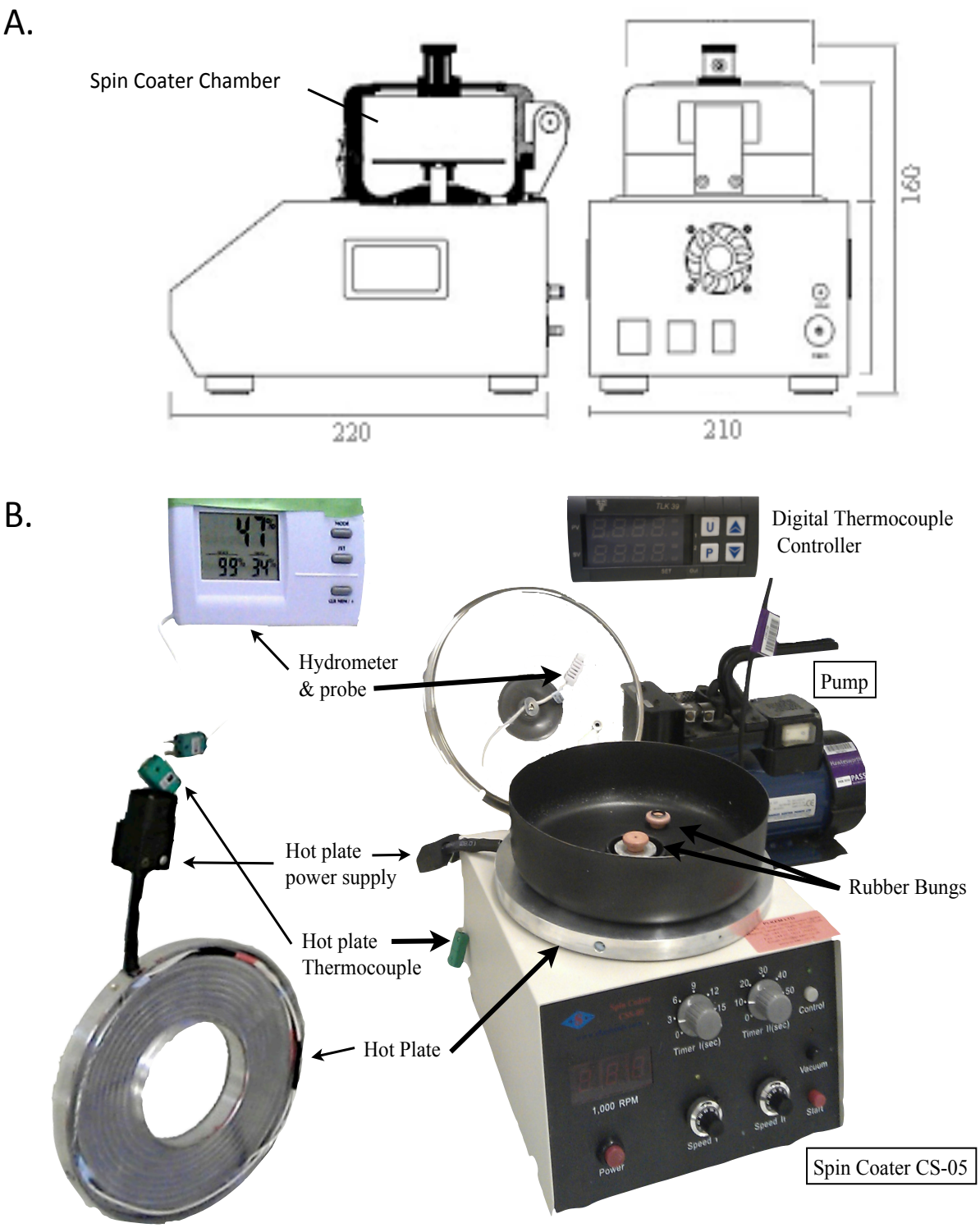

Figure 5. Illustrated Spin Coater dimensions (A) and labelled images of modified humidity chamber made to spin coater, the original spin coater parts are labelled with boxes (B).

The Approach

Spin coating is a simple and well-established technique for the dispersal of liquid over a surface to produce a very fine film. When spun at high speeds a liquid polymer is stretched thinly over the surface, creating polymer films of ≥ 1μm in depth.

Fabrication:

- Glass substrates were submerged for piranha cleaning (H_2O_2:H_2SO_4, [1:1]);1h
- Glass silanization improves polymer adherence (2% [3-(Trimethoxysilyl) propyl methacrylate 98%] in absolute ethanol O/N)
- Spin coat various demixed polymers onto substrate (35μl; @ 8000rpm; 15s) under humid conditions (>80%)

Analysis:

- Water contact angle was used to determine the alteration to surface energy throughout different modification steps.
- Scanning electron microscopy imaged the surface at high magnification
- Atomic force microscopy
- Surface scanning by atomic force microscopy (contact mode, submerged [ultra pure water])

Cell Culture:

- Plasma cleaning for 60s (optimized to induce ~20º change of water contact angle)
- Different surfaces were loaded into tissue culture plates and sterilized by UV light (λ245 nm)

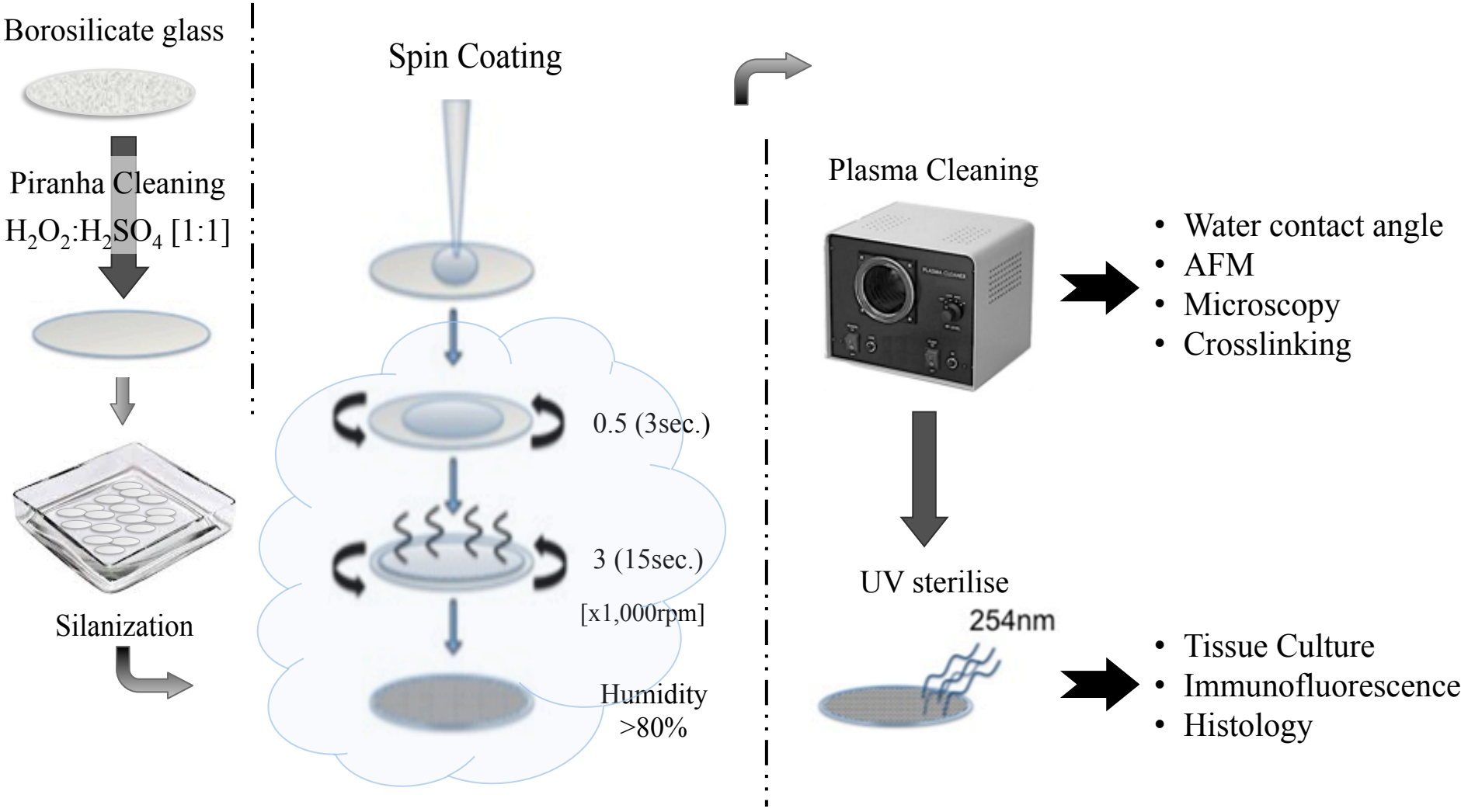

Figure 6. Schematic illustration of surface fabrication process; (*left* to *right*) glass substrate was cleaned of all physical artefacts including organic matter; polymer was applied and spin coated over surface under humid conditions; cover slips underwent plasma cleaning and/or UV treatment respective to their downstream application.

3.5. Results

Utilizing the immiscible phase-separation of polystyrene (PS) and poly(methyl methacrylate) (PMMA), thinly spread over a flat substrate leads to the fabrication of chemically distinct surfaces with scalable features due to the spin rate, solvent evaporation with an empirical relationship between polymer ratio mix, humidity and feature size[177].

3.5.1. *Spin Coating Setup*

The volume of liquid polymer was optimised for efficient coverage of; a glass substrate, minimal dewetting and waste of material. It was found that for a 13mm (diameter) glass cover slip (0.13cm^2 surface area) could be covered efficiently with 30µl of polymer. Two-stepped spin coating program was established with initial rotational speeds of 500rpm_2sec, increasing to 3,000rpm_10sec. This was maintained through out spin cycles and reproducible (±15rpm).

Isotopic evaporation was assumed across the surface due to small diameter and radial convection of the spin coating technique[192]. Flack *et al.* have shown that the evaporation rate typically alters with the square root of the spin speed $D \sim \omega^{-1/2}$.

Outside of the spin coater adjustable factors, other elements affect the quality of the surfaces generated. Non-uniform fluid spread during rotation due to direct acceleration and imperfect substrate wetting. Formation of streaks (comets or flares) or pinholes on/within surface probably a result of particles on the substrate surface or in fluid solution[193], Figure 4. Both of these problems were improved through preparation of the surfaces using piranha treatment pre-spin coating.

A far greater difficulty was the mirroring of the vacuum chuck on the polymer surface (chuck pattern), which remained irrespective of polymer concentration or volume. The identical chuck pattern was mirrored in the spin-cast polymer, while never in direct physical contact with the chuck, only in contact with the under-side of the substrate. Although devoid of physical contact with the liquid polymer, an exact pattern of the metal chuck was left on the dry casted surface of the film, identifiable by slight opaque colour change in the polymer, Figure 4_D. Since there is no direct contact there must be some form of interaction between the metal chuck and the coating solution. It was later determined to be a thermal conductive transfer due to the local temperature differences between the vacuum/metal chuck and the substrate/polymer solution. Similar observations have been found in industrial spin coating, who change to a Delrin spin

chuck (a thermoplastic chuck, Polyoxymethylene) or recommend introduction of an inert buffer zone. The spin coater used is far from industrial grade and unable to fit Delrin heads. So adaptation of this principle was applied by addition of a small rubber bung to the top of the metal chuck with a single pierced hole for vacuum. While the original chuck pattern was overcome, a new circular pattern was formed due to the circular orifice in the rubber bung enabling the vacuum suction and the flexibility of borosilicate glass. As a result, a modification was made binding a 10mm rubber O-ring to the top, raising the glass ~0.5mm and dispersing the vacuum forces over a greater surface area, rectifying any appearance of a chuck pattern.

3.5.2. ***Polymer Film Detachment from Substrate***

On progression of the fabricated surfaces to biological assessment difficulties were observed during prolonged periods submerged in aqueous solution (culture media or PBS), Figure 7*_centre*. Detachment of the polymer film from the glass substrate was suspected to be due to non-covalent binding of polymers to substrate; water molecules invading and occupying the interstitial zone between film and substrate inhibited the covalent adherence of the polymer to the glass surface. The glass substrate under gone piranha cleaning stripping the surface of all organic matter and quenching any possible binding sites for covalent linkage. To rectify this glass underwent a mild silanization treatment (2% 3-(Trimethoxysilyl)propyl methacrylate 98%) after piranha cleaning.

3.5.3. ***Introduction of Humidity Chamber***

The preliminary experiments to investigations the effects of water on the polymer surface involved direct addition of water to liquid polymer before spin coating and preformed in low percentage combinations (2-5% H_2O). Almost instantaneous polymerisation at the point of water addition resulted in an opaque, highly viscous hydrogel being formed. As a consequence to this introduction of the water needed to occur during the spin coating process. Simple addition of hot water (55-60ºC) to a sponge within the spin coating chamber provided enough condensation to fill the chamber, increasing the humidity and induced breath figure patterns on the polymer surface.

Further modification was required to finalise this principle due to the fact that water temperature with chamber and sponge would decrease over time, altering the humidity levels during each spin.

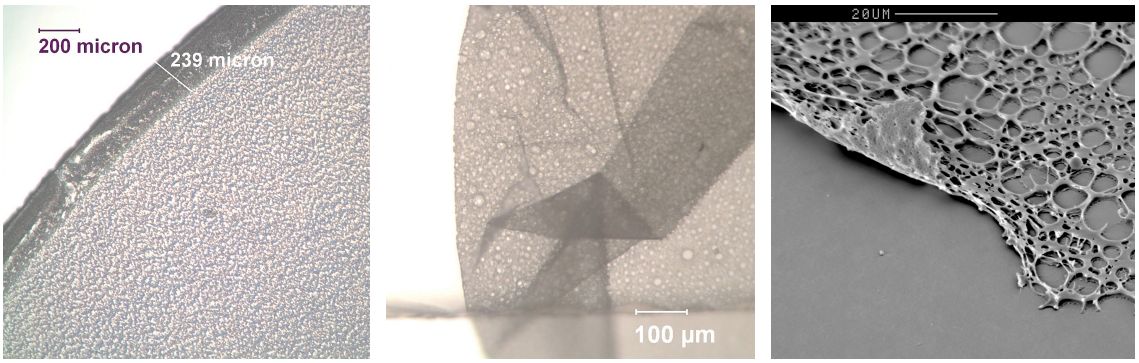

Figure 7. Images of spin coating technique anomalies; Edge-effect forms boarded at edge of substrate, PS_10x; Polymer film detachment and folding over, PS_10x; Porous-like topography shown to be a continuous film sheath and not polymer netting, by broken and peeling membrane, PMMA_SEM.

3.5.4. ***Solvent Selection***

Numerous commercially available organic solvents are used with both PS and PMMA. Several of these solvents were identified in the literature to be used with both polymers and frequently in combination for demixed purposes (chloroform[181], tetrahydrofuran[3], dioxane[11], dimethylformamide, ethyl acetate, toluene[3]). The ideal solvent was determined by comparing dilute polymer solutions in each solvent spin coated at static speeds. Comparison was determined by; rapid polymer solubilisation, ease of polymer deposition, thin uniform films and brightfield microscopy to identify pattern creation. The best solvent should readily dissolve polymer, disperse polymer throughout solution and enable topographical features.

Toluene was finally selected due to benefits in the downstream processes; toluene rapidly evaporates and has a high affinity for water. Selection of anhydrous toluene enabled accelerated surfaces fabrication with reproducible breath figure patterns (BFP) under saturated humidity conditions.

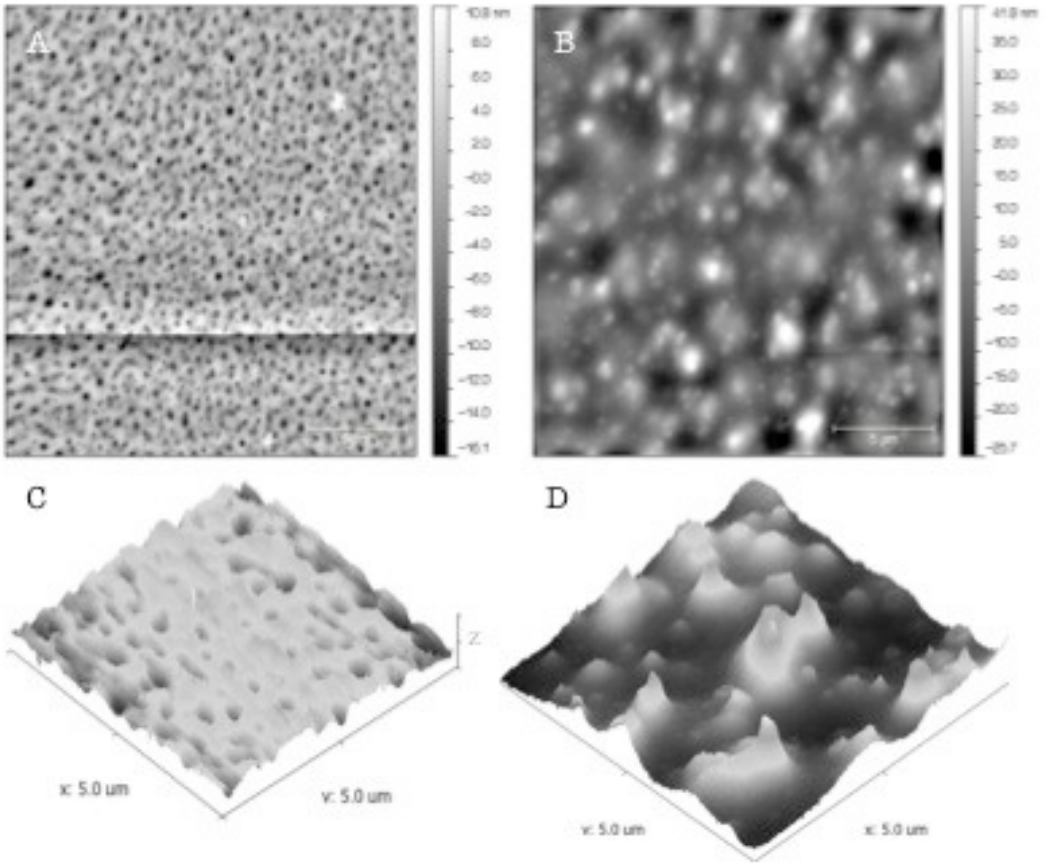

Figure 8. Areal AFM images of lateral dimensions 10µm x10µm (A,B) of demixed PS:PMMA at ratios 10:90 (A,C) and 90:10 (B,D), with complimentary three dimensional models (C,D) to show height (z-axis).

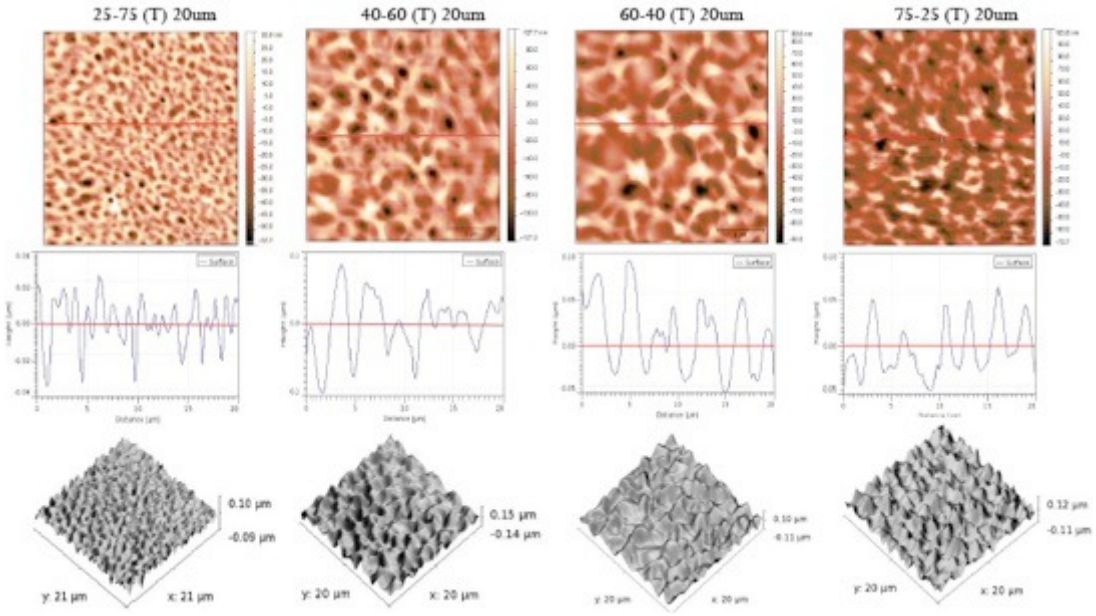

Figure 9. AFM analysis of demixed polymer blends of PS:PMMA (3%wt. in Toluene) at various ratios spin coated onto glass substrate. A) Areal AFM image of a 20x20µm; B) Height profile of indicated line on AFM image; C) 3D model of AFM surface with cross-reference lighting.

3.5.5. ***Demixed polymer ratio selection***

A range of surfaces created from different polymer blends were explored and analysed by AFM when fabricated using a fixed spin coating program. Surfaces were selected by the degree of phase separation; immiscible properties of individual polymer's chemistry and more definitively by raised height profiles for topographical features.

A broad spectrum of PS:PMMA ratios were used [1:9 / 2:3 / 1:3 / 1:1 and vice versa] maintaining the inverse numerator to denominator ratios throughout. Polymer blends were combined as v/v ratios and are named, recorded and denoted in figures as volume percentage ratios (e.g. 2:3 = 40:60).

The distinct gradient of phase separation is observed in the higher ratios of 25-75 and 75-25 (Figure 9). The low-lying PS regions appear concurrent with increasing PS ratio and vice versa for PMMA. Most notable are the closer ratio mixes, which provide greater height differential. This is clearly seen in Figure 9, where the red line denotes zero level in the height profile graphs in the centre. If the tallest peak from each graph is taken and compared, far greater heights are achieved by low blend ratios[§]. Both of these opposing ratios were selected and also [1:1] i.e. 50:50, to proceed for further evaluation.

25:75	40:60	60:40	75:25
0.026µm	0.88µm[§]	0.9µm[§]	0.054µm

Figure 10. Table of quantified peak heights for different demixed ratios, where the height shift is greatest at close polymer concentrations ratios[§].

The phase-separation between both polymers can clearly be seen in Figure 11, where greater PMMA concentration in 25:75 (*left*) dominates the image standing higher then the dark, speckled dots of PS 'pits'. This is reversed in 75:25 (*right*) where the majority of the image is dark, i.e. low lying (PS), and dotted within it are islands of raised (PMMA) standing up away from the surface like 'towers'. This becomes clear in the height profile graphs displayed beneath both areal AFM images. A single trace line is taken across the width of the AFM image to give a cross-sectional view of the surface and the *red line* highlights the altered height differential deviating from the surface zero level.

Dispersion patterns of the low-lying 'islands' and surrounding 'plateaus' change linearly with alteration to the concentration mix of the two polymers. In 25:75 (higher PMMA conc.); dotted, small area islands (~0.5µm^2) are formed due to greater dominance of the PMMA. Opposing in 75:25 (high PS conc.) is used; large, interconnected islands (~4.5µm^2) form with high standing PMMA peaks. In Figure 11 these two contrasting conformations are observed and have a direct antithetical link. As with the inverse relationship between height profiles; where PMMA-rich (25-75) displays heights of approximately ≤0.02µm with numerous peaks in close proximity, inversely PS-rich (75-25) shows heights of almost double that ≤0.05µm with fewer, dispersed peaks/'plateaus' surrounded by large interconnected 'islands'.

The patterns for these demixed polymers are well characterised in the literature, PS:PMMA immiscible polymers generating islands of +/- 10µm, surrounded by slightly raised borders of ~0.1µm. Topographical features of a different scale were created by the introduction of pores to the surface. This was achieved by employing an old phenomenon known as breath figure pattern, where condensing water on a surface forms a specific droplet array. When this is applied to a drying polymer surface the water droplets attack the surface leaving imprinted pores.

Demixed polymers when spin cast under humid conditions, offer a simple technique to generate different topographical features, in a reproducible manner for quick and easy evaluation; topographical height and dispersion dimensions alter linearly with concentration, moisture content and rotational speeds.

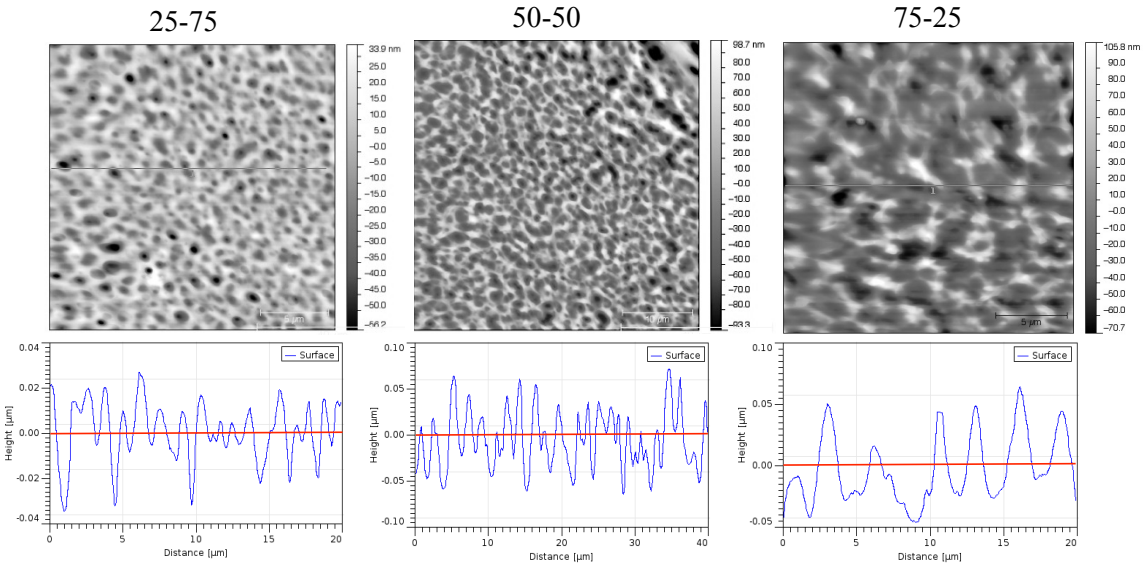

Figure 11. AFM images of contrasting polymer demixed surfaces, PS:PMMA ratios; 25:75, 50:50, 75:25 with correlating cross-sectional height profile graphs. Red line indicates the zero level of the surface.

Inducing breath figure patterns on individual polymers provokes different responses to pore formation. This is a result of water droplet formation at the surface as the solvent evaporates. Innate steric charges from the materials change how the water droplets form at the surface during the spin casting process. Greater water-resistance from PS results in numerous dimply-like divots and the occasional very large pore. PMMA with a lower water-resistance, but not hydrophilic, forms numerous pore-like structures of roughly similar shape within close proximity to each other. This is clearly observed in both homo-polymers (Figure 12_A-B).

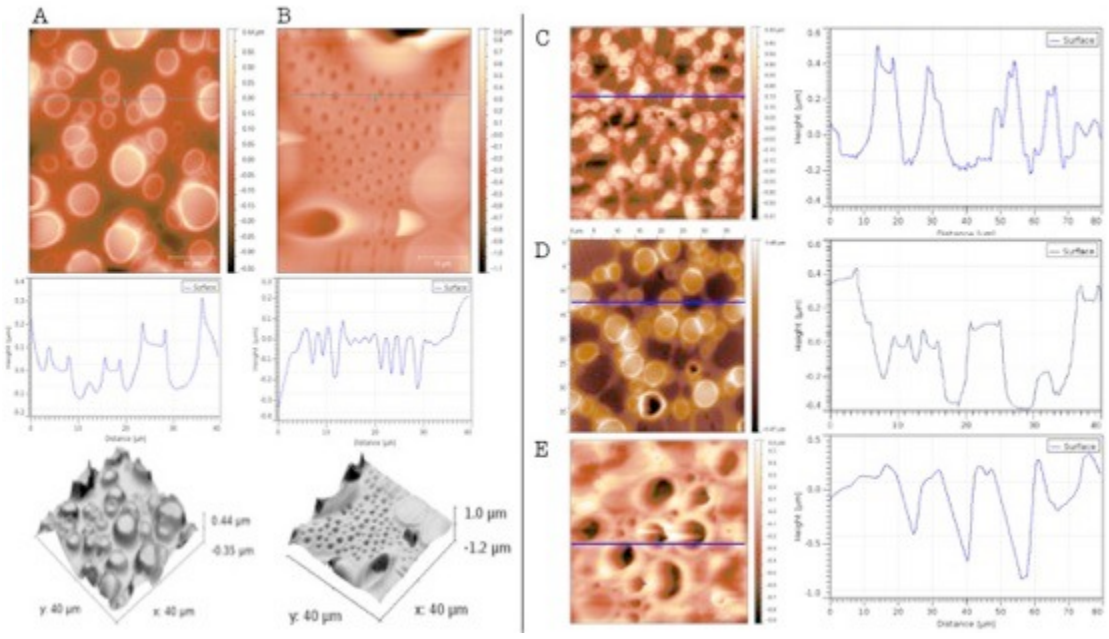

Figure 12. AFM profiles of individual polymers PMMA (A) and PS (B) showing aerial image *top*; height profile graph *middle*; 3D model of surface *bottom*. Different demixed ratios of interest [40:60 (C); 50:50 (D); 60:40 (E)] show adaptability of topographical landscape.

The distinctly elevated PMMA surface displays a large number of features, which are individually raised with crater-like appearance (Figure 12_A). Each independently standing 'crater' has a distinctly defined rim seen by the height profile cross-section these will be referenced to as *caldera*. The contrasting inverse is seen in the low-lying PS, where small 'dimple-like' pores (0.1 to -0.2µm) are created, penetrating the overall flat surroundings (Figure 12_B).

Demixed ratios of homo-polymers creates a combination of both characteristics; 40:60 with higher PMMA content forms tall sharp pronounced peaks ≥0.2µm; 50:50 forms softer, more rounded peaks ≤0.2µm with defined caldera; 60:40 with highest PS content is devoid of sharp peak but has raised mounds with deep cavernous pores > -0.4µm, (Figure 12_C,D,E).

This general tread would be in keeping with the features observed in the homo-polymers except for the fact that the demixed surfaces create peaks almost twice as tall. Both PMMA richer surfaces, 40:60 and 50:50, contain defined caldera structures that frequently surpass 0.4µm in height. This exacerbated feature enhancement is also observed in the PS-rich 60:40, where greater depth of 'dimples' form cavernous pores almost a micron in depth (Figure 12).

3.5.1. *High Magnification of Surfaces: Scanning Electron Microscopy*

Scanning electron microscopy imaged the topographical features detected by AFM, of demixed polymer films in combination with breath figure patterning. The sensitivity of this technique enabled high magnification of the surface with extremely high resolution. There are clear differences between each surface due to a shift in homo-polymer concentration, when viewed at low and high magnification. Although the height of the features cannot be determined from these images, distinct characteristics can be identified within the surfaces. The PMMA-rich surface (25:75) appears to have a greater number of large pore-like structures, tightly packed together, with very few interconnected sparse regions ('islands'). This mirrors what was observed in the AFM findings: PMMA-rich = numerous plateaus in close proximity, with few low-lying 'islands'. These islands grow and become more defined in the 50:50 images, displaying separate breath figure patterns. The PS-rich surface 75:25 presents the dominance of the 'islands' over the sparse and isolated pore-like plateaus.

Detailed image analysis of the SEM images was preformed using ImageJ2/Fiji software with the addition use of BioVoxxel toolbox plugin, for extended descriptor particle

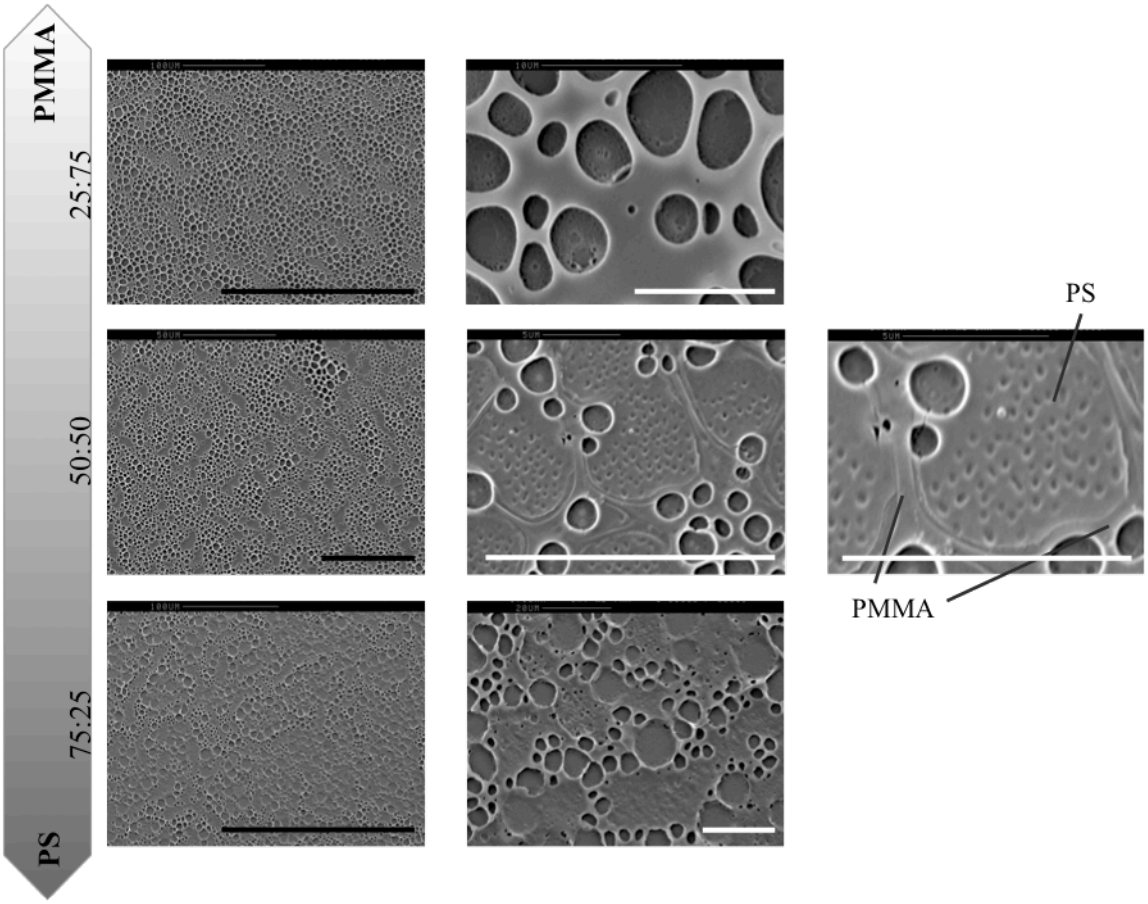

Figure 13. High resolution SEM images of varying ratios of PS:PMMA polymer blends when spin coated under BFP condition. Images are shown at different magnifications for the same surface blend, moving left to right, from low to high. With an additional 50:50 highest magnification image clearly identifying phase separation of polymers. Associated scale bars found at top of each image. Scale bar: Black – 50µm ; White – 10µm

analysis. Basic 8-bit images qualify the isolation and distributional quantification of the caldera centre points known as ultimate eroded points UEP (applicable with roundish structures). Identifying UEP gives a set of points called seeds, sites or generators, used to calculate Voronoi maps (partitioning of a plane into regions based on distance to points). The UEP sites can then be analyzed for area corresponding to a circle with the specified neighborhood radius around the centroid of each particle

A clear change in morphological pattern can be seen descending the threshold images (Figure 14). This change moves with the shift of polymer ratio from PMMA towards PS. Using the UEPs this shift can be quantified for the number of caldera per surface, seeing a dramatic drop from <3,000 down to >1,000. Greatest density of caldera were found as expected on the PMMA surface, with a slow and steady drop toward the PS surface at the lowest population. The sliding scale in numbers is not perfectly linear but does follow the general trend between both controls (see *n* number in table, Figure 14).

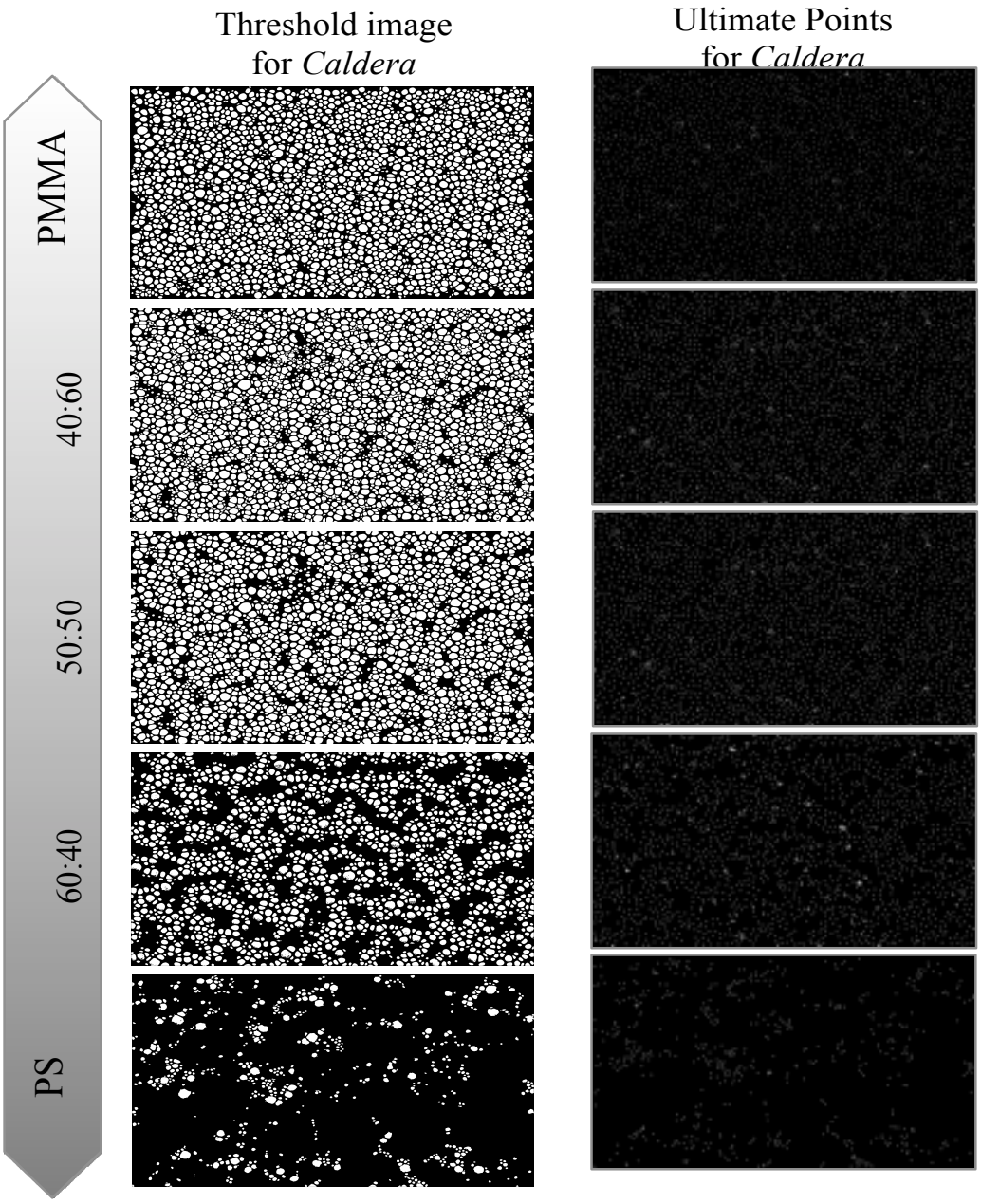

	Theoretical Random Nearest Neighbor			
	Distance	StdDev	n	Sig.
PMMA	23.10	4.80	2972	$p < 0.05$
40:60	24.09	4.90	2735	$p < 0.05$
50:50	24.25	4.92	2501	$p < 0.05$
60:40	28.76	5.36	1774	$p < 0.05$
PS	36.56	6.05	1100	$p < 0.05$

Figure 14. Detailed image analysis of caldera location and distribution on polymer surfaces. Original SEM images >> 8-bit binary were threshold for pronounced features and isolate for caldera shape parameters [Circularity: 0.4-1]. The ultimate eroded points of each caldera site were identified and the particle analysis enabled quantification of caldera per surface and the median neighbour distribution distance.

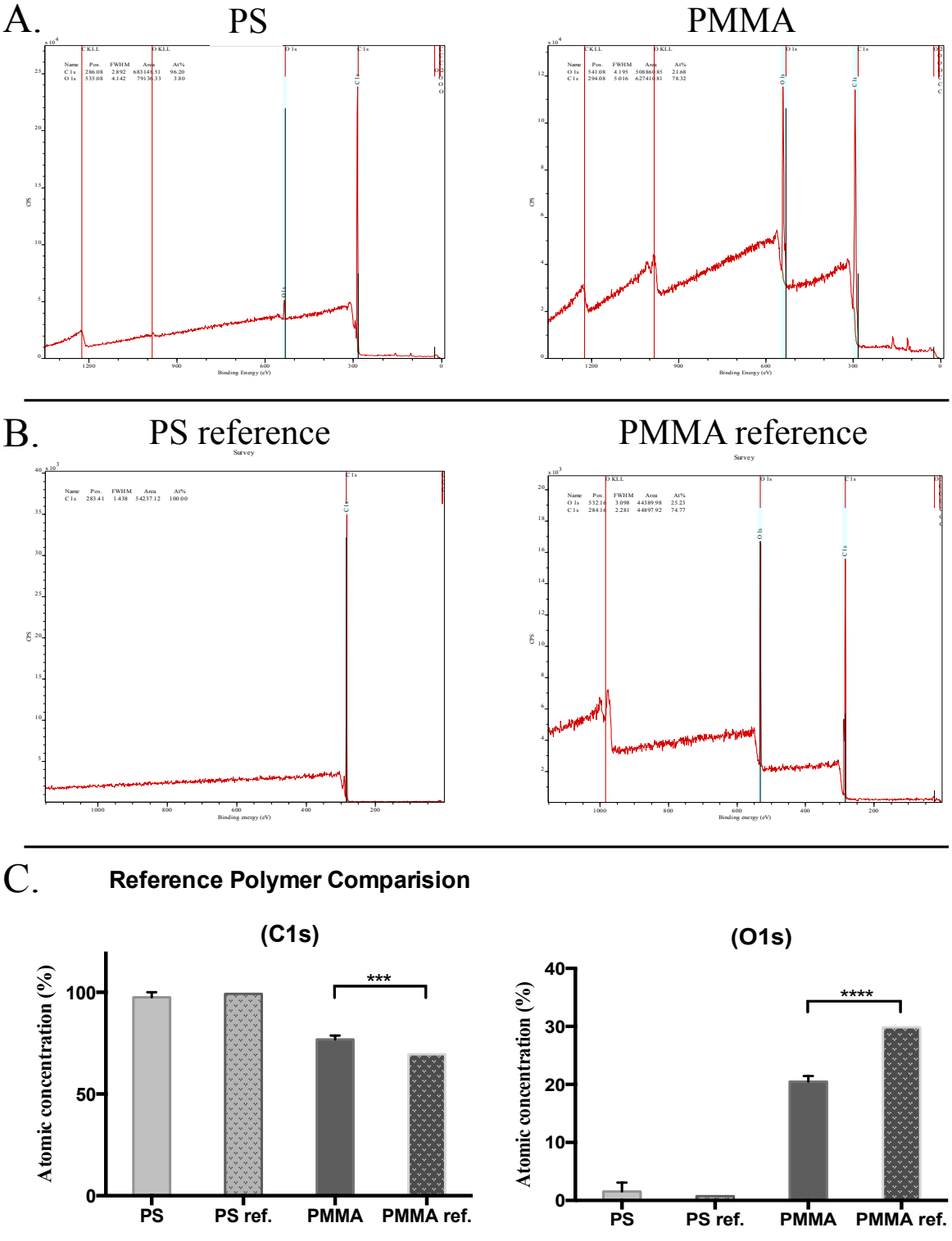

Figure 15. Polymer corroboration XPS survey spectra for (A.) homo-polymer materials generated by in-house spin coating technique, compared to (B.) the Beamson-Briggs polymer database spectra. Quantification of spectra for carbon and oxygen (1s) peaks were plotted together in (C.) an atomic concentration percentage graph.

3.5.2. *Chemical Composition of surfaces: XPS material analysis*

Detailed atomic chemical compositions were obtained for each polymer film material. The molecular formula for PS [C6H5CH=CH2]n and PMMA [CH2C(CH3)(CO2CH3)]n, contains similar elemental components but differ in bound energy between those elements. Each polymer contains unique arrangements; of particular note is the double bond found within PS (C=C) and the contrasting oxygen element bound in PMMA (C=O). The shift in bond energy of carbon makes the two discrete polymers distinguishable, PS energy at π*C=C 286.5eV and PMMA energy at π*C=O 293eV.

Note: XPS spectra are detected by machine in kinetic energy (KE) values and then converted to bind energy (BE) [KE=hν-BE-Ø]. All spectra are plotted for bond energy (BE) on the x-axis increasing from right-to-left, as XPS collects energy readings as kinetic energy (KE) that is left-to-right. Using BE plots is more applicable to materials with similar elemental composition. So where hydrogen, if detectable, would be found on the far right due to very low bond energy of a single electron, the much stronger carbon-carbon bonds (C=C) are found further along to the left and slightly higher again is the carbon-oxygen (C=O), all dependant on the level of electron bound rings shared by atoms.

First both individual polymer surfaces were cross-referencing with the Beamson and Briggs Polymer XPS database for PS and PMMA standards, where the two individual homo-polymer controls match up well, Figure 15. Discrepancy between the in-house and reference PMMA spectra was found to be statistically significant and maybe attributed to low product quality and/or suspected contamination due the greater number of available carboxyl groups. Lower detected oxygen levels would indicate towards the former, given the higher energy requirements to bind oxygen, and the opposing raised levels of carbon would indicate towards an organic carbon-containing contaminate. To note: PMMA used was purchased in powder form as opposed to PS pellets, offering greater surface area for contamination.

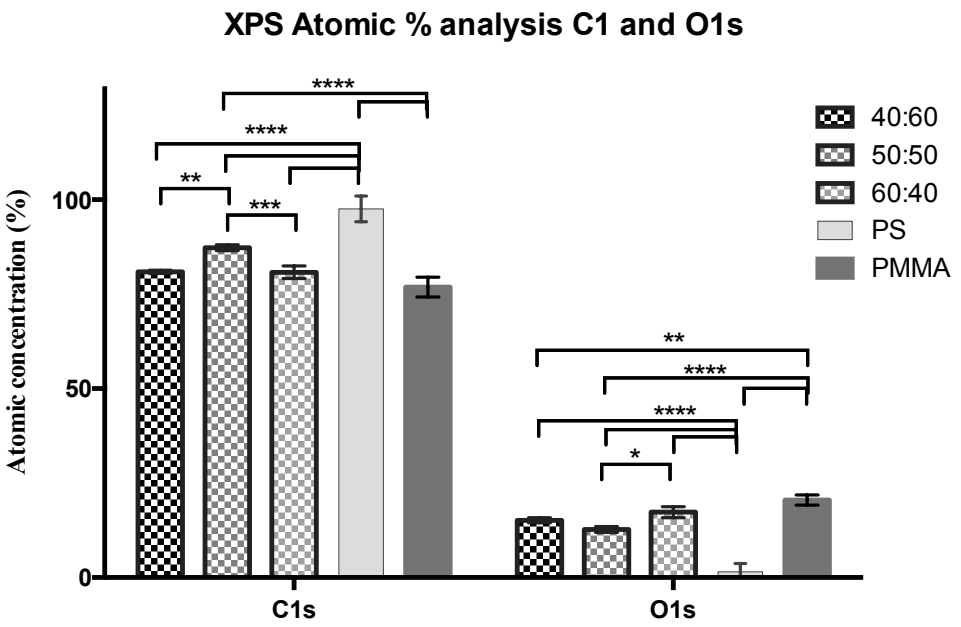

Figure 16. Graph of Atomic % concentrations for each material C1s and O1s spectra, with statistic comparison preformed by multiple ANOVA (Tukey's) test.

Strong statistical difference was determined between both homo-polymers for C1s and O1s, giving definite individual material separation (<0.001). PS was found to have similar significant separation from demixed materials in both carbon and oxygen. But PMMA was not significantly separated from demixed surfaces nor were they predictably separated from each other. Carbon levels in 50:50 were far greater then either opposing blends (<0.005) and once again shows inferior oxygen levels but only with 60:40 (<0.01). Statistical analyses of the atomic % concentrations were preformed using multiple comparisons ANOVA (Tukey's) at 95% confidence levels.

We observer a small anomaly were a thin skin of PS covers outer surface, first noted by Walheim *et al.*[3] When analysed for depth profiling of a surface the spectra peaks dramatically change between 0-60s within the first cycle and then returned to a more stable, predictive spectrum (substrate depth was found at 1141s). This time frame with atomic length etching would be ≤ nm thick, making an extremely thin PS 'skin' layer. It is also note worthy that this was more obvious in PS-rich surface blends (60:40 and slightly in 50:50).

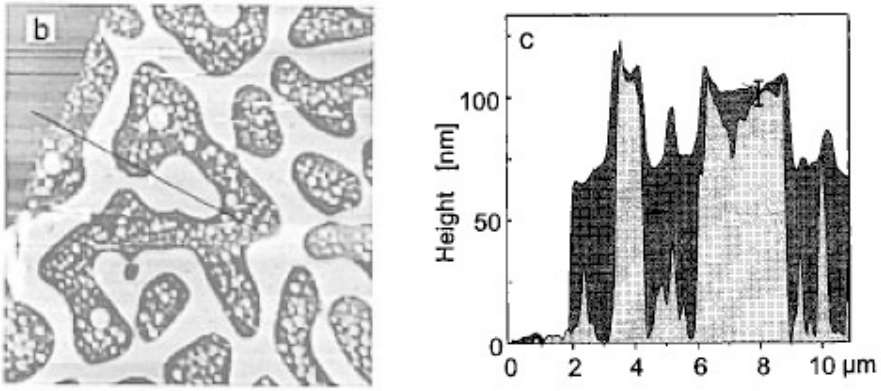

Figure 18. AFM image (14µm x 14µm) of PS/PMMA mixture spin-cast from (b) Toluene solvent and cross-sectional image of the topography. Where the error bar (c) highlights the superposition produced by the solvent favouring PS (dark), over rapidly depleted PMMA(light). Images referenced from Walheim *et al.* 1997[3]

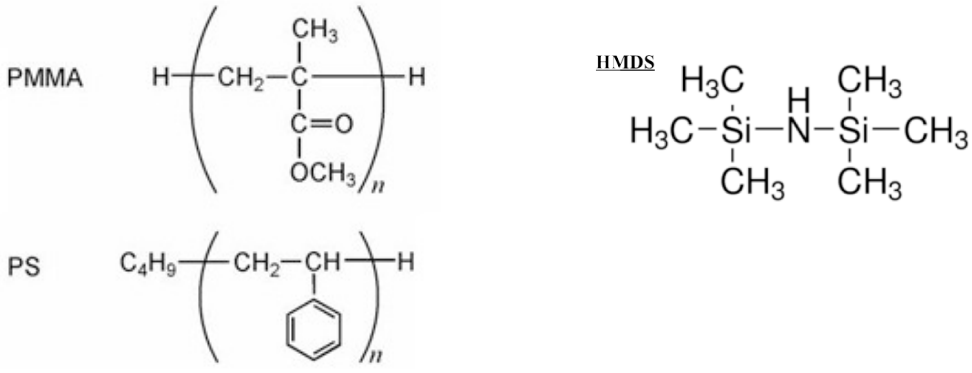

Figure 17. Structural element formula for the chemical composition of polystyrene and poly(methyl methacrylate)

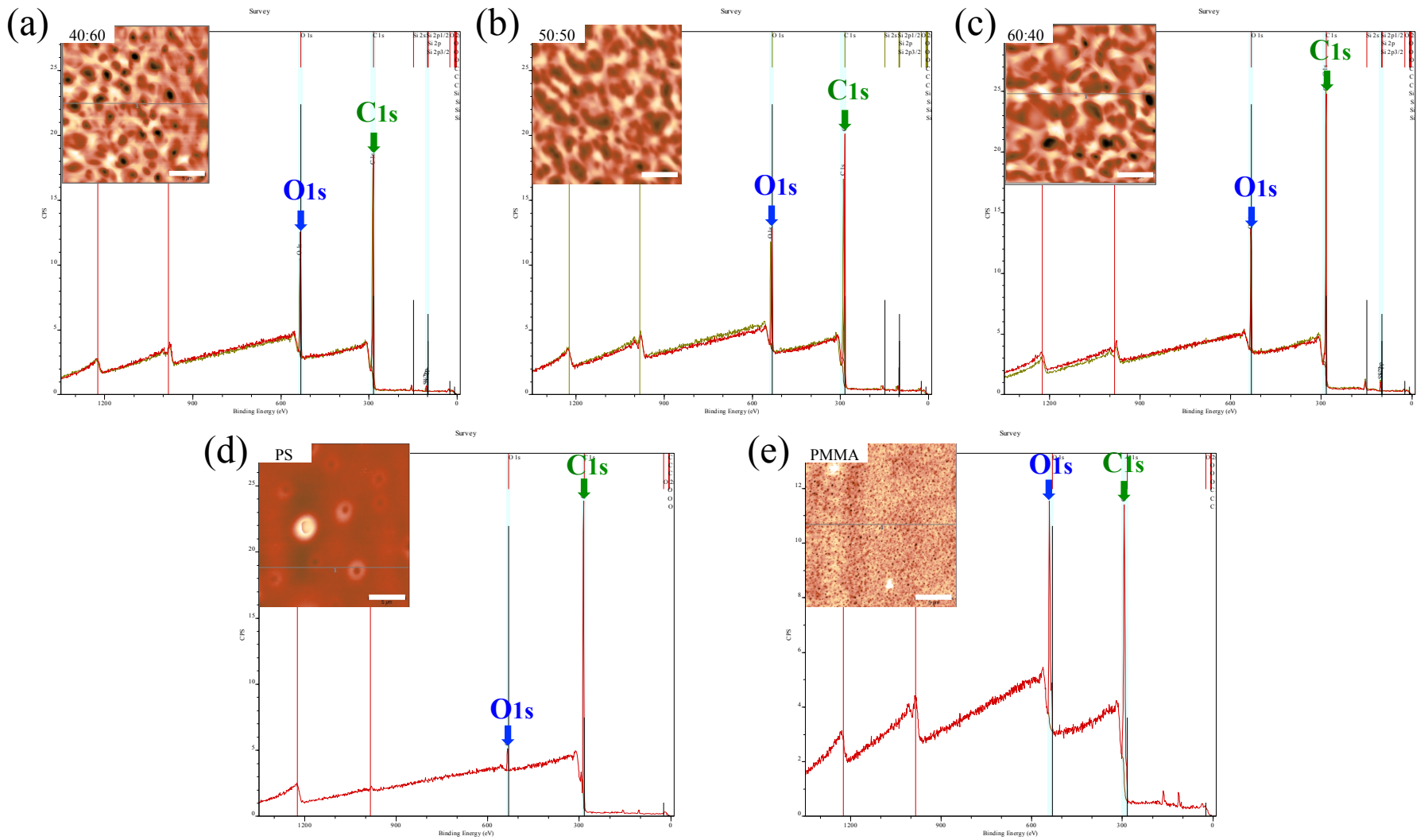

Figure 19. Average XPS spectra for demixed surfaces at first two cycles (0s and 60s);(a) 40:60, (b) 50:50, (c) 60:40, and the individual polymer surfaces for only first cycle: (d) PS and (e) PMMA. The shift in C-H to C=O is observable in the demixed materials (a-c) and very obvious in the control homo-polymer surfaces (d-e). Carbon 1s peaks are highlighted by green arrows and Oxygen 1s peaks by blue arrows. Instep within each spectrum graph is corresponding AFM images of the surfaces at 20µm (scale bars 5µm).

3.5.7.1. Chemical Variation between different Demixed Surfaces

The contrast of 0 and 60s spectra (red and green plots) for the demixed surfaces can help identify a contamination layer at the surface. In the surface spectra (0s) no oxidised / contamination layer was found at the demixed surfaces (Figure 19), but contamination of silicon can be observed (Figure 20_a) where the presence of Si double peaks to the left of the dominant Carbon peak. Where comparison of similar layers gives an average element composition within the material providing better analysis of the material.

Entire XPS spectra for demixed surfaces averaged from the first two cycles (0s and 60s) are displayed in Figure 19_(a-c) with individual control polymer surfaces below (d,c). It is from the two homo-polymer spectra (d,e) that we see the contrasting elemental composition ratios for carbon (C1s, *green*) and oxygen (O1s, *blue*). On the PS spectra, double bound C1s (C=C) is clearly the main peak compared to the PMMA spectra, where the O1s (C=O) is almost equivalent to carbon. This observable difference between material spectra is maintained in the demixed materials (a-c). A sliding scale separation of C1s and O1s intensity peaks are observed, throughout the respective demixed polymer surfaces (a-c).

As the individual element composition of PS and PMMA are identical in (carbon, hydrogen and oxygen) the identification of each surface is not based on the peak energy positions (carbon: 285eV and oxygen: 562eV) rather between the ratios of intensity (CBS, arbitrary units) of Carbon to Oxygen within each material. Hydrogen with only a single electron surpasses the detection sensitivity of this instrument and cannot be accurately quantified in this technique.

Illustrated in Figure 20_b are individual carbon 1s and oxygen 1s spectra, which displayed in descending order of etching of PS over time. The decrease in peak profiles during decent is equal to decreases in element presence within the polymer film. Most notably is the sudden drop off of the C1s peak in PS, which maybe accountable for the PS thickness on the surface of substrate. The oxygen spectra also displays a very late O1s peak on the final cycle, this can be attributed to the silane layer on the glass substrate.

Note the shift in C-to-O levels within different demixed surfaces, when compared to the control PS and PMMA materials. The control PS material has high levels of carbon π*C=C bonds with low traces of oxygen, while the line formula contains no oxygen atoms $(C_8H_8)_n$, the material would have obtained oxygen during fabrication from moisture absorbance in toluene and/or from exposure to the atmosphere during polymer dissolving and spin casting. In contrast the control PMMA $(C_5O_2H_8)_n$ material contains

oxygen, even though the same fabrication method was used and the polymer was exposed to the same oxidizing factors. The peak intensities for O1s and C1s are almost level due to levels of π*C=O bonds. This contrasting ratio of C1s to O1s intensities distinguishes the two individual polymers and can identify the differences between demixed materials.

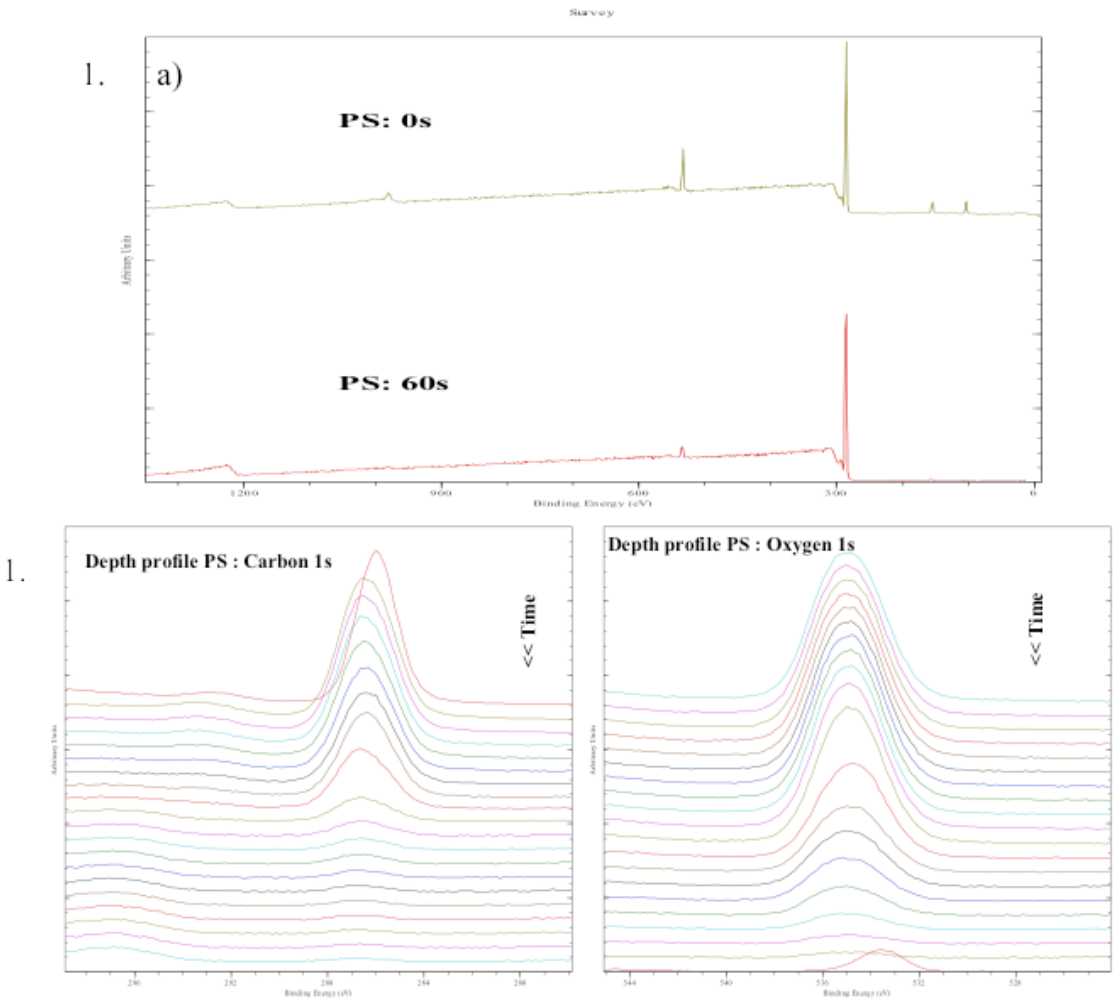

Figure 20. XPS Depth profiling spectra for (a) Polystyrene during initial etching, 2 cycles, at 0 & 60seconds. Its complimentary (b) carbon *left* and oxygen *right* profiles are below, showing change in elemental composition down through the material etching for 20cycles, 0 to 1141seconds.

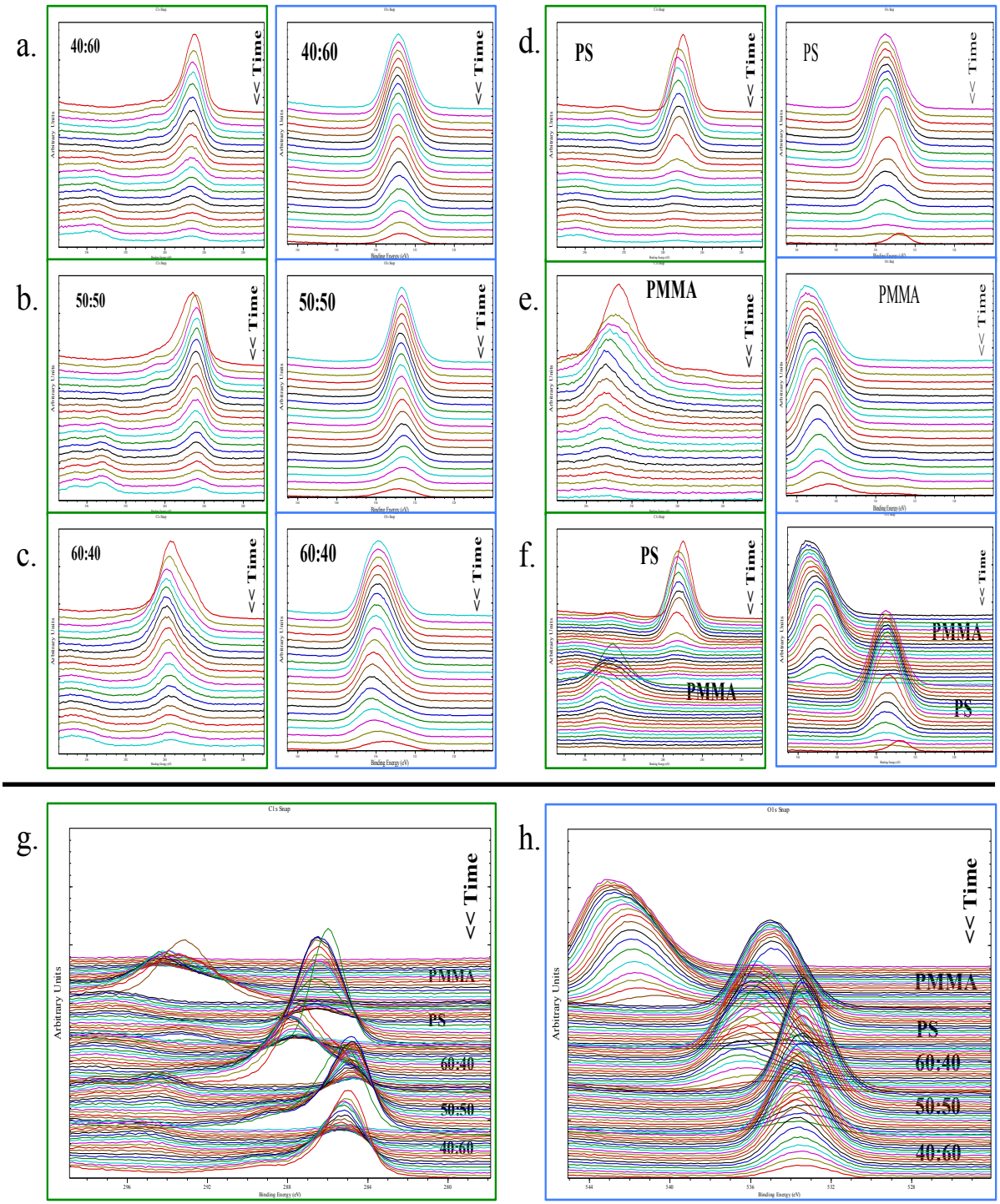

Figure 21. Depth profile XPS spectroscopy of carbon 1s (*green*) and oxygen 1s (*blue*). All spectra contain 20 sputter cycles, spanning 0-1141seconds, with increasing time moving vertically downward. Time is equivalent to the depth into the polymer material. All C1s and O1s spectra are displayed side by side for; demixed blends (a-c) and both homo-polymers (d,e). Both homo-polymers are also displayed together for C1s and O1s to contrast the different binding energy peaks for each individual polymers (f). Combined material C1s and O1s spectra, identifying the change in binding energies between each material (g,h).

3.5.7.2. Depth Profiles of each Demixed Surface

The depth profiles for demixed surfaces (Figure 21_a-c) depict the altered C1s *green box* and O1s *blue box* peak energy profiles during time related etching through each material. The individual homo-polymer surfaces are presented similarly for comparison (Figure 21_d-e). The combined spectra of the homo-polymer spectra (f), show both polymers side by side with contrasting difference between the C1s *green* and O1s *blue* BE peaks and morphology. The C1s spectra *green* shows a clear sharp peak of PS in contrast to the softened low intensity peak of PMMA. The quantified BE for average PMMA peaks correctly remains higher (C1s~294eV; O1s~542eV) over the BE energies of PS peaks (C1s~286eV;O1s~535eV) due to the great bind between C=O bonds, aforementioned. When this is observed with demixed surface in (g) we observe dampened peaks in similar BE as the PS with secondary bumps found at high BE that are inline with PMMA peak. This illustrates nicely the combination of both polymers by the demix technique.

The different demixed material elements are close to their expected stoichiometric values for both encompassing homo-polymers.

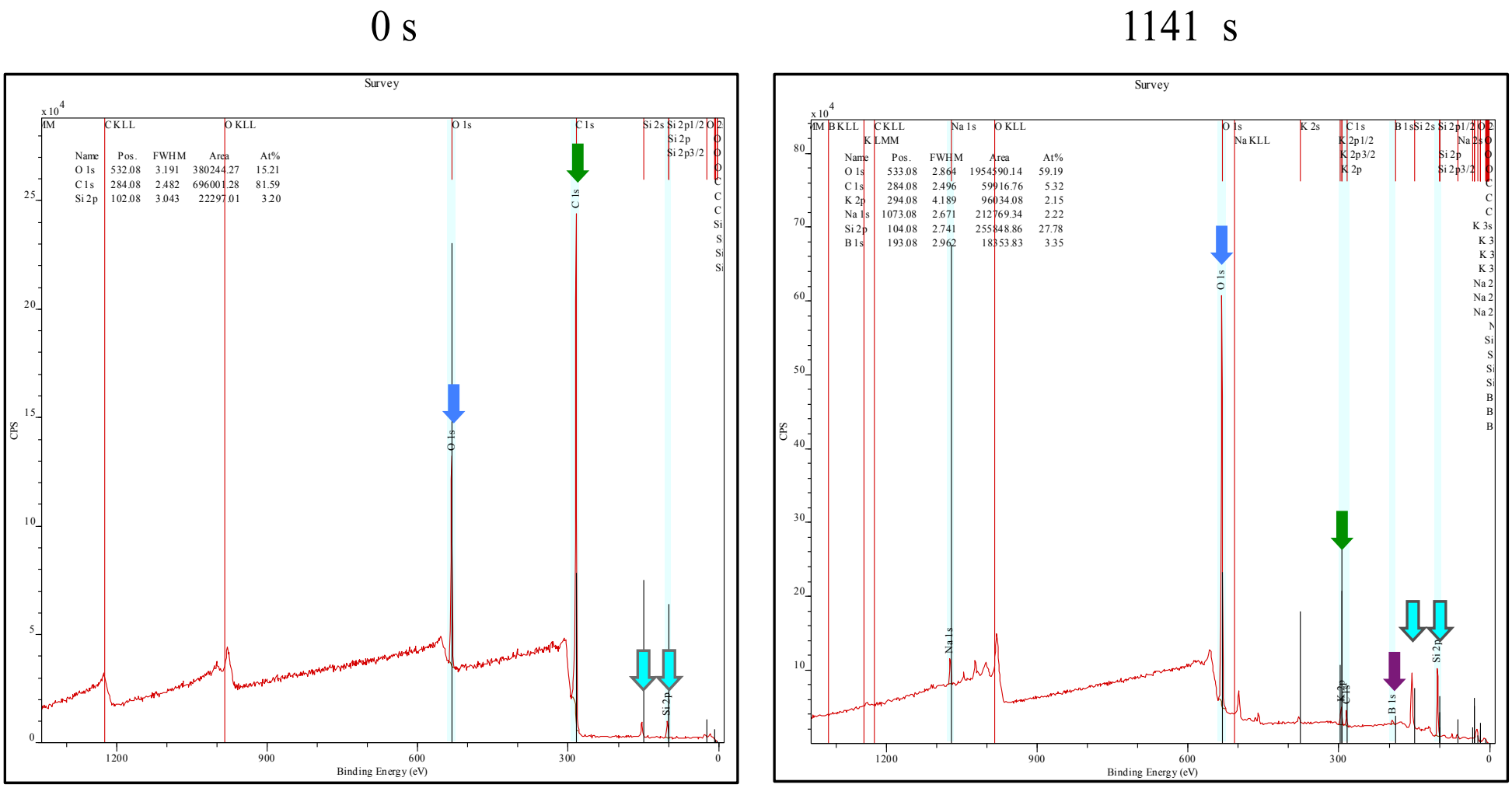

Figure 22. Depth profile spectra at time zero (*left*) and comparison to deepest spectrum after 20 cycles, 1141seconds (*right*). Kratos element library identified peaks shown by arrows; Carbon (C1s), Oxygen (O1s), Silicone (Si2p) and Boron (B1s).

During depth profiling detection of the substrate was readily identifiable, as the cover slips used for spin coating were borosillicate glass, containing boron trioxide. At (1141s) etching the XPS spectra clearly shows B1s peak at a slightly higher eV position then Si2p (Figure 22_ *purple arrow*). Having a clear defined end point for the substrate enables each complete set of spectra act as a measurement to the thickness of individual polymer films. The complete depth profile spectra for 40:60 was used to depicted this, Figure 23, highlighting the atomic conc. at timely intervals to show the quantified change in elements trough the material. Service spectra are shown *right* with colour-coded arrows for respective elements. Time increases vertically downwards relative to the etching depth of the spectra (0/300/600/900/1,141seconds) into the polymer film (represented by silhouetted blue image) until it reaches the borosilicate glass. The quantified atomic concentration % is carbon rich initially, PS 'skin', before increased O1s content for the PMMA-rich 40:60 material. The sharp (3.3%) boron 1s is detected at 1141seconds, determining the surface of the substrate.

This was preformed on all homo-polymer and demixed-polymer surfaces to determine at what etching cycle boron first appears. These were compared to the AFM height profiles to see if measurements correlate (Table 2).

Surface	AFM height (µm)	Boron detection cycle (time)
40:60	0.88	9/10 (~ 500s)
50:50	0.54	7/8 (~ 400s)
60:40	0.9	9/10 (~500s)
PS	~ 5 nm	8 (~ 420s)
PMMA	~ 3 nm	5 (~ 250s)

Table 2. Comparison of different polymer film thickness measured by AFM and relative depth by XPS

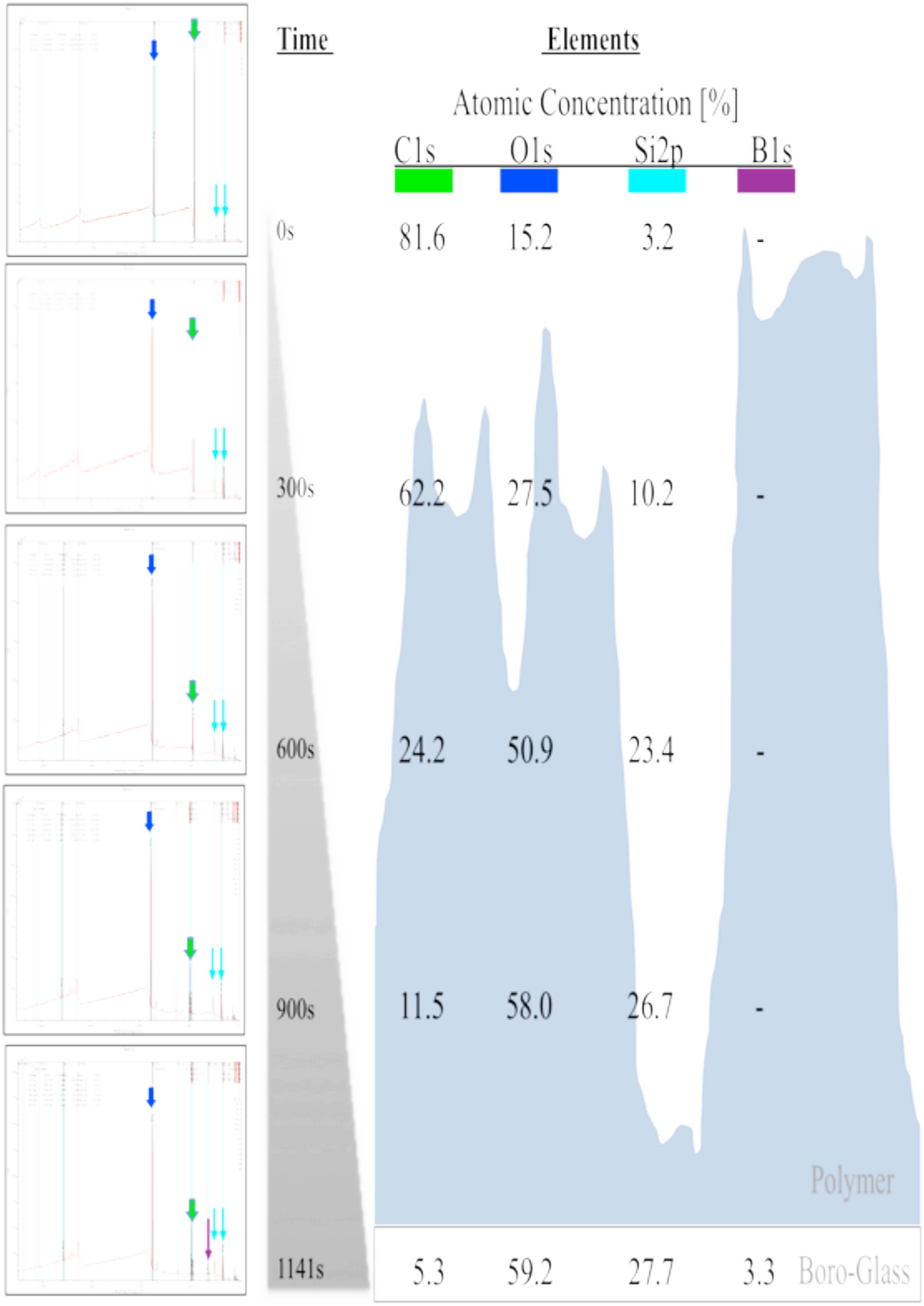

Figure 23. Depth profiling XPS of 40:60 demixed surface: survey spectra at different time points (*left*); Individual periodic elements carbon, oxygen, silicone and boron are highlighted with different colours in the table and with corresponding arrows on the spectra graphs (*right*). Quantified spectra readings are represented as percentage atomic concentration, with the presence of boron indicating the depth of substrate, borosilicate glass.

3.5.8. *Polymer Surface Wettability*

Water contact angle measurement for all polymer surfaces and blank glass control were evaluated simultaneously under identical conditions to determine surface energy. Individual polymers under normal spin coating conditions displayed opposing θ values to one another, as expected given their characteristics, PS displayed high (~100º) compared to PMMA (~60º). Both are in stark contrast to the glass surface control (~45º). The angles of the mixed polymer surfaces all fell in-between the individual polymer values and showed a slight trend towards the dominant polymer type.

All contact angles (θ) were increased on the demixed surfaces (Figure 24_A Demixed surfaces) most noticeably when in comparison to PMMA and glass controls. This general trend persisted amongst the demixed surfaces with BFP, but also increase in the individual homo-polymer control surfaces (Figure 24_A BFP surfaces).

When the same surfaces undergo plasma treatment for 60 seconds, striking decrease in contact angle is seen on all surfaces except for PMMA. This dramatic decrease is clearly shown in Figure 24_C, where direct comparison of the different conditions can be seen on these identical.

Plasma cleaning surfaces for 60 seconds in a vacuum aptly increased the hydrophilic nature of the polymer surfaces to be more in line with that of glass. With the exception of PMMA, that displays the previously stated characteristic of initially increasing before returning back to a basal level, ≈ 60º.

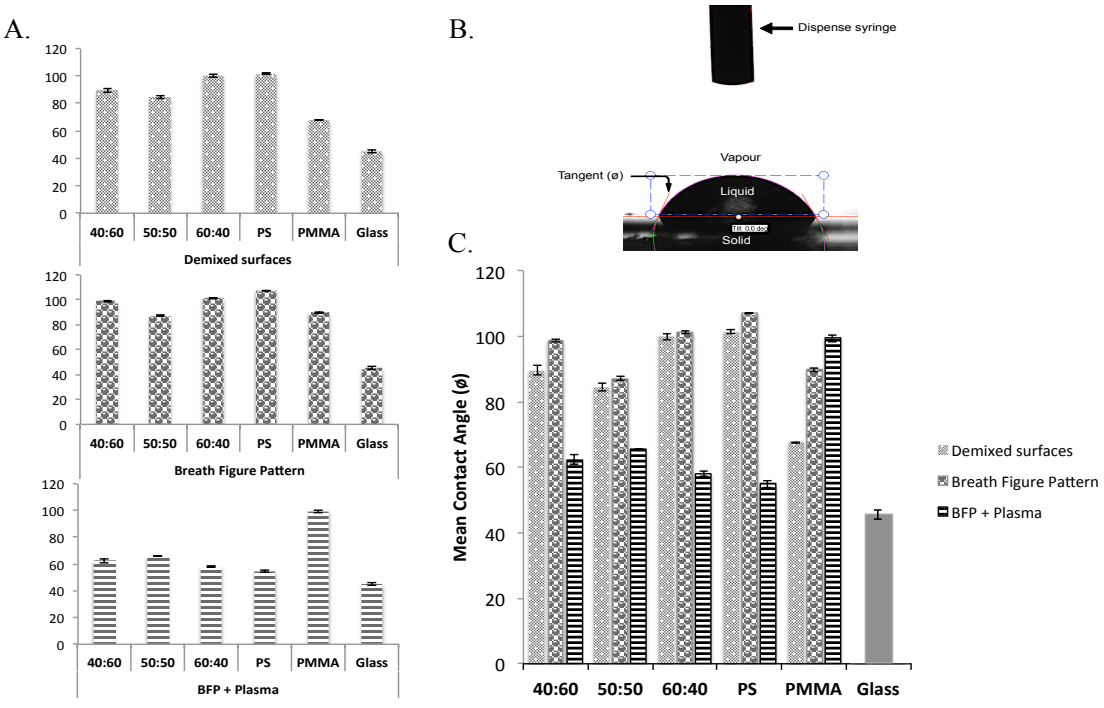

Figure 24. Water contact angle results for all surfaces under investigation separated into the three various stages of fabrication modification (A); Labelled image of water droplet on 50:50 surface during measurement (B); Collective wettability angles for each surface after each stage of preparation (C).

3.6. Discussion

The 3% polymer solutions used had very low viscosity and when the direct acceleration method was used, centrifugal forces did not allow enough time to evenly disperse the fluid on the substrate due to lack of tension between fluid and surface, creating areas of uncoated substrate see Figure 4_B. Demixed polymer surfaces were selected due to greater height differentials were obtained at closer ratio mixes, this is possibly due to higher tension between polymer chain structures of each polymer competing for space combined with relative rate of evaporation of solvent from each. Toluene is a better solvent of PS then PMMA, resulting in less toluene remaining in PMMA and during spin coating he swollen PS areas with collapse below the already solidified PMMA domains[3,151,179].

This is corroborated by the finding of S. Walheim et al[3] where they hypothesised two alternate topographic structure formations during spin coating. They noted that when PS is in combination with PMMA and dissolved in toluene that the toluene is a far better solvent of PS and therefore the PMMA is depleted of solvent more rapidly during spin coating. This leads to raised PMMA islands and collapsed PS troughs. They confirmed the theory by replacing toluene with methyl ethyl ketone (MEK) a far more favourable solvent for PMMA and an inverse relationship was observed, where rapidly depleted PS-rich regions solidifies first. More interestingly is that during their toluene experiments they noted that a thin layer of PS could cover the raised solidified PMMA.

Topography of PS-rich surfaces form dimply-like divots and the occasional very large pore, this is accountable due to a large number of water molecules attacking a single site and the centrifugal forces from the spinning open up the pore (these do not form when PS is cast under static humid conditions). Greater caldera pore size was observed with PS-rich blends as opposed to small diameter but greater frequency of pores observed in PMMA-rich blends. The observed degree of separation between caldera followed a trend in favour of greater separation in PS-rich surfaces over PMMA. This is concurrent with caldera size profiles as measurement of separation is taken for the ultimate end-point (central point of pore diameter) to the next nearest neighbour, if pore sizes of individual pores are greater in PS-rich surfaces the distance of separation will be also.

3.7. Summary

- The spin coating technique enabled in-house replication of established findings in the literature. With the premise to explore these topographically distinct surfaces for biological influence in the context of biophysical regulation of multipotent cells during differentiation.
- Overall the phase separation of these hetero-polymer films followed similar if not identical morphology as those found in literature[3,175-177].
- Spin coating of immiscible polymers enables the fabrication of lateral domains with distinct topographical patterns, texturized with particular differences in heights and chemically discreet regions, from the naturally occurring phase-separation of two immiscible polymers.
- The micropattern topography created is reproducible and highly adaptable for downstream processes.
- AFM measurements showed phase-separation geometries were generated from immiscible polymer solutions by demixing. The 'islands and plateaus' generated are as a result of incomplete dewetting process in a bilayer system, where PMMA is raised against low-lying PS. The phase separation of polymers generates taller feature protrusion raised from the surface of substrate. Tight contrasting blends of immiscible polymers showed heights almost double the size compared to the low ratio blends.
- Adaptation of the process to include humidity evolved the topography dynamic and diversity.
- Utilisation of water droplets induced crater-like pores on the surface, the structures had highly defined texture due to the presence of caldera.
- These textured peaks were diverse in shape, size and separation, highlighting the individual characteristics of both homo-polymers. Retention of individual characteristics diversified the topographical nature of the material presented to cells.
- Surface wettability directly relates to surface texture and roughness, due to chemical composition of polymers and their respond to water droplets.
- XPS analysis confirmed the individual chemistry's of each surface complimenting the observation made in AFM and SEM data.
- XPS confirmed the use of demixing as a technique to combine polymer properties and retain chemical integrity.

- XPS depth profiles revealed possible masking effects of PS over PMMA. This has previously been described in the literature along with the defining characteristic of elevated PMMA islands when in the presence of PS. Distinct topographical features are highly indicative of this di-polymer combinations.

Demixed polymer blends under humid conditions generated distinct micro-topographical surfaces, for investigation of altered cell adhesion due to physical and chemically distinct surfaces.

CHAPTER 4. SHORT-TERM EFFECTS OF SURFACES ON ADHESION AND MORPHOLOGY OF A VALIDATED MULTIPOTENT MESENCHYMAL STROMAL CELLS

4.1. INTRODUCTION

The physiological tissue response to injury is a highly conserved process throughout evolution and amongst different species. The formation of scar tissue in humans and the majority of mammals is the initial phase of wound healing, where its establishment self contains exposure to infection and enables the re-establishment of specialized tissue framework. Multicellular organisms produce a network of intercellular connecting elements to create a supporting architecture permitting the inflow and outflow of materials essential for life, and impart protection from the physical strains of the overall organism[10]. There are two main elements which accomplish the needs of these structures, known collectively as the extracellular matrix (ECM), they are insoluble fibres that resist tensile forces and interfibrillar polymers which inflate the fibrous network[194]. Collectively they offer resistance to compressive forces, while providing a suitable environment for cells. Collagen composes the majority of proteinaceous fibres, but can be in a ratio with elastin dependant on the location in the body, and the soluble interfibrillar polymers are typically carbohydrate-protein complexes appearing primarily as proteoglycans (e.g. glycosaminoglycan). Other factors contribute to the stability of the matrix through presentation of favourable RDG-motifs for cellular adhesion, like adhesive glycoproteins fibronectin and laminin, they provide 'foot-holes' within the matrix and promote embedment of cells within it. The framework or scaffolding of higher animals are far more complex than previously realized, where the pooling of essential elemental components in the presence of multipotent cells is not enough to regenerate a tissue[194]. Evolutionary mechanisms need to be strategically stimulated within a potent cell type for functional organisation of protein components to regenerate a tissue.

Multipotent mesenchymal stromal cells or mesenchymal stem cells (MSCs) are isolated from bone marrow or fat tissue. First described as adult "stromal" progenitors in the works of English scientist Owen *et al.* in London back in 1988[195]. Initially believed to be restricted to haematopoietic and osteogenic lineages due to their bone marrow source, it was found that the haematopoietic system had a separate stem cell population and a surrounding, nurturing population of mesenchymal stromal cells were found to also be multipotent for other mesoderm tissue lineages (bone, cartilage, fat, nerves and muscle)[105]. Purification is required from the complex bone marrow niche, but as they lack a specific cell surface marker cell sorting can be complicated. It is now known that

there are resident populations of MSCs in nearly all tissues, they migrate within tissues during injury or inflammation[98].

Adherent MSC culture conditions have been the preferred isolation technique employed, plastic adherence removes the non-adherent haematopoietic cell fraction through regular media changes and are eliminated from culture by passaging. Purer MSC cultures are obtained 12-16 days after collection[105].

Great interest was initiated by the multipotent capacity[26] of the cells but enhanced by the observation of MSC-mediated immunomodulation, due to cells ability to secreted soluble mediators at site of tissue trauma and regulate /supress inflamed immune response[196].

MSCs are adult stem cells exhibiting several functional properties that provide a window for a wide range of cell-based clinical therapies. The most recent revelations of these multifaceted cells is their ability to receive instructive adaptation from their physical environment, self-stimulating the innate repair mechanisms through temporal spatial awareness, an area still under investigation.

4.2. Aim

Identify and validate a source of multipotent mesenchymal stromal cells and determine their response to adherence to the modified polymer surfaces

4.3. Objectives

- Reproducibly isolate populations of mesenchymal stromal cells from trabecular bone
- Propagate and culture expand plastic adherent, fibroblast-like cells to a near homogeneous population
- Validate the MSC status by the international defined cell surface marker criteria for multipotent mesenchymal stromal cells and confirm the cells multipotent potential by tri-lineage differentiation
- Evaluate if the micro-texture 'Caldera' affects the focal adhesion of individual cells on each surface
- Determine the effects of adhesion on the cell morphology over short-term culture

4.4. Materials and Methods

4.4.1. *Optimization of FBS concentration for MSC Isolation and Expansion*

Aim: Decrease isolation time of MSC without effecting the quality and quantity of cells isolated.

Adherent mononuclear cells can be strongly affected by different concentrations of bovine serum, altering proliferation and potentially differentiation. Determining the minimum FBS required for rapid adherence, isolation and expansion of MSCs is still under contention. Low levels prolong culture time, limit proliferation and stress cells resulting in slow growth, potential differentiation over long period, and even apoptosis. High levels used during isolation maintain the growth of numerous cells not only plastic-adherent cells, resulting in heterogeneous cell population expansion.

Several concentrations of FBS were investigated on extracts of primary human bone fragments and bone marrow aspirates (P0). Assessment was performed using three patient samples, each individual sample was prepared in keeping with standard protocol.

- Primary MNC isolation preformed by density gradient Ficoll extraction
- FBS was added to complete basal media (detailed in Chp. Material & method)

Whole mixed population MNC cells isolated from ficoll layer (P=0) were cultured in 6-well plates initially, at 20% FBS culture media [$>1x10^6$ cells per well. 2 ml media per well] at 37°C and 5% CO_2. Cells were cultured at P=0 until heterogeneous cultures of adherent, fibroblast-like cells were obtained, changing medium every 3 days. When MSC's population were confluent they were passaged using trypsin and counted with a haemocytometer. At P=1 cells are seeded into 96-well plates at a density of 40 cells/cm^2. Individual plates represented different time periods [4,7,10 & 14 days] and each plate contained three concentrations of FBS in triplicate [10, 20 & 30%]. Cell proliferation and viability was asset using MTT/MTS assay and cell number was calculated by standard curve (Chp. Materials & Methods).

4.4.2. ***Histological Staining***

Safranin O, is a common stain of cartilage, staining the cartilage (i.e. type II, Collagen) orange to red, cell nuclei are stained black and the associated cytoplasm a bluish green[197].

Masson's trichrome, is commonly used to detect of collagen fibers in several tissues such as skin, heart, muscle, etc. The collagen fibers stain blue, with the nuclei black and the background, cytoplasm/keratin/muscle, stained red[198].

4.5. RESULTS

4.5.1. *Culture Conditions: Defined MSC Media*

Culture conditions vary widely for all cell types, but the artificial environment for mammalian cell growth is well established; regulated physicochemical environment (pH, osmotic pressure, temperature), gas exchange (O_2, CO_2) in a suitable vessel and a supply of substrates or medium containing essential nutrients (amino acids, carbohydrates, vitamins, minerals), growth factors and hormones.

The multipotent nature of MSCs makes them sensitive to change and maintaining their plasticity requires standardization of media and demands the use of defined media. A low glucose form of standard Dulbecco's modified eagles medium (DMEM) supplemented with antibiotics (1% Penicillin and streptomycin), thermally stable form of L- glutamine (Glutamax™) and foetal calf/bovine serum (FBS).

The use of animal products in the culturing of human tissue is continuously under debate; due to the limitations of cell therapy translation to the clinic. If serum is not obtained from a reputable source, contamination can pose a serious threat of infection. Unfortunately use of serum is vitally important to the healthy growth of mammalian cell *in vitro*, providing a source of growth and adhesion factors, hormones, lipids and minerals in basal media. Serum has not been fully characterised and artificially synthesised successfully.

Evaluation of a suitable serum source [New Zealand] was investigated for the proficient proliferation of primary MSC populations *in vitro.* Cell populations of plastic adherent fibroblast-like cells, after P=0 the initial isolation culture, were nourished by DMEM containing different concentrations of FBS. Cells were cultured over a two week period taking cell counts at regular intervals, in triplicate and preformed on three donor cells [N_2694; N_2693; N_2702] to give a more accurate average growth rate (Figure 25.) Performing cell counts using the MTT assay is a highly accurate quantitative method that assesses for viable cells (active mitochondria in the cytoplasm of cells reduce colourless tetrazolium dye by redox reaction into purple formazan crystals, this can then be read in a spectrophotometer at 570 nm). The relative growth populations were quantified by converting absorbance readings into cell number using a standard curve (see appendix pg. XXXII). Three central concentrations of serum were investigated [10%, 20%,30%] the most common used in literature is 10%,

two other extremes were also included; a very low concentration of 2% and a commercially available MSC medium (Millipore MSC media™), the contents of which are unknown.

Media containing high levels of serum [20% and 30%] displayed continuous growth over the two-week period, (Figure 25), achieving cell populations of [4,265 and 5,683 cells] respectively. Similar growth was observed in the commercial MSC media but displayed erratic growth pattern with high growth spurts after the first week, after two weeks populations was estimated at 8,052cells. Cells in lower serum media [2% and 10%] grew more slowly but with similar stable growth patterns over the time course, [1,460 and 2,356 cells respectively]. Both displayed steady initial growths that appear to plateau (Figure 25). Amongst the commercial, high serum and low serum groups little difference is observed but between them large discrepancies are seen. A noticeable growth increase is observed between 10% and 20% where 10% serum displays a more stable growth rate that plateaus, indicating controlled, symmetrical growth of cell populations.

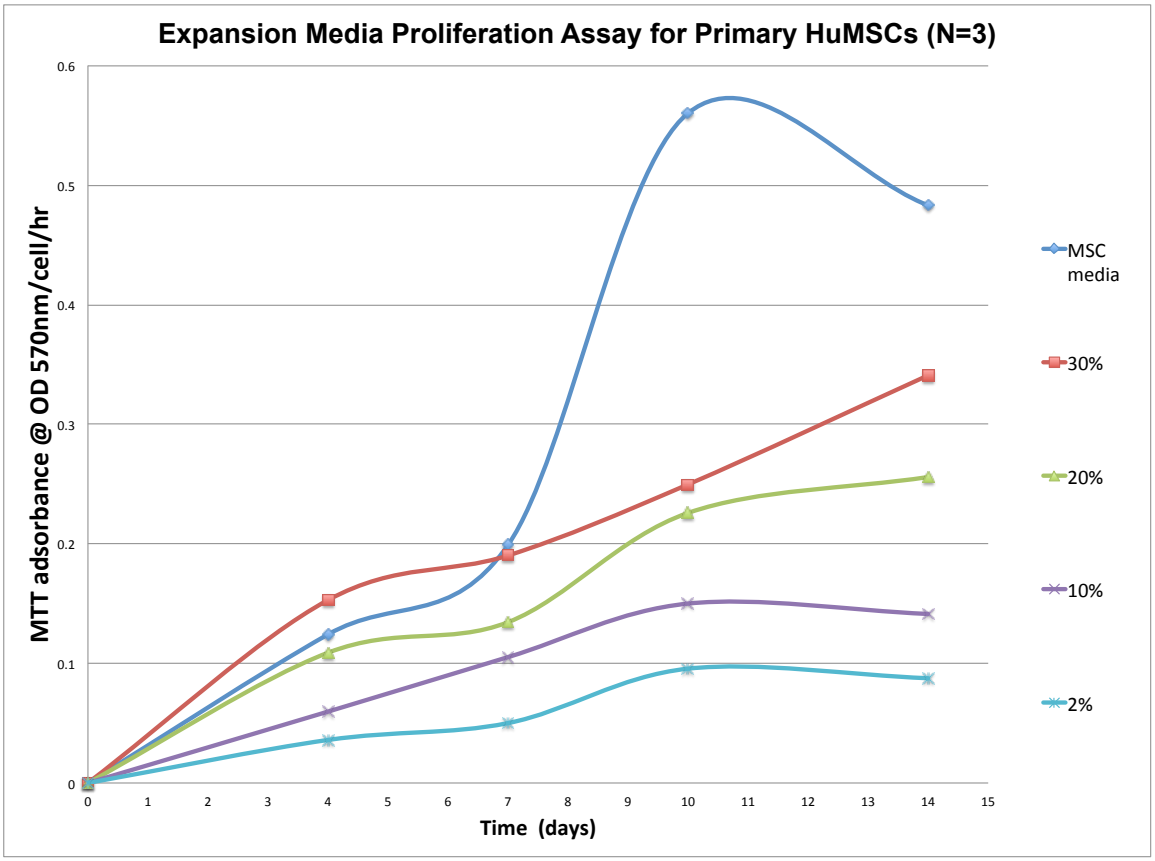

Figure 25. Proliferation assay of evaluation of different compositions of culture media in the expansion of primary mesenchymal stromal cells. Three donor cell population were evaluated for suitable media composition for stable MSC proliferation over a two week period.

4.5.2. *Identification of Mesenchymal Stromal Cells*

There is an ever-growing need for stem cell identification in the development of clinical therapeutic applications. Hindering this development is the isolation and confirmation of identity for individual stem cell populations. The most commonly studied type of stem cell is the mesenchymal stromal cell (MSC), extracted from the bone marrow they are rarely identified as homogeneous population and typically extracted together with a variety of different cell types (red blood cells, osteoblasts, hematopoietic stem cells). Enriched cultures of MSCs can be achieved by adapting culture conditons in favour of their individual characteristics, e.g. highly adherent nature, and providing time for cells to proliferate over prolonged periods (~8-10 days).

4.5.2.1. Isolation of Mesenchymal Stromal Cells

Bone marrow MSCs were isolated from the discarded waste of orthopedic surgery procedures, including femoral head and total knee osteotomy. Areas of cortical bone were separated to give bone fragments and physically minced by Liston bone cutters, before addition to wash buffer, shaken and filtered (50µm pores) to remove excess bone fragments. The wash buffer contains a low concentration of EDTA (5mM) to aid cellular detachment from ECM. Cell suspension was carefully poured on top of an equal measure of immiscible Ficoll™ and the cell fractions were separated by the density gradient during high-speed centrifugation. Mononuclear cells of interest were extracted from density gradient suspension, under went a secondary wash step, and were transferred to tissue culture plastic to select for adherent cells. HSC, non-adherent cell types and cell debris were removed during regular medium changes, selectively culturing for a fibroblast-like MSC population. A more homogenous population was developed with extended time in culture, passage 1, confirmed (~90-95%) by flow cytometry analysis.

Note: Full list of MSC isolations provided in appendix pg. XXXVI.

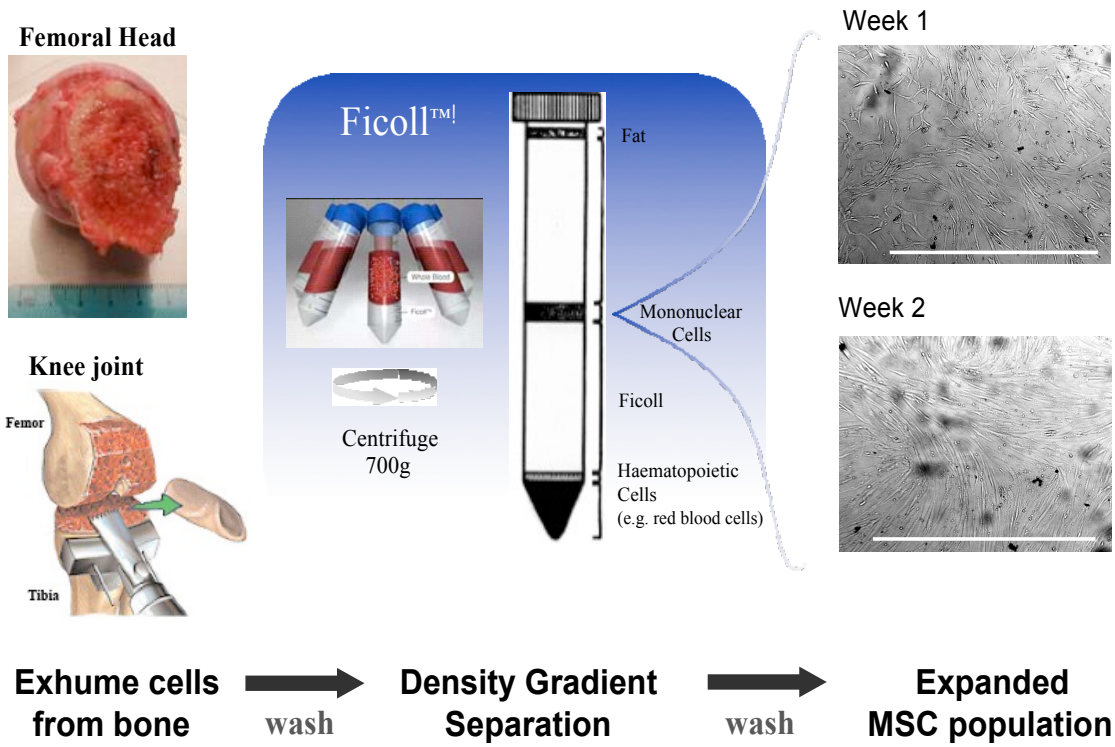

Figure 26. Schematic of mesenchymal stromal cell isolation from bone fragments post-orthopaedic surgery by density gradient separation and *in vitro* tissue culture expansion for adherent population. Scale bar - 1mm.

4.5.2.2. Characterisation by Flow Cytometry: Assessment of Cell Surface Markers

Tissue culture expansion of cell population selects for plastic-adherent cells and gradually removes non-adherent cell types (e.g. leukocytes, red/white blood cells, etc.) including hematopoietic stem cells. All mesenchymal cells were uniformly positive for three core surface markers CD73, CD90 and CD105. In contrast, MSCs were negative for hematopoietic lineage markers; CD14, CD19, CD34, CD45 and HLA-DR[26,199].
The expression of the positive markers: CD105, CD73, and CD90, have been associated with the plastic adherent characteristic of MSCs *in vitro*, and are often related to the potency ability for osteoblast, adipocyte, and chondrocyte differentiation[136,199]. The amalgamation of these positive and negative immune-markers allows for a better identification of multipotent MSC.

Positive	**Negative**
CD73	CD14
CD90	CD19
CD105	CD34
	CD45
	HLA-DR

Several patient isolates were evaluated using these cell surface markers to validate the isolation process. Due to the large volume of results generated by flow cytometry an example patient, N_2694, is described in detail and the other results combined in Figure 29.
Flow cytometry data is displayed as series of dot plots, both negative and positive form a panel to identify MSCs. Gating analysis enables the restriction for different portions of the cells of interest for more detailed analysis. Use of isotopic controls help define the gating background for each cell population, mouse IgG iostypes with identical fluorophores to the mouse antibodies are mixed with a sister cell population and processed before the experimental sample. Comparative gating of marker presence identifies the baseline for experimental sample (Figure 27).
Lineage-positive (Lin+) cells are cells expressing mature cell lineage markers, the rest of the cells are lineage-negative (Lin-) – they are devoid of cell lineage marker antigens

and so the specific antibodies failed to bind. All stem and progenitor cell activity are often identified within Lin- populations.

The basis of doublet discrimination is to detect and remove cell aggregates (doublet = two cells; clump= >two cells), as negative cells bound to positive will give a false positive result. Digital instruments have a built in function that allows disproportionate cell sizes to be measured *in situ* based on the change in voltage signal. Algorithms correlate length and time of voltage disturbance to width and height of cells passing the laser [Area = Width x Height], called Area Scaling on BD instruments. Using this a plot of SSC-A vs SSC-H can be plotted simultaneously in real-time (if a perfect sphere passed the laser a perfect 45º diagonal line passing through zero would be plotted). So disturbance to the voltage pulse is reported as an event on the dot plot. So based on Area Scaling, when the instrument is calibrated correctly (isotype), cells of the same size will have the same (or very similar) value in both axis (tight band plot). Therefore, all singlet events will be represented in a more diagonal display than doublets.

Figure 27_top left, forward scatter (FSC) is typically light scattered at a small angle

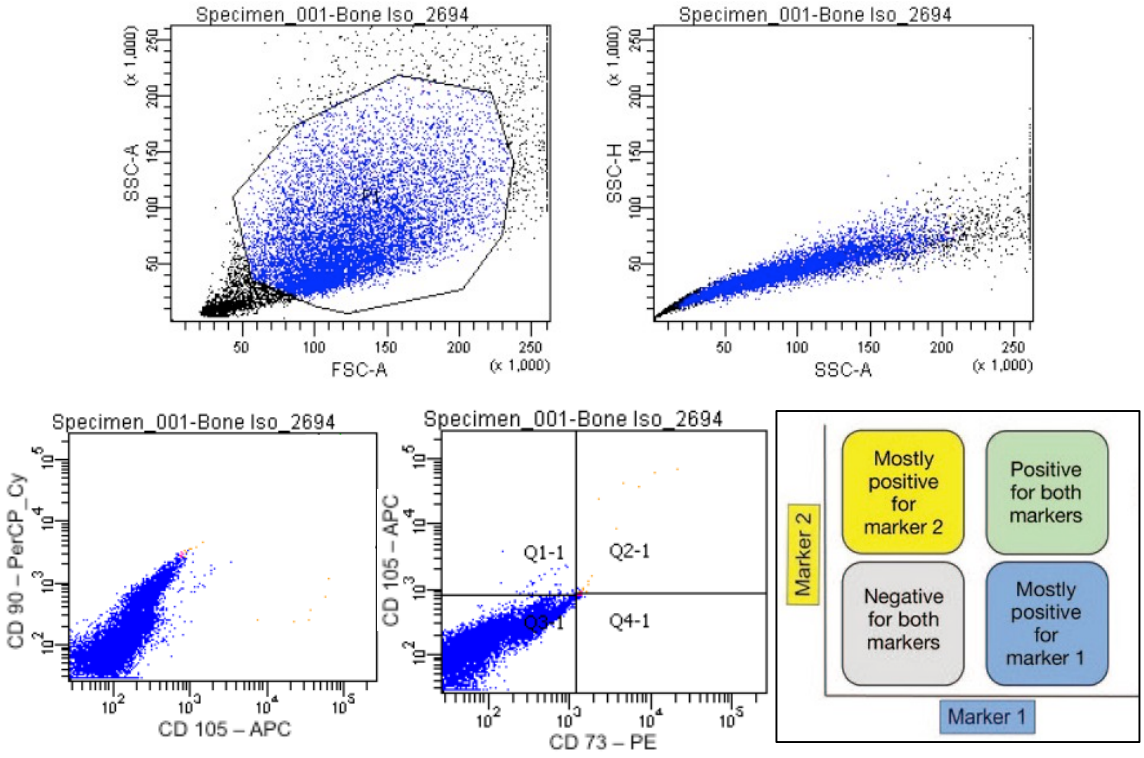

Figure 27. Isotype control plots for patient cell population N_2694 (THR) using IgG mouse antibodies, for controlled gating of MSCs (*top left*) and specifying for singlets by Area Scaling plot (*top right*). Restriction of LIN+ scattered portion brought forward to determine positive marker expression (*lower left*) in a fluorescent by fluorescent scatter 'quadrant' plot (*lower centre*). Cartoon illustration detailing the interpretation of a quadrant gate plot, referenced from 'Flow Cytometry' research techniques[5].

with a detector on the opposing side, 488nm/blue laser filter, this provides information on cell size and count.

Basic scatter plots are plotted as FSC on x-axis and SSC on the y-axis, (Figure 27*_top left*), which are gated for the central mononuclear population (heavy black concentration near origin of plot are debris or dead cell and further out on the logarithmic scale plot events are considered false or doublets). The exclusion strategy used for doublets was Area Scaling (BD instrument), forming a tight plot of SSC - A vs. H, Figure 27_top right. Where A is the area of the event passing the laser and H is the height or the time it takes to pass the laser, a tight plot indicates similar event/cell size, this is why cells were used as isotype controls and not beads.

Following this, samples were gated for specific fluorophore expression, Lin – (Figure 27*_bottom left*), and also accordingly for positive markers, (Figure 27*_bottom centre*), was gated tightly around negative expression for isotype (Q3-1), no detection of positive fluorophores should be detected (this is essentially 'zeroing' for this cell population).

The experimental samples of the same cells, N_2694, were processed directly after this, following a brief automated buffer wash, maintaining identical gated parameters. Gated experimental samples identified numerous MSCs/events [13,913 events] and displayed tight area scaling devoid of doublets (Figure 28_*top*). Mononuclear population were further analysed for presence of negative cell surface markers (LIN-) [9,852 events], detection of these markers (LIN^{+})[148 events] were omitted from further analysis (Figure 28_*bottom left*). The final quadrant scatter plot identifies the subpopulation of cells devoid of negative markers but expressing all the positive cell markers, Figure 28_*bottom centre* (Q2-1) [8,252 events]. Some cells only expressed one of the positive markers [210 events], Figure 28_table, *right*. The frequency of the complete parent population processed (13,913=100%) for the expression of MSC positive cell surface markers and devoid of haematopoietic cell surface markers, was found to be 97.5% MSCs.

These readouts can be further extrapolated for each individual fluorophore in more detailed flow cytometry analysis shown here in an example for the N_2694 patient MSCs. Once single cells were isolated and separated the analysis can be divided into the individual channels for each fluorophore or more accurately its respective cell surface marker (Figure 29_A). Each of the specific cell surface marker expression for all three

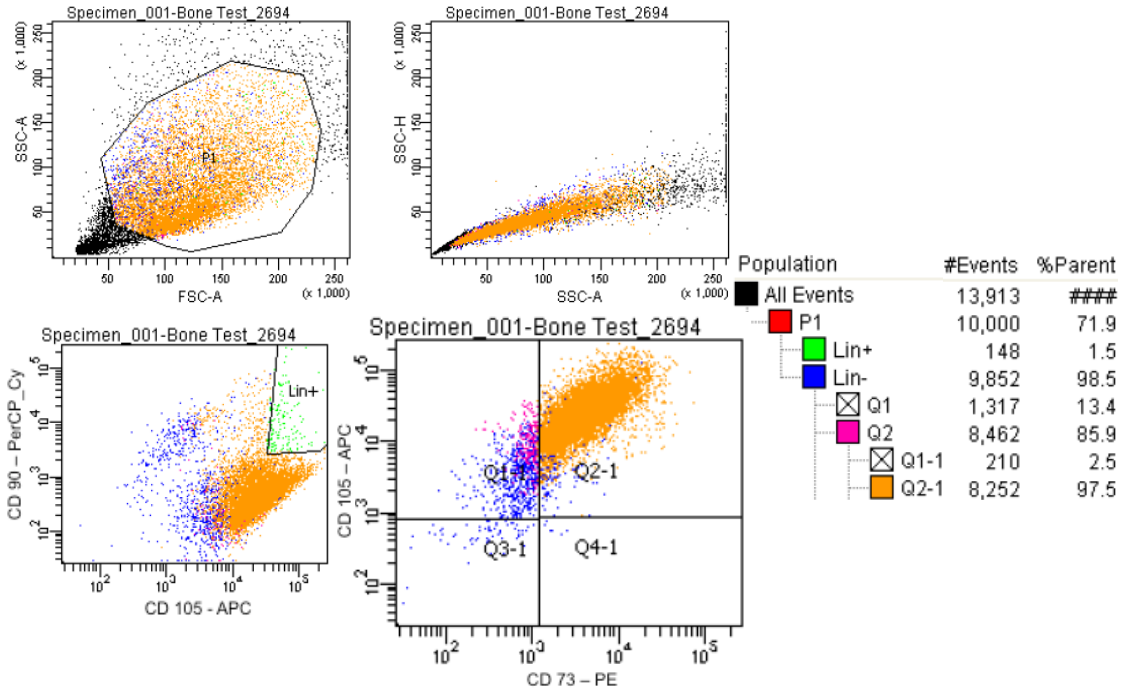

Figure 28. Experimental flow cytometry plots for patient cell population N_2694 (THR) using controlled isotypic gating by same cell comparison. Total MSC population (*top left*) are controlled specificity for singlets by Area Scaling plot (*top right*). Restriction of LIN+ scattered portion (*green*) removes lineage specific positive marked cells (*lower left*), the LIN- population were brought forward and contrasted for positive antibody marker in a fluorescent by fluorescent scatter 'quadrant' plot (*lower centre*). Quantified results for processed cell population through the different stages (table, *right*).

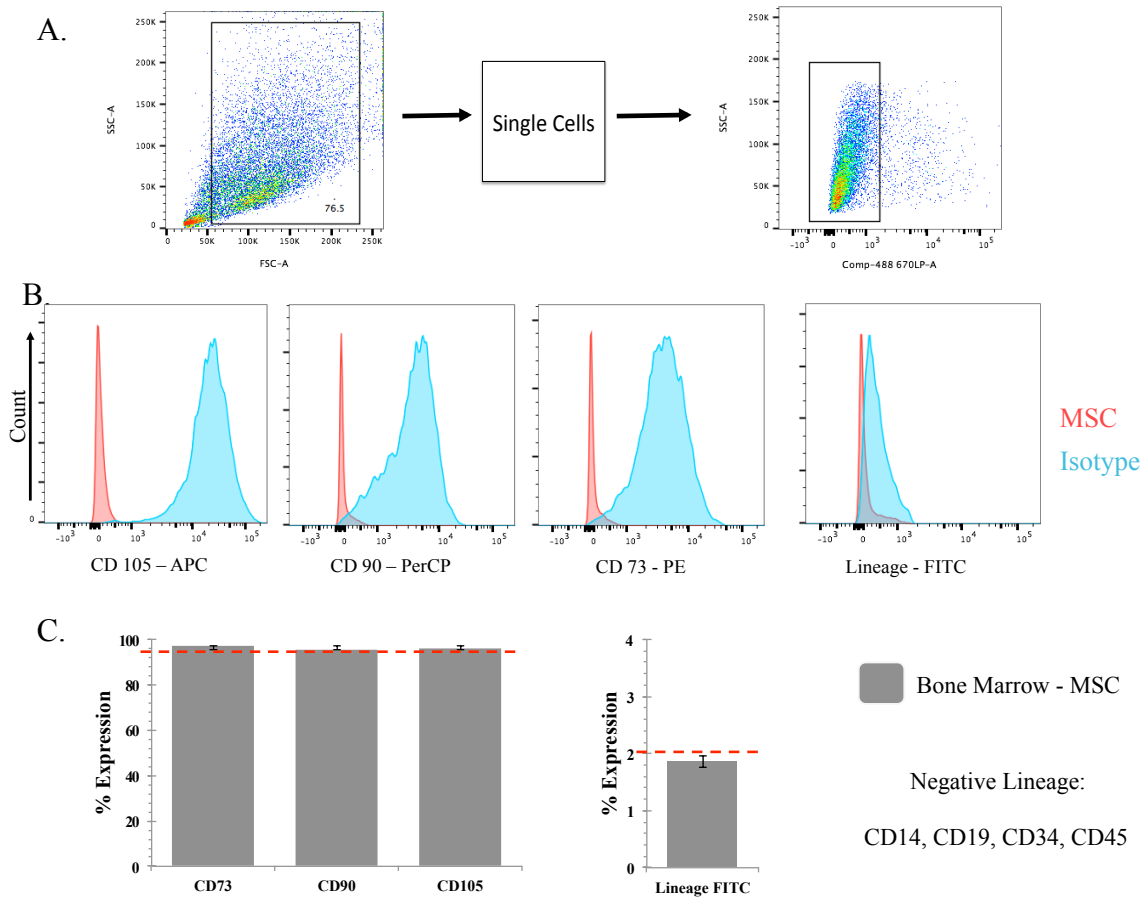

Figure 29. Example patient MSC N_2694 detailed flow cytometry analysis. A) Screening single cells B) positive markers (CD73, CD90 and CD105; *red*) were identified with contrast to isotype control (*blue*) and were also devoid of C) lineage specific negative markers (CD14, CD19, CD34, CD45) labelled by FITC (threshold for positive and neaative expression is represented by broken red line).

positive markers (CD73, CD90 and CD105)(Figure 29_B), known to be indicative of mesenchymeal stromal cells (expression ≥ 95%)(Figure 29_C). But as these markers cannot be used to solely to identify MSCs, the same cells must display a negative expression (≤ 2%)(Figure 29_C) of other lineage specific surface markers, represented by negative lineage specific markers labelled by FITC.

Identical flow cytometry assessment of different patient mesenchymal stromal cell isolates were evaluated, including isolates from the marrow of bone fragments in both total hip and knee replacements (THR & TKR). Four THR and two TKR isolates are detailed here (Figure 30), confirming isolation and extraction of MSCs from marrow in accordance with international identification standards[199]. Select subpopulations of cells were devoid of negative markers (LIN^-) and expressed all positive markers Figure 30_(*orange dots*; Q2-1). Quantified event analysis enabled the vast majority of processed cells to be confirmed as MSCs from all patient isolates, (Figure 30_*yellow boxes*). Please note that this is a small sample of cells (>10,000events) and can not completely confirm the entire expanded MSC population (>millions), which therefore cannot claim to be a homogenous population of cells.

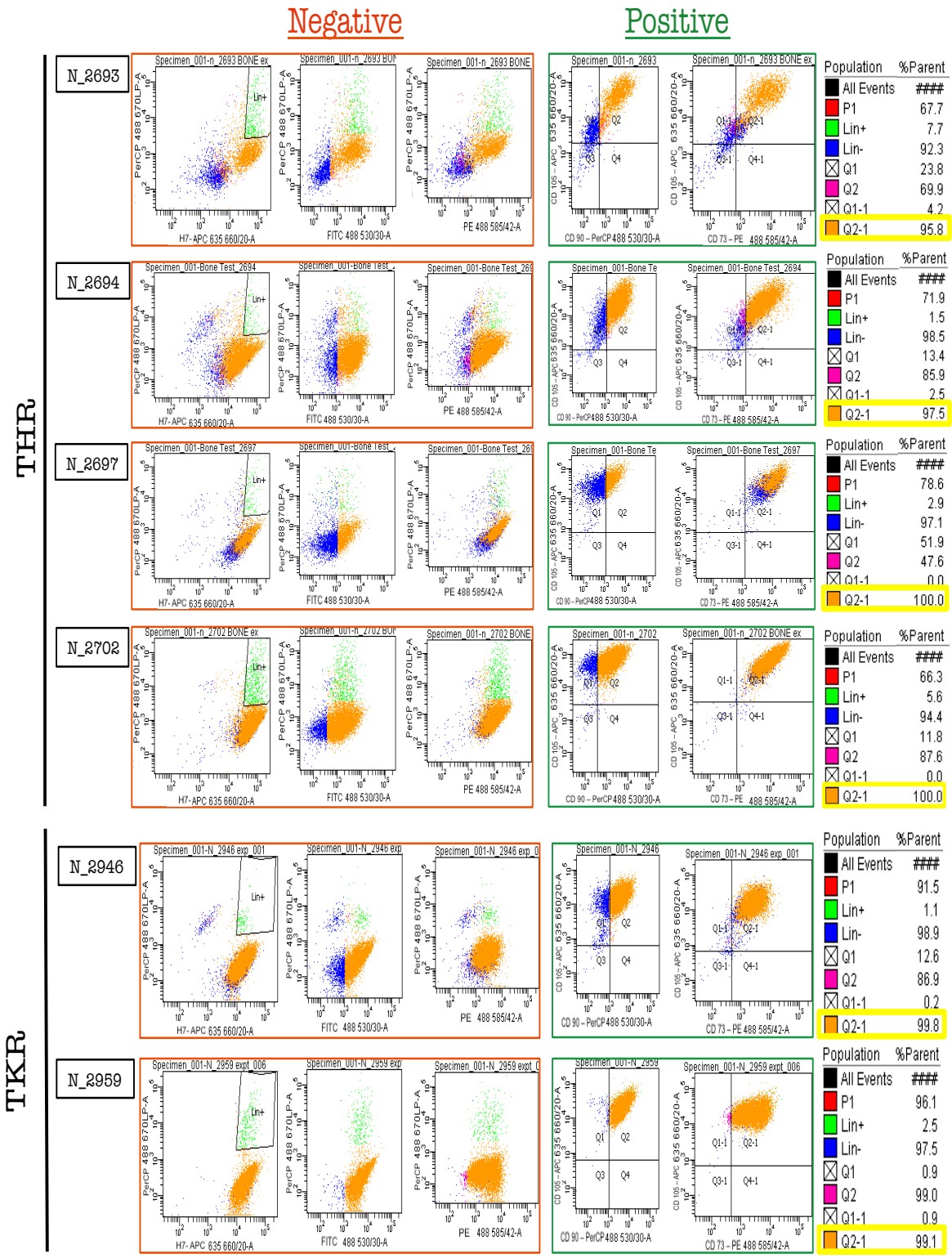

Figure 30. Flow cytometry analysis using density dot plots for patient mesenchymal stromal cells (N_♯) isolated from the bone fragments of both total hip & knee replacements (THR & TKR). Discrimination of lineage positive (LIN+) cells screened out events expressing negative cell surface marker antibodies (Red boxes; *green dots*). The LIN- cohort were further analysed for positive cell surface markers (Green boxes) using quadrant plots to identify cells expressing all positive cell surface marker devoid of negative markers (quadrant Q2-1; *orange dots*). Breakdown of quantified event readout are detailed at the end of each row. The event population identified as MSCs per total event population anaylsed is highlighted in yellow.

4.5.2.3. Characterisation by Differentiation: Assessment of Multipotency

To confirm the multipotency of MSC isolates, tri-lineage differentiation was preformed on several MSC populations with successful formation of osteogenic, adipogenic and chondrogenic phenotypes (Figure 32). An example patient MSC population, N_2848, is shown here (Figure 31).

Culture expanded populations of MSCs (P-2) were induced towards the different lineages, at the previously stated seeding densities (see Chp.2 M&M). Adipogenic differentiation was induced following exposure to dexamethasone, 1-methyl-3-isobutylxanthine (IBMX), insulin, rosiglitazone, Insulin-like growth factor 1 (IGF-1) and Indomethacin. The induction period ran over 14 days and was alternated between induction medium and maintaince medium (only basal media with insulin and IGF-1), during feeds a longer time period was left with induction medium (4 days) and shorter for maintaince medium (2-3 days). The formation of spherical lipid-rich vaculoes stained by Oil Red O (Figure 31_*top left*) with a general development of adipocytes across the cell population (Figure 31_*bottom left*).

Osteogenic differentiation was induced by exposure to dexamethasone, ß-glycerol phosphate, ascorbic acid and bone morphogenetic protein 2 (BMP-2). The induction period was performed over 14 days but differentiation was detectable after 7days. Osteogenic induction was associated with phenotypic morophology change with cells loosing the fibroblast-like morphology for a 'cobblestone-like' pattern observed including large aggregates or nodule formation (Figure 31). At the end of the culture period cells under went simple enzymatic colorimetric testing for alkaline phosphatase an indicator for osteogenesis, exposing the culture to colourless p-Nitrophenyl Phosphate converted it to p-Nitrophenol (yellow) when in the presence of alkaline phosphatase. This did not affect downstream histological staining for the cell surface bound ALP by Fast Blue SS as well as calcium nodule identification by Alizarin Red S, Figure 31_*centre*.

Chondrogenic differentiation was induced in serum-free medium including exposure to dexamethasone, ascorbic acid, proline, [insulin, human transferrin, and selenous acid] (ITS) and transforming growth factor beta 3 (TGF-ß3). MSC cultures were serum starved 12-24hrs before exposure to inductive factors. Some MSC populations induced towards chondrogenesis were assisted by culturing in a 3D environment, this involved spinning down a suspension of MSCs in a non-adherent v-bottom tube to form a tightly packed micro-mass of cells. This was gently disturbed to ensure a free-floating suspension or micro-mass and then exposed to chondro-inductive media. Cell induction

was preformed over 14 days where cell morphology displayed mass aggregation of cells into skin-like tissue with peeling of adherent cultures regularly observed. The peeling or contracting of the chondrogenic monolayer was mirrored in the 3D pellet culture by the cells forming tight micro-mass aggregates. Adherent and Pellet cultures were fixed with 4% PFA and the pellet cultures were paraffin wax embedded and sectioned, and then stained for glycosaminoglycans by Alcian Blue 8G (Figure 31_*right*).

Adipogenesis were induced through exposure of cells to alternating induction and manitaince media, inductive factors included; dexamethasone, proline, human insulin, insulin-like growth factor (IGF), rosiglitazone and indomethacin (I). As the key induction factor I is toxic the cells were exposed for 3-4 days before change to basal media contain rosiglitazone, IGF and insulin. Differentiation time period was over 14days and culture was terminated by fixation. The adipocytes were identified by staining the lipids contained within fat vesicles of the cytoplasm in differentiated cells. The histological stain Oil Red O stains lipids bright red readily identifying induced cells (Figure 31_*left*).

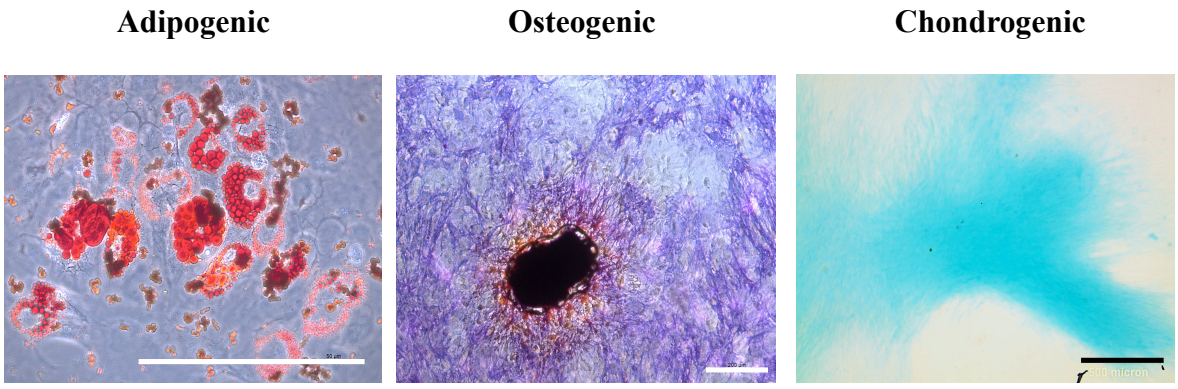

Figure 31. Tri-lineage differentiation of primary mesenchymal stromal cells isolated from marrow of bone fragments (N_2848). Purified cultures of plastic-adherent MSC populations were exposed to lineage specific factors. Cells were cultured under these conditions for 14 days before fixing cell in 4% paraformaldehyde and under going specific histological staining. Adipogenic [lipid vesicles – Oil Red O]; Osteoblast [ALP - Fast blue; Calcium – Alizarin Red S]; Chondrogenic [glycosaminoglycan – Alcian Blue 8GS]. Scale bar - white = 200µm and black = 500µm

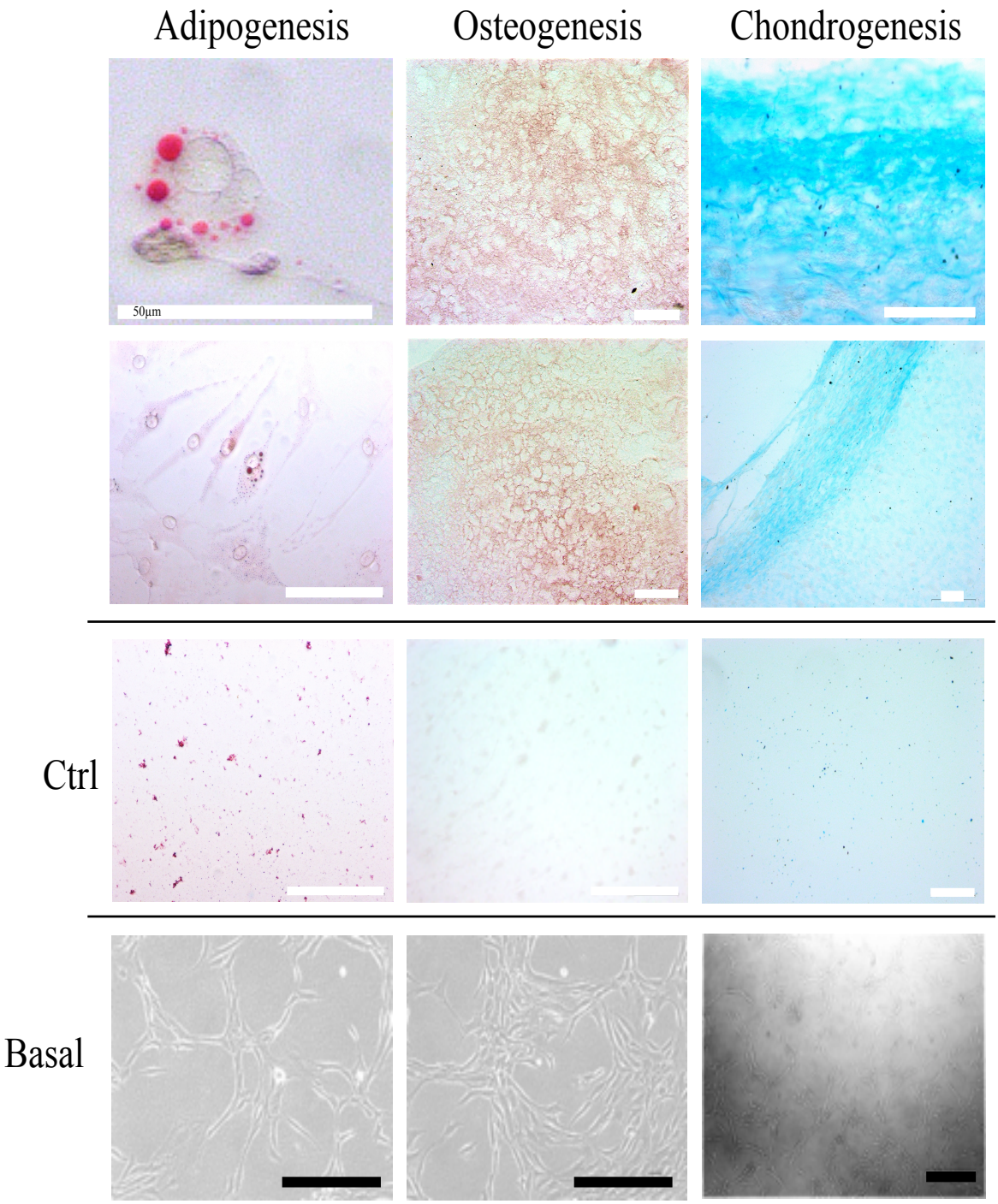

Figure 32. Tri-lineage differentiation of immortalized mesenchymal stromal cells (hTERT) Y201 when exposed to lineage specific factors. Cells were cultured under these conditions for 14 days before fixing cell in 4% paraformaldehyde and under going specific histological staining. Adipogenic [lipid vesicles – Oil Red O]; Osteoblast [ALP - Fast blue; Calcium – Alizarin Red S]; Chondrogenic [glycosaminoglycan – Alcian Blue 8GS]. Scale Bar: white = 100µm ; black = 1mm

4.5.2.4. Telomerase Reverse Transcriptase, human (hTERT) : Y201

The Y201 hTERT cells originated from a primary MSC culture isolated as described before, which were transfected with a lentiviral vector containing the human telomerase gene. After antibiotic selection (for stable transduction) individual cell colonies were grown up and assayed for the telomerase expression (TRAPeze® Telomerase Detection, Millipore).

Of the several donor populations characterised, four had the highest telomerase expression and of those four one with rapid proliferation and tri-lineage differentiation was selected to progress forward (collaborators work and impending publication).

While traditional mesenchymal stromal cell populations have a plastic-adherence, fibroblast-like morphology. Cultures of Y201 displayed slightly different morphologies where the cell-cell interaction formed colonies of pentagonal 'star' patterns (Figure 32_basal *left*) and this was observed widely across the cultures (Figure 32_basal *right*).

Multipotent capacity of Y201 was verified using established differentiation protocols. The Y201 cells showed development to all lineages (osteogenic, chondrogenic and adipogenic). The adipogenesis observed the formation of intracellular lipid vacuoles identified in individual cells by Oil Red O staining (Figure 31), but this was only a fraction of the entire population that was fully differentiated after a two-week period. Strong osteogenic and chondrogenic conversion was observed, histological staining identified commencement of interspersed calcium accumulation between cells (Figure 32*_red plumes*). Chondrogenesis was interspersed with found large deposits of proteoglycans in the ECM, stained blue by Alcian Blue 8GS (Figure 32). Chondrogenic cultures also displayed characteristic peeling of tissue layers commonly observed *in vitro* with chondrocyte differentiation.

4.5.2.5. Limitation of Y201 human TERT-MSCs: Collagen Deposition

Sections we cut out of the chondro-induced micro-mass pellets, to observe the internal organization of the individual TERT-MSCs (Y201) after 14 days in 3D suspended culture. Pellets were wax embedded and sectioned into thin 2µm thick slices before anchoring to glass microscope slides. Different sections of the same pellet were dewaxed and stained for different histological stains; Safranin O and Masson's trichrome, Figure 33_*top* and *bottom* respectively.

Each histological stain has a positive control of a mouse knee joint; *top* Safranin O is a lateral cross section of the knee joint including the meniscus, cartilage areas are highlighted in red; *bottom* Masson trichrome is a transverse section of the femoral condyles, where collagen deposits are highlighted blue. Experimental and positive controls were stained on the same day.

Within MSC micro-mass pellets both induced cultures (TGF-β and Krtgn) display tight pellet formation compared to the respective experimental controls. No collagens were detected in the Y201 pellets after 14days incubation, as opposed to sections of primary MSCs under the same conditions and at the same time point.

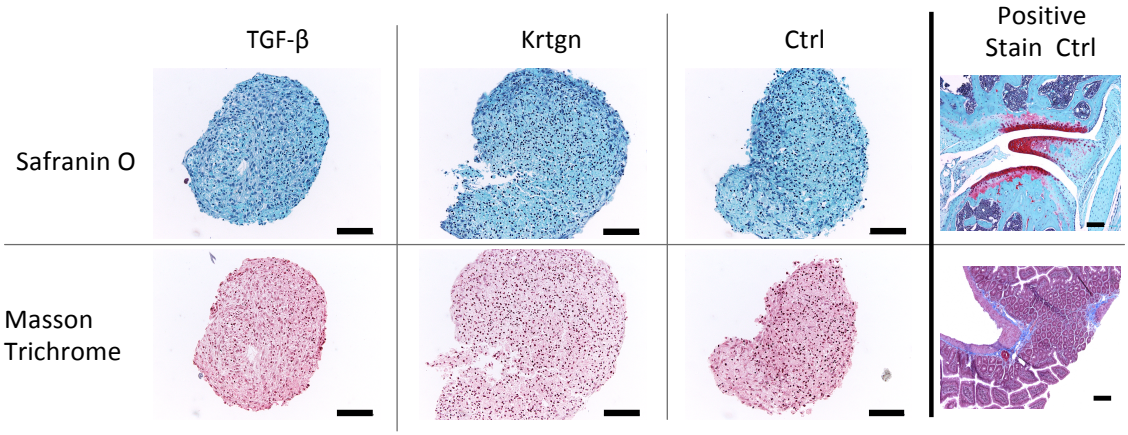

Figure 33. Sections of chondrogenic induced micro-mass pellets of TERT-MSCs (Y201) after 14 days in 3D suspended culture. *Top* row displays Safranin O staining and *bottom* Masson trichrome, of the experimental, control and positive control samples.

Schematic Overview of the Validation for MSC multipotency

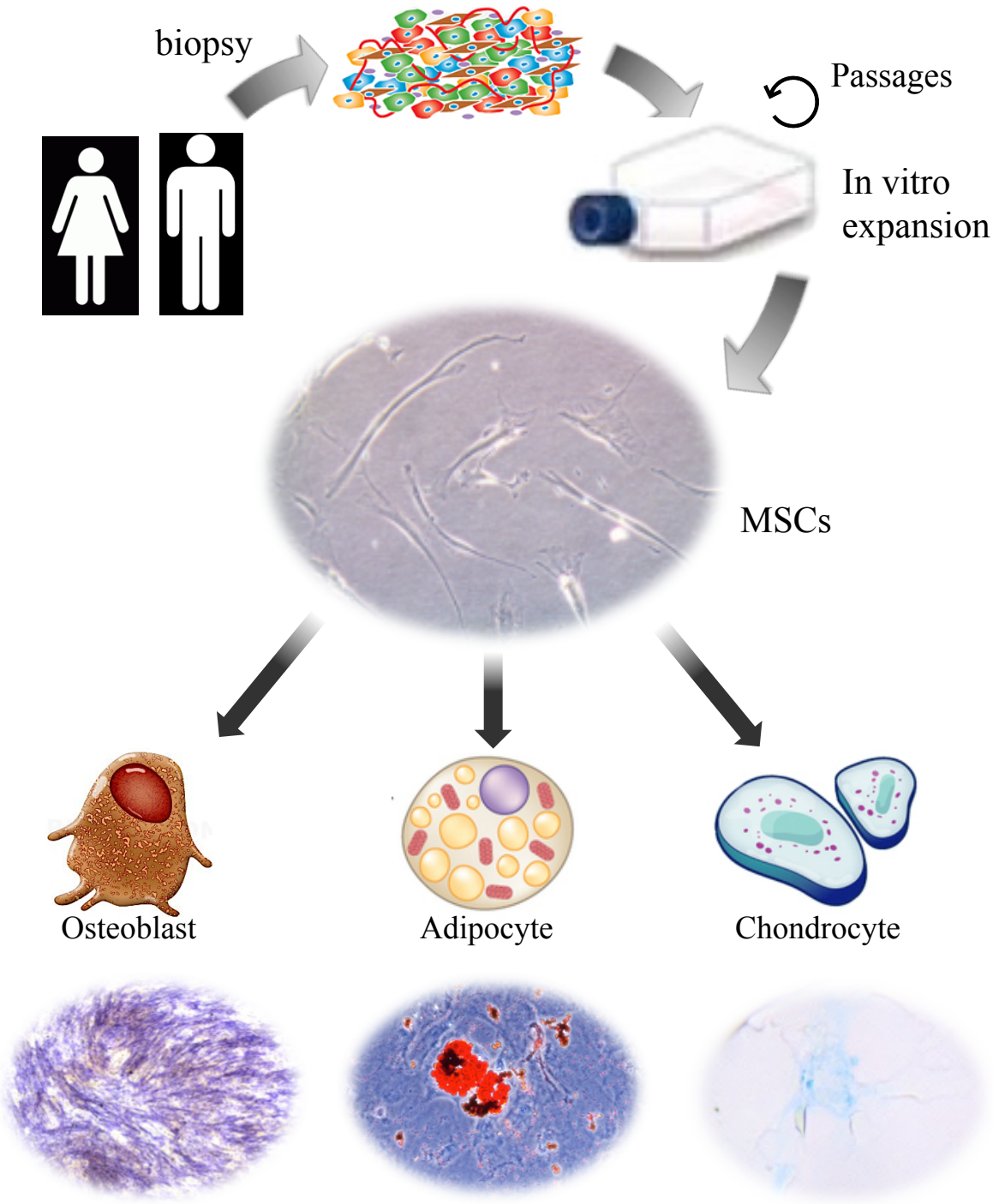

Figure 34. Schematic of patient mesenchymal stromal cell isolation expansion and differentiation. Extracted heterogeneous cell population is isolated from biopsy of patient bone marrow and expanded on tissue culture plastic by standard *in vitro* conditions for mammalian cells. When a more homogeneous cell population is achieved, cells were exposed to lineage specific factors and after appropriate time cells were fixed and histologically stained: Osteoblast [ALP - Fast blue; Calcium – Alizarin Red S]; Adipogenic [lipid vesicles – Oil Red O]; Chondrogenic [glycosaminoglycan – Alcian Blue 8GS].

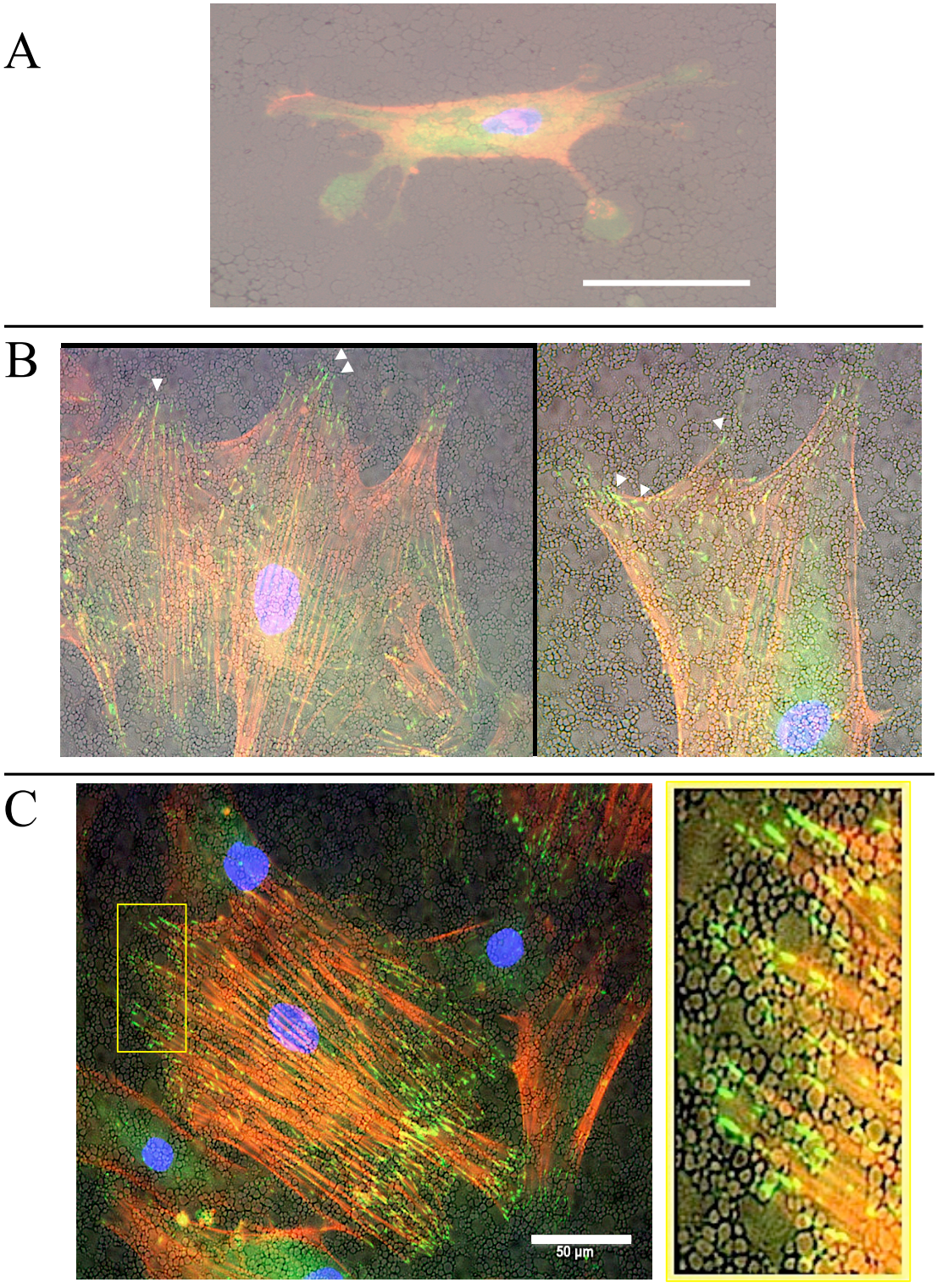

Figure 35. Fluorescent microscopy images of primary huMSCs cultured on textured polymer surfaces under basal conditions for A) 24h and B&C) 72h. Tri-colour fluorescent staining identifies; nucleus (Dapi; *blue*), F-actin cytoskeleton (Rhodamine phalloidin; *red*) and mature vinculin sites (huVinc Antibody-FITC; *green*). A&B) Fluorescent images are overlaid on brightfield images of polymer surface. B) White arrows highlight only a few areas where pseudopodia selectively form focal adhesion plaques at caldera rich sites. C) fluorescent image of single cell without brightfield overlay where a section of focal adhesions in the yellow box is magnified. Scale bar -50 µm

4.5.3. *Cell Morphology after Short-Term Adherence to Surfaces*

Cultures of primary huMSCs were cultured on six different surfaces in total; three demixed polymer surface [40:60/50:50/60:40] both individual control polymers [PS and PMMA] and flat surface controls [clean glass]. Cells were seeded at low seeding density ($10x10^3$ per surface) to allow cell-substrate interactions to pre-dominate and minimise possible influences of cell-cell interactions.

Separate wavelength probes fluorescently labelled different cellular components identifying, cell count by nucleus (Dapi_*blue*), the cytoskeleton (Rhodamine phalloidin_*red*) and vinculin at mature focal adhesion sites (huVinc-Ab-FITC_*green*). Surface topography was imaged by brightfield transmitted light microscopy.

Each surface was independently replicated four times and five images (10x) of each surface taken at similar sites on each cover slip (points of a compass including centre). Cell number was quantified by the nucleus count (DAPi only images) per field of view and this was used to normalise subsequent calculations to single cell measurements where appropriate.

Alteration to cell morphology was readily noticeable even after short periods of contact with surfaces, individual cells displaying numerous exploratory filopodia when observed on the polymer surfaces after 24h (Figure 35_A). When left over a longer time period (72h) the entire arrangement of the cytoskeletal structure was altered and numerous clustered focal adhesion plaques were observed. Increased intracellular tension was indicated by numerous aligned F-actin filaments of the cytoskeleton and cellular hypertrophy (Figure 35_B).

Pronounced mature focal adhesion plaques were repeatedly observed to hone around areas of caldera clusters on the textured surfaces (Figure 35_C). Parallel cultures on flat glass cover slips as controls to the raised, textured polymer surfaces, identified ‘plastic adherent’ stromal cells that displayed similar cellular size increase and spreading but failed to develop intensified areas of focal plaques and showed less apparent intracellular tension of the cytoskeleton (appendix pg. XL). It was therefore observed that slight elevated features (>1 μm) of the caldera at the surface interface, dramatically changed the individual cell morphology and adhesion profile, but also the adhesion profile of the entire cell population in contact with the surface.

4.5.3.1. Altered Cell Area and Circularity

In keeping with the caldera dispersion pattern profiles previously established and knowing the heightened focal adhesion interaction to raised caldera, it is unsurprising to find that cell morphology was influenced by surface topography. We observed small (28±7 μm^2), circular morphology on PMMA surfaces where an abundance of close proximity caldera were available, as opposed to, large (82±5μm^2) elongated morphology on PS surfaces with dispersed caldera conformation (Figure 36). There was a significant discrepancy between both homo-polymer ctrls ($P<0.0001$) (Figure 36_B).

Demixed polymer surfaces followed a trend that correlated with the major polymer constituent; on 40:60 a PMMA-rich surface, cells remained smaller and more circular (48±14μm^2) significantly smaller than either two demixed surfaces ($P<0.01$), where as the inverse 60:40 surfaces cells displayed greater area with lower circularity (72±5μm^2). The intermediate 50:50 blends containing equal parts of each polymer and if the relationship was linear would fall in-between either homo-polymer readings. All three demixed surfaces were significantly larger than PMMA, 40:60 ($P<0.05$) was lowest but both 50:50 and 60:40 showed significant difference ($P<0.0001$) contrastingly only 40:60 showed significant difference to PS ($P<0.001$) (Figure 36_B). However, whilst it maintains general circularity trend observed amongst demixed surfaces it moves away from the trend with larger cell areas (71±9μm^2) (Figure 35_C). This would suggest a threshold of caldera dispersion/separation to dictate increased cell size

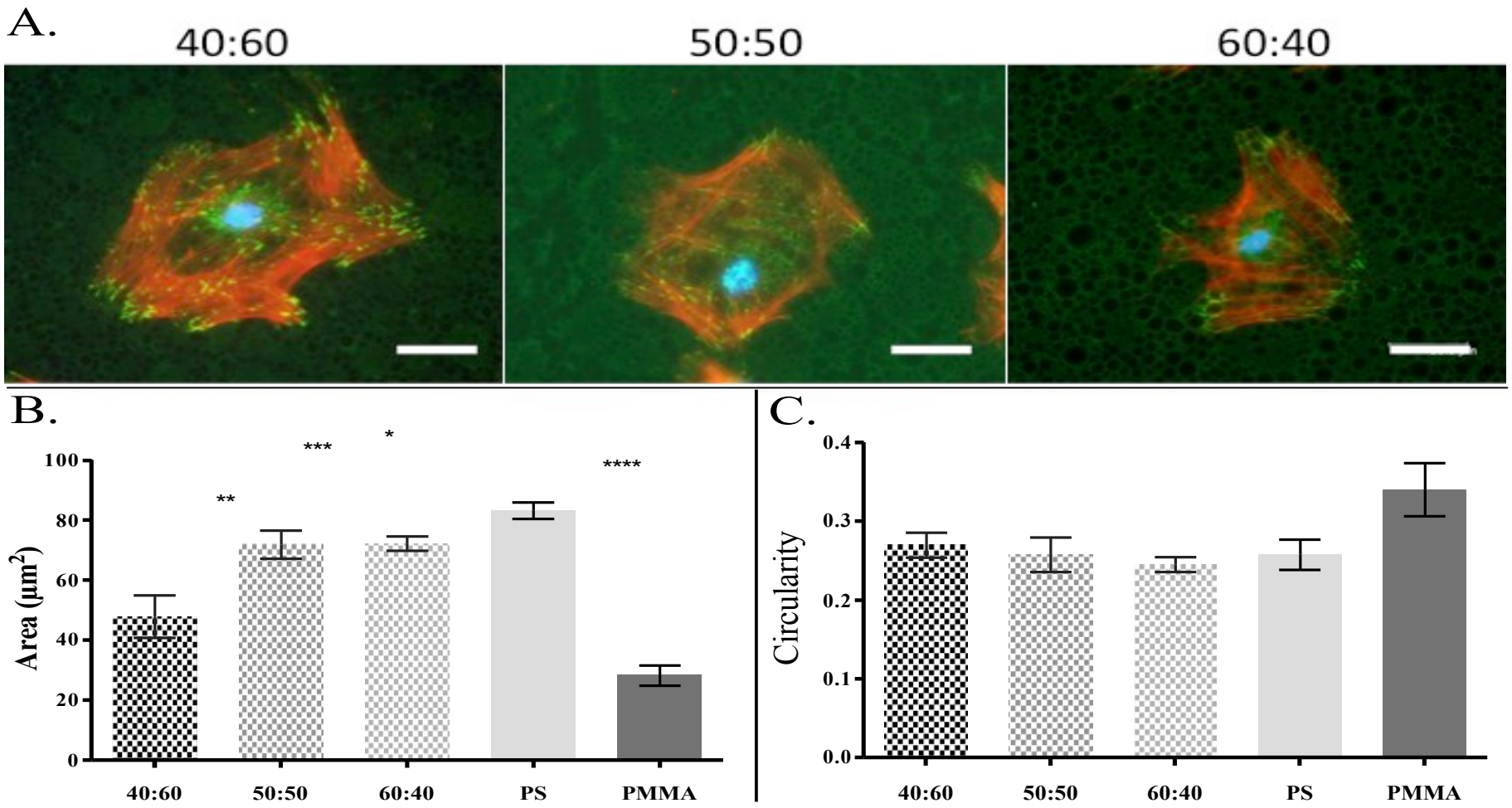

Figure 36. Altered cell morphology due to restrictions adhesion profiles on demixed polymer surfaces after 24h (A); average individual cell area (B) and average individual cell circularity (C) on each polymer surface per field of view. Circularity is described as a function [4π[((area)/(perimeter*2))] with 1 indicating a perfect circle and as function approaches 0 an elongated polygonal shape. Scale bar - 20 µm

4.5.3.2. Observations of Cell 'Bridging'

Observing adhered cells on specific areas of the textured polymer surface can be limited through the use of fluorescent microscopy alone. Antibody staining gave excellent insight to the cellular components, their arrangement and location, but at a cost to the image clarity. The polymer surface can only be imaged by brightfield microscopy and at a perpendicular areal angle, making adhesion features hard to distinguish.

An alternative imaging solution was scanning electron microscopy (SEM) this enables; uniform high magnification imaging of both adherent cells and polymer surface, with the ability to tilt objective to give an angled perspective. Images are in greyscale but features are still identifiable due to the sharp edges of synthetic polymer and soft edges of biological cells.

SEM imaging identifies the caldera of the PMMA polymer in a honey-comb-like pattern, as shown by AFM, with opposing lower lying PS regions with less protruding BFP in-between (Figure 36). All cells appear to make larger lamellipodia focal adhesions on brighter raised areas; one cell in particular, Figure 36_left, focuses one central main lamellipodium with two exploratory filopdia either side extended across to other raise areas of PMMA caldera (Figure 37_*white arrows*).

In Figure 37_*right,* a single cell can be observed with a hyperextended filopodium, just left of centre, captured 'bridging the gap' between raised PMMA caldera, surpassing easier focal adhesion contact with the under lying PS area, to make contact with a neighbouring cell.

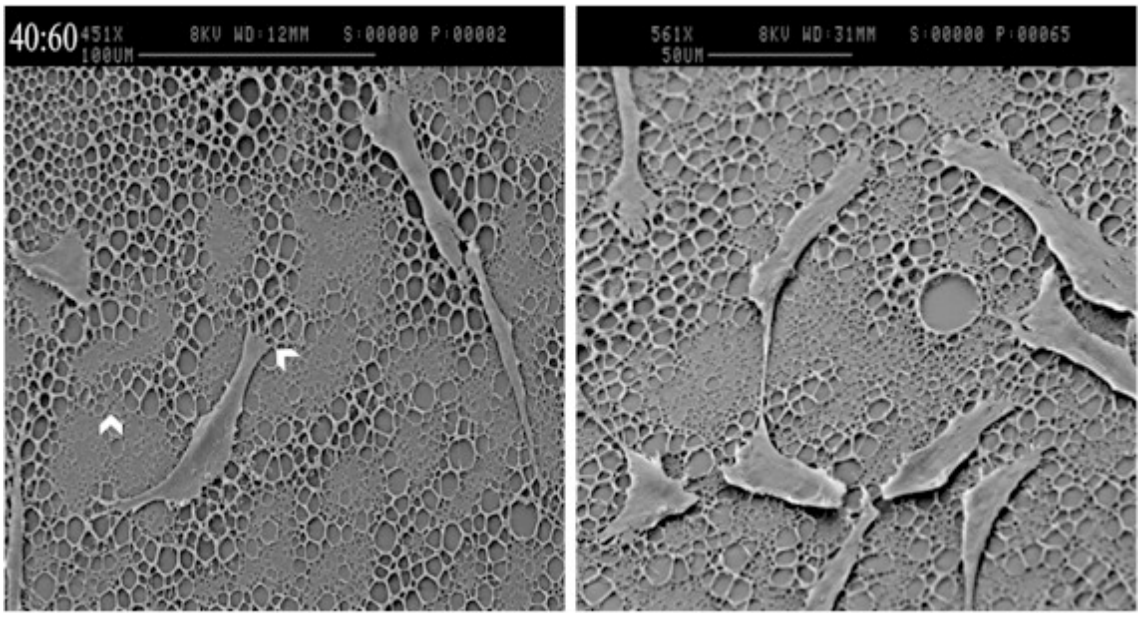

Figure 37. Scanning electron images of MSCs cultured on demixed polymer surface (40:60) for 24 h under basal conditions. Direct areal image (left) and slight tilt image (right) of two separate areas of polymer surface with adherent cells.

4.6. DISCUSSION

Selection of suitable basal media for the culture of primary MSCs favoured of 10% serum based on the fact that large discrepancies were observed between 10% and 20% but not observed between 20% and 30%. This large discrepancy may indicate a threshold for serum use and as serum is a complex of factors (i.e. hormones and growth factors) exposure to these elements are best limited when culturing multipotent cell populations. Suspicion lies around the commercial MSC media in containing recombinant proteins or elevated levels of these serum hormones and this may explain why cultures displayed highly inflated growth rates (e.g. fibroblast-like growth factor, FGF). Not only this but the minimal use of animal products throughout the process would be a closer simulation if it were to be a translational therapy.

Validation of culture expanded MSCs were determined by two different techniques, flow cytometry and differentiation. Conforming multipotency in all isolated cell populations would be time consuming and require cells from an already limited pool. So the isolation process was validated for several donor populations using both validation methods and subsequent isolates extracted by the same protocol were assumed the same (Figure 30). It is worth noting that only three of the initial validation donors are analysed in full here and that additional donor populations were validated at least once every year subsequently. Isolated MSC populations and successive populations were taken for testing after passage 1 and assumed as stable multipotent cultures up until passage 6, in accordance with literature[26,170].

Identification of the required cell surface markers for multipotent mesenchymal stromal cell criteria by flow cytometry is a powerful and sensitive technique but one that is often contested within the research community. While use of polychromatic flow cytometry is the most advanced method for high throughput single-cell screening and separation, it is also an excellent, high specificity tool for identification of cell subsets and rare populations. Unfortunately this technique requires a single-cell suspension for processing, this is less of an issue for blood based cells, but for analysis of adherent cells types this may incur cell surface damage as cellular detachment and separation were necessary, typically using enzymatic or mechanical means (e.g. trypsin, EDTA, scrapping, etc.). Multiplex fluorophores for analysis of cell subpopulations from same tissue source can display similar cell surface marker expression, this can be

difficult to analyse and may be subject to signal spillover[5]. Minimising this difficulty is still under investigation by the scientific community. Also in the establishment of a correct flow cytometry assay isotype controls with the experimental cells were used to discriminating against cell doublets using the SSC-H vs. SSC-A strategy and not with beads. This was more specific to each individual experiment (reduced chance of Area Scaling error compared to commercially available beads) but incurs more human involvement and calibration with ill-defined components of a heterogeneous population.

The most questionable limitation of flow cytometry was post-analysis interpretation of the data, the technique can generate massive amounts of data. Interpretation of this data is therefore complicated and lacks a standardized form of reporting; this is partially due to the absence of standardization in assay design and instrument setup for MSC investigation. The large amount of raw data generated cannot be automatically standardized and is therefore gated by human hand (incurring elements of personal interpretation and human error). Finally, the flow cytometry assessment of MSCs used was a terminal experimental process and can only reflect one time point or passage of the cell population, which at that point will have pasted.

Unequivocal proof of a multipotent cell population was the differentiation of the parent population into multiple lineage cell types (Figure 34), specifically here, the differentiation of mesenchymal stromal cells into osteoblasts, adipocytes and chondrocytes. Populations of MSCs were culturally expanded to a more homogeneous population, passage 1 or 2, before subpopulations were cultured under conditions favourable to osteogenic, adipogenic and chondrogenic lineages for up to 2-3 weeks. While there is no doubt in the multipotency of cells after this process, it is a terminal test using large numbers of cells from a finite pool of slow growing cells.

One fortuitous solution to this limitation of cells, was receiving immortalized human MSCs from collaborators in York University. These cells were isolated and expanded into homogeneous populations by an identical protocol to our primary isolations, before being transformed. Once these cells were characterised and differentiated (Figure 32) they could be safely assumed to be the same due to their immortalized nature.

Induced Chondrogenesis of the human Y201 cells showed positive deposition of proteoglycans, but fail to deposit a collagen matrix. Changes in cell behaviour are commonly observed in transformed immortalised cells. Repeated experiments with this cell line confirmed this observation. Real-time PCR analysis identified the mRNA

expression of specific chondrogenic genes (Chp. 5), including collagen, but the failure to detect deposition of protein by histological staining calls into question if the ECM can be made.

Irrespective of protein deposition both cell types, primary and TERT, responded identically over a short-term exposure (24-72 h) to textured polymer surfaces. The raised caldera of these surfaces provided pillar-like structures for cellular adhesion and formation of focal adhesion plaques. Dispersed organisation of caldera contributes to elevated internal cellular tension and altered morphology. Therefore surface adhesion, providing cells make contact with caldera at every focal adhesion plaque, will cause greater cytoskeletal tension due to the required bridging between caldera by the cell body. It has been previously described that altered cytoskeletal tension of multipotent cells can induce lineage specific differentiation[136]. Conducive to this is the physical interaction of cells on a soft material, with subsequent low cytoskeleton tension, resulted in cell quiescence[200] and the inverse stiff material, with high cellular tension resulted in osteogenic markers to be expressed[131].
Affects of topography alone as a biological stimulus in respect to cellular adherence cannot be without influence from the material stiffness. This should be clarified before evaluating results. Extremely thin polymer films generated by spin coating minimized influence of material elasticity but topographical features are not without it. But physical adhesion cannot be solely accountable for the altered cell response, as chemical composition and related piezoelectric forces of materials must be considered as a contributing factor.

It is difficult to make true comparisons of the results presented here with others, as there are no universal parameters for characterization of surface roughness. These findings do however, support observations that the physical environment, influencing cell shape, cytoskeletal architecture, and cell–cell communication, translate to influence bimolecular signals for differentiation. Others research has shown that his alteration to individual cells adherence as further reaching affects to intercellular communication and the over all development of a tissue[201].

4.1. SUMMARY

- Experimental protocols were developed for the isolation of and expansion of plastic-adherent fibroblast-like cells were extracted from marrow of bone fragments.
- Identification of mesenchymal stromal cells was confirmed by flow cytometry to the international cell surface marker standards[199].
- Tri-lineage differentiation and histological staining for lineage specific characteristics for osteoblast, chondrocytes and adipocytes confirmed multipotency of MSC populations.
- Cell morphology is directly altered as a result of the adapted adhesion profiles displayed by individual cells in response to the distinct topographies of the contact surface.
- While Y201 cells failed to deposit a collagen matrix during chondrogenesis and around the aggregated cell micro-mass, these cells were still capable of osteogenic and adipogenic differentiation.

CHAPTER 5. LONG-TERM EFFECTS OF DIFFERENT SURFACES ON CELLULAR DEVELOPMENT AND TISSUE ORGANISATION

5.1. Introduction

The pluripotent potential of stem cells necessitates the complex regulation of processes associated with cell differentiation, growth and phenotypic gene expression[132]. Their incorporation, as cell therapies, into advanced medicines appears to require scaffold assisted delivery and retention, depending on the tissue destination. The artificial ECM created by the scaffold chemistry, mechanical movement, architecture and topography all play influential roles in regulation of the cells just like natural ECM does *in vivo*. Cell shape and cell-to-cell and cell-to-substrate interaction with the environment are all pivotal to this control[128,129,202,203]. An expanding field of research addresses the question of how an engineered substratum can play a role in regulating gene expression as a result of mechanosensory response leading to cell differentiation[132,204].

A growing field of research into the control of stem cell fate has moved from the traditional molecular mediators (e.g. growth factors, transcription factors) to the diverse array of environmental factors contributing to the overall *in vivo* conditions found in the target tissue.

In particular there is increasing evidence for the role of the physical environment (i.e. extracellular matrix) through stimulus of cell surface receptors due to contact with ECM ligands[205] as well as other physical mechanisms like ECM geometry at the micro- and nano- scale, ECM elasticity[206], and mechanical stimuli[123].

The shape of a cell has been identified as a potent regulator of cell growth and physiology[207], with implications far beyond the influence of adhesion signalling alone[208]. Use of artificial ECM to manipulate cell shape has been implicated as a potential mechanism for myocardial[209], chondrogenic[210], endothelial[211] and osteogenic[132] differentiation[212].

Controlled temporal changes in the interactions between cells and their environment can alter the cell shape (elongated vs circular; spherical vs flattened). These morphologies are mirrored by the organisation of the actin cytoskeleton and its relationship to focal adhesion plaques[212,213]. The complete mechanism of MSCs commitment to lineage specific differentiation remains to be determined. Studies have shown inhibition of Rho prevents MSCs commitment to the osteogenic and chondrogenic phenotypes, connecting the alteration of F-actin organisation, tension and architecture through the Rho (ROCK) pathway with osteochondral differentiation[214-216]. Further development of

these observations identified the possibility of critical inter-pit size topography for directing changes, since larger adhesions are prerequisites for osteogenesis influencing the mitogen-activated protein kinase (MAPK) signalling pathway[217].

With respect to bone implant interfaces it is widely believed that skeletal integration is required to withstand the elevated mechanical forces and micromotion at interfaces compared with soft tissue implants[132,218]. Improper integration of implants can lead to a fibrous tissue layer around the prosthesis resulting in loosing and inhibition of bone remodelling[219].

From the developmental biology of the musculoskeletal system we know that cartilage is initially established before its calcification and ossification turning into bone. The slightest instigation of the chondrogenic cascade of cellular events, at the early phases of post-operative recovery after an orthopaedic implant, may encourage a more natural repair mechanism for tissue regeneration.

One such avenue would be characterising geometric patterns to stimulate cell surface signalling (e.g. Notch, Wnt, RhoA, etc.) that could provide a window to manipulation of intracellular signalling pathways linked to lineage specific differentiation (e.g. ROCK, TRP, MAPK, etc.). Tailoring implant surfaces for enhanced medical device tissue integration and function, by means of manotransduction.

5.2. Aim

Investigate the influences of surface topography on long-term cultures of mesenchymal stromal cell's adherence, morphology, and gene expression.

5.3. Objectives

- Evaluate if the raised 'Caldera' micro-texture surfaces follow an identifiable and tuneable pattern with demixed fabrication
- Knowing altered cell adherence can the surfaces influence the cell phenotype?
- Can alterations to cell cytoskeleton change the gene expression?
- Investigate if the effects are universal amongst MSC populations
- Explore what effects to individual cells has on overall tissue development

5.4. Method

5.4.1. *Fiji/Image-J Analysis of Surface Texture*

Using the additional BioVoxxel toolbox plugin on Fiji (imageJ) images were simplified to 8-bit binary images and 'shape descriptor maps' performs a number of simultaneous tests. This macro performs several investigations for a single image; area, perimeter, fret area, fret angle, aspect ratio, solidity, compactness, extract. Only a few shape description parameters calculated are relevant to this investigation, namely; Circularity $[4\pi*(\text{Area})/(\text{Perimeter})^2]$ where a value of 1 indicates a perfect circle. Solidity: [Area]/[Convex area] convex area is the area inside the convex hull of a 2D object the closer the convex hull approaches the perimeter of the original object,
the closer its value is to 1.

5.4.2. *Total RNA Isolation and Reverse Transcription to cDNA*

Initial attempts to isolate RNA from adhered cell populations was performed using Trizol™ but it was revealed to interact with the polymer surfaces, causing degradation of the thin polymer films. This contamination of the samples hindered successful amplification of the RNA to cDNA during reverse transcription (Superscript™ III, Sigma, UK). An alternative approach of detaching the cells from surface, using trypsin, before cell lysis aided purity of RNA isolation but lower overall yield due to additional steps. Given the low seeding densities used , an alternate was required.

Whole DNA and RNA was extracted using a total lysis buffer from an entire adherent cell populations in a single step using Cell-to-cDNA™ II kit (AM1722 Ambion, Life Technologies, UK). Single step extraction ensured highest yield and clean isolation of nucleic acid material by corrosive-free cell lysis buffer.

Thermal destabilisation (65ºC, 5mins) dissolves RNA, and with the addition of DNase enzymatically removes genomic DNA. The mixture was then directly amplified by reverse transcription using 1µg total RNA with non-specific primers (Oligo $dT_{12\text{-}18}$), to convert into first strand complimentary DNA (cDNA). An established thermo-cycle amplification program was used (50ºC_50mins, 70ºC_15mins, 4ºC_END).

All samples were uniformly processed and amplified, samples were stored at -20ºC (short term) and -80ºC (long term). Samples of cDNA can be stored at -20ºC for up to 2 years but RNA should only be stored at -80°C, as aqueous for <1month and as an ethanol precipitate forever.

5.4.3. ***Quantitative Real-Time PCR (q-PCR)***

Each samples of reverse transcribed cDNA was diluted 1:25 as template to quantify the relative RNA content for specific genes by qRT-PCR (ABI PRISM 7900HT, Applied biosystems, Foster City, CA, USA). Genes of interest are listed in Table 3 with their associated primer sequence. All primers were selected and designed using Homo sapien Gene libray (PubmMed) and Universal ProbeLibrary Assay Design Center (Roche). PCR reactions were performed using TaqMan master mix with primer and cDNA cocktail previously described. The PCR amplifications were preformed under the following conditions: 94ºC_4mins, then 50 cycles at 94ºC_25s, 53ºC_30s, 72ºC_45s and final extension at 72ºC_10mins. The Human glyceraldehyde 3-phosphate dehydrogenase (GAPDH) housekeeping gene was used as a control. All samples were run as technical triplicates per plate and experimental samples were tested in duplicates as minimum, this helped to eradicate outliers.

Due to low RNA yields higher PCR cycles (50) were used for gene detection but threshold values for genes of interest were determined as per ABI systems instructions.

5.4.4. ***Statistical Analysis for q-PCR***

Statistical significance between groups was assessed by two-way analysis of variance (ANOVA) with Sidak's and/or Tukey's multiple comparison post-hoc tests.

(* denotes significant difference $p<0.05$, **denotes $p<0.01$, *** denotes $p<0.001$ and **** denotes $p<0.0001$)

Gene Name	Acronym		Primer sequences	Annealing temperature (ºC)	Probe library ♯	Accession number
Glyceraldehyde 3-phosphate dehydrogenase	GAPDH	Fwd.	AGCCACATCGCTCAGACAC	60	60	M33197.1
		Rv.	GCCCAATACGACCAAATCC	60		
CCAAT/enhancer binding protein α	C/EBP	Fwd.	GGAGCTGAGATCCCGACA	59	28	NM_004364.3
		Rv.	TTCTAAGGACAGGCGTGGAG	60		
Fatty Acid Binding Protein-4	FABP4	Fwd.	CCTTTAAAAATACTGAGATTTCCTTCA	59	72	NM_001442.2
		Rv.	GGACACCCCCATCTAAGGTT	60		
Runt-related transcription factor 2	RUNX2	Fwd.	GTGCCTAGGCGCATTTCA	60	29	NM_004348.3
		Rv.	GCTCTTCTTACTGAGAGTGGAAGG	60		
Alkaline Phosphatase	ALP	Fwd.	CTCGTTGACACCTGGAAGAGCTTCAAACCG	61	31	NM_000478.4
		Rv.	GGTCCGTCACGTTCTTCCTGTTCAGC	61		
Sex determining region Y (SYR)-box	SOX9	Fwd.	GTACCCGCACTTGCACAAC	60	61	NM_000346.3
		Rv.	TCTCGCTCTCGTTCAGAAGTC	59		
Aggrecan	ACAN	Fwd.	AGACGGCTTCCACCAGTGT	63	20	NM_013227.3
		Rv.	GGGAGTGTGGATGGGGTAT	64		
Collagen IIα1	COL2A1	Fwd.	CCCTGGTCTTGGTGGAAA	63	19	NM_001844.4
		Rv.	CATTGGTCCTTGCATTACTCC	63		
Collagen Iα1	COL1A1	Fwd.	GGGATTCCCTGGACCTAAAG	59	67	NM_000088.3
		Rv.	GGAACACCTCGCTCTCCA	59		
FK506 binding protein 5,transcript variant 2	FKBP5	Fwd.	AGCCCTGTGTGTGCAAGG	60	27	NM_001145775.1
		Rv.	TGGGGGTCGGAGAGTCTA	59		

Table 3. A list of the genes of interest identified on PubMed gene library, see corresponding accession number, for *Homo sapiens*. Each primer sequence used is listed with details of annealing temperatures and the associated probe. The expression levels of GAPDH were used as a housekeeper gene for the relative expression levels of the other genes under investigation.

Adipogenesis

A cascade of transcription factors are involved in adipocyte differentiation, most notably those of the **C/EBP** and **PPAR-γ** families. Both are interconnected and self-regulating, during the expression of adipocyte genes. Altered expression of one modulates the other, and antagonist expression is assumed as dampening in the opposition[220].

Fatty acid binding proteins (**FABP**) are the key mediators of intracellular transport and metabolism of fatty acids in adipose tissue, and as such, are adipocyte specific proteins. Within skeletal muscle tissue FABP3 is notably the dominant protein with a regulatory relationship with FABP4, a more conservative protein within the tissue[221].

Osteogenesis

The **RUNX** family of genes play a multitude of roles; RUNX1 (hematopoiesis and leukemia), RUNX2 (osteogenesis and cleidocranial dysplasia), and RUNX3 (T-cell development and dorsal root ganglion neurons)[222].
Involvement of RUNX2 in osteogenesis is essential in skeletal development, regulating osteoblast differentiation and chondrocyte maturation[223]. Runx2 (or Cbfa1) has been shown to be phosphorylated and activated by the mitogen-activated protein kinase (MAPK) pathway[224]. Phosphorylation of the endogenous Cbfa1 was shown in vivo by physical interaction of MAPK with RUNX2, providing a molecular link between mechano-stressing and stimulation of osteoblast differentiation[225].

Alkaline Phosphatase (**ALP**) a known marker for skeletal ECM mineralization[226]. It is found in at least three isoenzyme forms in *Homo sapiens*: a heat-stable placental enzyme, a less heat-stable intestinal form (IAP), and the very heat-labile (ALP) enriched in liver, bone and kidney. Elevated levels of ALP within MSCs cultures are indicative of osteogenic specific lineage differentiation[26,169].

Chondrogenesis

A mutation of the gene **SOX9**, a transcription factor of the mammalian sex-determining factor SRY, causes severe dwarfism affecting all cartilage-derived structures[227]. SOX9 is an essential component in the differentiation programme of chondrocytes and a potent

activator of the chondrocyte-specific activation of COL2A1 gene[228,229]. Specific intercellular antibody tracking for SOX9 revealed that expression of SOX9 protein mirrored the distribution of Sox9 mRNA in a murine model[230].
Studies have shown that SOX9 directly interacts with RUNX2 repressing its activity[231] and the Smad3 pathway is key to the SOX9-dependent transcriptional activation of primary chondrogenesis[232]. Disruption of actin stress fibres by specific inhibition of the RhoA effector kinases 1 and 2 enabled the superinduction of SOX9 when stimulated by cycloheximide[233]. Combining the regulatory role over RUNX2 and actin skeleton dependence, may identifying a possible link through MAPK pathway for mechanotransduction during chondrogenesis.

Aggrecan (**ACAN**) or chondroitin sulphate proteoglycan 1 is a cartilage-specific proteoglycan, comprising the core protein of most cartilage proteoglycans found in mammals[234]. It is a major component of articular cartilage matrix and important as it provides the tissue with its ability to withstand compression[235,236]. Mutation of the variable repeat region of the aggrecan gene (AGC1) causes a form of spondyloepiphyseal dysplasia associated with severe, premature osteoarthritis[234,237].

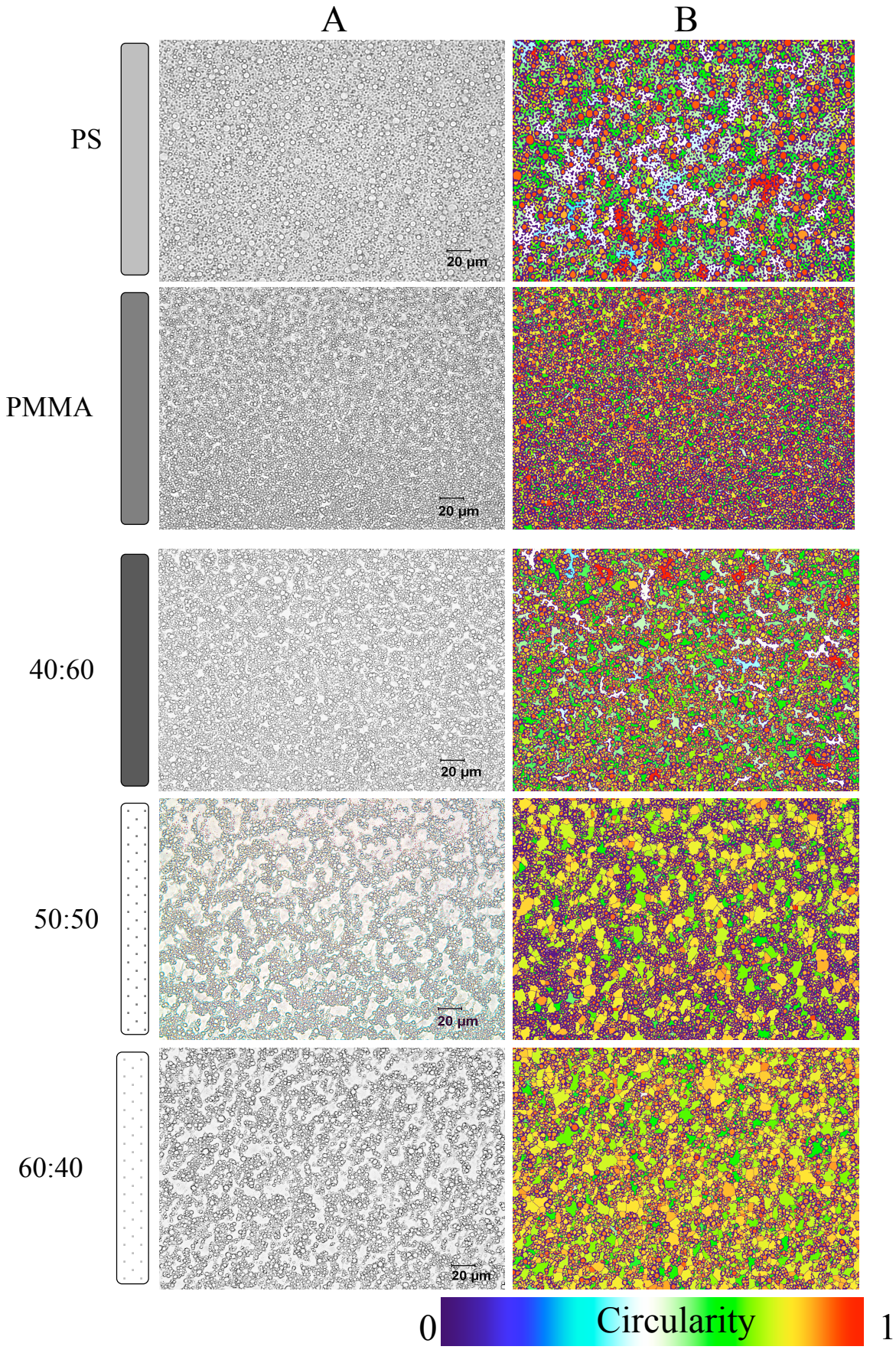

Figure 38. Surface analysis of brightfield microscopy images of all polymer surfaces using Image-J >> Shape Descriptor, pattern recognition software, to identify the circularity of caldera. Brightfield areal images were simplified to 8-bit threshold images and identified 'pore-like' structures, caldera, by a thermal calibration map denoting degree of circularity between 0 (non-circular, *purple*) to 1 (a perfect circle, *red*).

5.5. Results

5.5.1. *Micro-Topographical Evaluation of Textured Surface Interface*

Given the previous evaluation and characterisation of each surfaces by AFM 3D modelling, the raised peaks of caldera are known to appear as pore-like circles when observed from an aerial perspective. This association of circles in 2D images can be assumed to directly correspond to caldera positions when viewed by brightfield microscopy. This provides a simple insight into the micro-topography encountered by individual cells. Use of brightfield microscopy is far less time consuming then AFM and can be captured in unison with fluorescent images of cells.

Using imageJ/Fiji (BioVoxxel toolbox plugin>>shape descriptor) simple analysis of 2D brightfield images can visualise the distribution and geography of caldera dispersion and hence map the potential adhesion areas for cells (Figure 38_A&B). Understanding the adhesion sites presented to cells is key to characterising specific geometric patterns as stimuli for directing cell fate. Characterising pattern geometries provides an opportunity to tailor signalling pathways between cells and implant devices.

The mean circularity of each control polymer surface shown in Figure 38, was calculated to be 0.731 (PS) and 0.825 (PMMA) in is represented in Figure 39. The greater circularity or closest to a perfect circle would relate to the ease of water molecules ability to form an unhindered droplet at any specific site, but also the frequency of sites relates to the difference in both polymers. The count for individual sites of water droplets on the polymer surface differed greatly between both, 4,337 (PS) and 12,789 (PMMA) almost a three-fold discrepancy in site count (Figure 39).

The size of these sites differs greatly as well, which can be assumed easily by the thermal maps generated by this analysis. In Figure 38_B the circles closest to 1 are highlighted in red and it can readily be observed that there are larger caldera in the PS surface compared to the numerous smaller ones on the PMMA surface. This reflects the hydrophobic nature of PS, where a single attack site becomes enlarged due to accumulative aggregation of water molecules as opposed to wider dispersion in the slightly more hydrophilic PMMA.

The dispersion patterns are characteristic of the underling polymer and when observed in the demixed blends we can trace the polymer phase separation due to the reaction with water molecules. In 40:60 a PMMA-rich surface, high frequency (11,863)(Figure 39) sites are observed with a number of lower inter-dispersed areas in green (Figure

38_B). These green inter-dispersion areas increase in the 50:50 blend with a decrease in the count of red sites (9,382). In 60:40 the green areas become dominant and inter-connect around dispersed red sites (9,429)(Figure 39).

Of the sites identified a large range for circularity was obtained on each surface, this is displayed by the individual surface Max and Min values in corresponding graphs (Figure 39). By calculating the Mode for each data set we can see some separation between the surfaces. In the control polymer surfaces PS showed a mode of 0.904 compared to the slightly more circular 0.916 for PMMA (Figure 39). The demixed surfaces display increasing increments through the mode, 0.908 / 0.92 / 0.923, exceeding that of the homo-polymer surfaces, indicating the subtle changes in surface topography (Figure 39).

Within each image field of view, sites of caldera are identified in *red* and a tapered change in their dispersion occurs with demixed blends. Concomitantly, a greater interconnect area (plateau) *green/white* develops between each caldera (Figure 38_B). Having characterized distinct surface topographies, determined the distribution of caldera varied across each of the different surface. Next was to determine if these slight alterations in micro-textured surfaces can induce a phenotypic response from cells.

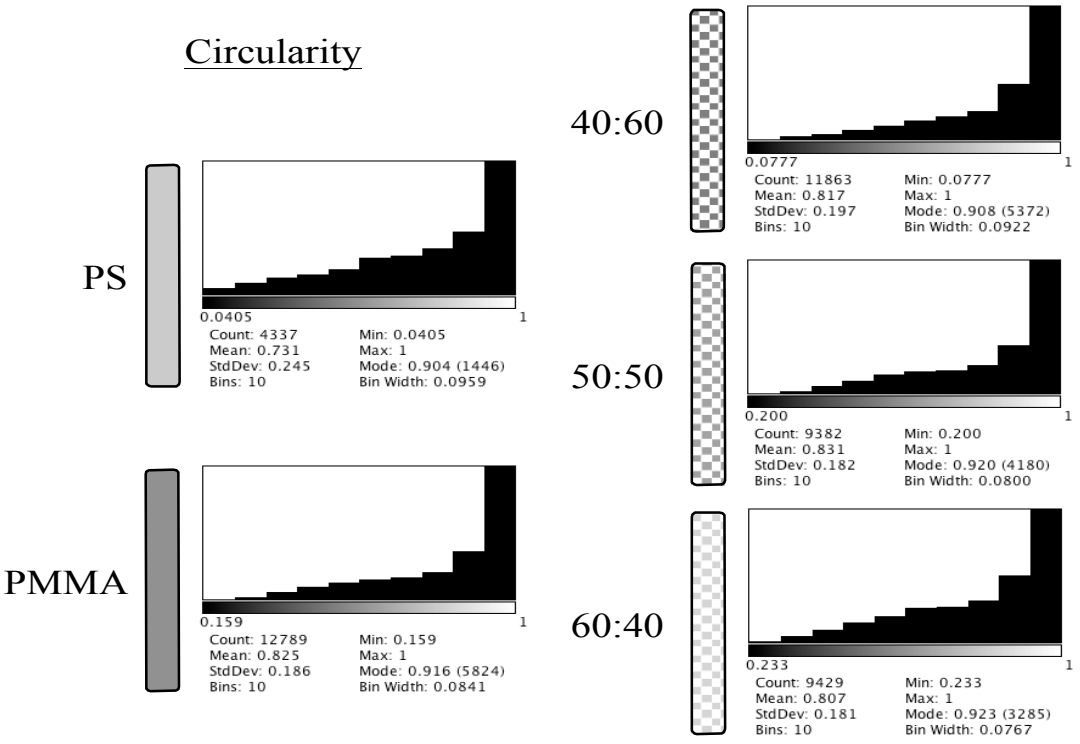

Figure 39. Quantitative graphs of surface structure's circularity on complete panel of textured polymer surfaces. Frequency of structures are grouped and plotted according their circularity were 1 is a perfect circle. The frequency count, max. and min. and mode of count are all displayed beneath each graph.

5.5.2. ***Detection of Lineage-Related Gene Expression by qPCR***

To analyse relative gene expression for differentiation in MSCs total RNA was reverse transcribed to give complementary DNA (cDNA). This enabled amplification of small mRNA transcripts into a stable constructs for robust replicate analyse.

It has been shown that careful housekeeping gene selection is dependant on target tissue or cells under investigation. There is no universal control gene for all cell types but best overall control genes are UBC, HPRT1 and GAPDH[238]. The use of GAPDH was selected as a suitable normalizer marker given its use in mesenchymal studies throughout the literature, which enables comparable gene expression between experiments.

The gene coding for Glyceraldehyde 3-phosphate dehydrogenase (GAPDH) has the biological function as an enzyme involved in glycolysis but it is also an abundant, stable housekeeping gene conservatively expressed in quantity throughout almost all human tissues.

Identification of lineage specific gene expression across potential tri-lineage (Osteogenic, Chondrogenic and Adipogenic), selected established master transcription genes RUNX2, SOX9, and C/EBP in association with abundant lineage associated proteins ALP, ACAN and FABP4.

5.5.3. *Lineage Gene Expression in Primary MSCs on Surfaces Cultured under Basal Media Conditions*

Cells isolated from several patients after total hip replacement (THR) were studied but only three examples are discussed below. Mesenchymal stromal cells were isolated and characterised as previously described and the details of the cells used for gene analyses can be found in Table 4.

Patient No.	Age	Gender	Surgery
N_2840	64	Male	THR
N_2848	74	Male	THR
N_2864	77	Male	THR

Table 4. List of patient details used for mesenchymal stromal cells isolation, pluripotency and investigation with polymer surfaces; Total hip replacement (THR)

Due to the known variability between patients, primary cells were selected from populations that were isolated and readily expanded into populations within a relatively short time period (<2 weeks). The patient gender and age were kept similar; a higher frequency of hip replacements in elderly males offered the greatest selection pool. Focusing on a single joint site for cell extraction; MSCs were isolated from trabecular marrow of the femur proximal epiphysis.

Each primary huMSC population was cultured on the panel of experimental surfaces for two time points, 7 days and 14 days. The resulting cDNA was tested by real-time PCR for expression of the lineage specific genes. Described in detail below are the results for the eldest patient of the three, N_2864 (77y), with comments presented in relation to other patients, data can be found in appendix pg. XLV.

5.5.3.1. N_2864 Analysis

Gene expression analysis revealed that after 7 days in culture on the polymer surfaces SOX9 was elevated on the demixed surfaces compared to the individual polymer surface and glass control surface, (Figure 40_*left* hand side of each surface). Greater propensity for SOX9 expression was noted on the PMMA only surface over the PS only surface, this remained the case at 14 days (Figure 40_*right* hand side).

The inverse of this was observed on PMMA rich demixed surface 40:60, where initially strong SOX9 signal was detected (almost parallel with PMMA) but dropped off by 14 days. The SOX9 levels seen on its counterpart 60:40 exhibited similar elevated levels but stable over the two week period. This was inverse to the low levels observed on the PS homo-polymer.

Only one of the demixed surfaces, 60:40, retained a stable and comparatively high expression of SOX9. But no significance was found between demixed surfaces or the controls (Two-way ANOVA: P=0.1137); Tukey's multiple comparison compared each surface against every other at both time points without significance (not shown here); Sidak's multiple comparison compared each surface at both time points directly, without significance.

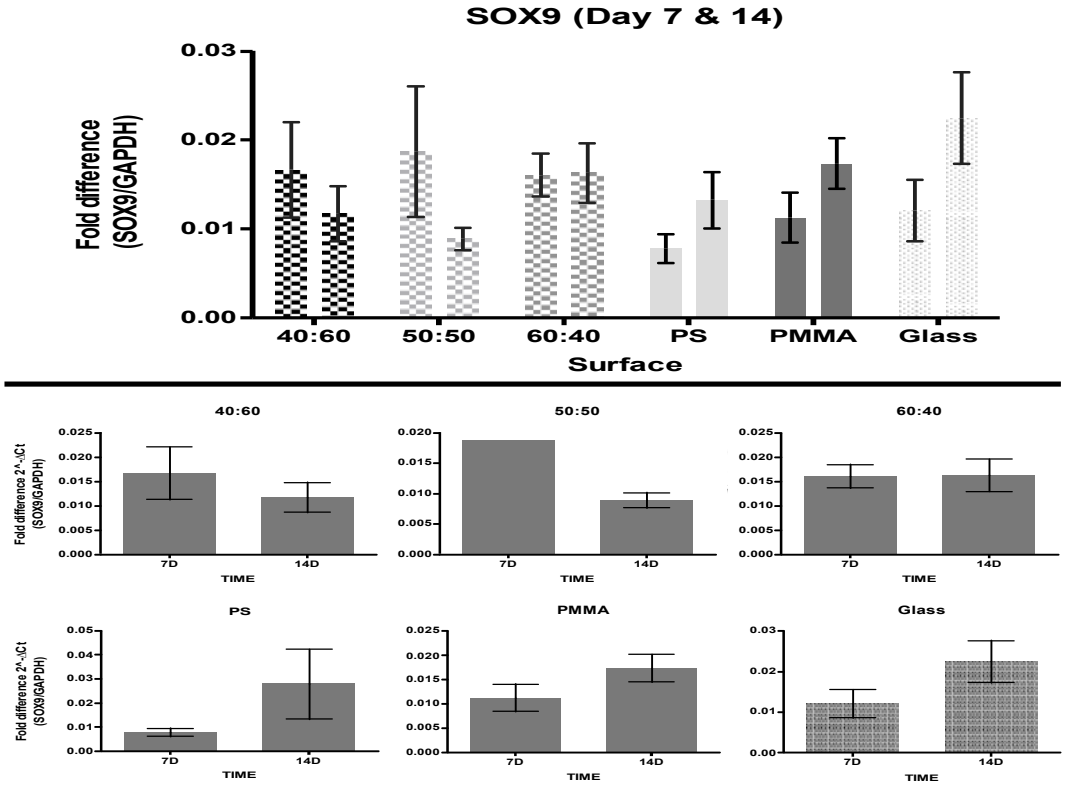

Figure 40. Real-time PCR results for SOX9 gene expression for N_2864 after culturing on panel of surfaces for 7&14 days. Surface-to-surface comparison (*top*) and time point comparison (*bottom*) are shown. All samples were normalised to housekeeping gene GAPDH and expressed as fold change [2^-ΔCt].

- *N_2864*

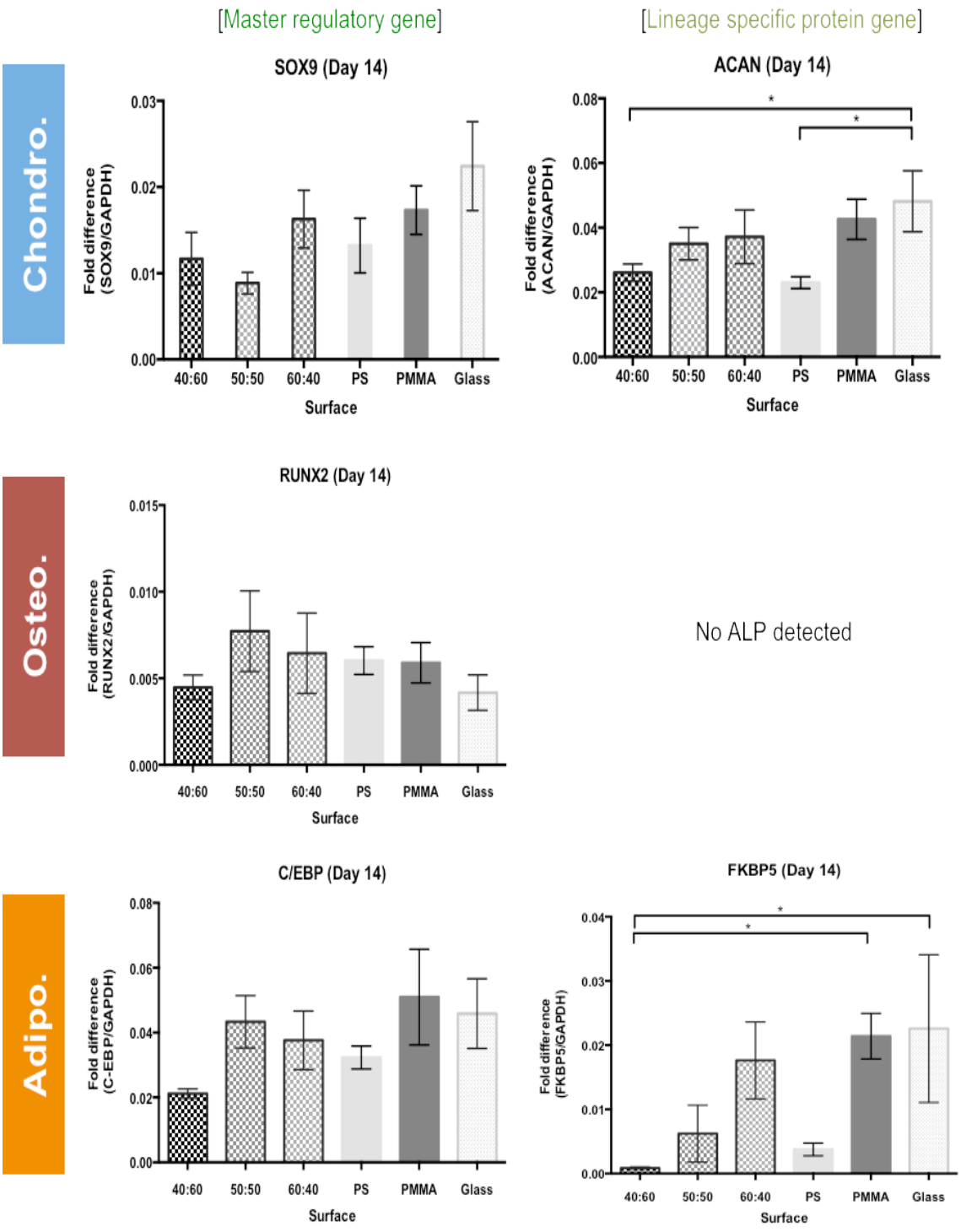

Figure 41. Graphs of real-time PCR results for expression of tri-lineage regulator genes and proteins specific genes, for N_2864 primary MSCs, cultured on demixed polymer surfaces for 14 days with basal Medium.

Equivalent transcriptional analyses were performed across lineage specific genes and are displayed at the 14 day time point for comparison (Figure 41).

Notable was the low levels of osteogenic expression across all patient cells given their stromal origins of the cells. Of the master regulatory genes RUNX2 expression was with a lowest overall fold difference (<0.012) and negligible differences between each individual surface (<0.005). Furthermore there was a failure to detect any ALP expression (primers were verified and technical repeats failed to clarify a signal).

This was not the case for chondrogenic or adipogenic readouts. Overall levels of SOX9 expressed consistent (Figure 40_SOX9), and in N_2864 the PMMA ctrl surfaces showed slightly higher expression over PS ctrl. This did not transfer linearly over to the demixed surfaces where PS-rich 60:40 showed highest of all three and the lowest at 50:50 (Figure 41_SOX9).

The ACAN expression of the same samples displayed a linear increase in expression across the demixed surfaces towards the 60:40 blend (Figure 41_ACAN). Following the SOX9 expression pattern the individual polymer controls showed an inversed correlation, with PMMA ctrl higher then PS ctrl.

The adipogenic gene C/EBP, was the highest overall fold difference (<0.07)(Figure 41_C/EBP), with PMMA ctrls the highest surface for expression but also has the greatest standard error (±0.03). No coherent trend was observed on the demixed surfaces with highest expression on the 50:50 blend (Figure 41_C/EBP).

Expression of FKBP5, an immunophilin-binding protein and key regulator to early MSC differentiation[239], displayed similar rising trend towards 60:40 amongst the demixed surfaces. With inversed relationship to homo-polymer controls; PMMA levels were higher then PS and even expressed significantly higher then 40:60, the PMMA-rich demixed blend.

Expression of common ECM proteins was also explored in this sample case N_2864, additional analysis of the common COL1 protein gene expression displayed significantly higher expression on PMMA ctrl surfaces over all demixed surfaces. With similar rising trend between 40:60 and 60:40 amongst demixed surface (Figure 42).

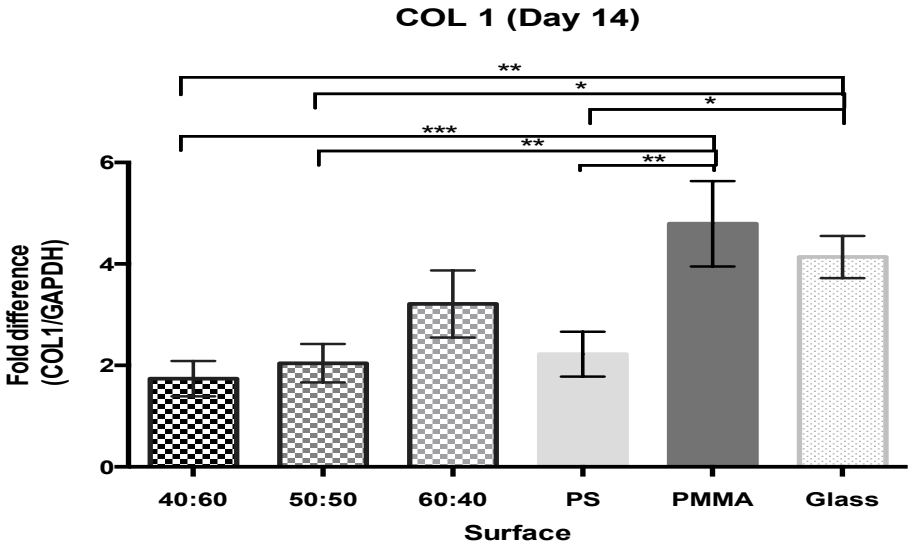

Figure 42. Fold change expression of collagen type 1 (COL1) at 14 days on panel of polymer surfaces for patient N_2864.

Of the other focus patient samples analysed, N_2840 & N_4848, no equivalent transcriptional trend was noted amongst MSCs cohorts. Performing identical experimental conditions and gene expression analysis across the lineage specific genes at 14 days displayed similar down regulation of osteogenic gene expression, but prompt detection of chondrogenic and adipogenic gene expression.

Detect trends between surfaces for each patient sample shifted considerably; most notable was the detection of RUNX2 and reduction/lost of detection of ALP in both N_2840 and N_2848.

Amongst chondrogenic expression of SOX9 on individual surface PS ctrl displayed higher amongst controls for N_2840 but the demixed surfaces show coherent trend with he control surface (Figure 43_SOX9). Again PS ctrl appeared highest for N_2848 with a very slight opposing trend in the demixed surface decreasing from 40:60 toward 60:40 (Figure 44_SOX9). These observations were mirrored in the protein gene detection of ACAN for each patient.

Conversely the adipogenic gene expression of C/EBP opposed any trend on demixed surfaces, displaying elevation on 50:50 greater then its respective controls and failed to detect FABP4 for N_2840 (Figure 43_Adipo.). Where as N_2848 displayed concurrent trend of demixed surface with controls and similarly with protein gene expression FABP4 (Figure 44_Adipo.)

The contrasting variation between all three patients is a reflection of patient-to-patient variability.

- *N_2840*

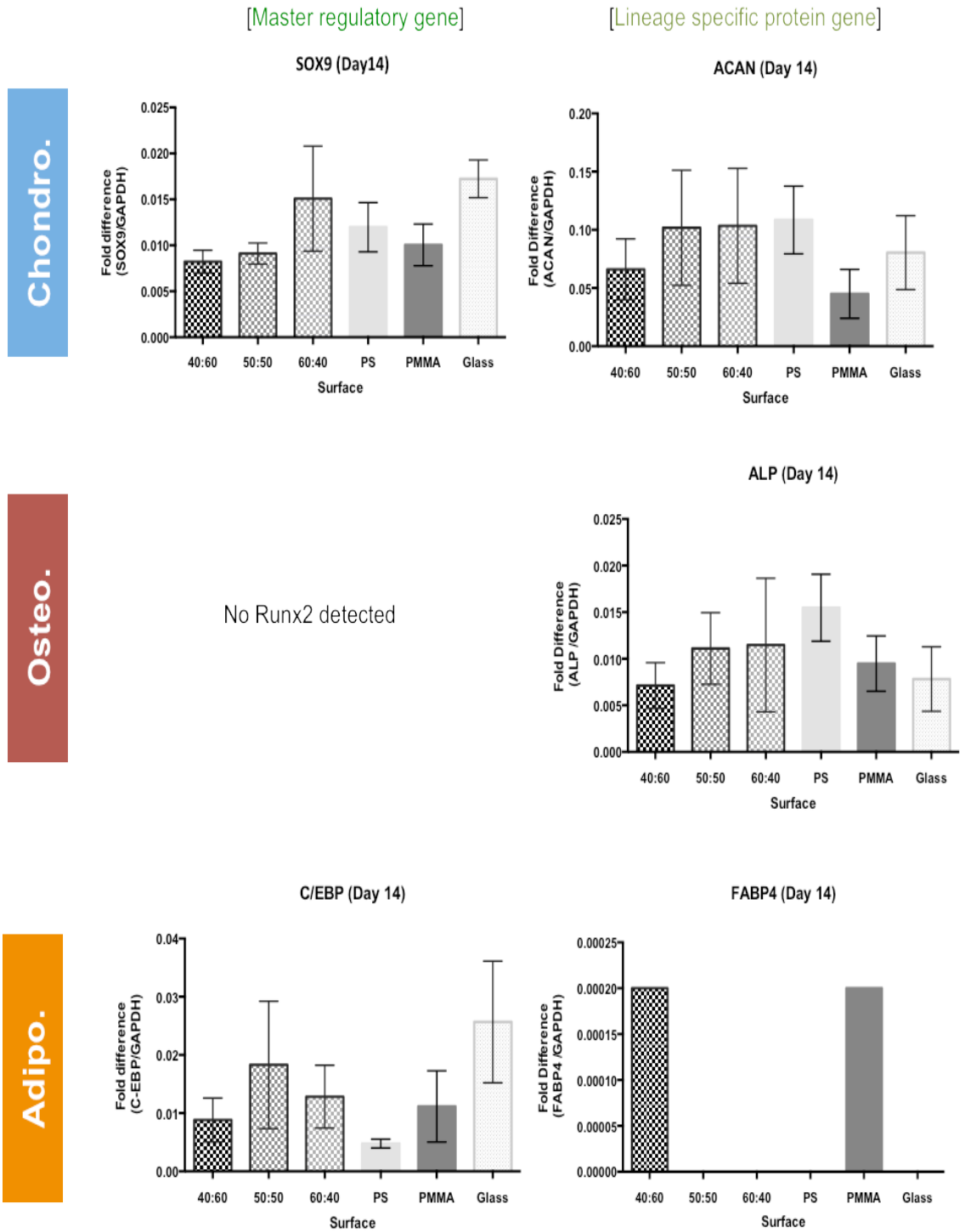

Figure 43. Graphs of real-time PCR results for expression of differentiation genes with N_2840 primary MSCs, exposed to demixed polymer surfaces for 14days under basal conditions. N=4.

- *N_2848*

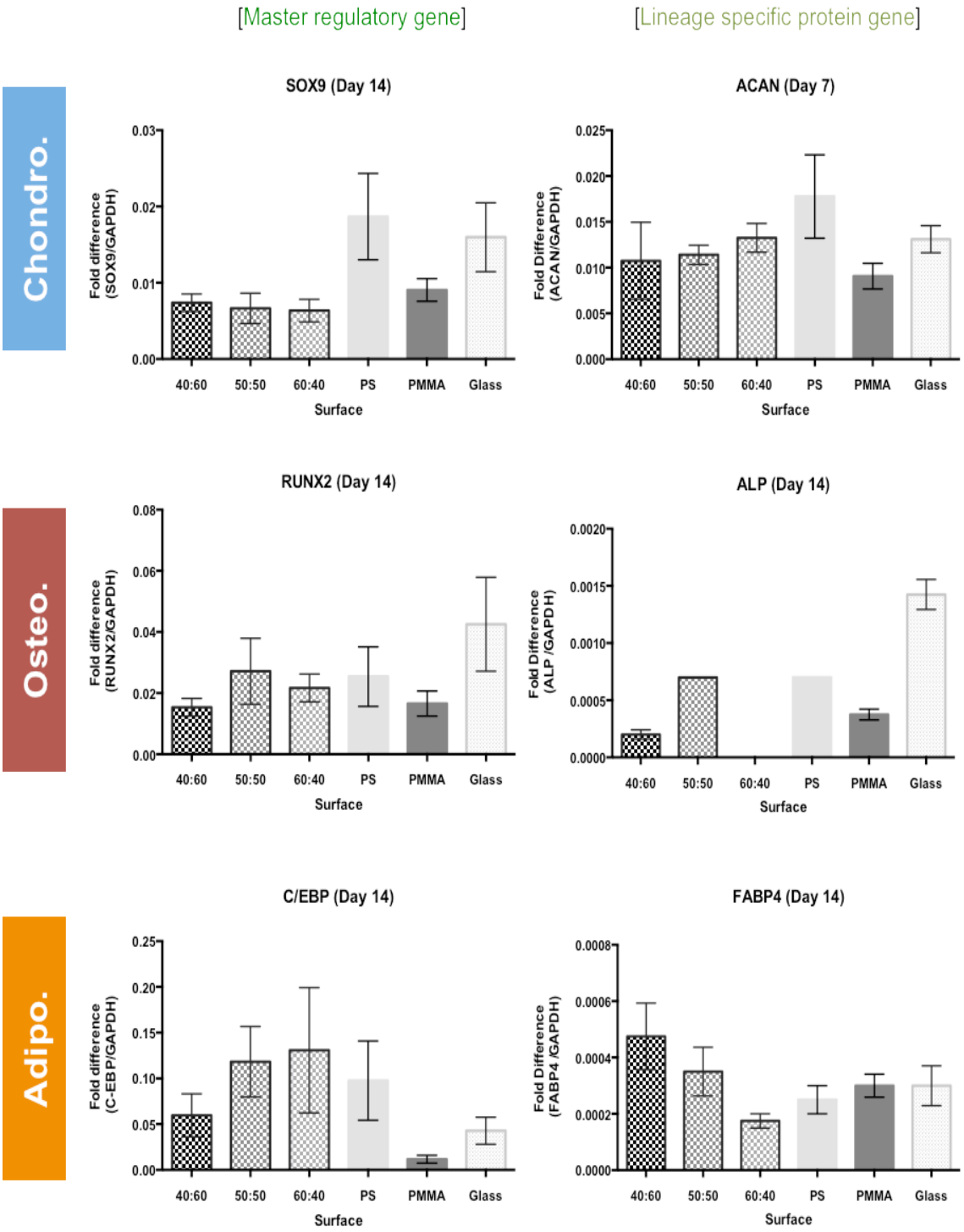

Figure 44. Graphs of real-time PCR results for expression of tri-lineage regulator genes and proteins specific genes, for N_2848 primary MSCs, cultured on demixed polymer surfaces for 14 days with basal Medium. N=4

There was little consistent mesenchymal stromal cell response observed for transcription gene expression across all three patient cell populations presented in these studies. This is highlighted and compared for the SOX9 expression across different patients in Figure 45. Each patient sample was run as four experimental repeats with greater then five technical repeats preformed for real-time analysis of isolated RNA. Use of heterogeneous populations of cells crudely selected by 'plastic-adherent' phenotype with the dominant ability to self-renew, fails to screen out cell population variation.

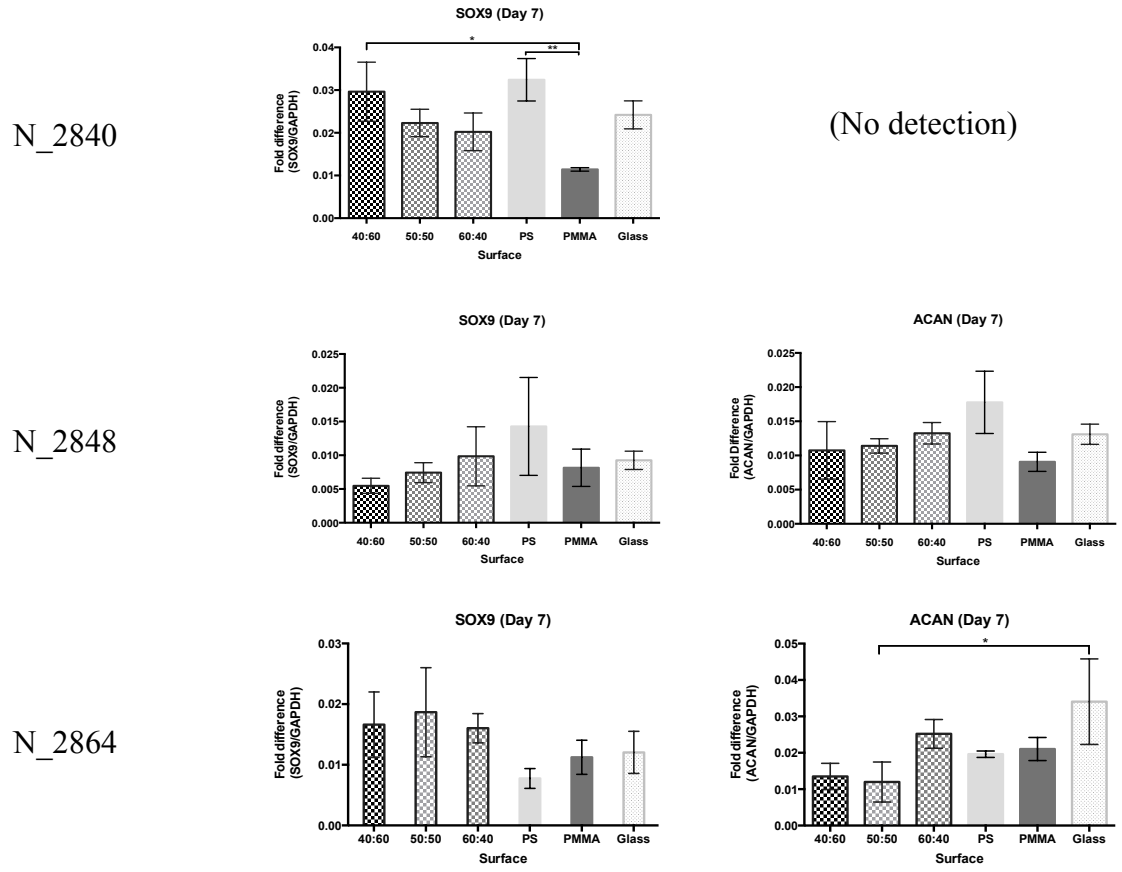

Figure 45. Collective chondrogenic gene expression profiles of each primary MSC population. Cultured on panel of surfaces for 7 days. Normalised to GAPDH and expressed as fold change.

5.5.4. *Lineage Gene Expression in HuTERT MSCs: Y201, on Surfaces Cultured under Basal Media Conditions*

Gene expression between populations of primary MSCs displayed variability. To better evaluate the influence of the surfaces in question the use of a stable immortalized cell lines offered a more reproducible cell population for further study.

The cells used were a human telomerase reverse transcriptase (hTERT) immortalized cell line, produced by collaborators at York University. Several primary mesenchymal stromal cell populations, isolated like the primary cultures using density gradient separation, under went lentiviral vector transduction and culture expansion to identify single population colony's with antibiotic resistance. Y201 was one such successful population retaining MSC phenotype and multipotency, validated by flow cytometry and tri-lineage differentiation, were utilised to replicate experiments of primary cultures.

Under identical conditions as primary MSC cultures, the Y201s were cultured on each polymer surface for 14 days without additional soluble molecular mediators (i.e. growth factors). One resounding similarity is the very low or lack of expression for osteogenic markers RUNX2 and ALP (Figure 46_Osteo.). No RUNX2 expression was detected on demixed surfaces with extremely low expression found on homo-polymers and glass ctrl (<0.0008 fold difference)($P<0.05$). Some ALP expression was detected on 40:60 demixed surfaces with significance ($P<0.0001$) over the extremely low levels of both homo-polymers and glass ctrl, but none detected on 50:50 or 60:40 surfaces (Figure 46_Osteo.).

Higher levels of adipogenic markers were observed in cells o some surfaces, elevated C/EBP expression on 60:40 and 40:60 surfaces (Figure 45_Adipo.), both expression significantly higher ($P<0.001$) over low levels of controls (note: in a replicate experiment of this, 60:40 failed to express and 40:60 was dwarfed by high expression on the 50:50 surface (see appendix pg.XLV). The linked FAB4 expression failed to present any detectable expression on demixed surfaces (Figure 46_Adipo.) and very low expression on both homo-polymer surface but significantly higher on glass ctrl ($P\leq 0.0001$).

Elevated SOX9 expression across demixed surfaces was corresponded with increased ACAN expression. The expression of SOX9 was highest on 40:60 and 60:40, with the

former expressing greater variability (SE±0.0154). The 60:40 surface was significantly higher over 50:50 surface ($P<0.001$) and both homo-polymers PS ($P<0.001$) and PMMA ($P<0.01$) (Figure 46_Chondro.). In contrast, ACAN expression displayed a stepwise increase through demixed surfaces with lowest expression at 40:60 up to 60:40. Correspondingly amongst the two homo-polymers PS is higher then PMMA. Highest overall fold change was PS it was significantly higher then PMMA and 60:40 surfaces ($P<0.05$) and 40:60, 50:50, glass ctrl ($P<0.001$).
Second highest fold change was 60:40; this to had significantly higher expression over 40:60 and glass ctrl ($P<0.01$) as well as 50:50 ($P<0.05$).

No type II collagen gene expression was detected, even at longer time periods and with a verified COL2a1 primer using primary human articular chondrocytes (HAC).

Relevant significant P-values [* <0.01; ** <0.005; *** <0.001]

- *Y201*

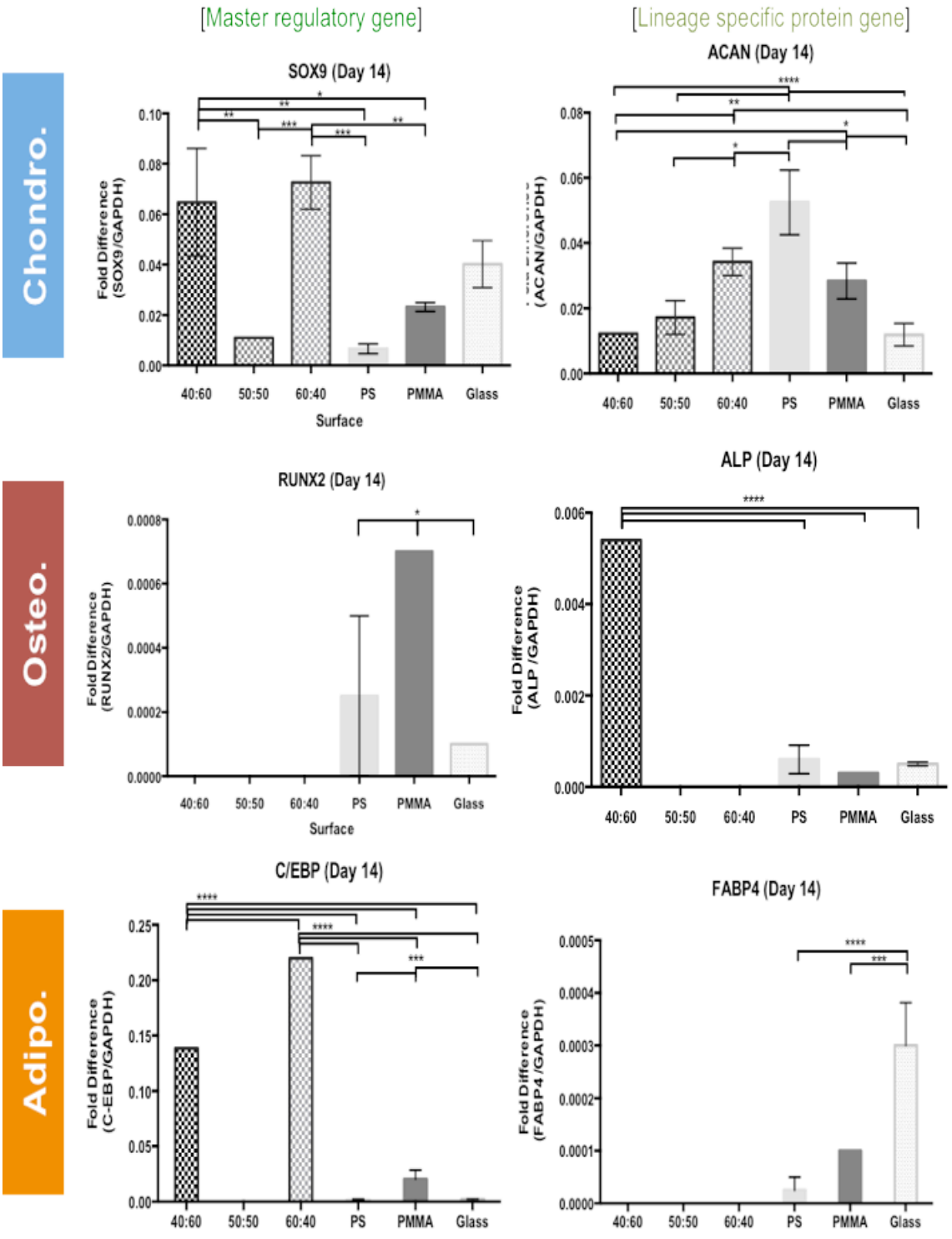

Figure 46. Graphs of real-time PCR results for expression of tri-lineage regulator genes and proteins specific genes, for Y201 huTERT MSCs, cultured on demixed polymer surfaces for 14days with basal Medium.

5.5.5. *Influence of fabricated surfaces on Cell-Cell Interaction*

Topography has a great influence over an individual cells adhesion to the surface and definitely affects cellular interaction with ECM components, but the effects of the surface are far further reaching then that. Topography has an associated effect on how cells interact with each other[240,241] and the ability to proliferate/differentiation as a population[132,211,219]. Upon the demixed surfaces populations of cells were repeatedly observed aggregating together in colonies, when culture for longer time periods (>2days). Cell to cell attraction on demixed polymer surfaces were observed by SEM, (Figure 47_B), where the cells appear to be congregating together after only 48h, no discernable topographical features appear to be the focus, only cells moving together. Fluorescence microscopy highlights the density of cells in a cluster by identifying the number of nuclei (blue) and the cytoskeletal morphology (red) and the symmetry between the group of cells (Figure 47_A). [clustering of cells was observed on all polymer surface, see appendix pg. XLI]

Similar observations can be made by fluorescence confocal microscopy (Figure 47_C) where a large population cluster can be observed in the top right hand side of the image (top). This was a 3 days culture of MSCs but with a larger seeding density (~50,000 cells/surface). Greater cell numbers displayed aggregating characteristics of the smaller populations showing global organisation of the population. Confocal microscopy also enabled the overall cell membrane to be viewed transversely, giving sections through the layers of cells. Observing organisation of cell nuclei in the section (Figure 47_C *lower*), reveals cells stacking vertically on top of each other. This perpendicular arraignment up from the adherent surface is the formation of a micro-mass cell structure.

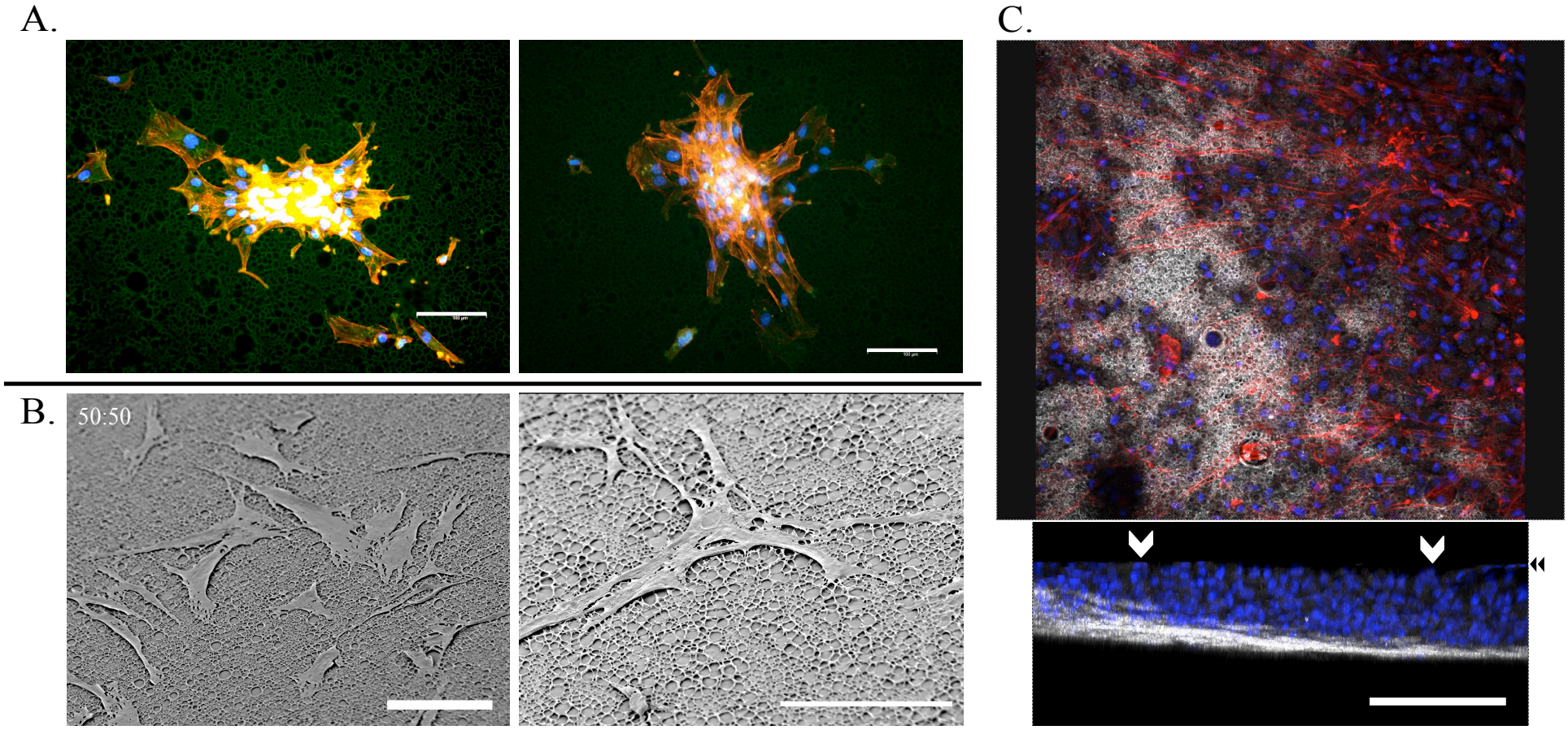

Figure 47. A) Cell aggregates are observed on demixed surfaces after 72 h in culture. Dense colony's are formed with multiple cell layers. B) SEM images of congregating cell populations on demixed polymer surfaces after 48 h. C) Fluorescent confocal microscopy, top, of aggregated MSC colony forming a micro-mass (in the top-left hand corner of image). Cells stained red for F-actin of cytoskeleton by Rhodamine phalloidin and nuclei blue by DAPi, after 72 h in culture on demixed surface (50:50); bottom, Transverse section of cell nuclei (DAPi) on 50:50 surface, with polymer surface at base of image (grey/white). White arrows highlight areas were stacked cells form vertical structures (pillar-like). The black arrow highlights image cut-off height with incomplete nuclei showing, this is a result of the cell later surpassing the confocal microscopy z-axis stack height (>24µm). Scale bar - 100 µm

5.5.6. *MSC Condensation on Surfaces under Chondrogenic Stimulus*

Induced chondrogenesis of MSCs has been shown previously[127], when preformed in conjunction with polymer surfaces cultures display altered adhesion profile and tissue development[242]. Cultures display condensed micro-mass aggregates on the surface after 14 days in culture. The formation of colonies were readily identifiable on the demixed polymer surfaces (Figure 47), 40:60 an extreme micro-mass is observed but dispersed micro-mass colonies can be observed on 50:50 and 60:40 and are more typical. 60:40 surfaces exhibited dense colonies formation, this dark colour can be attributed to high proteoglycan deposition. Comparable observations were made on homo-polymers, and notably on PMMA ctrl. All non-induced cultures did not develop the same level of chondrogenesis, with the exception of some GAG staining visible on 50:50 ctrl and PMMA ctrl. Possibly corroborating the chondro-inductive potential of the surfaces.

Development of extreme micro-mass 'bulbs', as seen on 40:60 surface (Figure 48), were found on other surfaces as well. During downstream processing of surfaces these larger micro-masses became detached due to the shearing forces of the wash steps. Once in suspension these micro-mass pellets were isolated and processed for histological analysis. They provided insight to the organisation effects of polymer topography during cell population organisation and orientation.

Chondro-pellets isolated from suspension were wax embedded and sectioned before histological staining. Masson's trichrome stain provides simple cellular identification by H&E but with the added benefit of differentiating collagen deposition around the cells. All isolated pellets displayed some form of collagen deposition with the exception of non-induced glass control, (Figure 49*_bottom right*), which is devoid of blue staining, small pellet size and has poor structure.

Demixed surface pellets, (Figure 49*_top*), all have clearly identifiable areas of collagen deposition; 40:60 has collagen dispersed throughout whole pellet, with concentrated collagen deposition areas observed with a wall-like concentration at the periphery of the lower left-hand side. The 50:50 surface also supported pellet with concentrated areas of collagen deposition, arranged into central columns within the pellet, while interconnected areas of blue/collagen can be seen between cellular areas; 60:40 the concentration of collagen regions is even more striking, dominating the central spine of

the pellet, with once again a wall-like layer at the base of pellet coated by cells above and below.

Unfortunately as the pellets were detached and collected from free-floating suspension, the orientation of their attachment to the surface is unknown. There are some strong indicators to the possible attachment orientation of pellets, particularly on 50:50 and 60:40 samples we observe intently flatted sides (Figure 49). Counterintuitive to the spherical shape observed in the free-floating chondro-pellets discussed in Chapter 4. The orientations of these images have been rotated to better observe the possible adhesion profile of the over all pellet. Both pellets appear to have deposited large basal layers of collagen with vertically growing columns of collagen perpendicular to the surface (Figure 49_50:50 & 60:40), from which cell areas has aggregated in an outward growth away from surface. No definable flattened side is apparent on the 40:60 sample but this maybe a horizontal section through the pellet (Figure 49_40:60). If we consider 50:50 and 60:40 to be vertical sections, the intense blue colour at top right-hand side and intense blue circle in the lower right-hand side, maybe the pillar-like structure observed in 50:50 and 60:40 from an areal objective.

Within the two homo-polymer controls, substantially heavier collagen deposition was observed in PMMA compared to PS (Figure 49_*bottom left*), as opposed to the dispersed interconnected deposition within PS and 40:60.
The induced glass ctrl also displayed a large store of collagen in a single intense area but pellet displayed no definable orientation and so collagen cannot be determined as a directed growth.

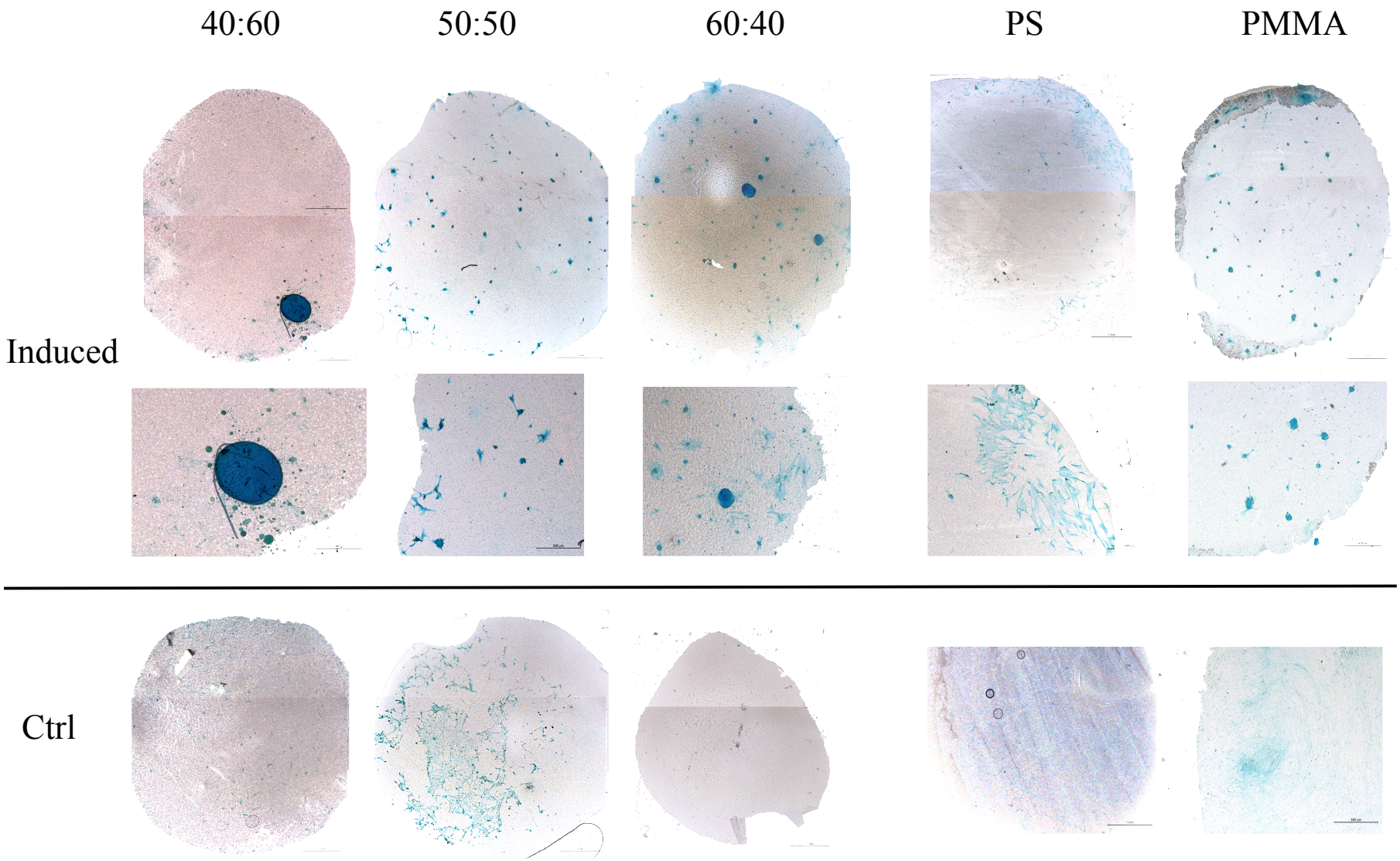

Figure 48. Induced Chondrogenic differentiation of huMSCs (Commerial source, Lonza) P-6, cultured on different polymer surfaces for 14 days. Histological staining with Alican Blue 8GS identifies presence of proteoglycan, indicative of chondrogenesis. Scale bar – 1 mm

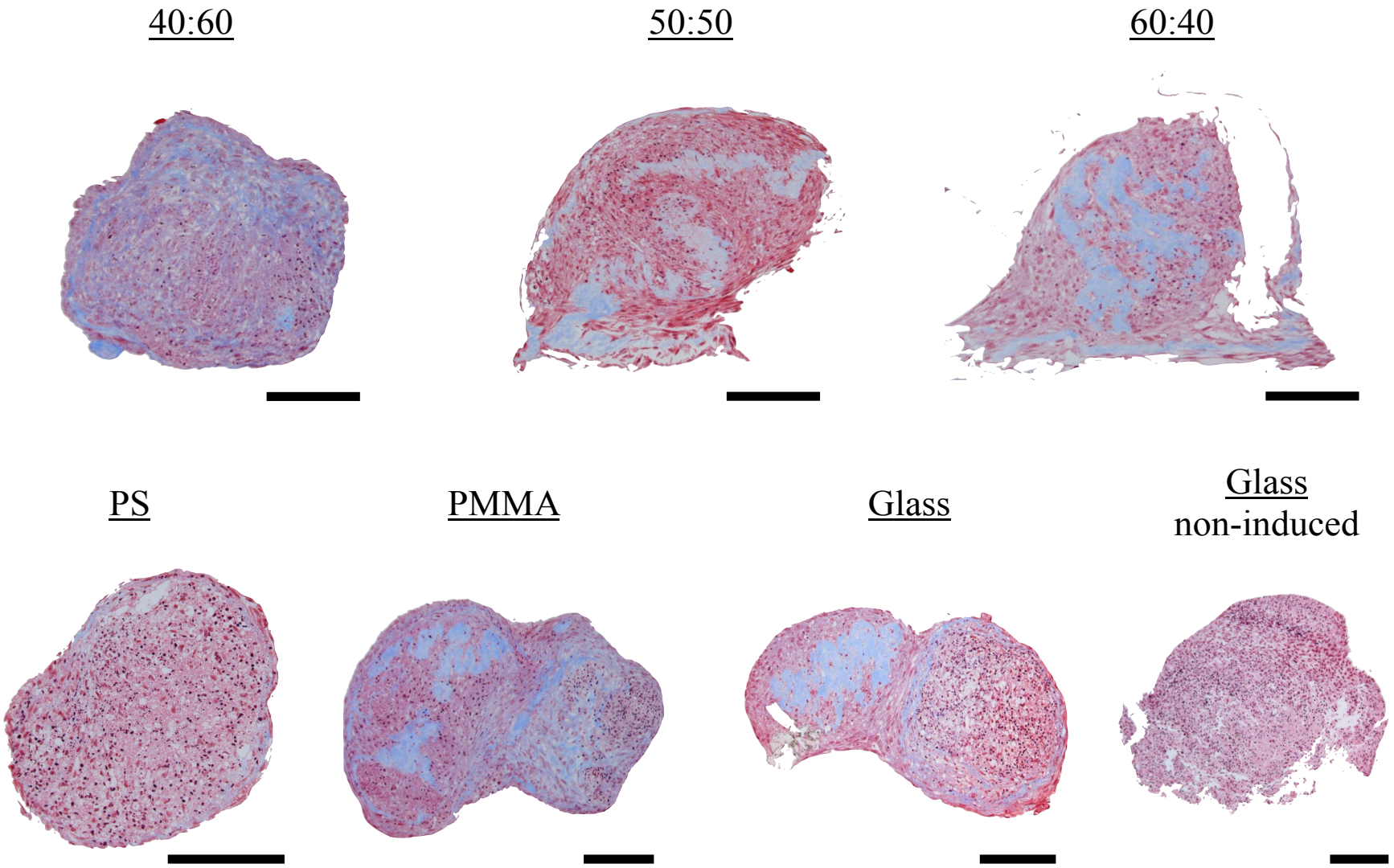

Figure 49. Masson's trichrome stained sections of MSC (Lonza, P-6) pellets after 14 days with chondrogenic media. Simple staining of cellular components by H&E (nuclei-black; cytoplasm-pink/red) with contrast for extracellular matrix proteins (collagen-blue). Pellets isolated from demixed surfaces, top, and both homo-polymer ctrls and glass ctrl, bottom. Scale bar = 200 µm

5.6. Discussion

A number of studies, in both adult and embryonic stem cells, have identified 3-dimensional cultures to be conducive for chondrogenesis. Spheroidal cell shape maintained through pellet (micro-mass) or encapsulation (agarose, alginate, etc.) reinforces cell phenotype[210,243] even with partial cell attachment an improved fibrochondrogenic phenotype is maintained[244]. But also textured topography have been shown to influential pro-chondrogenesis stimuli with extensive effects on tissue formation, organisation and development[245].

The raised caldera induced at the surface, provides focal adhesion motifs for cellular interaction and appear to be tuneable and adjustable by demix ratios. Polymer demixing induced phase separation during spin coating, due to an accelerated rate of solvent evaporation, the affinity of polymer for solvent dictates which polymer will dominant. Of the Polymers presented here, PS has high affinity for solvent toluene where as PMMA does not, this enables the physical height to dominate over low lying PS. A side from the physical element the rapid evaporation, water droplets (BFP) and exposure to air during spinning alter the hydrophobicity and functional molecular group presented. This altars the protein adsorption at the surface, Zuyderhoff et al. showed this with the protein adsorption of collagen type I on PS-PMMA surfaces[246]. The deposited proteins are essential for successful anchoring of cell population to surface.

No definitive conclusions can be drawn from these findings on MSC mechanical signal transduction, due to the growing evidence on intracellular signalling cascades in modulating cell fate. Contractile forces and cytoskeletal tension[136] affecting the downstream regulatory systems like; Rho Kinase (ROCK) in Osteogenesis (elevated) and Adipogenesis (lowered)[212]. Similarly several classes of ion channels (Ca^{++}) like TRPV4; affected by mechanical, temperature and osmotic change in Chondrogenesis[247]. Direct links have been suggested between RhoA-mediated actin organisation and TRP channel-mediated signalling[212,248-251].

Expression of osteogenic markers across all three patient cell populations appeared lower on textured polymer surfaces with minute fold change in the gene expression. Janson *et al.* 2014 observed similar findings on nanogratings of PMMA films ~0.5 μm gaps emerged to be poor drivers of osteogenic phenotype[252].

For the effects of demixed polymer surfaces to be deemed as solely mechanical transduction of MSC differentiation, the mechanisms of action would need to be established intracellularly.

Primary mesenchymal stromal cells represent heterogynous populations within the bone marrow niche, with culture expansion on tissue culture plastic crudely selecting a plastic adherent population of cells. It is relevant to note that interpretation of these results may reflect cell populations more adaptable to culture conditions and select for subpopulations influenced by adhesion changes, rather then a universal regulatory mechanism[123].

The stromal niche of the mesenchymal cell origin has been previously described in the literature as highly likely to differentiate down the osteogenic lineage if over confluent or stressed. This does not appear to be the case on the demixed polymer surfaces, where the cells do undergo increase cellular tension and abnormal cytoskeletal morphology.

These alterations of cell-surface adhesion profiles appear suspect to influence a variety of different intracellular pathways, as the most likely *modus operandi*, according to current knowledge.

Chondrogenic ability of huTERT MSC-line, Y201, was inconclusive due to the lack of expression and deposition of any collagens. The same cells were subjected to the identical conditions as primary patient cells which displayed collagen expression, including enhanced *in vitro* 3D culture environment[253], but showed no expression of any collagen at the RNA level or deposition of collagen detectable by histological staining.

Elevated gene expression of chondrogenic genes [SOX9 and ACAN] and the condensing of mesenchymal cells into tight micro-mass clusters, suggests condensation-like growth pattern. Studied during embryonic skeletal development, where cells condense into dense aggregates during the formation of articular cartilage[254].

The failure to detect COL2α1 (type II, collagen) means this cannot be definitively deemed ‘cartilage’ but suggests an alternatively organised fibro-cartilage. By the same standards it cannot be ruled out as potential cartilage growth as it is known that intracellular expression of SOX9 mRNA is mirrored by SOX9 protein expression[230] in mice, this coupled with the finding of Jinping XU *et al.* 2008 showed delayed gene expression of COL2α1 of MSC in 3D culture at later then >24 days[253].

The stark contrast of cellular aggregation on the two homo-polymer controls, and knowing the characteristically different topographical patterns generated by BFP on these two chemically distinct polymers, enables comparisons to be made with the demixed surfaces. The similarities between PS ctrl and 40:60 demixed surfaces are quite analogous, but with the main component of 40:60 being PMMA the two surfaces are chemically very different. The PS-rich demixed surface of 60:40 also opposes the PS ctrl, displaying large intensified collagen deposition. The only connecting factor, out side of the chemical composition, between the demixed surfaces is elevated caldera height, caldera dispersion and consequentially alter adhesion cell morphology due to topography. This adds weight to the theory that chemical composition of the polymer surfaces has less of an effect on the biological growth altered cell adhesion.

5.7. Summary

- Distinct topographical features were identified for each variation of the polymer blends. The demixed surfaces display individual characteristics distinct to the fabrication process.
- Interaction of individual cells on these surfaces altered their morphological profiles through adapted physical adhesion to the polymer surface.
- Cell-surface; polymer topography directly dictates cell adhesion and cell shape, which in turn influences cell phenotype.
- Cell-Cell; effects of constrained cell adherence, polymer chemistry, and possible alternate steric forces of phase separated polymers, enhances cell aggregation and clustering.
- Demixed topographies show a trend towards influencing primary MSCs towards the adipogenic lineage. No universal effect was noted amongst the different MSC populations.
- Altered phenotypic expression is not only in cells juxtaposed to the surface, but also in subsequent cell layers distant from the surface.
- Demixed polymer surfaces appear to reinforce cell aggregation and colony formation, with existential effects on micro-mass formation, cell-surface orientation and expansive growth.

CHAPTER 6. SURFACE MODIFICATION, FUNCTIONALIZATION AND ADAPTATION WITH IMMOBILISED BIO-LIGANDS

6.1. INTRODUCTION

The importance of cell-ECM interaction has been previously mentioned in the introduction, identifying it as a stand-alone mediator with critical roles in cell function and regulation including proliferation, homeostasis and differentiation[106,114,241].

It was these observations that have driven the design of synthetic biomimetic substrates and surfaces, to support, incorporate and present bioactive signals mimicking native tissue as well as providing structural protection and housing during delivery of implant[109,149,255]. The use of synthetic material, like polymers, enables advantageous adaptation due to tuneable chemico-physical properties. In the case of bone repair synthetic polymer materials have been investigated extensively with generally a limited integration due to sub-optimal biological interaction[256,257]. Studies with decellularized bone matrix showed increase physiological functionality due to the complex nature of bioactive signals encased in the ECM[112,113]. When reviewed; decellularized mature bone tissue induced bone formation when re-populated with undifferentiated MSCs[113]; alternatively, decellularized ECM produced by undifferentiated MSCs *in vitro* showed improved proliferation and enhanced osteogenic capacity with fresh reseeded population of MSCs[258]. Similarly a culture of MSCs osteogenically differentiated on a 3D scaffold *in vitro* when decellularized and re-populated with fresh MSCs and no stimuli, showed spontaneous Osteogenesis with accelerated osteoblastic differentiation[259]. The combination of these finding over a 20year period lead to tissue engineering's first blockbuster medical device in 2002, INFUSE® by Medtronic[99], a BMP-2 soaked collagen I (bovine). This premises continues to modern day where Ben-David *et al.*(2013) show effective bone formation with low dose BMP-2 on a PEGylated fibrinogen hydrogel.

The previously discussed interactions of cells with their ECM maybe recapitulated by a minimal set of purified components like; adhesion molecules, peptides, calcium phosphate-based particles and growth factors[240]. The inclination of this collective knowledge indicates that successful bio-mimicry of synthetic substrates for biological functionally may be achieved by decorating material with only a handful of basic ECM components[239,240,257].

Immobilisation of factors to a surface benefits the ability of an implant to enhance compatibility and tailored tissue specific directive. Adaptation of 'smart' materials[260] has improved the biocompatibility of materials and enabled delivery of therapeutic

directly to the injured site, one exciting therapeutic is cell therapy, the delivery of pluripotent or tissue specific cells to the infarction/injury site.

The immobilisation of natural protein ligands can enhance cellular adhesion to the scaffold pre-/post-implantation, saturating the scaffold surfaces with basic RGD-motiffs, e.g. fibronectin, can increase efficiency of cell adherence or migration into scaffold, aid population establishment within scaffold and minimising any lag phase in growth. Impregnating the implant scaffold with growth factors and/or other stimuli (i.e. physical, mechanical) can provide tissue specific direction for cell population. This can be a pre-emptive growth for multipotent stem cells seeded *in vitro* or a stimulus for recruited cells *in situ*.

Additional benefits of this approach include easier regulatory approval of medical device as the process can be tightly controlled and use minimal animal products. The immobilised factors can be sourced from bacterial sources[261] and use recombinant human proteins (growth factors), in combination with a renewable materials, making the process financially more viable and enables tighter regulation over the entire production process.

The patient benefits from a diverse selection of pre-fabricated, tailored and tissue-specific devices in a ready-to-use format for straightforward surgical procedures (minor or major).

6.2. Aim

Identify adaptability of surfaces and technique for downstream modification with biomolecules and scale-up manufacturing.

6.3. Objectives

- Covalently bind proteins to discrete areas of the polymer surface using selective crosslinking chemistry
- Stable immobilisation of organic mediators to polymer surface with possible restrictive immobilization to distinct features or polymer.
- Investigate the retention of biological activity for covalently bound immobilised factors on the surface.
- Study the ability to stimulate multipotent cells down a specified lineage by an immobilized factor over its soluble diffused form.
- Substitute new polymer in demixed blends to determine the adaptability of the process and technique.
- Explore ability of technique to expand into 3D scaffold.

6.4. Materials and Methods

6.4.1. *Zero-Length Crosslinking*

1-ethyl-3-(3-dimethylaminopropyl)carbodiimide hydrochloride (EDC) is a water-soluble carboxyl and amine-reactive zero-length crosslinker. Where the EDC reacts with carboxyl group first to form an amine-reactive *O*-acylisourea intermediate that quickly reacts with an amino group to form an amide bond and release of an isourea by-product. The intermediate is unstable in aqueous solutions and therefore, two-step procedures rely on *N*-hydroxysuccinimide for stabilization.

EDC and sulfo-NHS, typically stored at -20ºC, was let come to room temperature before opening, the powder will remain in clumps and be difficult to weight out accurately if not allowed to thaw. Two weak solutions of EDC (2 mM, final concentration) and sulfo-NHS (5 mM, final conc.) were made up in the activation buffer fresh every use and combined together *in situ* on the polymer surfaces, EDC was applied at 10-times the NHS volume. Left to react for 15mins at room temperature. The factor to be immobilised was added to mixture and left for 2hours under the same
conditions (20 mM 2-mercaptoethanol can be used to quench EDC but we did not find this necessary as immobilisation factor solution diluted activity proficiently[§]). Multiple submerging wash steps terminate reaction and remove excess factor. Modified surfaces were stored in fridge to maintain biological integrity of factor or continued immediately for further processing/analysis.

Reagents

1-ethyl-3-[3-dimethylaminopropyl] carbodiimide hydrochloride, EDC
(22980, Thermo scientific; M_W 191.7. CAS:25952-53-8)
Sulfo-NHS (24510, Thermo scientific; CAS:106627-54-7)
Activation buffer: 0.1M MES + 0.5M NaCl , pH 6.0

[§] Full protocol and an example reaction are detailed in appendix pg.XLII

6.4.2. ***Immobilized Factors***

The covalent addition of factor to the polymer surface followed manufactures protocol for EDC crosslinking in combination with organic factor (protein/enzyme) at 1-10mM. Incubate @RT 1-2 h

Large common mammalian protein: Albumin
[Albumin - Fluorescein isothiocyanate Conjugate from bovine] (A9771, Sigma Aldrich)
AL-FITC [100 µM; 10 µl per surface]

In mammals Albumin (66kDa) is one of the most abundant serum proteins, constituting up to 60% of the proteins in blood plasma. Regulating of the colloidal osmotic pressure in blood is one of the main functions of albumin[262]. The protein is conjugated with a FITC isomer I (F7250, Sigma; 389.4Da; λmax: 495nm) at the ε-amino group of lysines in albumin (A4378, Sigma). The excitation is measured at absorption at OD 495nm.
This hydrolysis product is prepared in 10 mM Tris at pH 7.0 (stock conc.10 mg/ml).

Bioactivity assay, enzyme: Phosphatase
[Phosphatase, Alkaline from bovine intestinal mucosa] (P0114, Sigma Aldrich)
Phosphatase [1 µg/ml; 10 µl per surface]

Isolated from bovine intestine, alkaline phosphatase (140–160 kDa) is a dimeric membrane-derived glycoprotein. The enzyme preforms numerous functions as it has a broad specificity for phosphate esters of; alcohols, amines, pyrophosphate, and phenols[263,264].
Preparation of alkaline phosphatase solution was diluted in 10 mM Tris HCl, pH 8.0 including (1 mM $MgCl_2$, 0.2 mM $ZnCl_2$) and storage at 2–8 °C. The enzyme is stable and operates best in the pH range 7.5–9.5.

Growth Factors
Osteogenic factor: BMP-2
Evaluation of the effects of an immobilised osteogenic growth factor (BMP-2) was evaluated over a 14 day period for affects on gene expression of three osteogenic genes; the master regulator gene RUNX2, tissue specific alkaline phosphates (ALP) and osteocalcin [bone gamma-carboxyglutamic acid-containing protein] (BGLAP). Both

negative and positive controls were run concurrently with experimental immobilised BMP-2 (I-BMP) surfaces. The negative ctrl surfaces were processed as normal with UV sterilisation, the positive ctrl used soluble BMP-2 and same concentration as that immobilized and followed differentiation protocol outlined in Chp.2 Materials & Methods. The I-BMP surfaces under went established crosslinking EDC protocol previously mentioned for immobilisation of BMP-2 at concentration of 100 ng/ml for 1 h with EDC. After UV-sterilisation surfaces were seeded with 50,000 cells N_3100 (primary MSCs, referenced in appendix) incubated at 37ºC 5% CO_2 over a 14 day period feeds cells every 3 days.

Chondrogenic factor: TGF-β and KRTGN

The setup for immobilized Chondrogenic factors on panel of surfaces was split into only two parts immobilised factors [I-CM] and soluble factors [I-CMS] as the negative surface controls have already been shown to be slightly chondrogenic and therefore not true representations of a negative control.

Two different chondrogenic stimuli were evaluated in duplicate, transforming growth factor beta 3 (TGF-β3) and kartogenin (KRTGN) at concentration of [§]~100 ng/ml. Immobilized surfaces were crosslinked by EDC for each growth factor at 100 ng/ml per surface for 1 h. Basal serum-free media was used with addition of ascorbic acid. Surfaces were UV-sterilized before seeding cells, hTERT MSCs (Y201) were used at 500,000 cells per surface and incubated for 21days at 37ºC 5% CO_2. All samples under went media change every 3 days. The positive control (I-CMS), was preformed identically to the previously established differentiation protocol, see Chp.2 Materials & Methods.

[§] This concentration of growth factor (~100ng) can only be an approximation otherwise assumption the cross linker is 100% efficiency.

Reagents

TGF-β3 (PHG9305 ; Gibco, Thermo Fisher Scientific)
Kartogenin (CAY11826 ; Cambridge Bioscience)

6.5. Results

6.5.1. *Immobilisation of a Protein*

In the evaluation of how proteins might interact with the polymer surfaces, a common mammalian protein Albumin with a fluorescent probe was used to map localised retention on surfaces. Utilising fluorescent microscopy the natural or assisted (crosslinking) immobilisation of protein can be observed.

In Figure 50 we observe the natural adherence of a conjugated protein Albumin with FITC flourophore (green), within both homopolymers (A & B) clear retention of protein can be detected, between the two control polymers PS has slightly higher retaining of the protein this maybe due to a natural isoeletric bind, the slightly higher hydrophobic nature of PMMA or the physically larger BFP sizes observed on PS. A zoomed in image of the PS surface shows retention of the protein around the caldera (Figure 50_C). When compared to the median demixed polymer surface 50:50 the retention of the protein is once again observed around the circular BFP pores Figure 50_D, in fact the retention is substantially better and maybe as a result of elevated caldera height.

Utilising alternative imaging techniques like fluorescent confocal microscopy gives precise dispersion geography of the protein, the identification of Al-FITC down into the pores appears to line the wall of the BFP pore and is not isolate to the mouth or caldera, Figure 51_A. Similar imaging was preformed on 40:60 surface with EDC assisted immobilisation, the aided higher protein adherence to the surface but appears to be selective in area of attachment, favouring the raised caldera-rich areas, previously identified as PMMA-rich areas on the

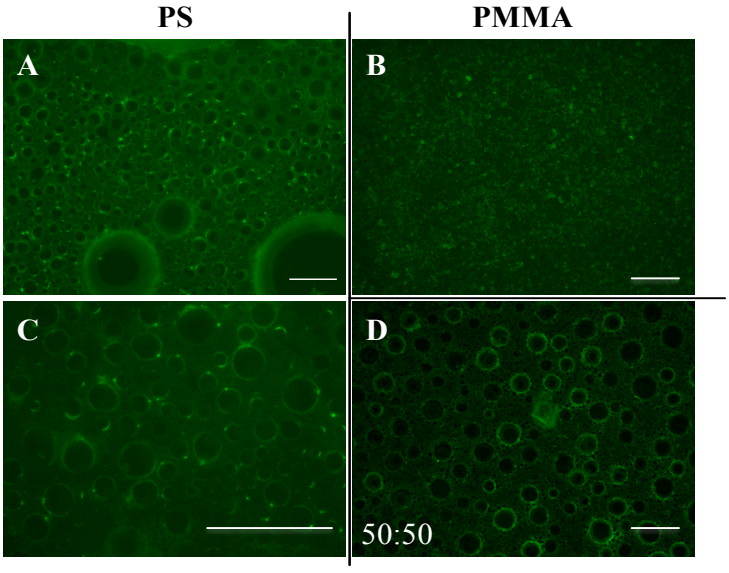

Figure 50. Natural retention of fluorescently labelled albumin protein to polymer surfaces. Retained protein is observed on both homopolymer surface A) PS and B) PMMA. Magnified image C) identifies the retention around the caldera of BFP pores. D) demixed surface 50:50 show similar but intensified retention at caldera site. Scale bar – 100 µm

phase separated surface. This would stand to reason as EDC assists carboxyl (available on PMMA monomer) with primary amine groups (four amine groups available on Albumin). This restricted immobilisation of Al-FITC at PMMA caldera enabled collaboration of exposed height differential between phase separated polymers observed in AFM images, a visual observation of surface z-axis, Figure 51_B far right, shows outermost image (top) to only have green protein outline PMMA regions compared the lowest image (bottom) at the polymer surface.

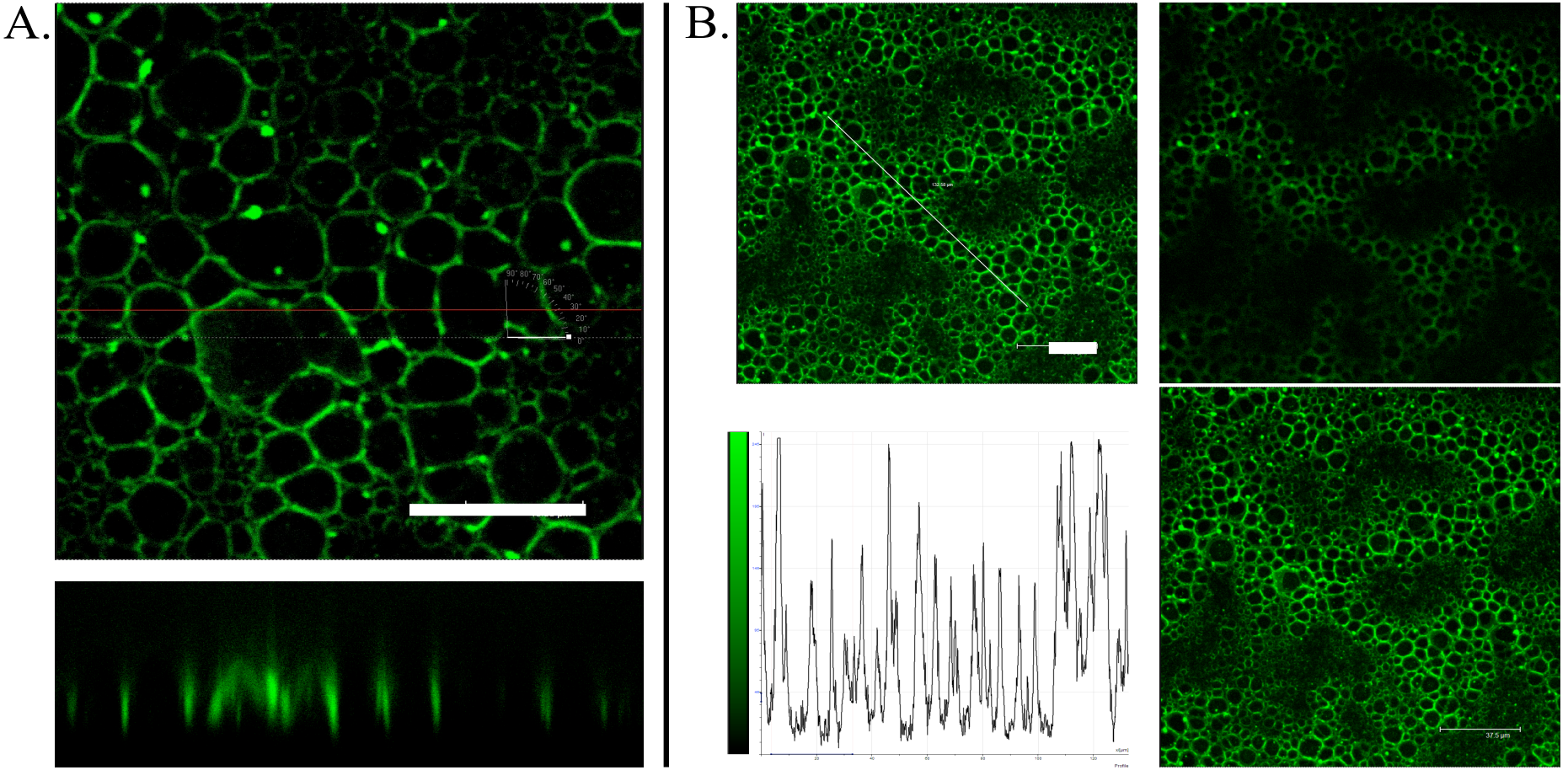

Figure 51. Confocal fluorescent microscopy of immobilised Al-FITC (green) on demixed polymer surface 40:60. A) An aerial image of surface from above (top) identifies dispersion of AL-FITC around polymer surface and its corresponding cross sectional image about the red line (bottom) identifies retention of AL-FITC upon the walls of BFP pores. Additionally, assisted EDC Immobilised Al-FITC on 40:60 B) an alternate confocal cross section of pixel intensity (bottom) following white line through spine of elevated caldera-rich section of surface (top). C) Individual images of z-axis extremities for the polymer surface, identifying the distinction in height deferential between polymer phase separation. Scale bar – 20 µm

6.5.2. *Covalent Crosslinking Protein to Surface*

To evaluate the immobilization of a protein to the surfaces, we have employed the use of a large common serum protein (Albumin, 66 kDa) with an attached fluorophore (FITC) to efficiently image and map the protein location. Comparing both natural protein adhesion/trappment and assisted crosslinking of protein to the surfaces.

An established carbodiimide (carboxyl-to-amine) crosslinker was selected as does not incorporated into the bind and therefore leaves no residue (zero-length crosslinker). Zero-length Carbodiimides providing direct conjugation of carboxylates (–COOH) with primary amines ($–NH_2$) by an amide bond (peptide bond) without incorporation into the final structure crosslink between target molecules. For targeted conjugation to occur EDC crosslinking reactions must only occur in conditions devoid of extraneous carboxyls and amines. Acidic (pH 4.5 to 5.5) MES buffer (4-morpholino-ethane-sulfonic acid) is most effective. Additionally *N*-hydroxysuccinimide (NHS) or its water-soluble analog (Sulfo-NHS) is often included in EDC coupling protocols to stabilize amine-reactive intermediate and improve efficiency[265].

The reaction occurs because EDC reacts with a carboxyl group on molecule on polymer surface (Dia.1_*left*), forming an amine-reactive *O*-acylisourea intermediate, it is this intermediate that can react with a primary amine on protein, but the efficacy of this reaction is inefficient and unreliable. If the amine-reactive *O*-acylisourea intermediate fails to react quickly with an amine, it will result in hydrolysis and regeneration of the carboxyl. If an amine molecule is present and does react it will yield a conjugate of the

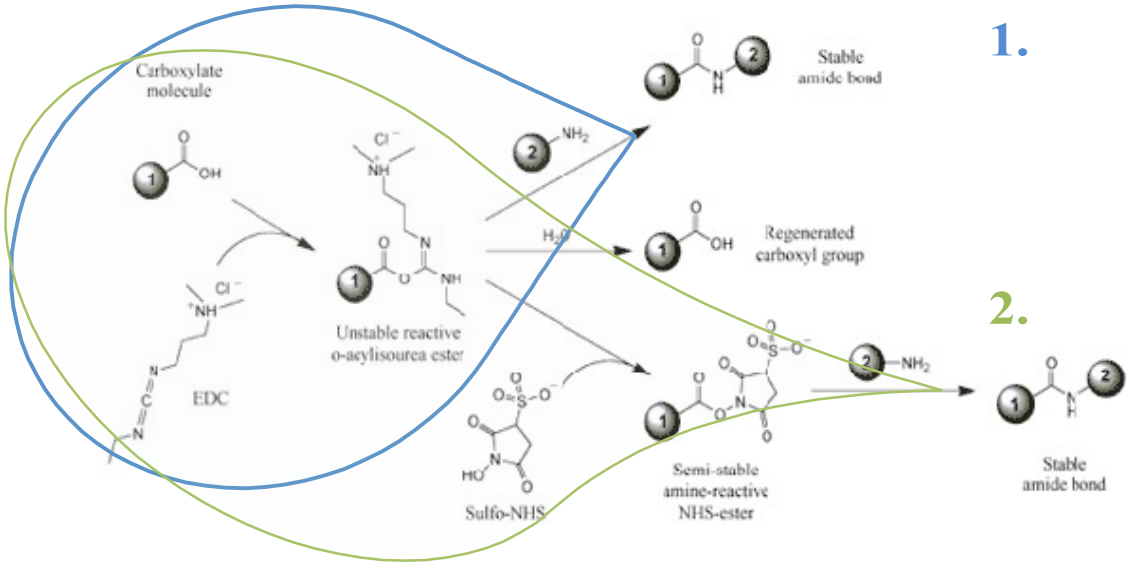

Diagram 1. Possible reaction pathways for amide-carboxyl bound by crosslinking agent EDC alone (1) and/or assisted reaction with Sulfo-NHS (2). Illustration adapted from Thermo Scientific- Pierce product information[2].

two molecules joined by a stable amide bond. This intermediate is unstable and short-lived in aqueous solution, rendering it susceptible to hydrolysis.

Improving the efficiency of EDC coupling, Sulfo-NHS (*N*-hydroxysulfosuccinimide) and its uncharged analog NHS (*N*-hydroxysuccinimide) are chemical modification reagents for converting carboxyl groups to amine-reactive Sulfo-NHS esters (Diagram 1._2). The addition of Sulfo-NHS (5 mM) stabilizes the amine-reactive intermediate by converting it to an amine-reactive Sulfo-NHS ester, thus increasing the efficiency of EDC-mediated coupling reactions.

A weak protein solution (1 mg/ml) of Al-FITC was immobilized on polymer surfaces and glass controls. Duplicate batches of panel, containing different surfaces, were preform in unison to observe variability for each crosslinking pathway, Figure 52. The secondary pathway (Diagram 1._2.) with stabilizing sulfo-NHS (Figure 52_*top*) proved to be excellent at immobilizing the protein across all surfaces include the glass control Figure 52_F & L. The EDC alone, Figure 52_*bottom*, also proved excellent at covalent immobilization of protein to surface without retention on glass surface, it also appeared to have selective retention on areas of the polymer surface when viewed at higher magnification, Figure 51.

Bioconjugation of the large albumin protein to the polymer surface is presumed to be best immobilized through EDC alone covalent bonding between one of the Proteins amino groups and the PMMA carboxyl groups more exposed near caldera.

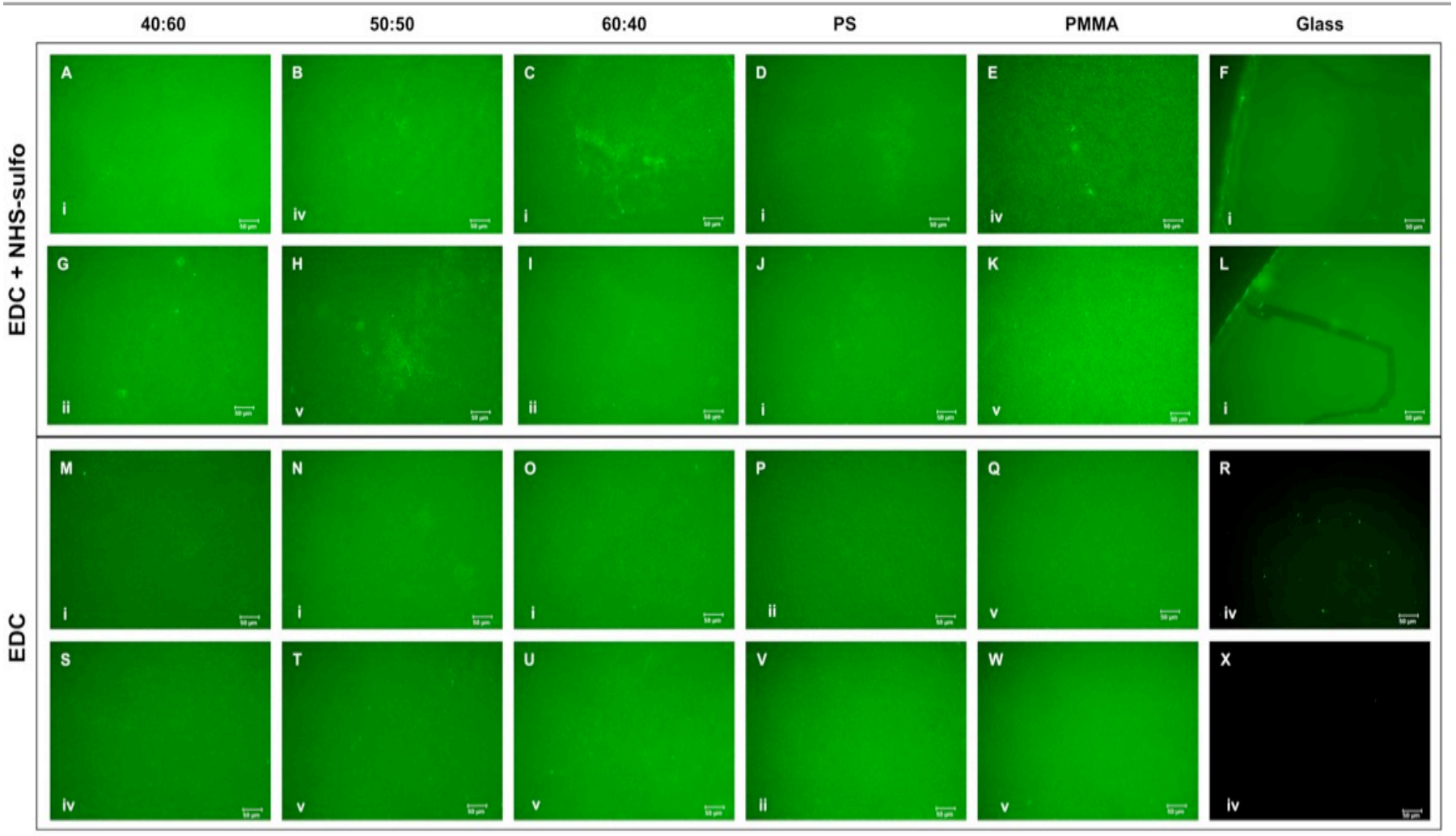

Figure 52. Complete panel of polymer surfaces and glass control surfaces evaluated in duplicate for covalent immobilisation of Al-FITC with stabilised EDC + NHS-sulfo (*top*) and EDC only crosslinking (*bottom*).

6.5.3. *Immobilized Phosphatase Enzyme – Bioactivity Retention Assay*

Basic adaptation of the histological ALP colorimetric assay used in MSC differentiation enabled evaluation and quantification of the immobilised phosphatase enzyme on the surface. The test utilised a clear liquid substrate (pNPP) that developed a coloured end produced (PNP) if enzymatic cleavage occurred, this in turn can be quantified by spectrophotometer, Figure 53. Equal substrate exposure meant the relative colour

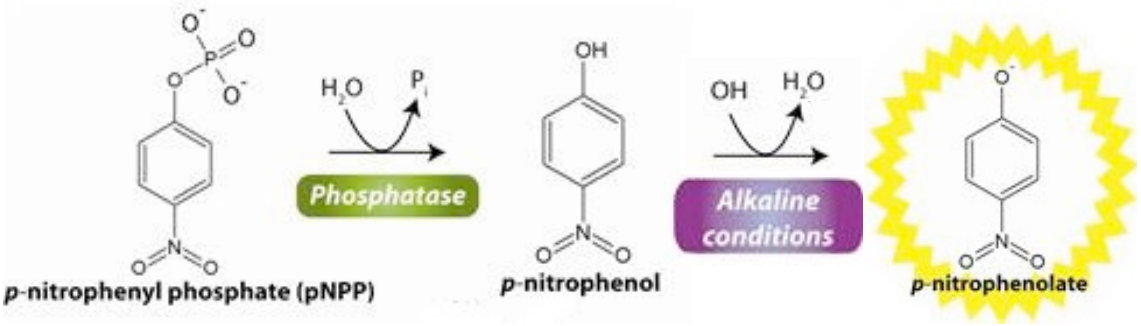

Figure 53. Schematic of an absolute chemical reaction for the alkaline phosphatase colorimetric assay.

change was comparative to the presence of phosphatase on the surface. The concentration of colour (PNP) developed was calculated using a standard curve of soluble enzyme and substrate.

Phosphatase at a concentration of 1 µg/ml (100%) was immobilised onto all test surfaces in unison and in triplicate. Reading for phosphatase activity were taken at day 1, 4, 12, and plotted out accordingly, Figure 54.

At day one time point approximately ~70% retained of immobilized factor retention was detected. The greatest drop in activity was noted at the next time point measurement -15% drop (55% preserved). Subsequent measurements dropped < 10% activity and by the end of the two week period 30% preservation of the overall immobilized factor was retained.

Observing day 1 values only (highest values for a stored cross-linked surface) greatest retention of enzyme was observed on PS amongst the two homo-polymers. When contrasted with the demixed surface we once again see an inverse relationship as 40:60, the PMMA-rich surface, and 50:50 shares the higher retention (37.35 nMol pNPP) compared to 60:40, PS-rich surface, with the lowest of the three (33.83 nMol pNPP). While the demixed surfaces decrease laterally from 40:60 to 60:40, the discrepancy between 40:60 and 50:50 is <0.00001.

The slope of the plot line is relative to the degradation of the phosphatase immobilized on the polymer surface. Plotting of the tentative data over the time course enabled extrapolation of the degradation potential, all three demixed surface retaining the phosphatase activity longer then either homo-polymer. The PS homo-polymer while having one of the highest up takes showed the most rapid decade in phosphatase activity, see appendix pg. XLIV.

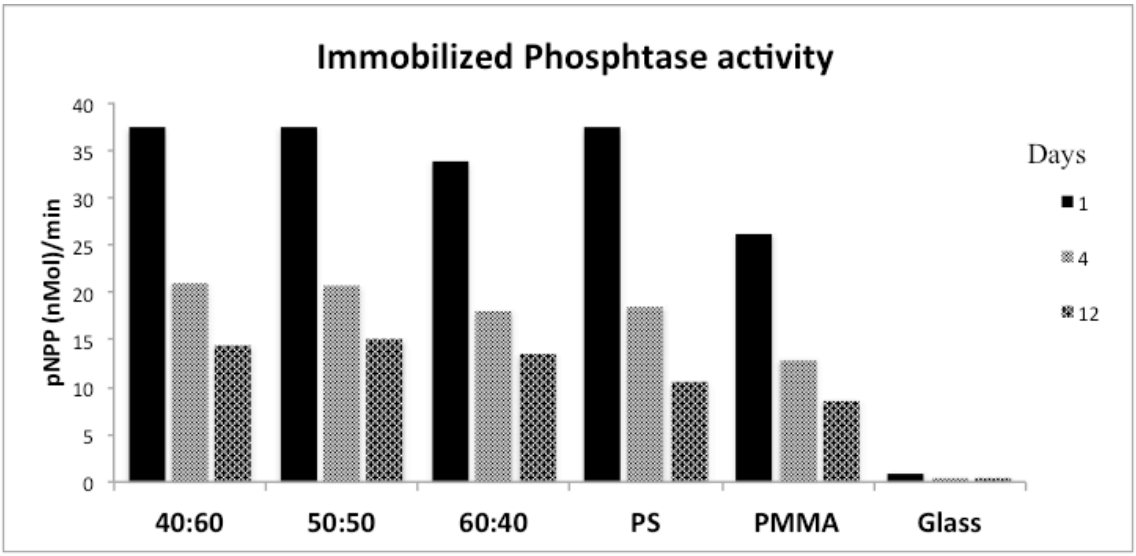

Figure 54. Graph of active immobilised phosphatase on surfaces determined by colorimetric evaluation of pNPP levels at different time point on each surface.

6.5.4. ***Immobilized Growth Factors***

6.5.4.1. Osteogenic Factor Immobilisation: BMP-2

The individual osteogenic genes assessed under all three conditions were compared together (Figure 55_ grey frame) and separately (Figure 55_1, 2&3). Expression of RUNX2 was distinctly higher on in the higher in the positive control across most surfaces except PS where expression failed to be detected. The demixed surfaces (40:60/50:50/60:40) showed a gradual step-wise decrease from PMMA-rich 40:60 down towards PS-rich 60:40, this elevated expression on 40:60 was significantly higher then its apposing surface 60:40 ($P<0.001$) and the PMMA ctrl ($P=0.05$)(Figure 55_3). In the contrasting negative control, no discernable pattern was observed on the demixed surfaces (Figure 55_1), the 50:50 surface was dominant and significantly higher then 60:40 and PS ctrl ($P\leq0.05$), while amongst the homopolymer controls PMMA showed higher expression levels over PS but not significantly. No expression was detected on the I-BMP surfaces (Figure 55_2).

Similar dominance of the positive control was observed in the overall ALP gene expression (Figure 55_grey frame) with an overwhelming expression detected on PS homopolymer that was significantly higher then all demixed surfaces ($P<0.001$)(Figure 55_3). This was not recapitulated in the I-BMP where highest levels of expression were detected on the glass surface (Figure 55_2), with little or no discrepancy between the demixed surfaces even when compared to the PS ctrl. PMMA showed slightly higher expression between the two homopolymer ctrls (Figure 55_2). This weak, low-level expression was mirrored with the negative control levels, (Figure 55_1), ALP expression appear higher on PS ctrl and on the PS-richer demixed surfaces 50:50 and 60:40 (Figure 55_1) but not significantly. Both PMMA and the PMMA-rich 40:60 surface remained low, with glass ctrl failing somewhere in-between PS heights and PMMA lows.

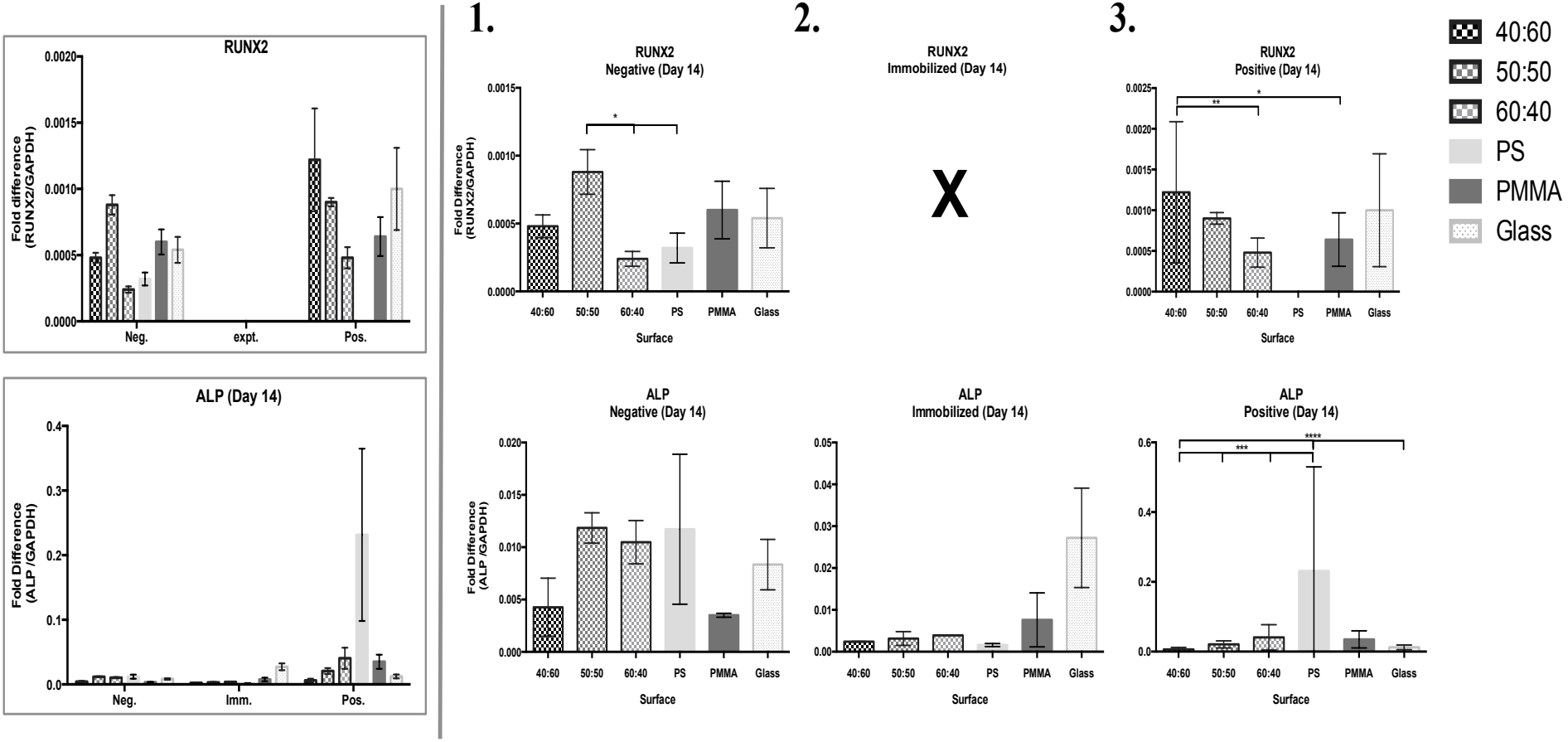

Figure 55. Quantitative real-time results for effects of immobilized bone morphogenic protien-2 (BMP2) on gene expression of osteogenic genes; RUNX2, ALP and BGLAP. Three formats of stimuli 1) Negative for BMP2, 2) immobilized BMP2 to surface, and 3) Positive soluble BMP2 in medium, were exposed to primary MSCs [N_3100] population over a 14 day period. P-values (* ≤0.05; ** ≤0.001; * ≤0.001). N=4**

6.5.4.2. Chondrogenic Factors Immobilization; TGF-β3 and KRTGN

Direct comparison of both chondro-inductive factors were displayed on same graph to assess altered trend gene expression (Figure 56_1. grey frames), with each individual factors on all the different surfaces displayed side-by-side on separate graphs (Figure 56_2&3. TGF-β and KRTGN).

The immobilised factors, I-CM, saw similar treads for the chondrogenic master regulator gene SOX9 (Figure 56_A1 grey frame) between both TGF-β and KRTGN. The PMMA surface appeared dominant for both factors with slight variation in standard error margins. Conversely weak induction was observed the PS ctrl surface for both factors and an verse relationship was once again observed on the demixed surface as in Chp. 5. The demixed surfaces (40:60/50:50/60:40) for both factors (Figure 56_A2&3) displayed a stepwise increase towards the PS-rich 60:40 and lowest expression on the PMMA-rich 40:60, this is counterintuitive to the homopolymer controls.

Similar analysis of the chondro-specific protein gene ACAN mRNA expression, but very different observations were made for each factors (Figure 56_B1 grey frame) the immobilised KRTGN appeared to have higher expression levels across all surfaces in comparison to TGF-β_I-CM. When reviewed for the individual surface, immobilised TGF-β did appear stronger on the PS and PS-rich 60:40 but large error bars makes these results hard to interpret clearly (Figure 56_B2). Opposing the ACAN expression on demixed surfaces of immobilised KRTGN displayed a characteristic step-wise trend with surfaces (Figure 56_B3), once again displaying an inverse relationship with homopolymers. PS ctrl does display a higher ACAN expression over PMMA, as with TGF-β, but it counterpart PS-rich demixed surface 60:40 is the lowest ACAN expression of the demixed surfaces. The 40:60 surface, a PMMA-rich surface hold the highest expression of ACAN.

When the soluble chondrogenic factors are analysed under the same conditions some similarities were noticed (Figure 56_I-CMS). The highest SOX9 expression was found with TGF-β and on PMMA homopolymer, but was in stark contrast to low level expression on the other surfaces. The over expression level of SOX9 on PMMA (Figure 56_C2) was significantly higher then all the other surfaces ($P<0.0001$). KRTGN displayed better all round SOX9 expression on all surfaces (Figure 56_C1 grey frame), between two homopolymer controls PS was higher but with greater std error. The demixed surfaces did follow the tread of a higher SOX9 expression on the PS-rich

60:40 surface and lower on PMMA-rich 40:60 but the discrepancy was not linear (Figure 56_C3).

The KRTGN growth factor once again stimulated greater ACAN expression across all surface above TGF-β (Figure 56_D1 grey frame). With greatest expression detected on the PS homopolymer surface (Figure 56_D3), this was significantly higher then the opposing homopolymer control PMMA ($P<0.001$) and flat glass control ($P<0.0001$). All demixed surface expression level fell in-between either of the homopolymer levels, displaying a very slight declining trend from 40:60 PMMA-rich surface down to 60:40 PS-rich surface observing the inverse relationship again. The 40:60 surface was significantly higher then both PMMA ($P<0.05$) and glass ($P<0.01$) surfaces but 50:50 was only significantly higher then glass ($P<0.01$) and 60:40 significantly higher then PMMA ($P<0.01$).

Under TGF-β stimulation the PS control maintained a higher level over PMMA control but this was relatively low and on par with glass (Figure 56_D2). The demixed surfaces followed a non-linear ascending trend from 40:60 to 60:40 (Figure 56_D2), in keeping with homopolymer controls. But the glass ctrl was only significantly higher then 40:60 demixed surface ($P<0.05$) and the PS ctrl was significantly higher then both 40:60 and 50:50 demixed surfaces ($P<0.05$).

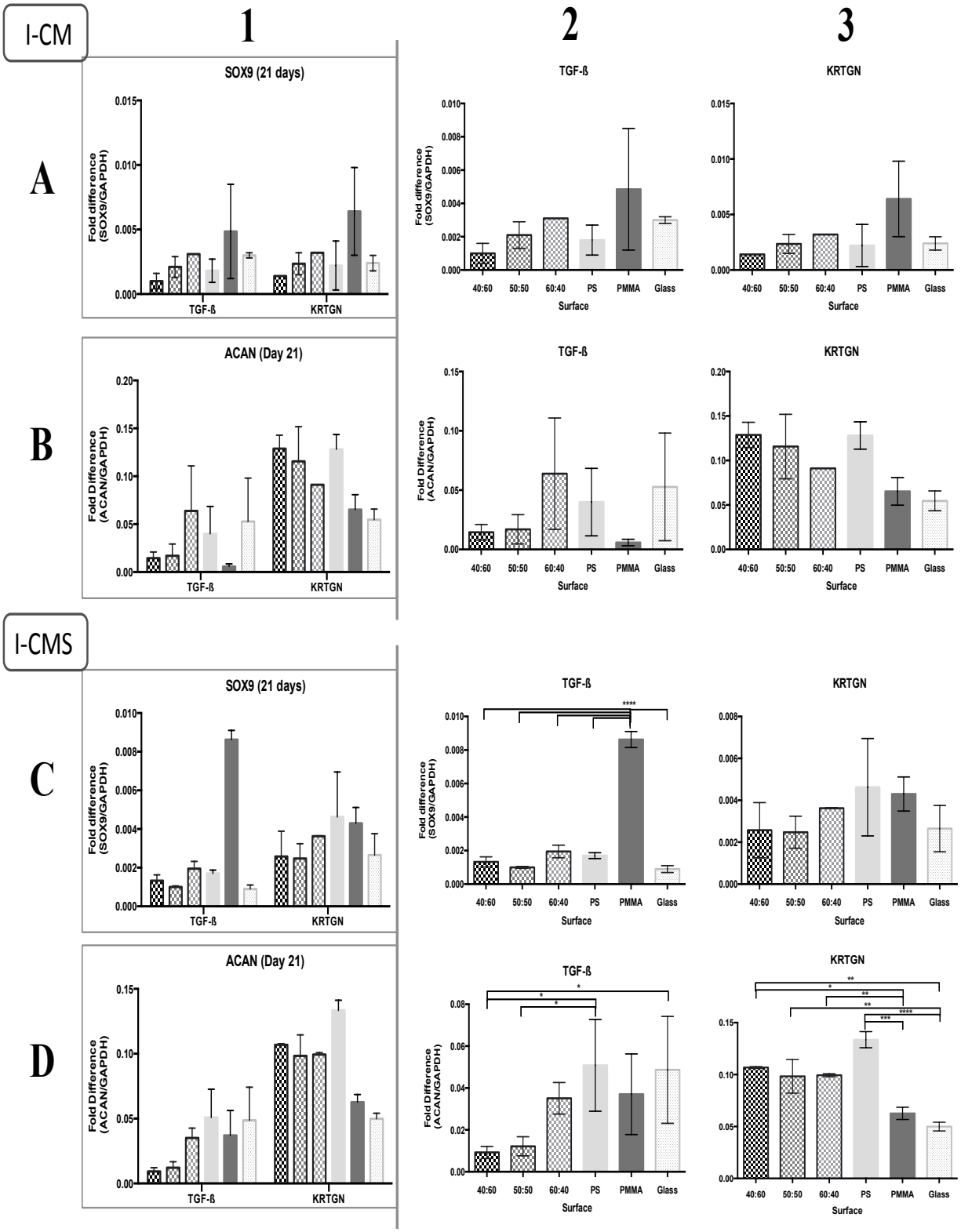

Figure 56. Quantitative real-time results for effects of chondrogenic immobilized transforming growth factor beta (TGF-*ß*) and kartogenin (KRTGN) on gene expression of chondrogenic genes; SOX9 and ACAN (*grey frames*). Divided into two formats immobilized chondro-inductive medium (I-CM)[N=2] and soluble chondrogenic medium (I-CMS)[N=4], were established on panel of polymer surfaces and exposed to 500,000 hTERT MSCs [Y201] per surface over a 21 day period. P-values (* ≤0.05; ** ≤0.01; * ≤0.001).**

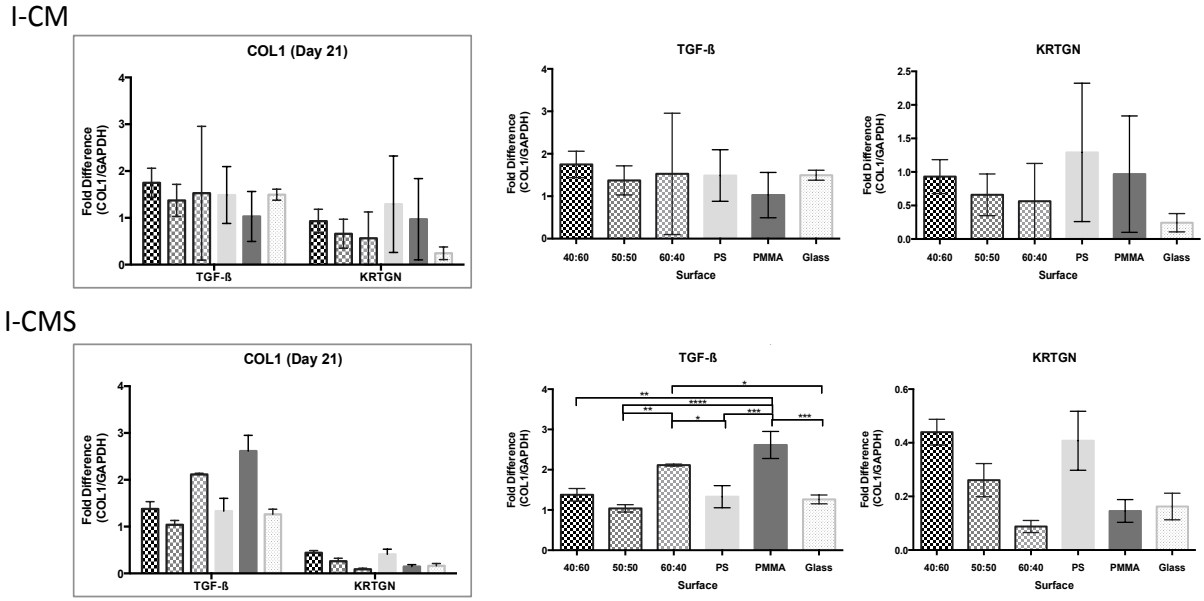

Figure 57. Continued quantitative real-time results for effects of immobilized and soluble Chondrogenic factors; transforming growth factor beta (TGF-*ß*) and kartogenin (KRTGN) on the gene expression of COL1. Comparison of two factors together (*grey frame*) and separately (TGF-*ß* & KRTGN). Both formats chondro-inductive medium (I-CM) and soluble chondrogenic medium (I-CMS), were investigated on panel of polymer surfaces and exposed to 500,000 hTERT MSCs [Y201] per surface over a 21 day period. P-values (* ≤0.05; ** ≤0.01; * ≤0.001).**

While collagen, type 2 (COL2) gene expression was investigated for chondrogenesis, not detectable levels were found and analysis primers were validated with known samples and primary isolates of human articular cartilage (HAC). This is maybe due to the hTERT MSC cell used and is noted in general discussion. Detection of COL1 was detected and in relatively large quantities (in the magnitude of ~1/2 fold differences), across all surfaces. Within the immobilised I-CM studies COL1 appeared higher in TGF-ß surfaces (Figure 57_I-CM) with no discernable trend observed; PS ctrl was higher then opposing PMMA ctrl but not significantly (Figure 57_I-CM TGF-*ß*). With immobilised KRGN stimulus PS surface also displayed highest COL1 expression but with very high std error. The PMMA homopolymer was lower then PS but still higher then all demixed polymer surfaces (Figure 57_I-CM KRTGN).

The soluble positive control for both stimuli had large discrepancy, COL1 expression was readily detected by TGF-*ß* stimulus but very low levels were detected by KRTGN (Figure 57_I-CMS grey frame). The KRTGN stimulus displayed a familiar trend of highest expression observed on PS homopolymer ctrl and opposing low level on PMMA with the demixed surfaces having decreasing inversed relationship going from PMMA-rich 40:60 step-wise descending to PS-rich 60:40 (Figure 57_I-CMS KRTGN). This was not correspondingly observed with the TGF-*ß* stimulus (Figure 57_I-CMS TGF-*ß*), where a complex of different relationships are observed as not trend is found between demixed surface significant difference between 50:50 and 60:40 ($P<0.01$) but

not between 60:40 and 40:60. Dominance of PMMA homopolymer ctrl was significantly higher then both glass and PS ctrls ($P<0.001$) but only with 40:60 ($P<0.01$) and 50:50 ($P<0.0001$) demixed surfaces, (Figure 57_I-CMS TGF-ß).

6.5.5. *Adaptation of Surface Fabrication using new Polymer Combination*

Polycaprolactone (PCL) is a semi-crystalline linear polymer comprised of cyclic monomer that is relatively cheap due to low production cost and is a readily obtained by-product from the petroleum industry. The raw material is easily converted by ring-opening polymerization of ε-caprolactone in presence of tin octoate catalyst[266].
One of a number of biodegradable polyesters [Polylactide (PLA), Poly(lactide-co-glycolide) (PLGA)] they are of particular interest due to their diversity and synthetic versatility[267]. PCL has a low glass transition (Tg) temperature at -60 °C, and its melting point is 60 – 65 °C. It is a semi-rigid material (modulus 23 MPa at room temperature) and excellent elongation properties (breaks at >700%)[267], commonly used as a soft block spacer in rigid structures added to resins in order to enhance properties such as impact resistance. Quite recently PCL has been successfully incorporated with another advantageous materials, grapheme, and this show promising results in application for tissue engineering[268].
PCL is easily biodegraded by enzymes and fungi with adaptable degradation rates, through several copolymers with lactide or glycolide[269]. It is commercially available under various trade names CAPA® (Solvay, Belgium), Tone® (Union Carbide, USA) or Celgreen® (from Daicel, Japan) and FDA approved as a drug delivery system[270].

Adaptation of topographies generated on polymer surfaces using the humidified spin coating process, was adapted by substitution of one homopolymer (PS) for a new polymer PCL. Unfortunately a straight substitution was not possible due to large discrepancy in molecular weight between PMMA (Mw 550,000) and PCL (Mw – 80,000) giving a fold difference of 6.875. To compensate for this difference altered percentage concentration of each homopolymer solutions were made up; 3%wt PMMA and 20%wt PCL.
Three demixed solutions of equally spaced out ratios were investigated [25:75 / 50:50 / 75:25] including both homopolymers. All polymer solutions were processed in identically to previous PS:PMMA surfaces.

Surfaces were imaged using brightfield (BF) and scanning electron (SEM) microscopy, Figure 58. On the whole polymer surface generally resemble those of PS:PMMA blends, with a few notable differences. In the demixed surfaces 25:75 PMMA-rich surface very large pore structures are seen, Figure 58_BF, and display a small resemblance to the distinctive caldera 'trails' observed before, Figure 58_SEM. As the concentration of homopolymer shifts to the opposing polymer 75:25 the large pores dissipate and a more homogeneous surface is observed, with an almost hexagonal shape to the BFP pores arranged into a 'honey-comb'-like pattern, Figure 58_75:25. The clear contrast of these two elements are obvious in the individual homopolymer, distinct circular BFP pores observed on PMMA surface while this new hexagonal BFP pore as the characteristically majority of the PCL surface, Figure 58.

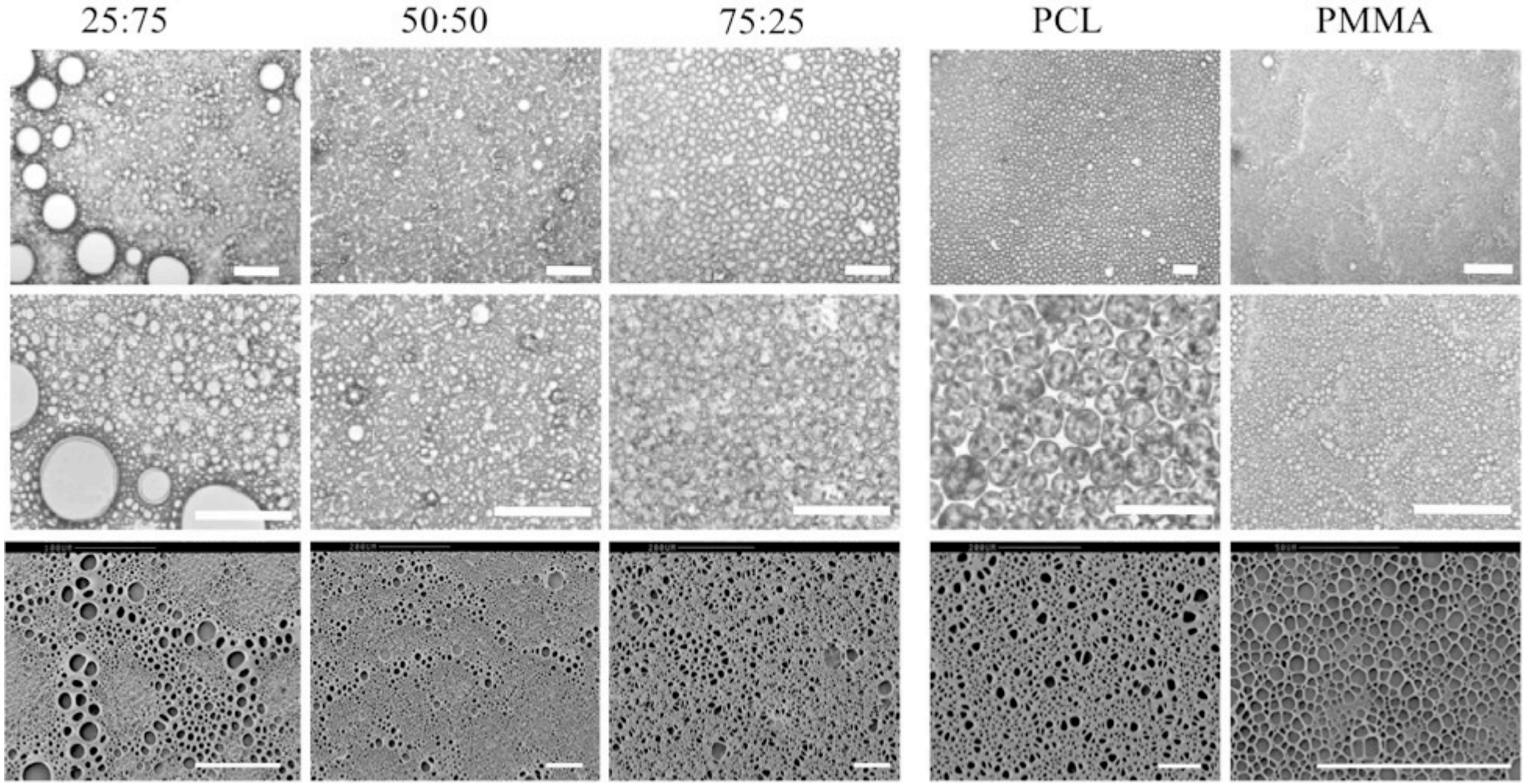

Figure 58. Microscope images of PCL:PMMA [20%:3% v/v] demixed surfaces by brightfield microscopy (*top & middle*) and high magnification scanning electron microscopy (*bottom*). Scale bar – 100 µm

6.5.6. *Mapping of Immobilised Fluorescent Protein on the Surface Al-FITC*

Similar protein retention is observe on new polymer surfaces as with PS:PMMA blends. A limited amount of natural protein retention was observed on the surfaces _top row, with distinctly better retention observed on the PMMA homopolymer and less on the PCL homopolymer. No retention of protein was observed on glass control surfaces even with EDC crosslinker small sporadic spots were observed but inconsistent and negligible. This natural retention on the PMMA surface was once again focused around caldera of BFP pores and similarly but to a lesser extent on the PCL, suggesting physical retention by polymer structure and possibly enhanced isoelectric retention by PMMA. The naturally bound protein on demixed surfaces show inverse retention to the polymer controls, the PMMA-rich 25:75 shows low levels retained while increased amount on the opposing 75:25 surface Figure 59_top left. Similar observations were seen on the crosslinker assisted demixed surfaces but PMMA control with crosslinker still maintains higher levels then PCL control, this suggests possibility of divergent bind sites being presentation at the caldera opening.

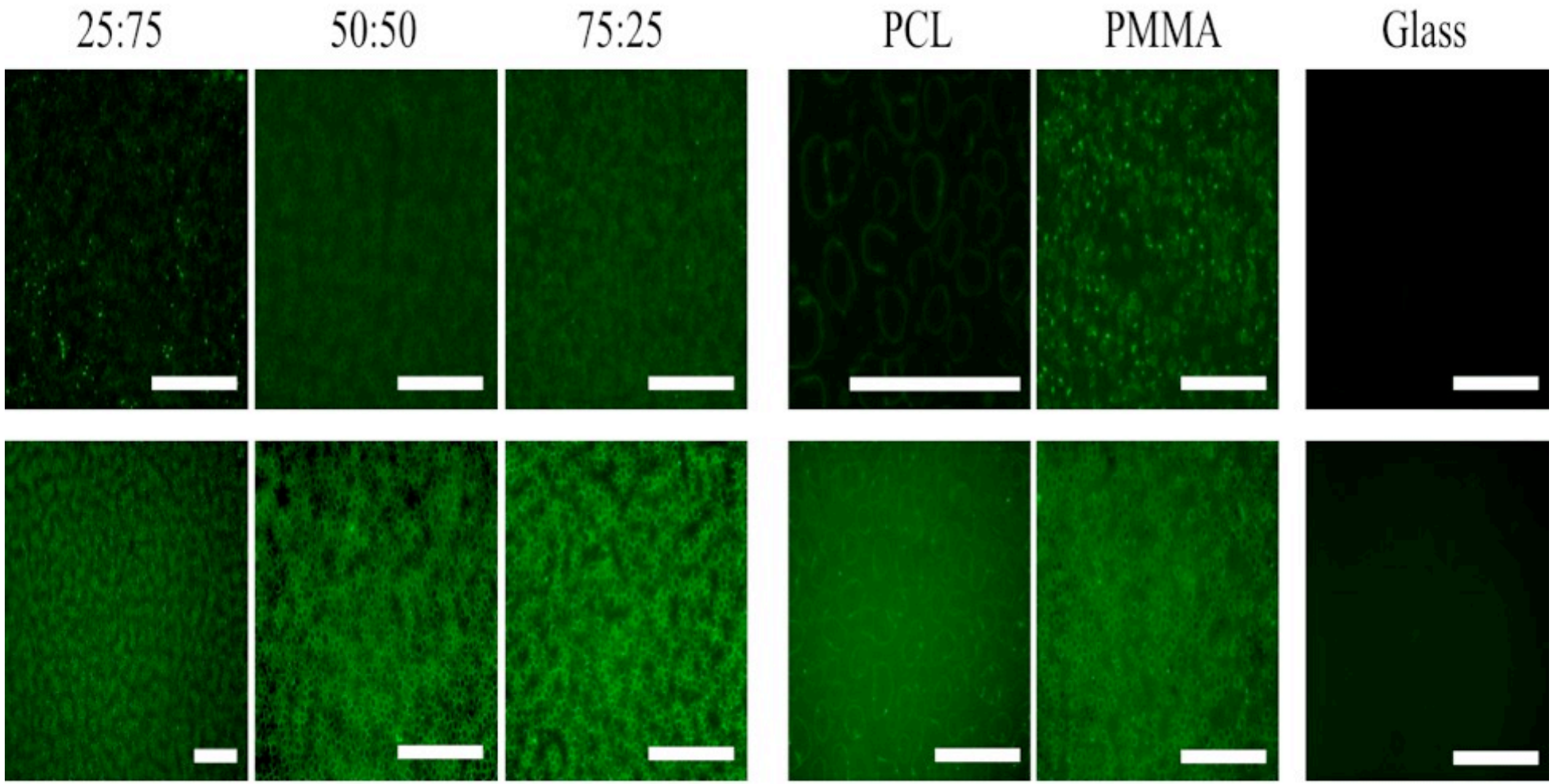

Figure 59. Fluorescent microscopy images of PCL:PMMA [20%:3% v/v] demixed surfaces with immobilised Al-FITC protein retained naturally (*top row*) and EDC assisted (*bottom row*). Scale bar – 100 µm

6.6. Discussion

In a solution the diffusible forms of growth factors are the established and gold standard for *in vitro* assays for driving cellular change, this was confirmed here in the differentiation experiments of Chp. 4, but *in vivo* most growth factors function at an interfaces, bound to other ECM components or incorporated into membrane complexes[271]. A natural apprehension arises if the cells can access and obtain bioactivity from the surface-immobilized protein, but this concern is unfounded, it is known that even a relatively basic tethering of growth factors to a biomaterial matrix can elicit a desired biological response[272,273]. In some cases bound factors, and in some cases less growth factor[274], out preformed identical diffused factors in biological stimulation[206,274,275].

The natural retention of a large protein like albumin (Al-FITC), without crosslinker assistance, was noticeably better on the demixed surfaces compared to the individual polymer components separately. This is difficult to interpret as the elevated level of retention on the 50:50 surfaces, a 1:1 ratio mix of both homo-polymers, have accentually identical chemical composition as homo-polymers and should therefore display similar protein retention if isoelectric binding is the method of action. Similarly with the steric effects, hydrophilicity of the individual control polymers should reflect similarities in the 1:1 blend, but this was not observed.

The only discernable difference we know for sure between the control surfaces and their equal parts demixed counterpart, was the increase physical height differentials (observed by AFM). It stands to reason that polymer surfaces with large, raised BFP pores can provide addition physical adhesion and tethering sites, over deflated low-lying polymer BFP pores and even more to a flat surface. It was there for suspected that the intensified green bands observed around BFP pores on 50:50 are not necessarily improved binding of Al-FITC but similar proteins retention on a taller BFP pore. The more numerous loosely bound proteins along the inner wall of the demixed BFP pores and the restricted aerial view from the vertical fluorescent microscopy, makes images appear to have superior retention but in fact was the same retention with a limitation to the perspective of observation. This observation was collaborated by finding of confocal microscopy of the same surfaces.

Covalent retention of the Al-FITC protein by chemical crosslinking, we discovered a favourable unassisted zero-length crosslinking (EDC alone) to be sufficient enough alone to permanently bind a protein to the polymer surface. This form of covalent retention was shown to retain biological activity of a bound enzyme over a prolonged period of time, immobilized phosphatase, when stored at 4ºC could successfully and effectively convert substrate to end product, repeatedly if incubated at 37ºC.
This identified simplistic chemistry that was safe, non-inhibiting and rapid to covalent bind organic material to the synthetic surface. This is highly beneficial for product scale-up potential, identifying a rapid downstream process with several tuneable adaptations[114,206].

Implementing this premise to a fate-directing MSCs influence by immobilization of specific growth factors, was not this simple. The osteogenic differentiation of MSCs was not as straightforward as the addition of BMP-2 to the culture. During the conversion of MSCs to osteoblasts using soluble factors, several diffusible stilumi were required (e.g. dexamethasone). This may explain the low levels of induction and obscure observations made.
The lack of detection of RUNX2 for I-BMP and the stromal nature of the cells used brings into question the reliability of the subsequent ALP and BGLAP detection. As RUNX2 is a key mediator in the osteogenic differentiation of MSCs it cannot therefore be demine an osteoinductive process. In determining if the absorbance of the BMP-2 molecule to the surface hinderers the osteogenic potential or if entire molecule absorbance is required by cells cannot be deciphered. One complicating hindrance lies in the post-fabrication sterilisation, as it was unknown what effect UV exposure had on the immobilized BMP-2 protein, weather it was denatured or even modified.
Also as BMP-2 is known to degrade in solution (i.e. in the media) so fresh batches were made each time medium was changed, no addition BMP-2 was introduced to the I-BMP surfaces so the relative bioactive effect cannot be expected to be on par with the positive control.

During the evaluation of chondrogenic factor immobilization to the panel of surfaces, the experimental setup was split into only two parts, negating the negative control group previous observed within I-BMP. As these surfaces were previously shown to be slightly chondro-inducive, their comparison with immobilized factors would not be a true representation of a negative control.

On the I-CM samples an inverse relationship between the individual polymer constituents (homopolymer controls) and the demixed polymer blends surface had opposing equivalent expression for both SOX9 and ACAN. This may indication that the chemical constituency of the surface may having less on an influence on the cell activity and more on the altered cellular adhesion due to topographical features. Or that the unique fabrication method of demixed surfaces, has extenuated the presentable chemical motifs of the raise polymer (PMMA) around the caldera.

Also an aim of the experiment was to evaluate the affect of an immobilized factors ability to stimulate over its traditional soluble stimulus. Comparing the relative fold change in chondro-specific genes mRNA expression when induced by the known stimuli, TGF-*β* and KRTGN, were very little difference was observed between both immobilised and soluble conformations of factors. This has positive implications for pre-fabrication of scaffold with pre-loaded growth factors, in an off-the-shelf style device[275].

Both chondrogenic factors, TGF-*β* and KRTGN, induced amicably with slight differences between the activated genetic components; regulatory gene SOX9 and lineage specific protein aggrecan gene. KRTGN displayed strongest ACAN expression between the two factors and appear to have a marginally higher expression when immobilised over its free-floating counterpart. The greatest ACAN expression due to KRTGN was noted on the PS homopolymer in both I-CM and I-CMS conformations, suggesting that the 60:40 surface should have the greatest expression of the demixed surfaces, but yet it was the lowest and highest expression was noted on the 40:60 ‘PMMA-rich’ demixed surface. This cannot be explained easily from these results but maybe due to the previously stated, altered presentation of binding groups available at the raised demixed surface.

The observed discrepancy between the two different stimuli, TGF-*β* and KRGN, did raise one surprising finding from these studies is the elevated chondro-ECM stimulation of KRTGN in the production of ACAN and a lower RNA levels of COL1 expression, collagen type I being synonymous with scar tissue. This should be considered in the progression of immobilised growth factors on scaffolds, particularly in the area of chondrogenic regeneration.

Adaptability of the fabrication technique appears to be interchangeable, exploratory finding of substituting PCL for PS appeared to generate thin films with similar topographical features but did have vaguely different patterns. The alternate BFP pores formed on PCL homopolymer surface are considered oblong struts of dense polymer chains. These frame the BFP pore site (Figure 60) as the columns of high tensile strength can resist the attacking displacement forces of the water droplet. This maybe a hydrophobic characteristic of the PCL monomer (this was not observed in the lab on flat PCL surfaces without BFP. But was not tested by water contact angle so cannot be confirmed) or a collective physical resistance due to the densely compact polymer unable to provide space to the water droplets. A personal inclination would be for the latter given the abundance and frequency of pores (i.e. water droplet during BFP) found on the PCL ctrl (Figure 60).

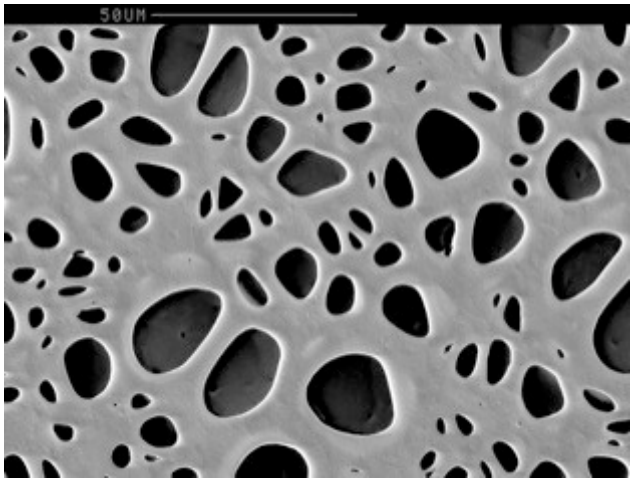

Figure 60. SEM image of spin coated PCL homopolymer under humid conditions (>80%) on glass substrate

6.7. Summary

- The addition of topographical features by induced BFP increased the surface area of the polymer surface, but also provided additional physical structures for the natural retention of proteins.
- Increase protein retention was mapped using Al-FITC and found to be most concentrated around the elevated caldera structures.
- Restrictive crosslinking by EDC covalently immobilized the protein to the surface, this increase the total protein concentration retention but was still concentrated around caldera. Potential due to more available carboxyl group exposed a caldera.
- Retained biological activity of an enzyme immobilized by identical covalent crosslinking as protein to the polymer surfaces and was maintained for extended time periods.
- Immobilization of growth factors for osteo-induction (BMP-2) and chondro-induction (TGF-β and KRTGN), showed tentative lineage induction but lacked convincing differentiation attributes.
- The topographical surface fabrication method was shown to be adaptable for different polymer combinations and showed similar induce topographies using this technique.

CHAPTER 7. GENERAL DISCUSSION AND FUTURE STUDIES

7.1. Final Discussion

This thesis sets out to investigate the influences of well characterised polymer demixed surfaces with distinct topography on mesenchymal stromal cell adherence, morphology, gene expression and differentiation. A characterised source of adult MSCs, were isolated from bone tissue which showed capabilities of multipotent lineage differentiation and displayed the international recognised cell surface markers for mesenchymal stem cells. These cells were suitable for cell type assessment of the effects of the fabricated surfaces on cell activity. Further more, the incorporation of specific proteins and/or growth factors, immobilized to the polymer surface(s), would be accessed in terms of influencing cell activity.

Several well known fabrication approaches were adopted to enable polymer surfaces to be reproducibly created; Spin coating was refined to incorporate and include a humid environment to induce breath figure patterns[276] on demixed polymer surface during material fabrication[178]. This approach produced unique surface topographies for further investigation.

Characterisation of these surfaces by atomic force microscopy revealed distinct raised islands of one material interconnected with low-lying plateaus of the other material. This phase separation is due to the immiscible nature of both demixed polymers [PS & PMMA], a phenomenon previously described[3,151,176-179,181]. These phase separated areas were chemically independent and when observed by XPS followed a distinct trend in relation to the ratio of polymer blends used amongst the demixed surfaces, compared to homo-polymer surfaces. Additionally, the BFPs on these surfaces created micro- and nano- topographical features within each discrete area, islands and plateaus, a response of each individual polymer to the attack of water molecules at the surfaces. The phase separated areas responded differently to the water due to the chemically distinct composition of each polymer and induced different features to be formed. More astonishingly was the extraordinary height elevation in BFP topographical features amongst demixed polymer surfaces of close blend ratios [40:60 / 60:40] as opposed to individual homo-polymers reaction to BFP. The elevated features observed in each demixed surface displayed distinct physical features, circular in nature due to the water droplet shape, and their structure albeit on a micro-scale similar to the raised lip or edge of a volcano i.e. caldera. It was these prominent structures, displayed across the surfaces in a disorganised distribution, which had potential to alter cellular adhesion and function.

Introduction of cells to the surface(s) caused a definite alteration to cell morphology. Previous observations have been published based on designed[128,129,132,277], organised[152,278-280] or purposely disorganised topographies[61,281] illustrating the potential of surfaces to regulate cell activity. Cells on the surfaces fabricated in the work presented here showed a prevalent alteration in adhesion profile and cytoskeletal organisation, irrespective of cell source. It was noted throughout the study that the use of primary cells resulted in large variation, associated with patient-to-patient variability, with heterogeneous cell morphologies observed during culture expansion. Stability of the fibroblast-like morphology of the TERT transformed MSCs, helped to clarify the observed alterations to cell morphology in response to different surfaces. During investigation it was noted that cells concentrated vinculin positive, focal adhesion plaques around the caldera. This was interesting, as other studies have identified that the organisation and clustering of focal adhesion plaques have a direct relationship with mechanotransduction pathways[123,282].

The alteration of cell adhesion to surface, whether through physical contact alone or in combination with the influences of the chemical distinct areas, alters individual cell cytoskeletal structure and is therefore likely to alter intra-cellular tension. Formation of contact plaques by cells at the raised caldera sites forces them to extend filopodia over greater distances, in preference to the low-lying plateaus. This 'bridging' of cell body across void, was tuneable to the distance generated between caldera decorating the surface. Measuring the caldera distribution patterns identified slight differences in the size, organization and distribution pattern of caldera on the different demixed surfaces. The numerous, small caldera observed on a PMMA surface translated to similar observations on PMMA-rich 40:60 with the size, height and distribution increasing towards PS-rich 60:40. This provided means to alter cellular morphology, through careful choice of the fabrication process. Additionally, the increased organisation and associated elevated cellular cytoskeletal tension observed in cells on these type of surfaces has previously been described as a mechanism to encourage multipotent cells towards differentiation[136,155].

Long-term exposure of a MSC population to the surface(s) altered gene expression with elevated phenotypic changes towards the chondrogenic lineage. The greatest expression was observed on 60:40 surfaces, the same surface that exhibited tall caldera heights at the greatest degree of distribution observed amongst all of the demixed surfaces. This suggests an association of altered cytoskeletal organisation and

cell morphology (hypertrophy), due to disrupted cell:surface adhesion leads to stronger cell:cell interaction and an aggregated development. At high cell densities individual cell morphologies lead to the collective cell population having an altered organisation and orientation, clustering into mirco-mass aggregates. The cell aggregates appeared to follow a distinctive chondrogenic condensation development pattern[245,283], whether cell-surface interactions meant that cell-cell interactions were stronger and therefore predominated, that grew and built ECM vertically up and away from the textured polymer surface. No definitive conclusion can be drawn from these specific results as to why cells reacted in this fashion, but it has identified as an area worth exploring further.

A number of studies have shown that the immobilisation of chemical and biomolecular mediators, into or onto a scaffold, can direct cellular growth to form specific tissue[83,85,90,109,135,284]. Several of these studies have shown commercial success and paved the way for single stage intervention, 'one-step', multifactorial implants. A similar premise was applied to these unique surfaces generated in this thesis, immobilization of common ECM proteins and lineage specific growth factors to the polymer surface for directed effect on cell activity. Covalent immobilization of albumin-FITC to the surface confirmed the robust anchorage of a large protein to the synthetic surface but also identified an added benefit of using polymer demixing. The bi-phasic surface enabled differential crosslinking restrictively immobilizing the protein to isolated areas. Characterisation of the surfaces mapped the locations of protein distribution and identified that the isolated areas of protein retention heavily coincided with caldera location. This approach is therefore a potential method for restrictively immobilizing selective adherence biomolecules or motifs (e.g. fibronectin or RGD-motifs[285]), this approach could be applied to other ligands identified in other studies[284].

Tailored surfaces with immobilised growth factors did not result in significant changes in MSC activity in the single study presented here but some alterations were noted. One conclusion could be that the topographical effects of the surfaces far outweigh any of the responses to the immobilised biomolecules. Similarly, the immobilised factors may have limited biological activity when attached to the surfaces and would only have an effect when released and available to bind to their cognate receptors. The tailored surfaces must be objectively analysed further, as they also only contained single factors [BMP-2, TGF-β, KRTGN], compared to the multi-factorial soluble differentiation media. In hindsight, further optimisation of each individual factor necessary for lineage differentiation should be accessed, followed by combinations of factors to determine the lowest common denominators necessary to induce positive effect.

The identified selective immobilization of ligands to specific areas of a surface may be beneficial for implant applications, restrictively isolating and promoting the retention of particular cell types[206]. Additionally, an alternate crosslinking method to the opposing polymer areas could immobilize chemoattractant stimuli (e.g. SDF-1 known to attract motile CXCR4 + MSCs[286]) and possibly lineage specific growth factors[274,275]. Biodegradable polymers like PLGA and PCL could give way to subcutaneous layers of different factors/cues or a permanent textured layer of implant. The known degradation of immobilized ligand's bioactivity would give way to the longer-term textured surface, which in itself can be directive and lineage promoting, and not simply an inert surface. Pro-mechanotransduction surfaces may also help identify novel possible avenues for off-the-shelf product development in medical implant devices [114,206,275]. These characteristics may enhance the implant biological interface, long-term integration and possibly repair.

Alternatively, the adaptation of a manufacturing process currently in use for stabilised medical devices could be altered to recreate these textured patterns on the surface of implants. The identified distinct, raised topographies could be added to surfaces directly; print embossing, laser etching, etc. or indirectly; through addition of humidified chambers during or after green scaffold fabrication. Irrespective of the method used revision of medical implants need to cater for the device function and biological application. Composition of the entire scaffold from material, design, architecture and even the surface finish should be and can be utilized for an enhanced biological response and formation of repair tissue.

7.2. Future Directions

7.2.1. *Three-Dimensional Printing Adaptation and Incorporation*

Investigating adaptation of these principles into 3D printing; a 3D printer nozzle extrudes (demixed polymer blend could provide phase separated islands for distinct chemical areas) onto a suitable non-adhesive table platform (Teflon). The entire construction platform could be encased by a balloon-like humidity chamber, where positive pressure of a saturated inert gas with water vapour, could induce breath figure patterns on the extruded polymer(s) before polymerisation (e.g. nitrogen containing steam of ultra-pure water).

Böker *et al.* (2004) show an optimised functional group organisation of nanoparticles at the polymer surface interface after humid nitrogen treatment, this enhanced surface modification increases the target immobilisation sites on the implant surface[287].

7.2.2. *Determining the True Meaning from* **in vitro** *Conditions: for Improved Structural Environments for* **in vitro** *Experimentation*

Discovery of adult multipotent stromal cells and their regulation through growth factor-mediated stimuli was fundamental in uncovering their regenerative ability. But these affects are observed under abnormal conditions *in vitro*.

Take the isolation process of MSCs; mechanically shearing separates cells from the native tissue and selects for adherent cells in a nutrient rich medium. What role does each cell sub-population play in this dynamic niche? Do non-adherent cells influence the MSCs or even maintain undifferentiated homoeostasis? Can culturing progenitor cells in nutrient abundant medium have simultaneously propagation, differentiation and repair pathways? What if tissue repair is a multicellular repair process? Studies that co-culture of these cells under different stimulus conditions (e.g. with immune cells while activated[288]) would better evaluate natural cellular response in the body and help develop better *in vitro* evaluation techniques? Developments of experimental conditions are necessary for the *in vitro* environment to better reflect the native *in vivo* conditions for enhanced research.

7.2.3. ***Regulation of Immobilised Surface Dosage***

For covalently cross-linked growth factors the method of action and exposure to cells is mainly restricted to the surface due to immobilization. Due to this, comparison with soluble factors in medium, the standard differentiation protocol, is extremely difficult. Experiments would be needed to access the relative dosage required to induce the same effects as standard differentiation protocol.

7.2.4. ***Investigate Cell signalling pathways***

The effects of cell shape on cellular signalling appear to extend well beyond adhesion signalling alone [208,289]. Direct comparison of cell and nuclear shape in bone marrow MSCs are implicated as mediators of gene expression, where altered cytoskeletal morphology with musculoskeletal changes can mechanoregulate the expression of transcripts and proteins. McBride and Knothe-Tate showed that spherical nuclear shape was associated with elevated chondrogenesis[137,290].

A study by Biggs *et al.* (2009), illustrated the influence of altered intercellular F-actin organisation, cellular tension and cell architecture through the Rho (ROCK) pathways and MAPK signalling pathways[217]. Future studies would asses the role of these pathways in osteo and chondrogenesis associated with these demixed polymer surfaces.

Investigating the cell-cell interactions of MSCs on the polymer surfaces would give greater insight into the signalling pathways simulated and the overall mechanisms of tissue development. Determining which hemichannel functions are active and beneficial during chondroprogenitor organization may allow this information to be incorporated into scaffold design with specific strategies to favour connexin activity. Gap junctions, like connexin-43 have a role influencing control on osteoblast behaviour and differentiation[132], and has also been identified in MSC differentiation towards the chondroprogenitor lineage which is lost when connexin activity is blocked [291].

CHAPTER 8. CONCLUSION

8.1 Conclusions

In conclusion, it is well understood that cells respond to spatial and temporal cues in their physical environment, but the challenge remains to use this commercially to create biomaterials better suited to tissue repair and replacement. The ever expanding knowledge base for stem cells has grown vastly but for the subsequent industries to capitalise on the powerful potential of these cells as new therapies, it is important to understand the mechanisms that mediate MSC interactions with biomaterial surfaces to promote the required biological responses. The challenge is to design a polymer surface with a suitable topography that can not only alter cell morphology but also mediate inherent properties to induce physiological response for functional tissue regeneration. Use of polymer materials offer potential for incorporation, adsorption and sequestering of signalling molecules (such as growth factors) at the organic/in-organic interface for enhanced integration.

Surface chemistry and stiffness cannot be underestimated in terms of their significance but the topographical influences are shown here as key to cell adhesion and activity. Surface's with a large contact area provides an abundance of adhesion points for cell adhesion and these cells are found to display typical cellular focal plaque dispersion with predictable morphology and growth. But if cells are presented with asymmetrical, sparse and dispersed adhesion points, an altered cellular morphology is observed with ensuing phenotypic changes. When the altered adhesion environment of the 60:40 surfaces was presented to a population of MSCs under basal culture, the conditions proved favourable for chondrogenic differentiation. No universal mechanism can be confirmed for this physiochemical induction but a repeated trend of osteogenic down regulation and chondrogenic up regulation was observed. While no definitive conclusion can be made for the mechanism underling these observations, altered cell adhesion, cytoskeletal tension, cell aggregation and micro-mass condensation, echo mechanotransduction explanations reported in the literature.

The objective here was to investigate the potential to improve implant osteochondral integration as well as mediate functional tissue regeneration. While the scope of this research can potentially influence implant device design in the future, the more immediate benefit to be gained is the applications as an important development tool, that may provide insights into the communicative language of progenitor cells and their environment, to elucidate the mechanisms for regulating cell fate by distinct material properties in a predictable and controllable way.

In conclusion, the data presented in this thesis illustrates:

- Development of an adjustable technique to produce distinct polymer topographies
- Characterisation of novel surface topographies by defining features and attributes
- That bi-phasic surfaces displayed restrictive retention of proteins in a decorative manner to favourable chemistries and topographical features of opposing polymers
- Demixed polymer topographies directly influence cell morphology, adhesion and gene expression *in vitro*
- Surfaces can differentially influence cell adhesion, promoting cell-cell interaction and clustering
- Elevated cytoskeletal bridging between caldera on 60:40 surfaces correlated with increased chondrogenic gene expression
- Phenotypic observations of MSCs undergoing chondrogenesis on these surfaces appear to stack on top of each other building vertically away from the surface
- Surfaces don't hinder MSC differentiation but can alter cell orientation, ECM deposition and therefore tissue development

APPENDIX

Materials and Equipment

Function	Name	Supplier	Product code
Cell Culture	Debeclo's Modified Eagles media (low glucose and without L-glutamine)	Sigma Aldrich	D5546
	Penicillin/Streptomycin	Invitrogen-Gibco	15140
	Dulbecco's Phosphate Buffered Saline (DPBS)	Lonza	BE 17-512F
	Glutamax (100x)	Invitrogen-Gibco	35050
	Fetal Bovine Serum (FBS)	Sigma Aldrich	F9665
	0.05% Trypsin-EDTA (1x)	Invitrogen-Gibco	25300-054
	0.1mg/ml Fibroblast growth factor (βFGF)	Millipore	GF003
	0.4% Trypan blue solution	Sigma Aldrich	T8154
Differentiation	Insulin	Sigma Aldrich	I 5500
	Human Insulin, recombinant	Sigma Aldrich	I2643
	Recombinant Human TGF-beta3	Invitrogen-Gibco	PHG9305
	Indomethacin 99%TLC	Sigma Aldrich	I 7378
	IBMX (3-isobutyl-1-methylxanthine)	Sigma Aldrich	I 7018
	Ascorbic Acid (2-phospho-L-ascobic acid trisodium salt)	Fluka biochemika	49752
	Human insulin, human transferrin, and sodium selenite (ITS+L premix)	Sigma Aldrich	I3146
	Hyaluronic acid sodium salt (bovine)	Sigma Aldrich	H 7630
	Dexamethasone	Sigma Aldrich	D4902
	Bone.Morphogenetic.Protein.2	Peprotech	120802
	Insulin-like Growth factor 1 (IGF-1)	Peprotech	100811
	Rosiglitazone	Cambridge Bioscie	CAY71740
	Kartogenin	Cambridge Bioscie	CAY11826
Chemical Drying	Hexamethyldisilazane	Sigma Aldrich	440191
Polymers	Polystyrene, atactic	Alfa Aesar	44537
	Poly(methyl methacrylate)	Alfa Aesar	43982
	Polycarbonate, granule	GoodFellow	306310/2
	Polycaprolactone [Mw ~14,000]	Sigma	440752
Crosslinker	1-Ethyl-3-[3-dimethylaminopropyl]carbodiimide hydrochloride (EDC)	Thermo scientific	22980
	Sulfo-NHS (N-hydroxysulfosuccinimide) (NHS-sulfo)	Thermo scientific	24510
Immobilized factors	Phosphatase, Alkaline (bovine)	Sigma Aldrich	P0114
	Albumin-FITC		
Piranha Cleaning	Hydrogen peroxide 30%	Sigma Aldrich	H1009
	Sulphuric acid 98%	AnalaR®	10276G
Silanization	3-(Trimethoxysilyl)propyl methacrylate 98%	Sigma Aldrich	M 6514
Immunofluorscence	Tween 20	Sigma Aldrich	P1379
	Triton x-100	Sigma Aldrich	X100
	Hank's Balanced Salt Solution	Sigma Aldrich	H8264
	Goat Serum	Sigma Aldrich	G9023
	Rodamin Phalliodin	Sigma Aldrich	P1951
	Vincullin		
	Albumin–fluorescein isothiocyanate conjugate (Al-FITC)	Sigma Aldrich	A9771
Solvents	Tetrahydrofuran 99%	Alfa Aesar	L 13304
	Acetone 99.5%	Sigma Aldrich	179124
	Toluene 99.5%	Sigma Aldrich	179418
	1,4-Dioxane 99.8%	Sigma Aldrich	296309
Fixatives	Formalin	Sigma Aldrich	HT501128
	Paraformaldehyde	Sigma Aldrich	P6148
Alcohol	Ethanol, absolute	Fisher Scientific	BP2818-4
	Isopropan-2-ol	Fisher Scientific	A416SK-4
	Methanol, absolute	Fisher Scientific	10675112
Stains	Fast Green FCF >85%	Sigma Aldrich	F7252
	Fast Blue		
	Von kossa		
	Aliziarn Red S		
	Alcian Blue GX8		
	Oil Red O		
	Toluidine Blue O (TBO)		
Buffers	Sodium Chloride (NaCl)	Sigma Aldrich	S7653
	2-[moropholino]ethanesulfonic acid (MES)	Sigma Aldrich	M5287
	(HEPES)	Sigma Aldrich	H3375
MSC isolation	DPBS without Ca++ and Mg++	Lonza	BE17-512F
	DPBS with Ca++ and Mg++	Sigma Aldrich	D8662
	Ficoll-Paque premium	GE healthcare	17-5442-02
Glassware	Cover glass (borosilicate)	VWR	
	13mm		631-0150
	22mm		631-0159
	Microscope slides	VWR	631-1563
	Glass Vials, tall screw Neck	SAMCO	T101/V3
	Black polypropylene Caps, with foil-faced wads		T001/C3
Cell$Culture	6.well.plate	Costar	3516
	12.well.plate	Costar	3513
	24.well.plate	Costar	3526
	96.well.plate	Costar	3599
	T825.flask	Costar	
	T875.flask	Costar	
Spin coater	Bench Top rotary spin coater	MTI tech. Ltd	CSS-05
	Vaccum pump	Charles Austin pu	Model-8100
Microscope	DMLB Fluorscent light Microscope	Leica	DMLB
	Mercury Lamp - 100W mercury burner	Leica	ebq 100
	Camera - Advanced SPOT		
Plate reader	Sunrise TM	Tecan	
Plasma Cleaner	Vaccum Plasma Cleaner	MTI corporation	PDC-32G
AFM	Atomic Force Microscopy	Agilent technologi	5500
	software- Picoview 1.8.2		
Software	Gwyaddion	Gwyddion	v.2.30
	Image J	Image J	1.49i
	Fiji	Image2J	2.0.0-rc-15/1.49m

Atomic Force Microscopy

AFM images were captured using Agilent technologies (S500 MAC mode III, USA) and Picoview 1.8.2 software for [80 / 40 / 20 / 10μm^2] areas at 1.2lines/s; 612 pts/line resolution. Data visualisation and analysis was preformed on Gwyddion 2.38 (Sourceforce.net, Czech Republic)

Materials and Equipment:

Atomic Force Microscope (S500 MAC mode III, Agilent Technologies, USA)

Picoview software (version 1.8.2)

Gwyddion software (version 2.38)

Sharp right-angle tipped tweezers

Ultrapure water

Method:

1. Equipment setup: AFM cantilever (contact mode, force constant = 0.02-0.77N/m) secured
2. CARFULLY load cantilever tip onto AFM head.
3. Secure sample face up in water cell mount. For submerged imaging add 500μl ultrapure water. Attached sample tray beneath cantilever base.

[Given suspended AFM setup used. Once sample is mounted; stabilize the equipment, close the door so in complete darkness and wait for water movement to settle ~3mins]

4. Picoview software setup:
    a. Mode – contact
    b. Main – I & P Gain (%) = 1, Set point = 0
    c. Scan & motor – size = 80μm, centered at 0
5. Active laser is calibrated to area of highest intensity and aligned with detector. Contact mode settings on software:
    a. Deflection = -1
    b. Friction = 0
    c. Sum ~1.5
6. Cantilever approach speed 4μm per second. Desist at surface contact.
7. Cantilever withdrawn to 100μm and laser is re-calibrated
8. Second approach speed 1.4um/s (as the distance to surface is known)
9. Preform ‘sweep’ of surface at:
    a. Duration – 5s

b. Datapoints – 5,000

10. The set point is dropped to just above the known base level
11. Detailed trace can then preformed for the first area size.
12. After each complete trace, repeat steps 6-10. Adjusting the sample area size for each trace [80 / 40 / 20 / 10 μm]
13. Tips: to improve quality:
    a. Restart trace approx.. x3
    b. Adjust the I Gain % (typically Increase to around 7%)
    c. Appropriate adjustment of setpoint (increase if contact lost and decrease if too much pressure)
14. When inspection of a sample is complete:
    a. Tip withdrawn to 500um
    b. Laser is turned off
    c. Sample removed from AFM and then from its holder
15. The process is then repeated from step 3 for the next sample
16. When all required data has been collected the AFM components were restored to storage space and both the AFM and computer shut down and left as found

Image analysis was preformed using commercial Gwyddion software (version 2.38).

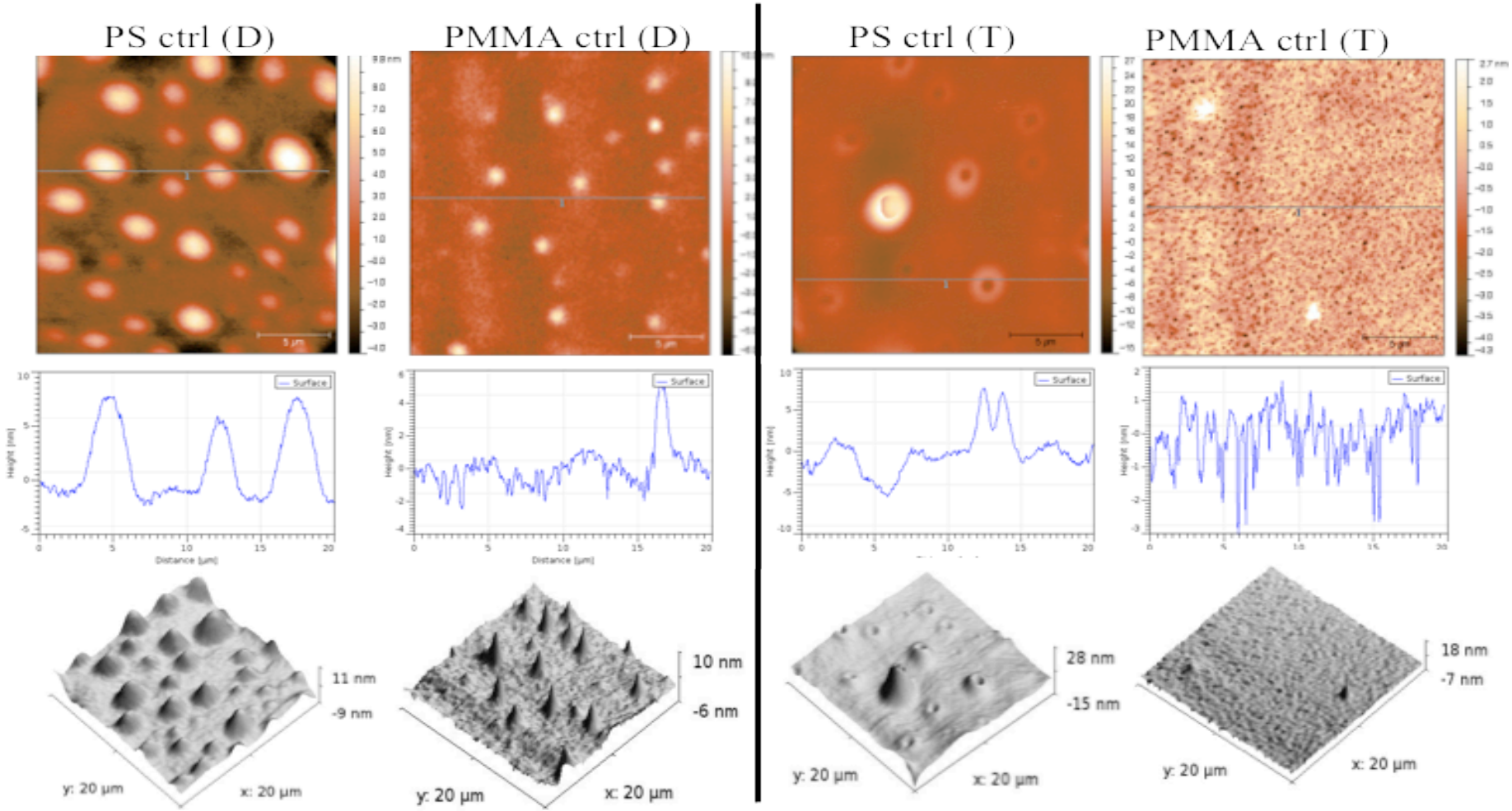

Topographical profiles of 100% PS and PMMA surfaces with two frequently used organic solvents 1,4-Dioxane (D) and Toluene (T). Surface profiles analysed by AFM show; aerial image, linear high profile graph, and 3D rendered model of aerial image. [presence of latent humidity can be observed on surfaces]

Polymer Spin Coating_The edge effect

A common complication in spin coating is the creation of a boarder around the substrate, known as the edge effect. Shown here is a SEM image of the initial surfaces and the edge effect seen (a.) and the improvement in later demixed surfaces by modification of spin coating parameters (b.)

a.

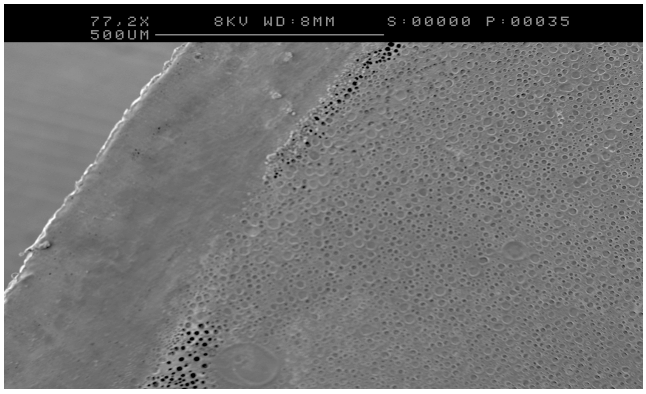

b.

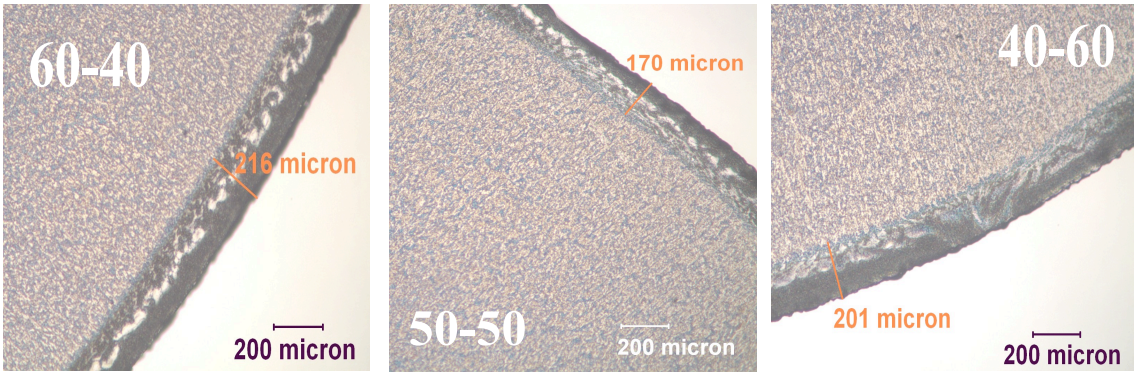

Figure 60. Polymer aggregation at circumference of substrate. a) SEM image of circumference and b) Brightfield microscopy of edge effect with measurements.

Isolation of mononuclear cells (MNCs) from Trabecular Bone Fragments:

1. Use sterile implements for bone marrow extraction: bone-cutting pliers, chainmail glove (autoclaved). Maintain sterility with 70% ethanol.
2. From the bone fragment(s) exhume red areas encased in marrow, taking care to avoid areas of high lipid content (yellow/orange), mincing the fragments with pliers will releases trapped cells in the highly compact ECM
3. Transfer exhumed fragments into sterile collection tube (25/50ml depending)
4. Rinse sample in wash solution A or B and mix sample well by shaking
5. Filter the mixture into a fresh tube with high gauge filter (100µm) to remove bone fragments
6. Carefully place 10ml Ficoll-Paque™premium as a top layer over the filtered cell mixture (slowly pore the Ficoll to form a clear layer above the cell suspension)
7. Centrifuge sample at 470g for 40mins (don't use brake assisted stopping)
8. The mononuclear cells (MNCs) form a 'scum' layer between the clear Ficoll (lower) and organge plasma (top) layer. Carefully extract the interface layer into a fresh tube taking care not to aspirate the top layer but can liberally take the lower (Note: MNCs have been found in clear Ficoll layer)

9. Rinse isolated MNCs with wash buffer (x2). Using 10ml buffer for first wash and 5ml buffer for second
10. Pellet the sample by centrifuge at 300g for 8mins. Resuspend purified MNCs in cell culture media pre-heated to 37°C
11. Plate out the cell suspension at ~800,000 cells/cm^2 into a 6-well plate or T-25 flask and incubate at 37°C, 5%CO_2 and 95% humidity
12. Cells should be accessed after 3-5 days and changing media when appropriate. Repetitive pipetting of media during this first media changes will select for adherent stromal cells (MSCs)
13. Thereafter culture should be routinely accessed every 3-4 days changing 50% of the media for replacement of nutrients.
14. Once cells reach 70% confluent they should be passaged using Trypsin/EDTA (1x)
15. The screened adherent cells can be then transferred into tissue culture flasks for cell expansion, seeding at 4500 cells/cm^2 [T-75 flask ~350,000cells]

16. Cultures of MSCs are stable *in vitro* for approximately 6 passages

Note: All cell culture procedures are preformed within Class II Laminar flow hood All surfaces are sterilized with 70% Ethanol.

Name	Contents	Volume
Wash Solution A	DPBS (with $Ca^{++}$and Mg^{++}) & 1%P/S	10ml
Wash Solution B	DMEM-LG & 1%P/S	10ml
Wash Buffer	5mM EDTA, 0.2% bovine serum albumin (BSA), in PBS (without $Ca^{++}$and Mg^{++})	
Cell Culture Media	DMEM (with low glucose and without L-glutamine), batch tested FBS 20%, Pen/Strep 1%, Glutamax 10%, β-FGF 8ng/ml	

Extraction of mesenchymal stromal cells using Human MSC enrichment cocktail and spin column

Ensure that bone marrow sample, wash buffer, Ficoll-Paque® and centrifuge are all at room temperature.

1. Aliquot a known volume of bone marrow into a 14 mL tube. Add 50 µL RosetteSep® Human Mesenchymal Stem Cell Enrichment Cocktail per mL of bone marrow and mix well.
2. Incubate 20 minutes at room temperature.
3. Dilute sample with twice the volume of PBS + 2% FBS and 1 mM EDTA. Mix gently.
4. Layer the diluted sample on top of the Ficoll. Be careful to minimize mixing of Ficoll-Paque® and sample.

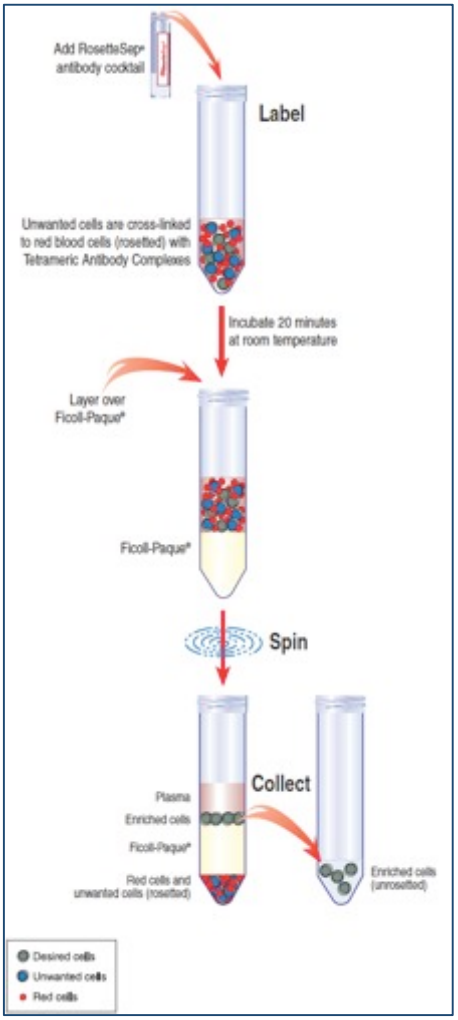

Unprocessed Bone Marrow	PBS + 2% FBS 1mM EDTA	Ficoll®	Tube Size
1 mL	2 mL	5 mL	14 mL
2 mL	4 mL	5 mL	14 mL
5 mL	10 mL	15 mL	50 mL
10 mL	20 mL	15 mL	50 mL

5. Centrifuge for 25 minutes at 300 x g (See Notes and Tips) at room temperature, with the brake off.
6. Remove the enriched cells from the Ficoll-Paque® : plasma interface.

It is advisable to remove excess plasma layer (*above* MNC 'scum' layer) to capture as many MNCs, due to difficulty identifying entire MNC layer. Note, avoid take any Ficoll (*beneath* MNC layer).

7. Wash enriched cells with PBS containing 2% FBS and 1 mM EDTA.
8. We recommend that enriched samples are lysed with ammonium chloride to remove residual red blood cells prior to flow cytometric analysis (this can be done as one of the wash steps) or if residual red blood cells will interfere with

subsequent assays. Resuspend cells in appropriate medium for culture or flow cytometric analysis.

Note: Extraction medium – PBS + 1mM EDTA + 2% FBS.

Convert *g* to rpm, using the following formula:

$$RPM = \sqrt{\frac{RCF}{(1.118\times10^{-11})\times(Radius)}}$$

RCF = relative centrifugal force (g)

RPM = centrifuge speed in revolutions per minute

Radius = radius of rotor in cm

MTT cell proliferation assay

Measurement of cell viability and proliferation was readily achieved through a quantitative colorimetric assay, identifying mitochondrial succinate dehydrogenase activity in living cells. The Thiazolyl Blue Tetralian Bromide (MTT), yellow colour in solution, is directly degraded by dehydrogenase in the mitochondria of living cells and converts the yellow coloured tetrazolium salt (insoluble) into blue/purple coloured formazan (soluble)[161].

The intensity of the blue/purple colour formed can be quantified by specific absorbance wavelength at 570nm and measured using a spectrophotometer plate reader (Tecan sunrise). Using a standard curve plot of known cell numbers vs absorbance, we can calculate the cell number of other unknown samples.

Method:

1. Typically: Cells plated in a 24-well plate or 96-well plate and let cells attach for appropriate time
2. Remove media from the wells (cells in culture or end of experiment)
3. Dissolve appropriate amount of MTT in culture media (serum-free) (used @ 1mg/ml), insuring to fully dissolve crystals. Heating to 37ºC helps.
4. 200µl of MTT solution was added, ensuring to cover submerge whole sample and incubate for 4h at 37°C, 5% CO_2
5. Completely remove the MTT reagent and add 100µl of isopropanol. This lysis cells and dissolves the Formazan.
6. Gently swirl by placing on a shaker for 30 minutes
7. Transfer into a 96-well plate, if not already in one.
8. Read in platereader at OD 570nm using reference wavelength ~620nm

Reagents and Equipment:

96-well plate_Flat bottom (Costar 3596)

Platereader (TECAN sunrise®)

DMEM (same as culture medium) or PBS

MTT [3-(4,5-dimethythiazol-2-yl)-2,5-diphenyltetrazolium bromide](Sigma M2128-1g)

Absolute isopropanol (Propan-2-ol, Fisher Ltd. P/7507/17)

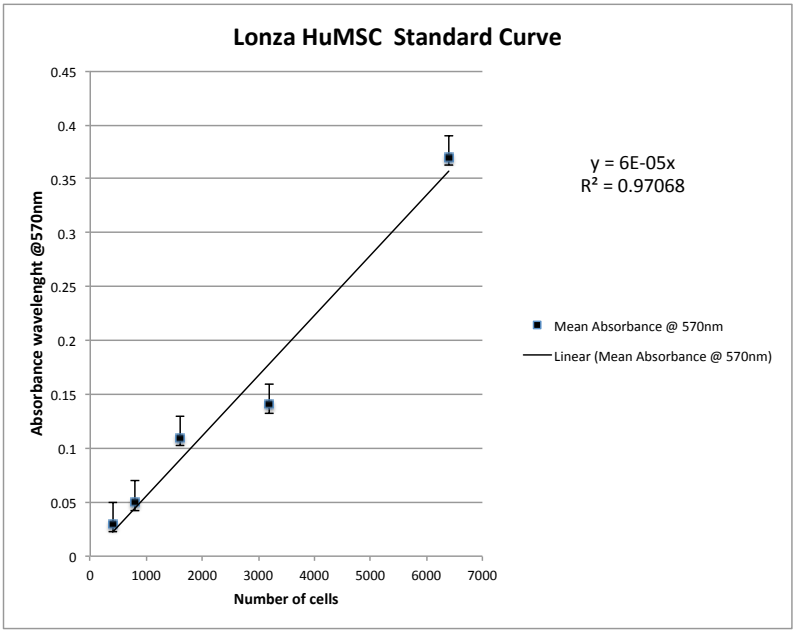

Figure 61. MTT proliferation assay for primary hMSC (N=3) cultured under the same conditions with five different media consistencies were quantitatively compared using a standard curve . Relative growth quantified by MTT absorbance readings at 570nm are converted to cell number using standard curve line equation.

Suspended Chondrogenesis pellet (3D culture)

Previous studies have shown improved differentiation of human MSCs when in 3D culture, weather it be alginate scaffold[167] or free floating micro-mass pellets in bioreactor[168]. This three-dimensional freedom of cells combined with chemical stimuli, showed improved hyaline cartilage formation. This technique is advantageous, *in vitro*, as monolayer cultures will display correct chondro-specific gene expression with limited protein deposition, but is unable to generate morphological structures exhibited by cartilage.

Method:

1. Passage Cells (Trypsin) and preform cell count.
2. Form micro-mass pellets by centrifuging cells in non-adherent 15 ml polypropylene conical tubes at concentration of ~$2.5x10^5$ cells/0.5ml medium @ 200***g*** 5 min.
3. Leave pellets to settle for 3 h in incubator at 37ºC with lids loose
4. Carefully replace medium with the serum-free medium @0.5 ml per tube leave O/N
5. At Day 1, carefully remove and replace media with 0.5ml of serum-free medium with TGFβ1 or serum-free medium alone for untreated control.
6. Replenish the medium every 2/3 days. Ensuring not to disturb the pellet.
7. Harvest cultures at appropriate time points.

Reagents and Equipment:

Trypsin (Gibco, 25300-054)

PolyPropylene tubes, 15ml (Starlab, E1415-0200)

Filter-sterilise (0.22µm pore size)

Growth Medium:

DMEM - low glucose, without L-Glutamine (Sigma D5546)

10% FBS (hMSC-tested)

1% Glutamax (Gibco, 35050)

1% P/S (Gibco, 15140)

Serum-free Medium:

DMEM - low glucose, without L-Glutamine (Sigma D5546)

50 µg/ml Ascorbic acid (Fluka Biochemika 49752)

Insulin, Transferrin, and Sodium selenite, human (ITS+L premix) (Sigma I3146)

100 nM dexamethasone (Sigma D4902)

and growth factor

Growth factor stimuli

TGF-β3 (Gibco PHG9204) @10 g/ml final concentration

Kartogenin (Cambridge Bioscience, CAY11826) @10ng/ml final concentration

Chondrogenic Staining of Wax embedded micromass Protocol

1. After culture of the chondrogenic pellets, fix in 10% formalin and embed in paraffin wax before taking thin sections for staining
2. Deparaffinise slides
    - Soak in xylene for 10 minutes
    - Soak in 100% ethanol for 5 minutes
    - Soak in 95% ethanol for 5 minutes
    - Soak in 70% ethanol for 5 minutes
3. Wash slides in 0.1N HCl for 1 hour
4. Incubate with 0.1% Alcian Blue solution overnight
5. Wash in 0.1N HCl
6. Assess for proteoglycan staining

Isolation of stromal cells from marro of bone fragments					201142014								
								Analysis					
Patient		number	operation date	isolation date	Seeded	first passage	Days	Flow cytometry	differeniation	Frozen (480C)	Cryo storage	Terminated	
DTOS_3924	76yr.F.THR	N_2693	17/01/2012	17/01/2012	17/01/12			X	X	X			
DTOS_3927	84yr.F.THR	N_2694	17/01/2012	17/01/2012	17/01/12			X	X	X	X		
	72yr.F.THR	N_2696	23/01/2012	23/01/2012				X	X	X			
	63yr.F.THR	N_2697	23/01/2012	23/01/2012				X		X			
DTOS_4210	64yr.M.THR.	N_2840	26/06/2012	26/06/2012	26/06/12	17/07/12	21		X	X	X		
DTOS_T114	68yr.F.THR	N_2847	03/07/2012	03/07/2012	03/07/12	**16/07/12**						169Jul	
DTOS_4229	74yr.M.THR	N_2848	03/07/2012	03/07/2012	03/07/12	24/07/12	21		X	X	X		
DTOS_4233	57yr.M.Hip.resurfacing.	N_2852	04/07/2012	05/07/2012	05/07/12	14/08/12	40		X			209Sep	
DTOS_4259	77yr.M.THR	N_2864	27/07/2012	27/07/2012	27/07/12	20/08/12	24		X	X	X		
DTOS_4260	.72yo.Female.THR	N_2865	30/07/2012	30/07/2012	30/07/12	23/08/12	24						
DTOS_4275	63yr.F.THR	N_2877	15/08/2012	15/08/2012	15/08/12	20/09/12	36					209Sep	
DTOS_4287	58yr.F.THR.(L)	N_2891	28/08/2012	30/08/2012	30/08/12	20/09/12	21					209Sep	
DTOS_4290	76yr.M.THR.R	N_2892	30/08/2012	30/08/2012	30/08/12	20/09/12	21					209Sep	
DTOS_4289	79yr.F.THR.(L)	N_2893	30/08/2012	31/08/2012	31/08/12	19/09/12	19					209Sep	
DTOS_4294	72yr.F.THR.R	N_2894	04/09/2012	04/09/2012	04/09/12	14/09/12	10			X	X		
DTOS_4295	68yr.F.THR.R	N_2895	04/09/2012	04/09/2012	04/09/12	19/09/12	15					219Sep	
NOF_T117	85yr.M.THR.R	N_2896	04/09/2012	04/09/2012	04/09/12	15/09/12	11					209Sep	
DTOS_4364	72yr.F.(L).THR	N_2942	10/10/2012	13/10/2012	13/10/12	31/10/12	18					319Oct	
DTOS_4369	66yr.F.(R).TKR	N_2943	10/10/2012	13/10/2012	13/10/12	31/10/12	18						
DTOS_4373	44yr.F.(R).THR	N_2945*	15/10/2012	15/10/2012	15/10/12	31/10/12	16	X			X		
DTOS_4374	58yr.M.(R).TKR	N_2946	15/10/2012	15/10/2012	15/10/12	31/10/12	16						
DTOS_4384	62yr.F..THR	N_2957	19/10/2012	31/10/2012	19/10/12	31/10/12	12			X	X		
DTOS_4386	83yr.M.TKR	N_2958	19/10/2012	31/10/2012	19/10/12	31/10/12	12						
DTOS_4388	67yr.M.TKR	N_2959	19/10/2012	31/10/2012	19/10/12	31/10/12	12						
DTOS_4397	52yr.F.(R).THR	N_2964	23/10/2012	24/10/2012	24/10/12	06/11/12	13			X	X		
DTOS_38	87yr.M.(L).THR	N_2968	26/10/2012	26/10/2012	26/10/12								
DTOS_4401	74yr.M.(R).THR	N_2969	26/10/2012	26/10/2012	26/10/12								
DTOS_4402	77yr.M.(R).THR	N_2970	26/10/2012	26/10/2012	26/10/12								
NBJS_4428	59yr.M.THR	N_2985	12/10/2012	13/10/2012	13/10/12					X	X		
NOF_T123	72yr.F.THR	N_3046	29/01/2013	30/01/2013	30/01/13	07/02/13	8	X		X	X		
NOF_T125	66yr.F.THR	N_3053	07/02/2013	07/02/2013	07/02/13								
NOF_T132	84yr.M.(L).THR	N_3100	02/04/2013	02/04/2013	02/04/13								
	47yr.F.TKR	N_3196	15/07/2013	15/07/2013	15/07/13	29/07/13	14	X			X		
NOF.T146	90yr.F.THR	N_3223	07/08/2013	07/08/2013	07/08/13								
DTOS_4869	73yr.M.THR.(B)	N_3251	17/09/2013	17/09/2013	17/09/13					X	X		
	73yr.M.THR.(Asp.)	N_3251	17/09/2013	17/09/2013	17/09/13					X	X		
huTERT.MSC	y201		15/11/2013	15/11/2013									
huTERT.MSC	y202		15/11/2013	15/11/2013									

Table 5. Itemised list of all MSC populations isolated throughout research period.

Fluorescence microscopy SOP

Cells are embedded in Formalin-substrates for long-term preservation of biological samples and immune-fluorescent staining. Use of 4% paraformaldehyde (Sigma P6148) insures the secure fixation of cells to surface during the rigorous staining and wash procedures.

Most formalin-fixed tissue requires and antigen retrieval step, to maximize antibody binding. This is due to the formation of methylene bridges during fixation, which cross-link proteins and therefore mask antigenic sites. Heat induces epitopes retrieval (HIER) is one of the most effective damasking methods, applicable to more than 80% of all antibodies, although in this particular case proteolysis is best in the liberation of extracellular epitopes. We utilize a combination of dilute detergents to liberate the desired epitopes of interest.

Method:

At end of culture period:

1. Aspirate the culture medium
2. Rinse once with ~300 µl per Hank's Balanced salt solution (HBSS)
3. Fix cell to polymer coated glass cover slips using 300 µl per well of 4% Paraformaldehyde* (PFA) preheated to 37°C to maximize linkage >20min

[Note: All use of PFA is to be preformed inside fume hood and volume adjusted to insure coverage of the sample surface]

4. Drain away fixative (PFA) and wash 3 times with PBS/0.1% Tween for 5mins each time.
5. Block with 300µl of 3%(v/v) Goat serum** in PBS/Tween for 30mins @RT.
6. Incubate with pre-diluted primary antibody ~200µl/well (add drop wise) for 90-120mins @RT or 4°C O/N [dilute at 1:200 in 3%goat serum/PBS tween]
7. Wash 3 times with PBS/0.1%Tween for 5mins each

[Optional: Preform additional Wash step with 0.1% Triton x-100 to increase permeability of cellular membrane]

8. Incubate with pre-diluted secondary antibody ~200µl/well in PBS for 40-60min @RT in the dark [dilute at 1:200 in PBS tween]
9. After 10mins incubation with secondary antibody, ~200µl/well of Rhodamine phalloidin pre-diluted [1:1000] with PBS/tween, for 20min @RT in the dark.

10. Wash with PBS/Tween for 5mins and finally wash twice in upH_2O to remove PBS
11. Mount onto clean glass slides
12. Load a single drop of mounting media (containing DAPI) onto each sample. Cover samples with a cover slip, taking care to apply cover slip at an angle to minimize air bubbles.
13. Samples imaged on fluorescent microscope [Leica microscope_DML] with SPOT advanced live imaging camera and images analyzed by image J sorftware.

* 4% PFA stock prepared in 250 ml glass bottle.

[Volume = 250 ml; Density = 0.88 g/ml]

$$Mass = Volume(ml) \times Density(^{g}/_{ml})$$

$$Mass = \left[\frac{[(250 \text{ x}(0.88))]}{100}\right] \times 4 = 8.8\text{g}$$

** 3% Goat serum

$$\left[\frac{(number\ of\ samples\ or\ wells \times 300\mu l)}{100}\right] \times 3 = Volume\ Goat\ Serum\ Required$$

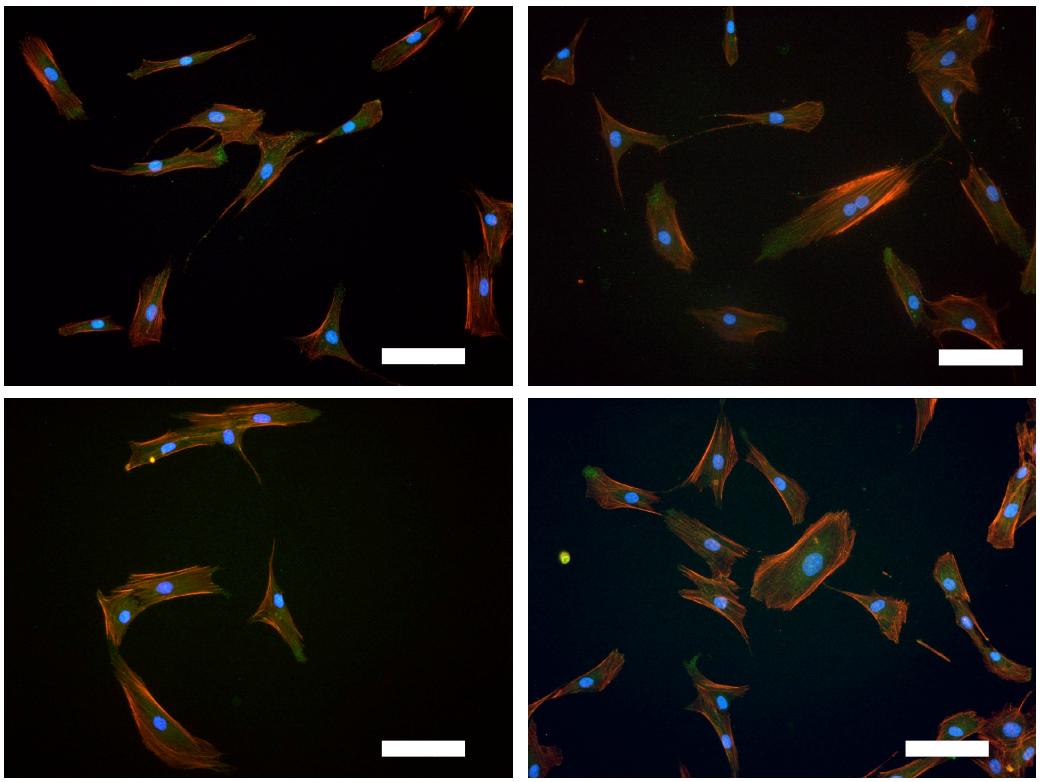

Figure 62. Basal cultures of MSCs adhered [Y201] to glass control surfaces after 24 h.

Cell morphology

24hr adherence		27/06/2013					
Summary of cell Morphology		40:60	50:50	60:40	PS	PMMA	Glass
Area	a	28.97	82.02	65.60	85.64	25.52	**56.71**
	b	48.69	77.95	76.62	86.00	20.17	48.34
	c	50.11	63.79	74.37	86.13	32.42	74.21
	d	63.51	63.74 .		75.01	34.84	57.88
Area	Av.	**47.82**	**71.88**	**72.20**	**83.20**	**28.24**	**59.28**
	STDV.	**14.23**	**9.51**	**5.82**	**5.46**	**6.67**	**10.82**
	SE	**7.12**	**4.75**	**3.36**	**2.73**	**3.34**	**5.41**
Cirularity	a	0.31	0.28	0.23	0.24	0.42	0.26
	b	0.28	0.20	0.27	0.22	0.37	0.00
	c	0.25	0.25	0.23	0.26	0.30	0.28
	d	0.24	0.30 .		0.31	0.27	0.31
Cirularity	Av.	**0.27**	**0.26**	**0.25**	**0.26**	**0.34**	**0.21**
	STDV.	**0.03**	**0.04**	**0.02**	**0.04**	**0.07**	**0.14**

Table 6. Summary of average cell area and circularity across four experimental repeat surfaces (a-d) which are comprised of numerous cells per field of view within a minimum of five (10x) images per surface.

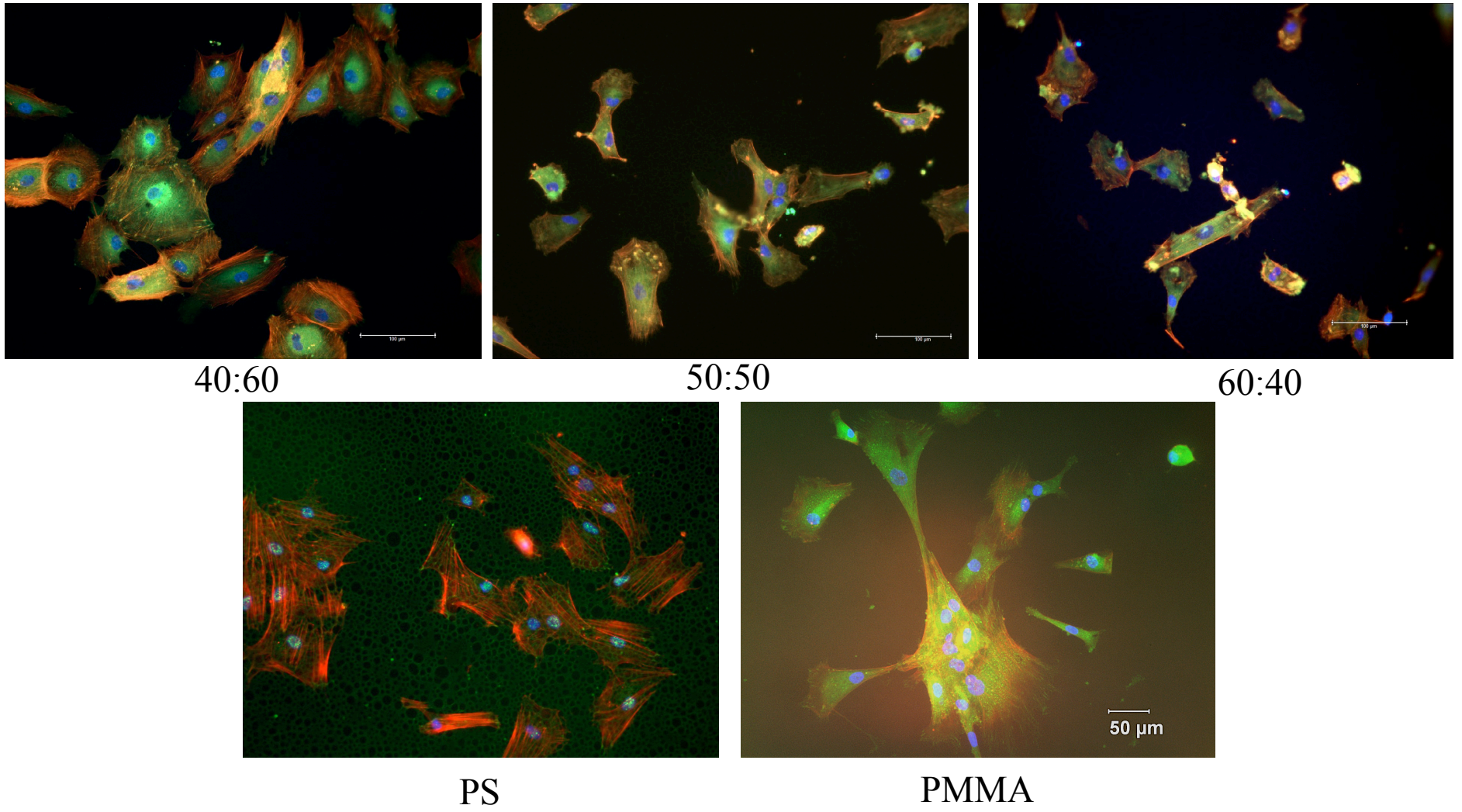

Figure 63. Cell clustering or aggregation of MSCs on different polymer surfaces. Discussed in chp.5

Zero-length Crosslinking factors to Polymer surface

EDC is a carboxyl and amine-reactive zero-length crosslinker. Where the EDC reacts with carboxyl group first to form an amine-reactive *O*-acylisourea intermediate that quickly reacts with an amino group to form an amide bond and release of an isourea by-product. The intermediate is unstable in aqueous solutions and therefore, two-step procedures rely on *N*-hydroxysuccinimide for stabilization.

Reagents

1-ethyl-3-[3-dimethylaminopropyl]carbodiimide hydrochloride, EDC
(22980, Thermo scientific; M_W 191.7. CAS:25952-53-8)
Sulfo-NHS (24510, Thermo scientific; CAS:106627-54-7)
Activation buffer: 0.1M MES + 0.5M NaCl , pH 6.0

Method

- Equilibrate EDC (and NHS) to room temperature before opening bottles.
- Add 0.4 mg EDC [final concentration, ~2mM] and 0.6 mg of NHS or 1.1 mg of sulfo-NHS [final concentration, ~5mM) to 1 ml of Polymer surface
- Mix reagents well and aloud react for 15mins @ room temperature.
- *Optional* : Add 1.4µl of 2-mercaptoethanol (final conc., 20mM) to quench the EDC.
- Add factor to be immobilized (protein, etc.) to the activated surface in an equal molar ratio to surface. Allow the protein-surface to react for 2 hours @ room temperature.
- *Optional* : to quench reaction add hydroxylamine (final conc. 10mM).
- Remove excess reagent and submerge in ultrapure water (X2)

- [Store in fridge, 4ºC or at appropriate temperature for immobilized factor]

Example

- Add 2mM EDC in activation buffer to surface. Incubate @RT 10mins (100 µl per surface, pH6)
- *Optional* : Add 100mM sulfo-NHS in activation buffer to surface. Incubate @ RT 15mins (10 µl per surface)

- *Optional* : Add 2-mercaptoethanol to quench EDC, final conc. 20mM (0.15µl per surface)
- Add "Factor" (protein) at 1-10mM. Incubate @RT 1-2 h
  - **AL-FITC** [100 µM; 10 µl per surface]
  - **Phosphatase** [1 µg/ml; 10 µl per surface]
- *Optional* : Add hydroxylamine, final conc. 10mM (1.2µl from 1M stock)
- Rinse in ultrapure H_2O (X3)

Immobilized Phosphatase enzyme – bioactivity retention assay

The LINEST formula **=LINEST (known Y value cells, known X value cells, 1, true)**
For example, if we had column A (time) as X and column B (concentration) as Y, and we had eight rows of data, we would type the following:
=LINEST(B1:B8, A1:A8, 1, true)

When we type this in Excel will return a single value, the slope. LINEST is an array function, which means that even though it is trying to give back a lot of values, it only displays one per cell. What Excel is expecting you to do is highlight a 2x2 set of cells with the LINEST formula in the upper-left cell. Once this is done, go up to the formula bar and highlight the entire LINEST equation you typed and hit Ctrl-Shirt-Enter (on Mac use Apple-Return). This will fill in the 2x2 square.
Upper left will be the slope, lower left will be the error on the slope. Upper right will be the intercept and lower right will be the error on the intercept.

LINEST fuction for the slope of the data

	40:60		50:50		60:40		PS		PMMA		Glass	
	Slope	Intercept	Slope	Intercept	Slope	Intercept	Slope	Intercept	Slope	Intercept	Slope	Intercept
	-1.83390178	34.591855	-1.7598895	34.3206461	-1.582429	30.7390924	-2.1432182	34.2288846	-1.3833766	23.7266184	-0.0465984	0.79234638
error of slope/Inte	0.995187161	7.29049599	1.0378815	7.60326417	1.01231767	7.41598989	1.14074153	8.35679143	0.82856234	6.06984357	0.03723828	0.27279844

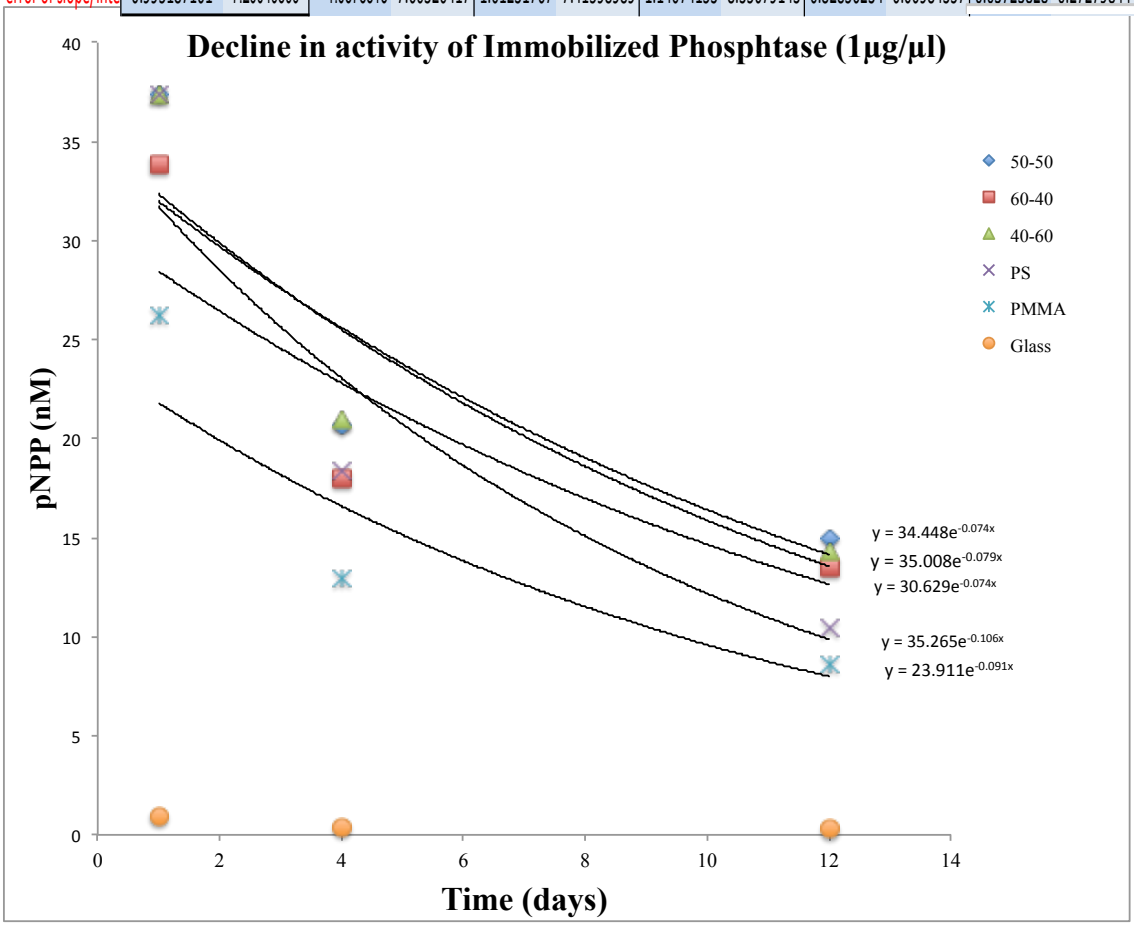

Complete Primary MSC gene expression results

Three patient populations validated as multipotent MSCs were used to illustrating effects of the fabricated surfaces. One patient results were discussed in full in chapter 5, here are the others:

1.1.1.5. 1) Patient N_2840

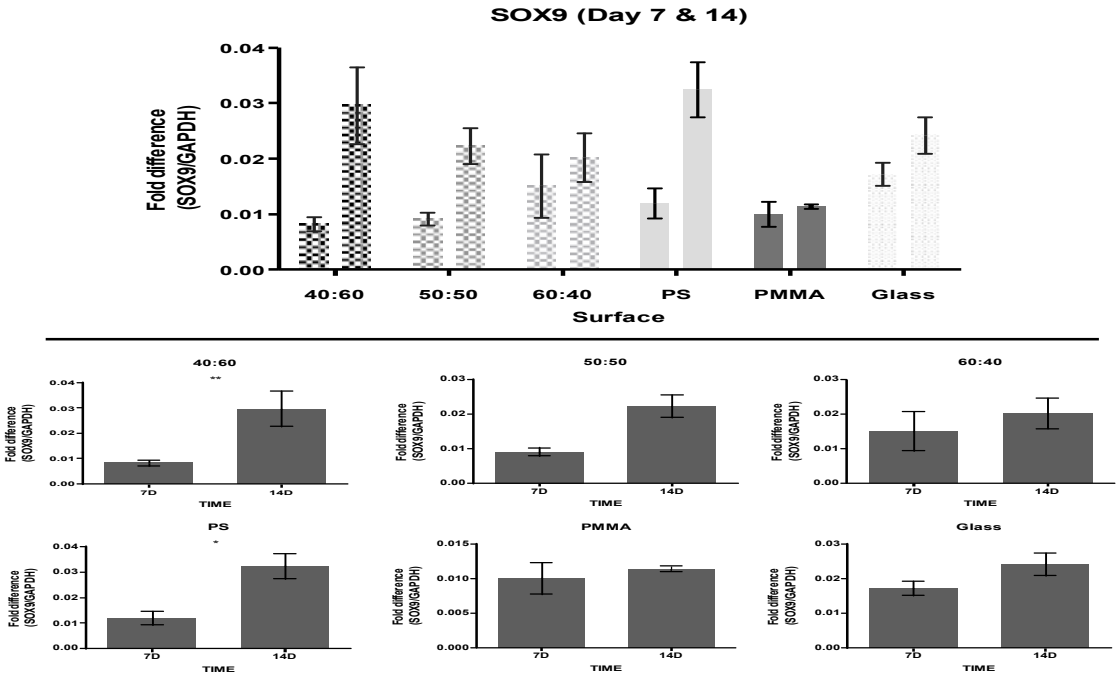

No ACAN detected at Day 7 therefore no time point comparison.

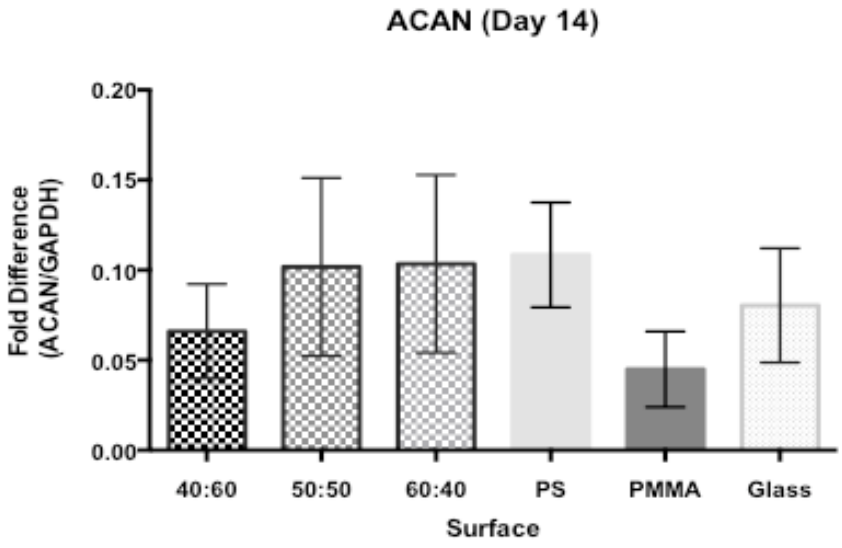

[No RUNX2 detected]

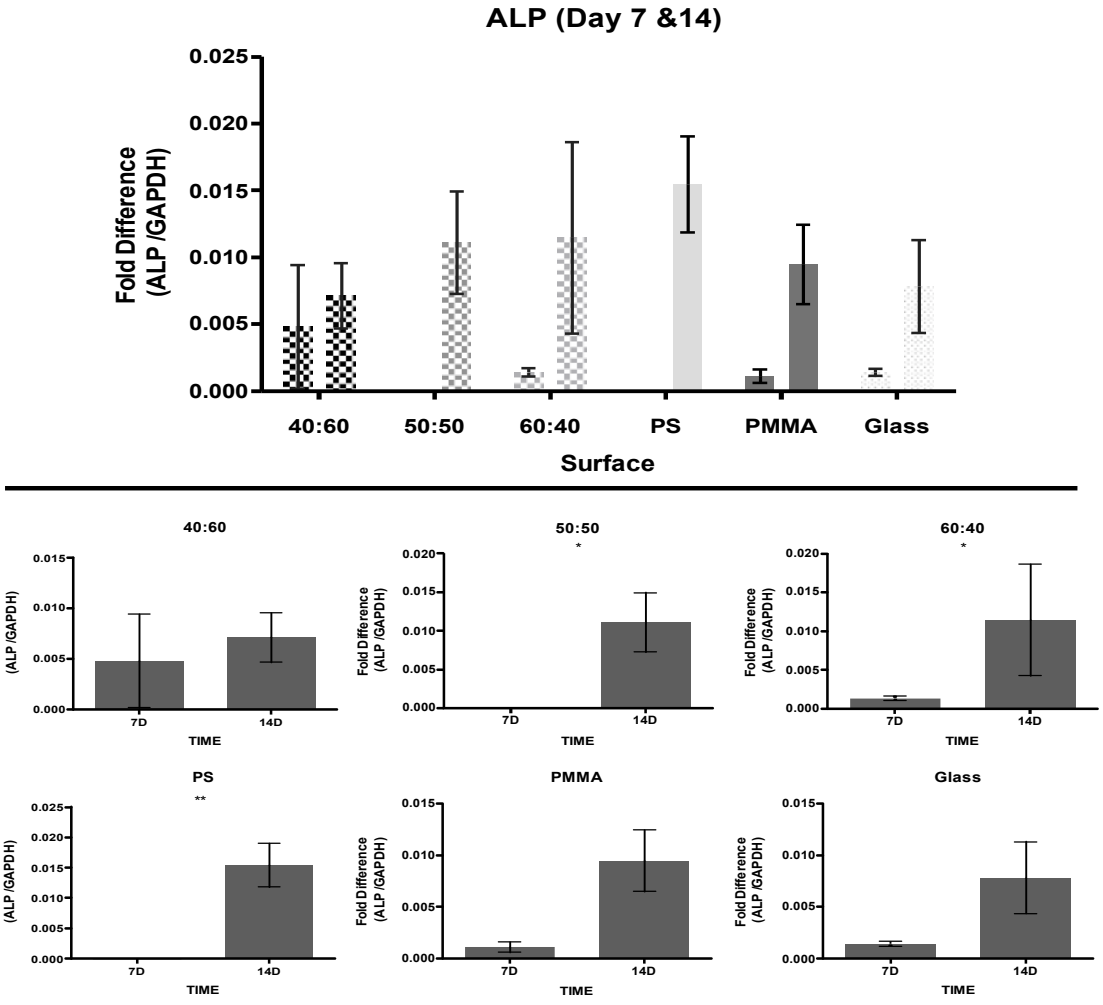

No detection of C/EBP at Day 7

Therefore no time point comparison

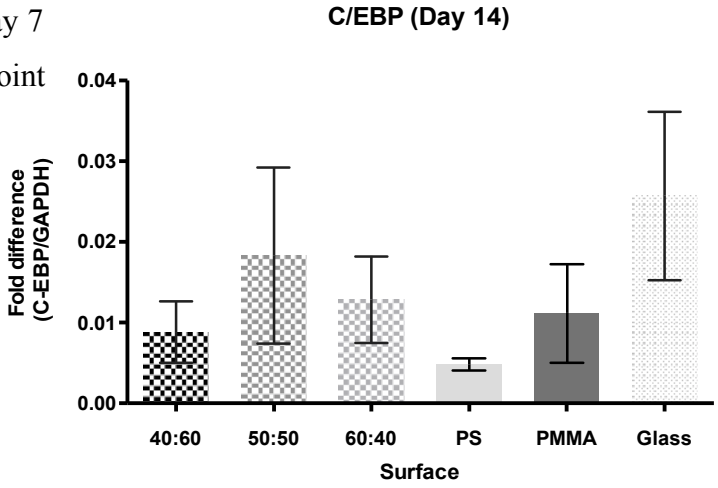

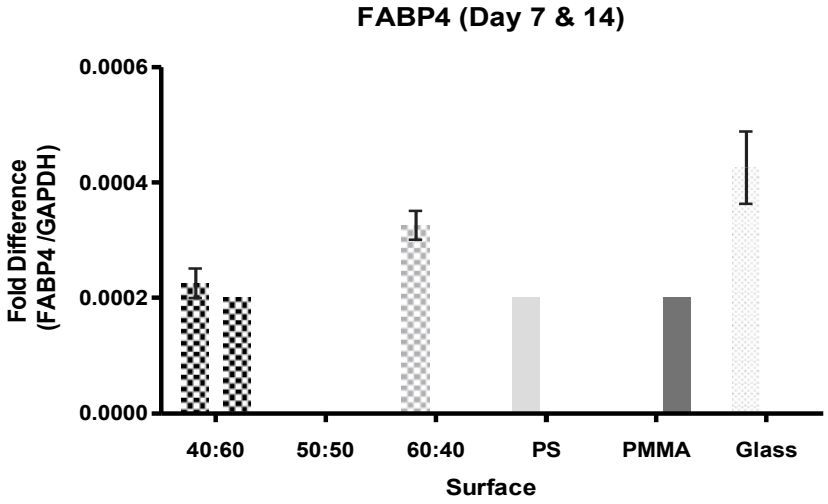

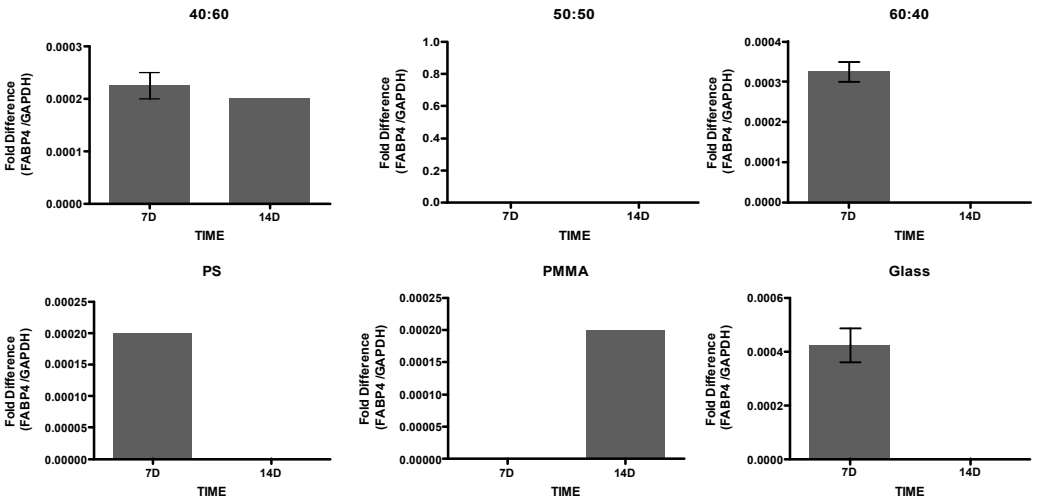

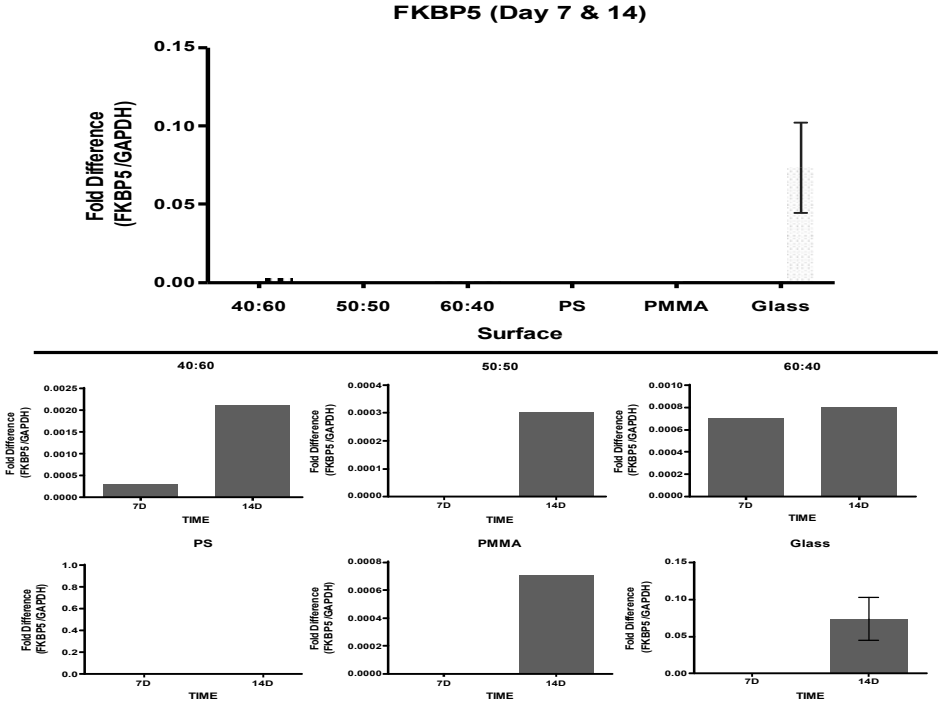
FKBP5 (Day 7 & 14)
Fold Difference (FKBP5 /GAPDH)
0.15
0.10
0.05
0.00
40:60
50:50
60:40
PS
PMMA
Glass
Surface
40:60
50:50
60:40
PS
PMMA
Glass
Fold Difference (FKBP5 /GAPDH)
7D
14D
TIME

2) Patient N_2848

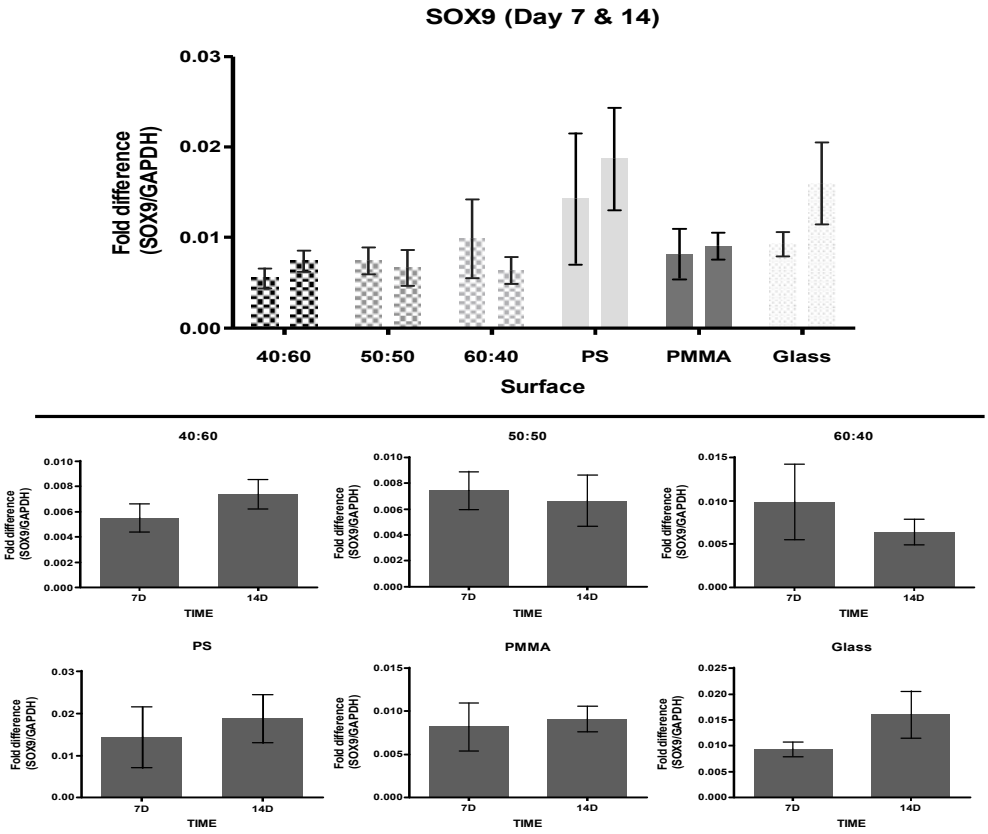

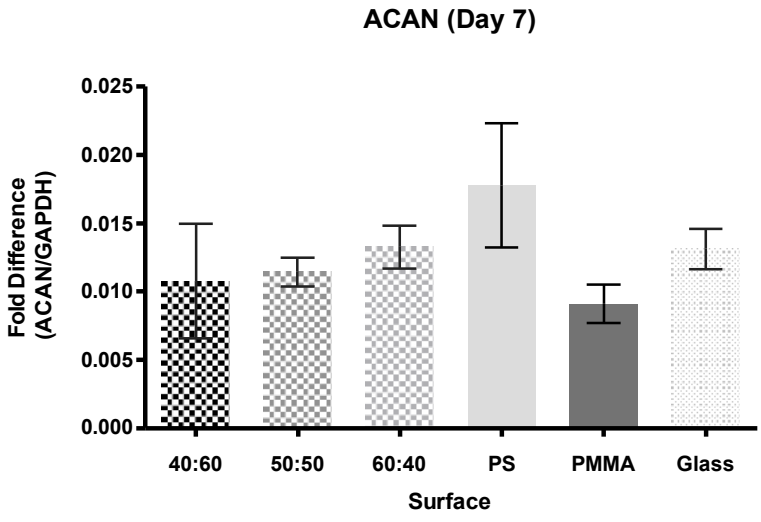

No ACAN detected at Day 14.

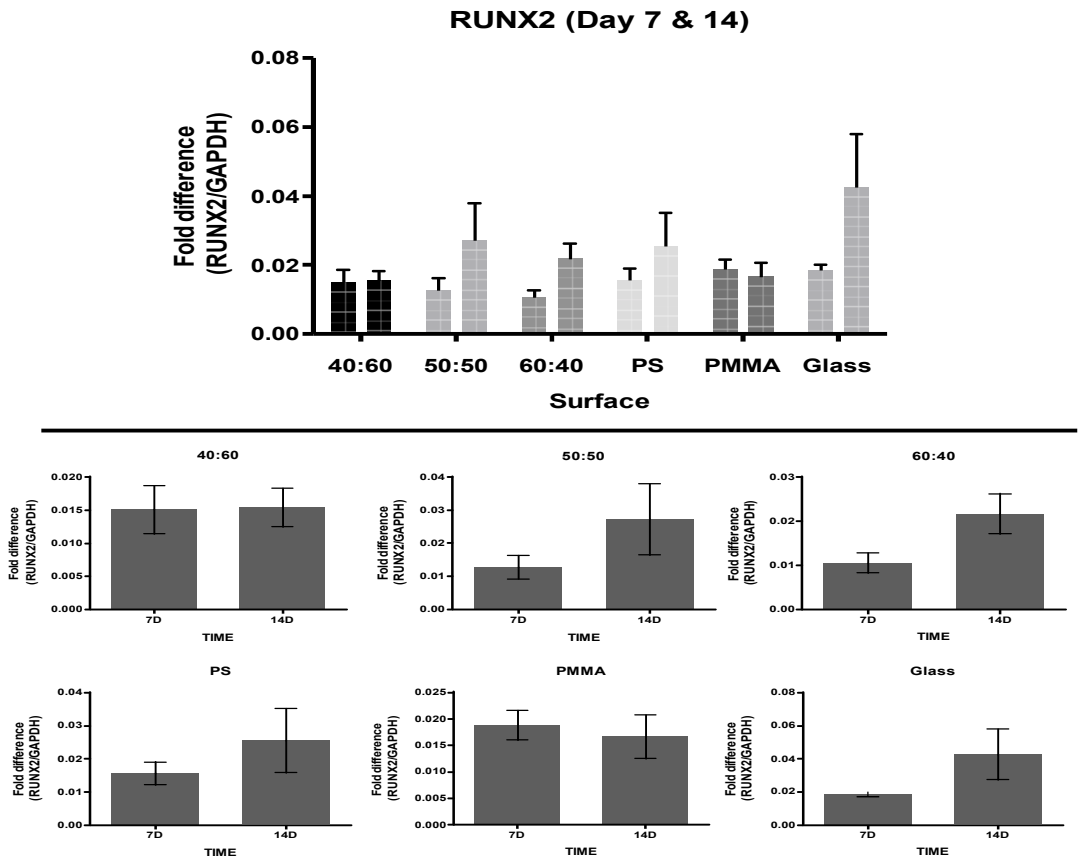
RUNX2 (Day 7 & 14)
Fold difference (RUNX2/GAPDH)
0.08
0.06
0.04
0.02
0.00
40:60
50:50
60:40
PS
PMMA
Glass
Surface
40:60
50:50
60:40
PS
PMMA
Glass
Fold difference (RUNX2/GAPDH)
7D
14D
TIME

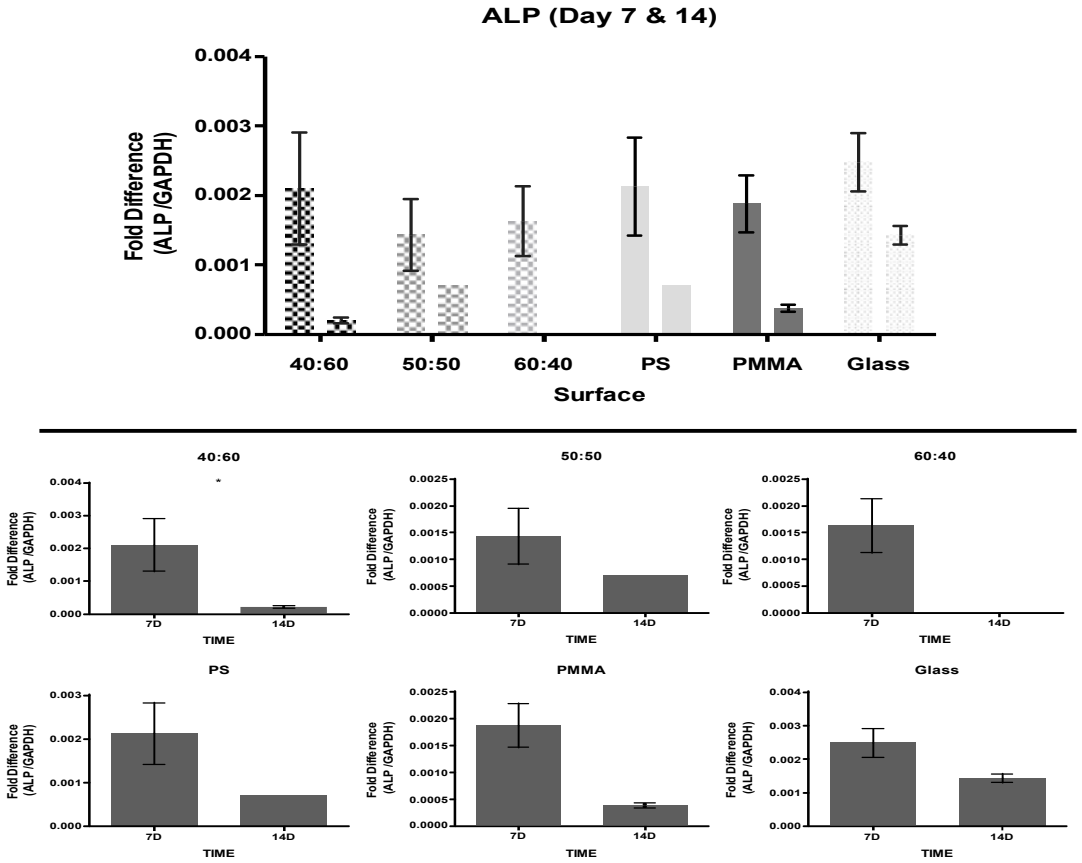
ALP (Day 7 & 14)
Fold Difference (ALP /GAPDH)
0.004
0.003
0.002
0.001
0.000
40:60
50:50
60:40
PS
PMMA
Glass
Surface
40:60
50:50
60:40
PS
PMMA
Glass
Fold Difference (ALP /GAPDH)
7D
14D
TIME

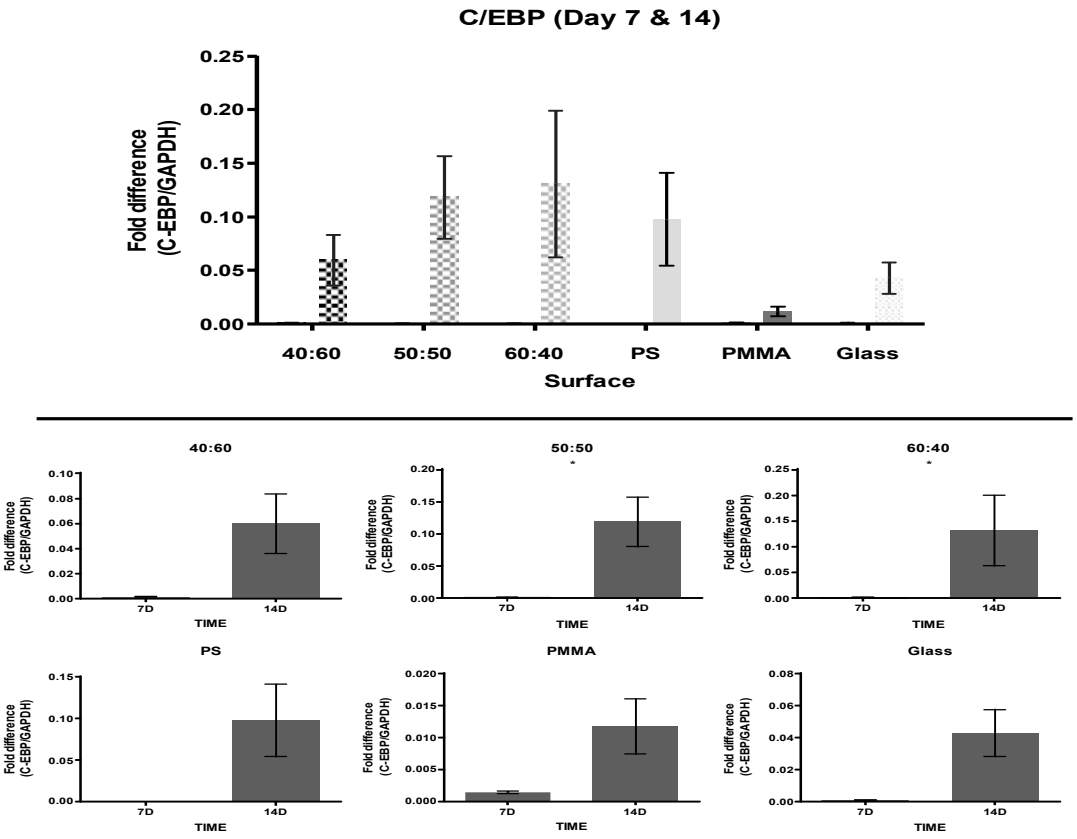

No FABP4 detected at Day7

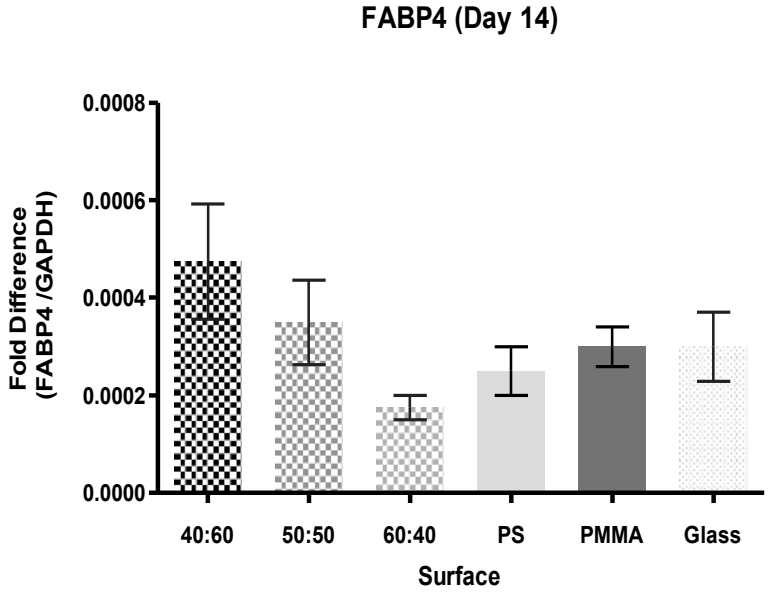

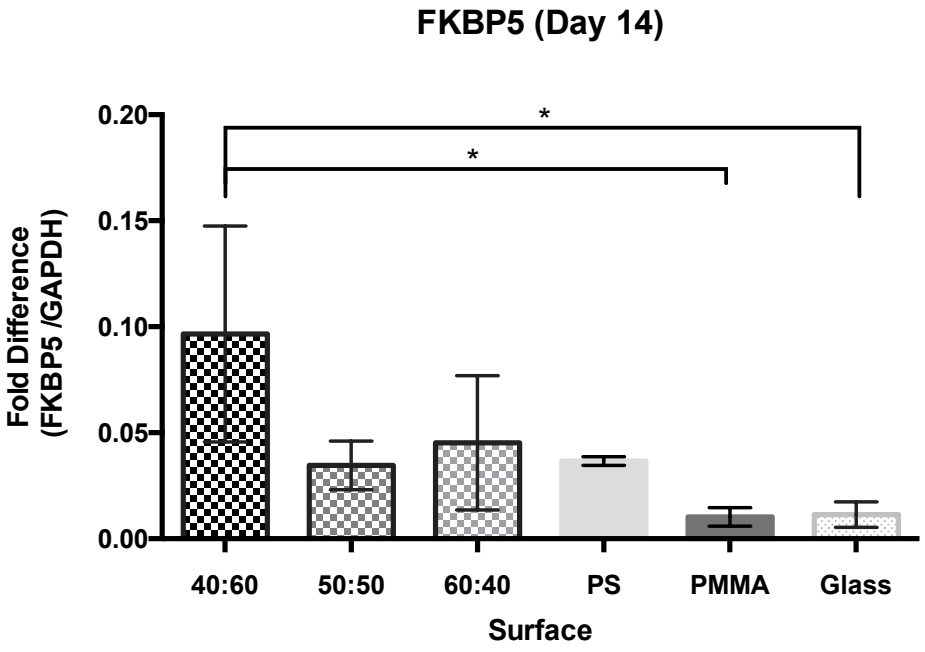
FKBP5 (Day 14)
Fold Difference (FKBP5 /GAPDH)
0.20
0.15
0.10
0.05
0.00
*
*
40:60
50:50
60:40
PS
PMMA
Glass
Surface

Y201.1 (plastic) 14 Days

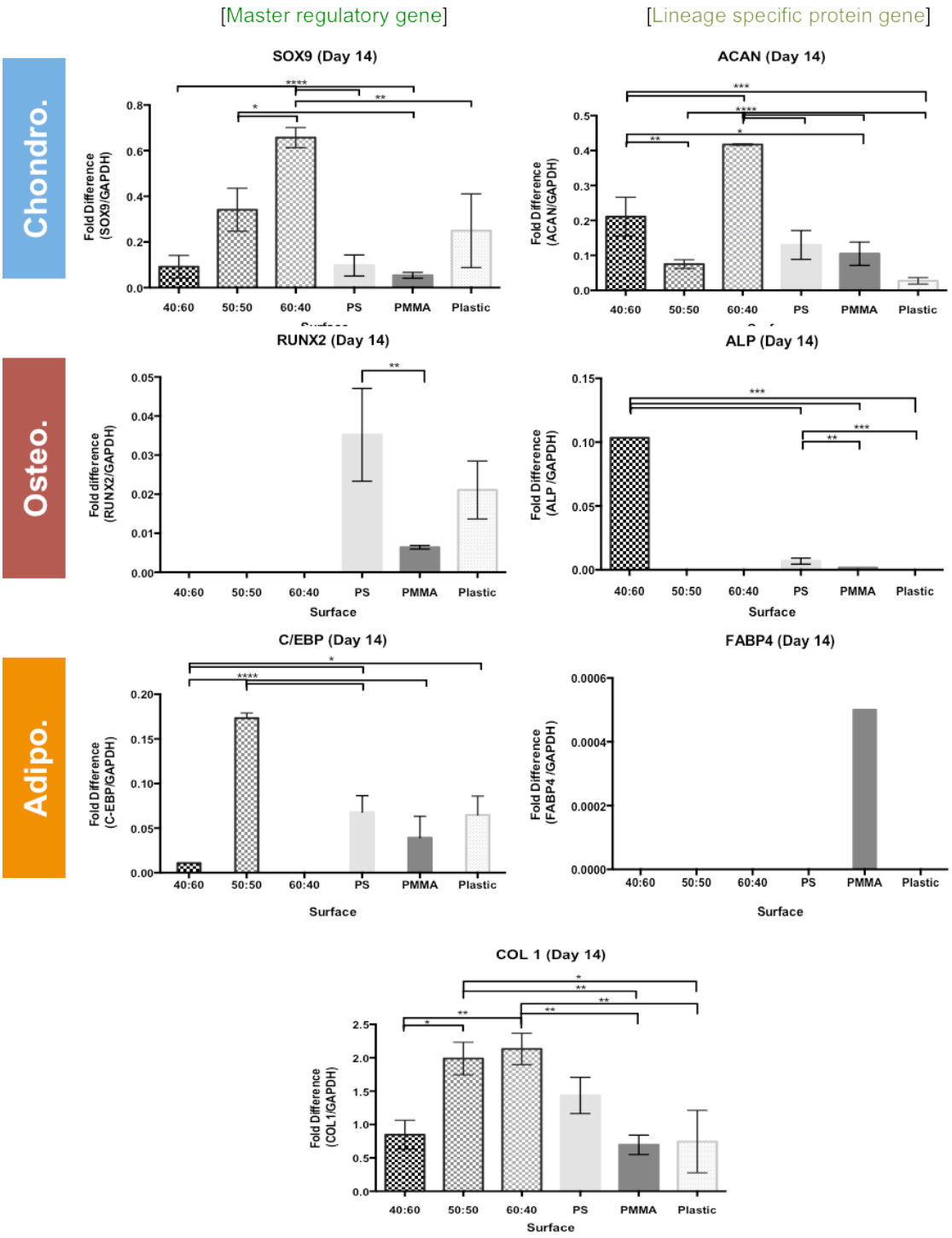

Figure 64. Real-time PCR results for different lineage gene expression of Y201 MSCs on panel of polymer surfaces, cultured for 14 days under standard culture conditions. Duplicate experiment as one in Chp.5 but Tissue culture plastic is used as control.

REFERENCES

1 Westone. *Cancellous (spongy) bone structure* <http://tle.westone.wa.gov.au/content/file/969144ed-0d3b-fa04-2e88-8b23de2a630c/1/human_bio_science_3b.zip/content/003_musculo_skeletal_support/page_06.htm>

2 Thermo-scientific_Peirce. *NHS and Sulfo-NHS*, <http://www.piercenet.com/browse.cfm?fldID=02040114>

3 Walheim, S., Böltau, M., Mlynek, J., Krausch, G. & Steiner, U. Structure Formation via Polymer Demixing in Spin-Cast Films. *Macromolecules* 30, 4995-5003, (1997).

4 Sophia Fox, A. J., Bedi, A. & Rodeo, S. A. The basic science of articular cartilage: structure, composition, and function. *Sports health* 1, 461-468, (2009).

5 Jahan-Tigh, R. R., Ryan, C., Obermoser, G. & Schwarzenberger, K. Flow cytometry. *The Journal of investigative dermatology* 132, e1, (2012).

6 Gierer, A. *et al.* Regeneration of hydra from reaggregated cells. *Nature: New biology* 239, 98-101 (1972).

7 Morgan, T. H. Experimental studies of the regeneration of Planaria maculata. *Archiv für Entwickelungsmechanik der Organismen* 7, 364-397, (1898).

8 Neeham, J. Biochemistry and Morphogenesis. *Cambridge University Press* (1942).

9 Simpson, S. B. Studies on Regeneration of the Lizard's Tail. *Am Zool* 10, 157-165, (1970).

10 Poss, K. D. Advances in understanding tissue regenerative capacity and mechanisms in animals. *Nature reviews. Genetics* 11, 710-722, (2010).

11 Illingworth, C. M. Trapped fingers and amputated finger tips in children. *J Pediatr Surg* 9, 853-858 (1974).

12 Takahashi, K. & Yamanaka, S. Induction of pluripotent stem cells from mouse embryonic and adult fibroblast cultures by defined factors. *Cell* 126, 663-676, (2006).

13 Conboy, I. M. *et al.* Rejuvenation of aged progenitor cells by exposure to a young systemic environment. *Nature* 433, 760-764, (2005).

14 Liu, H. *et al.* Augmented Wnt signaling in a mammalian model of accelerated aging. *Science* 317, 803-806, (2007).

15 Mason, C. & Dunnill, P. A brief definition of regenerative medicine. *Regen Med* 3, 1-5, (2008).

16 Langer, R. & Vacanti, J. P. Tissue engineering. *Science* 260, 920-926 (1993).

17 Cohen, S. *et al.* Design of synthetic polymeric structures for cell transplantation and tissue engineering. *Clinical materials* 13, 3-10 (1993).

18 Vunjak-Novakovic, G. *et al.* Dynamic Cell Seeding of Polymer Scaffolds for Cartilage Tissue Engineering. *Biotechnology Progress* 14, 193-202, (1998).

19 Duan, B. & Wang, M. Customized Ca-P/PHBV nanocomposite scaffolds for bone tissue engineering: design, fabrication, surface modification and sustained release of growth factor. *Journal of the Royal Society, Interface / the Royal Society* 7 Suppl 5, S615-629, (2010).

20 Gilbert, S. F. *Developmental biology*. 6th edn, (Sinauer Associates, 2000).

21 Bruder, S. P. & Caplan, A. I. Cellular and molecular events during embryonic bone development. *Connective tissue research* **20**, 65-71 (1989).

22 Weiner, S. & Wagner, H. D. The material bone: structure-mechanical function relations. *Annual Review of Materials Science* **28**, 271-298 (1998).

23 Civitelli, R. Cell-cell communication in the osteoblast/osteocyte lineage. *Archives of biochemistry and biophysics* 473, 188-192, (2008).
24 Ash, P., Loutit, J. F. & Townsend, K. M. Osteoclasts derived from haematopoietic stem cells. *Nature* 283, 669-670 (1980).
25 Tondravi, M. M. *et al.* Osteopetrosis in mice lacking haematopoietic transcription factor PU.1. *Nature* 386, 81-84, (1997).
26 Pittenger, M. F. *et al.* Multilineage potential of adult human mesenchymal stem cells. *Science* 284, 143-147 (1999).
27 Eggenhofer, E., Luk, F., Dahlke, M. H. & Hoogduijn, M. J. The life and fate of mesenchymal stem cells. *Frontiers in immunology* 5, 148, (2014).
28 Barry, F. & Murphy, M. Mesenchymal stem cells in joint disease and repair. *Nature reviews. Rheumatology* 9, 584-594, (2013).
29 Otsuru, S. *et al.* Transplanted bone marrow mononuclear cells and MSCs impart clinical benefit to children with osteogenesis imperfecta through different mechanisms. *Blood* 120, 1933-1941, (2012).
30 Muir, H. The chondrocyte, architect of cartilage. Biomechanics, structure, function and molecular biology of cartilage matrix macromolecules. *Bioessays* 17, 1039-1048, (1995).
31 Ghosh, P. & Smith, M. Osteoarthritis, genetic and molecular mechanisms. *Biogerontology* 3, 85-88 (2002).
32 Bruckner, P. & van der Rest, M. Structure and function of cartilage collagens. *Microsc Res Tech* 28, 378-384, (1994).
33 Setton, L. A., Zhu, W. & Mow, V. C. The biphasic poroviscoelastic behavior of articular cartilage: role of the surface zone in governing the compressive behavior. *J Biomech* 26, 581-592, (1993).
34 Maroudas, A. I. Balance between swelling pressure and collagen tension in normal and degenerate cartilage. *Nature* 260, 808-809 (1976).
35 Carney, S. L. & Muir, H. The structure and function of cartilage proteoglycans. *Physiol Rev* 68, 858-910 (1988).
36 Scott, J. E. Proteodermatan and proteokeratan sulfate (decorin, lumican/fibromodulin) proteins are horseshoe shaped. Implications for their interactions with collagen. *Biochemistry-Us* 35, 8795-8799 (1996).
37 Murray, C. J. *et al.* UK health performance: findings of the Global Burden of Disease Study 2010. *Lancet* 381, 997-1020, (2013).
38 International Cartilage Repair Society Cartilage Injury Evaluation (2000).
39 Scopp, J. M. & Mandelbaum, B. R. A Treatment Algorithm for the Management of Articular Cartilage Defects. *Orthopedic Clinics* 36, 419-426, (2005).
40 Cawston, T. *et al.* The regulation of MMPs and TIMPs in cartilage turnover. *Annals of the New York Academy of Sciences* 878, 120-129 (1999).
41 Pelletier, J., Martel-Pelletier J, Howell DS. Arthritis & Allied Conditions. A Textbook of Rheumatology. *Koopman WJ* Williams & Wilkins (2000).
42 Smith, A. J., Dieppe, P., Howard, P. W. & Blom, A. W. Failure rates of metal-on-metal hip resurfacings: analysis of data from the National Joint Registry for England and Wales. *Lancet* 380, 1759-1766, (2012).
43 OECD. *Health at a Glance 2013*. (OECD Publishing, 2013).
44 Chen, A., Gupte, C., Akhtar, K., Smith, P. & Cobb, J. The Global Economic Cost of Osteoarthritis: How the UK Compares. *Arthritis* 2012, 6, (2012).
45 Paunipagar, B. K. & Rasalkar, D. Imaging of articular cartilage. *The Indian journal of radiology & imaging* 24, 237-248, (2014).
46 Gurtner, G. C., Werner, S., Barrandon, Y. & Longaker, M. T. Wound repair and regeneration. *Nature* 453, 314-321 (2008).

47 Mankin, H. J. *The response of articular cartilage to mechanical injury*. Vol. 64 (1982).
48 Learmonth, I. D., Young, C. & Rorabeck, C. The operation of the century: total hip replacement. *Lancet* 370, 1508-1519, (2007).
49 Malviya, A. & McCaskie, A. Surgery for osteoarthritis. *Medicine* 34, 369-372 (2006).
50 Lieberman, J. R. & Hsu, W. K. Prevention of venous thromboembolic disease after total hipand knee arthroplasty. *J Bone Joint Surg Am* 87A, 2097-2112, (2005).
51 Straw, R. & Moran, C. Hip and knee replacement. *The Practitioner* 246, 741, 744-746, (2002).
52 Dan Daniels A U, T. R. E., Harkess J W. . *Arthroplasty: introduction and overview.*, Vol. 9th ed (Campbell's operative orthopaedics. , 1998).
53 Konyves, A. & Bannister, G. C. The importance of leg length discrepancy after total hip arthroplasty. *J Bone Joint Surg Br* 87B, 155-157, (2005).
54 Malchau, H., Herberts, P., Eisler, T., Garellick, G. & Soderman, P. The Swedish total hip replacement register. *J Bone Joint Surg Am* 84A, 2-20 (2002).
55 Morrey, B. F. Results of reoperation for hip dislocation - The big picture. *Clin Orthop Relat R*, 94-101, (2004).
56 Alexey, B. Results of regenerative medicine clinical studies from 2014. *CellTrials blog.* (2015, March 1.).
57 VanEnkevort, B. A., Markel, M. D. & Manley, P. A. Alterations in bone remodeling in the femur after medullary reaming and cemented hip arthroplasty in dogs. *American journal of veterinary research* 60, 922-928 (1999).
58 Calvi, L. M. *et al.* Osteoblastic cells regulate the haematopoietic stem cell niche. *Nature* 425, 841-846, (2003).
59 Kim, H. N. *et al.* Nanotopography-guided tissue engineering and regenerative medicine. *Advanced drug delivery reviews* 65, 536-558, (2013).
60 Dalby, M. J., Gadegaard, N., Curtis, A. S. & Oreffo, R. O. Nanotopographical control of human osteoprogenitor differentiation. *Current stem cell research & therapy* 2, 129-138 (2007).
61 Dalby, M. J. *et al.* The control of human mesenchymal cell differentiation using nanoscale symmetry and disorder. *Nature materials* 6, 997-1003, (2007).
62 McMurray, R. J. *et al.* Nanoscale surfaces for the long-term maintenance of mesenchymal stem cell phenotype and multipotency. *Nature materials* 10, 637-644, (2011).
63 Bannuru, R. R., Natov, N. S., Dasi, U. R., Schmid, C. H. & McAlindon, T. E. Therapeutic trajectory following intra-articular hyaluronic acid injection in knee osteoarthritis--meta-analysis. *Osteoarthritis Cartilage* 19, 611-619, (2011).
64 Brittberg, M. *et al.* Treatment of Deep Cartilage Defects in the Knee with Autologous Chondrocyte Transplantation. *New Engl J Med* 331, 889-895 (1994).
65 Brittberg, M. *et al.* Treatment of deep cartilage defects in the knee with autologous chondrocyte transplantation. *The New England journal of medicine* 331, 889-895, (1994).
66 Steadman, J. R. *et al.* Outcomes of microfracture for traumatic chondral defects of the knee: Average 11-year follow-up. *Arthroscopy* 19, 477-484, (2003).
67 Punwar, S. & Khan, W. S. Mesenchymal stem cells and articular cartilage repair: clinical studies and future direction. *The open orthopaedics journal* 5 Suppl 2, 296-301, (2011).
68 Steinert, A. F., Rackwitz, L., Gilbert, F., Nöth, U. & Tuan, R. S. Concise Review: The Clinical Application of Mesenchymal Stem Cells for

Musculoskeletal Regeneration: Current Status and Perspectives. *Stem Cells Translational Medicine* 1, 237-247 (2012).

69 Blanc, K. L. & Pittenger, M. F. Mesenchymal stem cells: progress toward promise. *Cytotherapy* 7, 36 - 45 (2005).

70 Murphy, J. M., Fink, D. J., Hunziker, E. B. & Barry, F. P. Stem cell therapy in a caprine model of osteoarthritis. *Arthritis Rheum* 48, 3464-3474, (2003).

71 Davatchi, F., Abdollahi, B. S., Mohyeddin, M., Shahram, F. & Nikbin, B. Mesenchymal stem cell therapy for knee osteoarthritis. Preliminary report of four patients. *International journal of rheumatic diseases* 14, 211-215, (2011).

72 Nejadnik, H., Hui, J. H., Feng Choong, E. P., Tai, B. C. & Lee, E. H. Autologous bone marrow-derived mesenchymal stem cells versus autologous chondrocyte implantation: an observational cohort study. *The American journal of sports medicine* 38, 1110-1116, (2010).

73 Kaneshiro, N. *et al.* Bioengineered chondrocyte sheets may be potentially useful for the treatment of partial thickness defects of articular cartilage. *Biochemical and biophysical research communications* 349, 723-731, (2006).

74 Wakitani, S. *et al.* Human autologous culture expanded bone marrow mesenchymal cell transplantation for repair of cartilage defects in osteoarthritic knees. *Osteoarthritis Cartilage* 10, 199-206, (2002).

75 Haleem, A. M. *et al.* The Clinical Use of Human Culture-Expanded Autologous Bone Marrow Mesenchymal Stem Cells Transplanted on Platelet-Rich Fibrin Glue in the Treatment of Articular Cartilage Defects: A Pilot Study and Preliminary Results. *Cartilage* 1, 253-261, (2010).

76 Kuroda, R. *et al.* Treatment of a full-thickness articular cartilage defect in the femoral condyle of an athlete with autologous bone-marrow stromal cells. *Osteoarthritis Cartilage* 15, 226-231, (2007).

77 Wagner, W., Ho, A. D. & Zenke, M. Different facets of aging in human mesenchymal stem cells. *Tissue engineering. Part B, Reviews* 16, 445-453, (2010).

78 Rombouts, W. J. & Ploemacher, R. E. Primary murine MSC show highly efficient homing to the bone marrow but lose homing ability following culture. *Leukemia* 17, 160-170, (2003).

79 Eggenhofer, E. *et al.* Heart grafts tolerized through third-party multipotent adult progenitor cells can be retransplanted to secondary hosts with no immunosuppression. *Stem Cells Transl Med* 2, 595-606, (2013).

80 Jaklenec, A., Stamp, A., Deweerd, E., Sherwin, A. & Langer, R. Progress in the tissue engineering and stem cell industry "are we there yet?". *Tissue engineering. Part B, Reviews* 18, 155-166, (2012).

81 Saw, K. Y. *et al.* Articular cartilage regeneration with autologous peripheral blood stem cells versus hyaluronic acid: a randomized controlled trial. *Arthroscopy : the journal of arthroscopic & related surgery : official publication of the Arthroscopy Association of North America and the International Arthroscopy Association* 29, 684-694, (2013).

82 Hubbell, M. P. L. a. J. A. in *Advances in Tissue Engineering* (edt. Julia Polak co-editors Sakis Mantalaris and Sian E. Harding) Ch. 13, 253-271 (Imperial College Press, 2008).

83 Gentile, P. *et al.* Composite films of gelatin and hydroxyapatite/bioactive glass for tissue-engineering applications. *Journal of biomaterials science. Polymer edition* 21, 1207-1226, (2010).

84 Abou Neel, E. A. *et al.* Collagen--emerging collagen based therapies hit the patient. *Advanced drug delivery reviews* 65, 429-456, (2013).

85 Cen, L., Liu, W., Cui, L., Zhang, W. & Cao, Y. Collagen tissue engineering: development of novel biomaterials and applications. *Pediatric research* 63, 492-496, (2008).
86 Mithieux, S. M., Wise, S. G. & Weiss, A. S. Tropoelastin--a multifaceted naturally smart material. *Advanced drug delivery reviews* 65, 421-428, (2013).
87 Kundu, B., Rajkhowa, R., Kundu, S. C. & Wang, X. Silk fibroin biomaterials for tissue regenerations. *Advanced drug delivery reviews* 65, 457-470, (2013).
88 Lakhkar, N. J. *et al.* Bone formation controlled by biologically relevant inorganic ions: role and controlled delivery from phosphate-based glasses. *Advanced drug delivery reviews* 65, 405-420, (2013).
89 Perez, R. A., Won, J. E., Knowles, J. C. & Kim, H. W. Naturally and synthetic smart composite biomaterials for tissue regeneration. *Advanced drug delivery reviews* 65, 471-496, (2013).
90 Chan, A., Orme, R. P., Fricker, R. A. & Roach, P. Remote and local control of stimuli responsive materials for therapeutic applications. *Advanced drug delivery reviews* 65, 497-514, (2013).
91 Chang, Y. *et al.* Dual-thermoresponsive phase behavior of blood compatible zwitterionic copolymers containing nonionic poly(N-isopropyl acrylamide). *Biomacromolecules* 10, 2092-2100, (2009).
92 Huang, W. M. *et al.* Shaping tissue with shape memory materials. *Advanced drug delivery reviews* 65, 515-535, (2013).
93 Grande, D. A., Pitman, M. I., Peterson, L., Menche, D. & Klein, M. The repair of experimentally produced defects in rabbit articular cartilage by autologous chondrocyte transplantation. *Journal of orthopaedic research : official publication of the Orthopaedic Research Society* **7**, 208-218, (1989).
94 Steadman, J. R., Rodkey, W. G., Briggs, K. K. & Rodrigo, J. J. [The microfracture technic in the management of complete cartilage defects in the knee joint]. *Der Orthopade* 28, 26-32 (1999).
95 de Girolamo, L., Bertolini, G., Cervellin, M., Sozzi, G. & Volpi, P. Treatment of chondral defects of the knee with one step matrix-assisted technique enhanced by autologous concentrated bone marrow: in vitro characterisation of mesenchymal stem cells from iliac crest and subchondral bone. *Injury* 41, 1172-1177, (2010).
96 De Bari, C. Skeletal muscle repair by adult human mesenchymal stem cells from synovial membrane. *J. Cell Biol.* 160, 909-918 (2003).
97 Brady, M. A., Waldman, S. D. & Ethier, C. R. The Application of Multiple Biophysical Cues to Engineer Functional Neocartilage for Treatment of Osteoarthritis. Part I: Cellular Response. *Tissue engineering. Part B, Reviews* 21, 1-19, (2015).
98 Ponte, A. L. *et al.* The in vitro migration capacity of human bone marrow mesenchymal stem cells: comparison of chemokine and growth factor chemotactic activities. *Stem Cells* 25, 1737-1745, (2007).
99 Lysaght, M. J., Jaklenec, A. & Deweerd, E. Great expectations: private sector activity in tissue engineering, regenerative medicine, and stem cell therapeutics. *Tissue engineering. Part A* 14, 305-315, (2008).
100 McNamara, L. E. *et al.* Nanotopographical control of stem cell differentiation. *Journal of tissue engineering* 2010, 120623, (2010).
101 Perez, R. A., Won, J. E., Knowles, J. C. & Kim, H. W. Naturally and synthetic smart composite biomaterials for tissue regeneration. *Advanced drug delivery reviews*, (2012).
102 Union, T. E. E. in *Opinion on the State of the Art* (2001).

103 Diaz-Romero, J., Nesic, D., Grogan, S. P., Heini, P. & Mainil-Varlet, P. Immunophenotypic changes of human articular chondrocytes during monolayer culture reflect bona fide dedifferentiation rather than amplification of progenitor cells. *J Cell Physiol* 214, 75-83, (2008).
104 O'Brien, T. & Barry, F. P. Stem cell therapy and regenerative medicine. *Mayo Clinic proceedings. Mayo Clinic* 84, 859-861, (2009).
105 Barry, F. P. Biology and clinical applications of mesenchymal stem cells. *Birth Defects Res C Embryo Today* 69, 250-256, (2003).
106 Schenk, S. & Quaranta, V. Tales from the crypt[ic] sites of the extracellular matrix. *Trends in cell biology* 13, 366-375 (2003).
107 Pierschbacher, M. D. & Ruoslahti, E. Cell attachment activity of fibronectin can be duplicated by small synthetic fragments of the molecule. *Nature* 309, 30-33 (1984).
108 Lee, C. H. Regeneration of the articular surface of the rabbit synovial joint by cell homing: a proof of concept study. *Lancet* 376, 440-448 (2010).
109 Singh, M., Berkland, C. & Detamore, M. S. Strategies and applications for incorporating physical and chemical signal gradients in tissue engineering. *Tissue engineering. Part B, Reviews* 14, 341-366, (2008).
110 Atala, A., Bauer, S. B., Soker, S., Yoo, J. J. & Retik, A. B. Tissue-engineered autologous bladders for patients needing cystoplasty. *Lancet* 367, 1241-1246, (2006).
111 Macchiarini, P. *et al.* Clinical transplantation of a tissue-engineered airway. *Lancet* 372, 2023-2030, (2008).
112 Damien, C. J. & Parsons, J. R. Bone graft and bone graft substitutes: a review of current technology and applications. *Journal of applied biomaterials : an official journal of the Society for Biomaterials* 2, 187-208, (1991).
113 Urist, M. R. Bone: formation by autoinduction. *Science* 150, 893-899 (1965).
114 Sadr, N. *et al.* Enhancing the biological performance of synthetic polymeric materials by decoration with engineered, decellularized extracellular matrix. *Biomaterials* 33, 5085-5093, (2012).
115 Assis, A. C. *et al.* Time-dependent migration of systemically delivered bone marrow mesenchymal stem cells to the infarcted heart. *Cell transplantation* 19, 219-230, (2010).
116 Barbash, I. M. *et al.* Systemic delivery of bone marrow-derived mesenchymal stem cells to the infarcted myocardium: feasibility, cell migration, and body distribution. *Circulation* 108, 863-868, (2003).
117 Eggenhofer, E. *et al.* Mesenchymal stem cells are short-lived and do not migrate beyond the lungs after intravenous infusion. *Frontiers in immunology* 3, 297, (2012).
118 Kunter, U. *et al.* Transplanted mesenchymal stem cells accelerate glomerular healing in experimental glomerulonephritis. *Journal of the American Society of Nephrology : JASN* 17, 2202-2212, (2006).
119 Amin, H. D. *et al.* Stimulation of chondrogenic differentiation of adult human bone marrow-derived stromal cells by a moderate-strength static magnetic field. *Tissue engineering. Part A* 20, 1612-1620, (2014).
120 Funk, R. H., Monsees, T. & Ozkucur, N. Electromagnetic effects - From cell biology to medicine. *Progress in histochemistry and cytochemistry* 43, 177-264, (2009).
121 Wong, M. & Carter, D. R. Articular cartilage functional histomorphology and mechanobiology: a research perspective. *Bone* 33, 1-13 (2003).

122 Chang, H. Y. *et al.* Diversity, topographic differentiation, and positional memory in human fibroblasts. *Proc Natl Acad Sci U S A* 99, 12877-12882, (2002).
123 Guilak, F. *et al.* Control of stem cell fate by physical interactions with the extracellular matrix. *Cell stem cell* 5, 17-26, (2009).
124 Halbleib, J. M. & Nelson, W. J. Cadherins in development: cell adhesion, sorting, and tissue morphogenesis. *Genes & development* 20, 3199-3214, (2006).
125 Cavey, M., Rauzi, M., Lenne, P. F. & Lecuit, T. A two-tiered mechanism for stabilization and immobilization of E-cadherin. *Nature* 453, 751-756, (2008).
126 Verkhovsky, A. B., Svitkina, T. M. & Borisy, G. G. Myosin II filament assemblies in the active lamella of fibroblasts: their morphogenesis and role in the formation of actin filament bundles. *The Journal of cell biology* 131, 989-1002 (1995).
127 Mammoto, T. *et al.* Mechanochemical control of mesenchymal condensation and embryonic tooth organ formation. *Developmental cell* 21, 758-769, (2011).
128 Clark, P., Connolly, P., Curtis, A. S., Dow, J. A. & Wilkinson, C. D. Cell guidance by ultrafine topography in vitro. *J Cell Sci* 99 (Pt 1), 73-77 (1991).
129 Curtis, A. S. & Wilkinson, C. D. Reactions of cells to topography. *Journal of biomaterials science. Polymer edition* 9, 1313-1329 (1998).
130 Discher, D. E., Janmey, P. & Wang, Y. L. Tissue cells feel and respond to the stiffness of their substrate. *Science* 310, 1139-1143, (2005).
131 Engler, A. J., Sen, S., Sweeney, H. L. & Discher, D. E. Matrix elasticity directs stem cell lineage specification. *Cell* 126, 677-689, (2006).
132 Kirmizidis, G. & Birch, M. A. Microfabricated grooved substrates influence cell-cell communication and osteoblast differentiation in vitro. *Tissue engineering. Part A* 15, 1427-1436, (2009).
133 Thery, M. *et al.* Anisotropy of cell adhesive microenvironment governs cell internal organization and orientation of polarity. *Proc Natl Acad Sci U S A* 103, 19771-19776, (2006).
134 Akimov, S. S. & Belkin, A. M. Cell-surface transglutaminase promotes fibronectin assembly via interaction with the gelatin-binding domain of fibronectin: a role in TGFbeta-dependent matrix deposition. *J Cell Sci* 114, 2989-3000 (2001).
135 Wells, R. G. & Discher, D. E. Matrix elasticity, cytoskeletal tension, and TGF-beta: the insoluble and soluble meet. *Science signaling* 1, pe13, (2008).
136 Zhang, D. & Kilian, K. A. The effect of mesenchymal stem cell shape on the maintenance of multipotency. *Biomaterials* 34, 3962-3969, (2013).
137 McNamara, L. E. *et al.* The role of microtopography in cellular mechanotransduction. *Biomaterials* 33, 2835-2847, (2012).
138 Ingber, D. E. Integrins, tensegrity, and mechanotransduction. *Gravitational and space biology bulletin : publication of the American Society for Gravitational and Space Biology* 10, 49-55 (1997).
139 Ingber, D. E. Tensegrity: the architectural basis of cellular mechanotransduction. *Annual review of physiology* 59, 575-599, (1997).
140 Weinbaum, S., Duan, Y., Satlin, L. M., Wang, T. & Weinstein, A. M. Mechanotransduction in the renal tubule. *American journal of physiology. Renal physiology* 299, F1220-1236, (2010).
141 Sperry, R. W. Chemoaffinity in the Orderly Growth of Nerve Fiber Patterns and Connections. *Proc Natl Acad Sci U S A* 50, 703-710 (1963).
142 Weber, G. F., Bjerke, M. A. & DeSimone, D. W. Integrins and cadherins join forces to form adhesive networks. *J Cell Sci* 124, 1183-1193, (2011).

143 Onodera, T. *et al.* Btbd7 regulates epithelial cell dynamics and branching morphogenesis. *Science* 329, 562-565, (2010).
144 Brieher, W. M. & Yap, A. S. Cadherin junctions and their cytoskeleton(s). *Current opinion in cell biology* 25, 39-46, (2013).
145 Radice, G. L. *et al.* Developmental defects in mouse embryos lacking N-cadherin. *Developmental biology* 181, 64-78, (1997).
146 Guan, X., Bidlack, F. B., Stokes, N. & Bartlett, J. D. E-cadherin can replace N-cadherin during secretory-stage enamel development. *Plos One* 9, e102153, (2014).
147 Keselowsky, B. G., Collard, D. M. & Garcia, A. J. Integrin binding specificity regulates biomaterial surface chemistry effects on cell differentiation. *Proc Natl Acad Sci U S A* 102, 5953-5957, (2005).
148 Song, J., Malathong, V. & Bertozzi, C. R. Mineralization of synthetic polymer scaffolds: a bottom-up approach for the development of artificial bone. *Journal of the American Chemical Society* 127, 3366-3372, (2005).
149 Liu, X. & Ma, P. X. Polymeric scaffolds for bone tissue engineering. *Annals of biomedical engineering* 32, 477-486 (2004).
150 Huang, L. *et al.* Synthesis and characterization of electroactive and biodegradable ABA block copolymer of polylactide and aniline pentamer. *Biomaterials* 28, 1741-1751, (2007).
151 Harirchian-Saei, S., Wang, M. C., Gates, B. D. & Moffitt, M. G. Directed polystyrene/poly(methyl methacrylate) phase separation and nanoparticle ordering on transparent chemically patterned substrates. *Langmuir : the ACS journal of surfaces and colloids* 28, 10838-10848, (2012).
152 Dalby, M. J., Riehle, M. O., Johnstone, H. J., Affrossman, S. & Curtis, A. S. Polymer-demixed nanotopography: control of fibroblast spreading and proliferation. *Tissue Eng* 8, 1099-1108, (2002).
153 Li, W. J., Laurencin, C. T., Caterson, E. J., Tuan, R. S. & Ko, F. K. Electrospun nanofibrous structure: a novel scaffold for tissue engineering. *J Biomed Mater Res* 60, 613-621 (2002).
154 Hollister, S. J. Porous scaffold design for tissue engineering. *Nature materials* 4, 518-524, (2005).
155 Dalby, M. J., Gadegaard, N. & Oreffo, R. O. Harnessing nanotopography and integrin-matrix interactions to influence stem cell fate. *Nature materials* 13, 558-569, (2014).
156 Gershman, A. B. a. S. in *Vacuum Technology and Coating* (ed Jinghong Shenzhen) (2008).
157 Sabatini, D. D., Bensch, K. & Barrnett, R. J. Cytochemistry and electron microscopy. The preservation of cellular ultrastructure and enzymatic activity by aldehyde fixation. *The Journal of cell biology* 17, 19-58 (1963).
158 S., C. A. a. V. Standard operating protocol (ref. OC02) MSC isolation from Bone. *OsteoCord:bone from blood* (2006).
159 Friedenstein, A. J., Chailakhyan, R. K. & Gerasimov, U. V. Bone-Marrow Osteogenic Stem-Cells - Invitro Cultivation and Transplantation in Diffusion-Chambers. *Cell Tissue Kinet* 20, 263-272 (1987).
160 Hung, S. C. *et al.* Isolation and characterization of size-sieved stem cells from human bone marrow. *Stem Cells* 20, 249-258, (2002).
161 Byun, J. W. *et al.* Evaluation of boar sperm viability by MTT reduction assay in beltsville thawing solution extender. *Asian Austral J Anim* 21, 494-498 (2008).
162 Shetty, P., Cooper, K. & Viswanathan, C. Comparison of proliferative and multilineage differentiation potentials of cord matrix, cord blood, and bone

marrow mesenchymal stem cells. *Asian journal of transfusion science* 4, 14-24, (2010).

163 Tew, S. R., Murdoch, A. D., Rauchenberg, R. P. & Hardingham, T. E. Cellular methods in cartilage research: primary human chondrocytes in culture and chondrogenesis in human bone marrow stem cells. *Methods* 45, 2-9, (2008).

164 Murdoch, A. D. *et al.* Chondrogenic differentiation of human bone marrow stem cells in transwell cultures: generation of scaffold-free cartilage. *Stem Cells* 25, 2786-2796, (2007).

165 Lee, J. W., Kim, Y. H., Kim, S. H., Han, S. H. & Hahn, S. B. Chondrogenic differentiation of mesenchymal stem cells and its clinical applications. *Yonsei Med J* 45, 41-47 (2004).

166 Baksh, D., Song, L. & Tuan, R. S. Adult mesenchymal stem cells: characterization, differentiation, and application in cell and gene therapy. *J Cell Mol Med* 8, 301-316 (2004).

167 Xu, J. P. *et al.* Chondrogenic differentiation of human mesenchymal stem cells in three-dimensional alginate gels. *Tissue Eng Pt A* 14, 667-680, (2008).

168 Tare, R. S., Howard, D., Pound, J. C., Roach, H. I. & Oreffo, R. O. Tissue engineering strategies for cartilage generation--micromass and three dimensional cultures using human chondrocytes and a continuous cell line. *Biochemical and biophysical research communications* 333, 609-621, (2005).

169 Jaiswal, N., Haynesworth, S. E., Caplan, A. I. & Bruder, S. P. Osteogenic differentiation of purified, culture-expanded human mesenchymal stem cells in vitro. *J Cell Biochem* 64, 295-312 (1997).

170 Dominici, M. Minimal criteria for defining multipotent mesenchymal stromal cells. The International Society for Cellular Therapy position statement. *Cytotherapy* 8, 315-317 (2006).

171 Lim, J. Y., Siedlecki, C. A. & Donahue, H. J. Nanotopographic cell culture substrate: polymer-demixed nanotextured films under cell culture conditions. *BioResearch open access* 1, 252-255, (2012).

172 Kim, D. H., Provenzano, P. P., Smith, C. L. & Levchenko, A. Matrix nanotopography as a regulator of cell function. *The Journal of cell biology* 197, 351-360, (2012).

173 Variola, F. *et al.* Nanoscale surface modifications of medically relevant metals: state-of-the art and perspectives. *Nanoscale* 3, 335-353, (2011).

174 Tanaka, K., Takahara, A. & Kajiyama, T. Film Thickness Dependence of the Surface Structure of Immiscible Polystyrene/Poly(methyl methacrylate) Blends. *Macromolecules* 29, 3232-3239, (1996).

175 Morin, C. *et al.* X-ray spectromicroscopy of immiscible polymer blends: Polystyrene-poly(methyl methacrylate). *Journal of Electron Spectroscopy and Related Phenomena* 121, 203-224 (2001).

176 Ton-That, C., Shard, A. G., Teare, D. O. H. & Bradley, R. H. XPS and AFM surface studies of solvent-cast PS/PMMA blends. *Polymer* 42, 1121-1129, (2001).

177 Ton-That, C., Shard, A. G. & Bradley, R. H. Surface feature size of spin cast PS/PMMA blends. *Polymer* 43, 4973-4977 (2002).

178 Dekeyser, C. M., Biltresse, S., Marchand-Brynaert, J., Rouxhet, P. G. & Dupont-Gillain, C. C. Submicrometer-scale heterogeneous surfaces by PS-PMMA demixing. *Polymer* 45, 2211-2219, (2004).

179 Zong, Q., Li, Z. & Xie, X. Inversion of Phase Morphology in Polymer-Blend Thin Films on Glass Substrates. *Macromolecular Chemistry and Physics* 205, 1116-1124, (2004).

180 Wu, S. Surface and interfacial tensions of polymer melts. II. Poly(methyl methacrylate), poly(n-butyl methacrylate), and polystyrene. *Journal of Physical Chemistry* 74, 632-638 (1970).
181 Ugur, S. & Pekcan, O. Effects of annealing on morphology of polymer/polymer (PS/PMMA) blend; a fluorescence study. *Journal of Applied Polymer Science* 100, 2104-2110, (2006).
182 Li, X., Han, Y. & An, L. Surface morphology control of immiscible polymer-blend thin films. *Polymer* 44, 8155-8165, (2003).
183 Heriot, S. Y. & Jones, R. A. L. An interfacial instability in a transient wetting layer leads to lateral phase separation in thin spin-cast polymer-blend films. *Nature materials* 4, 782-786, (2005).
184 Li, Y., Yang, Y., Yu, F. & Dong, L. - Surface and interface morphology of polystyrene/poly(methyl methacrylate) thin-film blends and bilayers. - 44, - 21 (2006).
185 Kawano, T. *et al.* Mechanical regulation of cellular adhesion onto honeycomb-patterned porous scaffolds by altering the elasticity of material surfaces. *Biomacromolecules* 14, 1208-1213, (2013).
186 Kawano, T., Sato, M., Yabu, H. & Shimomura, M. Honeycomb-shaped surface topography induces differentiation of human mesenchymal stem cells (hMSCs): uniform porous polymer scaffolds prepared by the breath figure technique. *Biomaterials Science* 2, 52-56, (2014).
187 Young, T. *Philos. Trans. R. Soc. Lond. 95, 65* (1805).
188 Bracco, G. & Holst, B. *Surface science techniques*. (Springer, 2013).
189 Jokinen, V., Suvanto, P. & Franssila, S. Oxygen and nitrogen plasma hydrophilization and hydrophobic recovery of polymers. *Biomicrofluidics* 6, 16501-1650110, (2012).
190 Russ, J. C. *The image processing handbook*. 6th edn, (CRC Press, 2011).
191 Science, B. *Spin Coating Theory*, <http://www.brewerscience.com/research/processing-theory/spin-coating-theory>(1997-2014).
192 Flack, W. W., Soong, D. S., Bell, A. T. & Hess, D. W. A mathematical model for spin coating of polymer resists. *J Appl Phys* 56, 1199-1206, (1984).
193 Bornside, D. E., Macosko, C. W. & Scriven, L. E. Spin Coating of a Pmma Chlorobenzene Solution. *J Electrochem Soc* 138, 317-320, (1991).
194 Steinmann, P. M. R. B. (Wiley-Liss Inc., New York, 2002).
195 Owen, M. Marrow stromal stem cells. *J Cell Sci Suppl* 10, 63-76 (1988).
196 Barry, F. P. & Murphy, J. M. Mesenchymal stem cells: clinical applications and biological characterization. *Int J Biochem Cell Biol* 36, 568-584, (2004).
197 Tran, D. *et al.* Hematoxylin and safranin O staining of frozen sections. *Dermatologic surgery : official publication for American Society for Dermatologic Surgery [et al.]* 26, 197-199 (2000).
198 Goldner, J. A modification of the masson trichrome technique for routine laboratory purposes. *The American journal of pathology* 14, 237-243 (1938).
199 Dominici, M. *et al.* Minimal criteria for defining multipotent mesenchymal stromal cells. The International Society for Cellular Therapy position statement. *Cytotherapy* 8, 315-317, (2006).
200 Winer, J. P., Janmey, P. A., McCormick, M. E. & Funaki, M. Bone marrow-derived human mesenchymal stem cells become quiescent on soft substrates but remain responsive to chemical or mechanical stimuli. *Tissue engineering. Part A* 15, 147-154, (2009).
201 Hamilton, D. W., Riehle, M. O., Monaghan, W. & Curtis, A. S. Articular chondrocyte passage number: influence on adhesion, migration, cytoskeletal

organisation and phenotype in response to nano- and micro-metric topography. *Cell biology international* 29, 408-421, (2005).

202 Dunlap, D., Cattelino, A., de Curtis, I. & Valtorta, F. Cytoplasmic topography of focal contacts. *FEBS Lett* 382, 65-72 (1996).

203 Hargrave, P. A. *et al.* The partial primary structure of bovine rhodopsin and its topography in the retinal rod cell disc membrane. *Neurochemistry international* 1C, 231-244 (1980).

204 Biggs, M. J., Richards, R. G., Gadegaard, N., Wilkinson, C. D. & Dalby, M. J. Regulation of implant surface cell adhesion: characterization and quantification of S-phase primary osteoblast adhesions on biomimetic nanoscale substrates. *Journal of orthopaedic research : official publication of the Orthopaedic Research Society* 25, 273-282, (2007).

205 Daley, W. P., Peters, S. B. & Larsen, M. Extracellular matrix dynamics in development and regenerative medicine. *J Cell Sci* 121, 255-264, (2008).

206 Trappmann, B. *et al.* Extracellular-matrix tethering regulates stem-cell fate. *Nature materials* 11, 642-649, (2012).

207 Folkman, J. & Moscona, A. Role of cell shape in growth control. *Nature* 273, 345-349 (1978).

208 Meyers, J., Craig, J. & Odde, D. J. Potential for control of signaling pathways via cell size and shape. *Current biology : CB* 16, 1685-1693, (2006).

209 Manasek, F. J., Burnside, M. B. & Waterman, R. E. Myocardial cell shape change as a mechanism of embryonic heart looping. *Developmental biology* 29, 349-371 (1972).

210 Johnstone, B., Hering, T. M., Caplan, A. I., Goldberg, V. M. & Yoo, J. U. In vitro chondrogenesis of bone marrow-derived mesenchymal progenitor cells. *Exp Cell Res* 238, 265-272, (1998).

211 Ingber, D. Extracellular matrix and cell shape: potential control points for inhibition of angiogenesis. *J Cell Biochem* 47, 236-241, (1991).

212 McBeath, R., Pirone, D. M., Nelson, C. M., Bhadriraju, K. & Chen, C. S. Cell shape, cytoskeletal tension, and RhoA regulate stem cell lineage commitment. *Developmental cell* 6, 483-495 (2004).

213 Chen, C. S., Alonso, J. L., Ostuni, E., Whitesides, G. M. & Ingber, D. E. Cell shape provides global control of focal adhesion assembly. *Biochemical and biophysical research communications* 307, 355-361 (2003).

214 Chen, H., Titushkin, I., Stroscio, M. & Cho, M. Altered membrane dynamics of quantum dot-conjugated integrins during osteogenic differentiation of human bone marrow derived progenitor cells. *Biophysical journal* 92, 1399-1408, (2007).

215 Titushkin, I. & Cho, M. Modulation of cellular mechanics during osteogenic differentiation of human mesenchymal stem cells. *Biophysical journal* 93, 3693-3702, (2007).

216 Yourek, G., Hussain, M. A. & Mao, J. J. Cytoskeletal changes of mesenchymal stem cells during differentiation. *ASAIO J* 53, 219-228, (2007).

217 Biggs, M. J. *et al.* The use of nanoscale topography to modulate the dynamics of adhesion formation in primary osteoblasts and ERK/MAPK signalling in STRO-1+ enriched skeletal stem cells. *Biomaterials* 30, 5094-5103, (2009).

218 Pilliar, R. M. Cementless implant fixation--toward improved reliability. *The Orthopedic clinics of North America* 36, 113-119, (2005).

219 Prendergast, P. J., Huiskes, R. & Søballe, K. Biophysical stimuli on cells during tissue differentiation at implant interfaces. *J Biomech* 30, 539-548, (1997).

220 Hwang, C. S., Loftus, T. M., Mandrup, S. & Lane, M. D. Adipocyte differentiation and leptin expression. *Annual review of cell and developmental biology* 13, 231-259, (1997).
221 Fischer, H. *et al.* Fatty acid binding protein 4 in human skeletal muscle. *Biochemical and biophysical research communications* 346, 125-130, (2006).
222 Jin, Y. H. *et al.* Transforming growth factor-beta stimulates p300-dependent RUNX3 acetylation, which inhibits ubiquitination-mediated degradation. *J Biol Chem* 279, 29409-29417, (2004).
223 Yoshida, C. A. *et al.* Core-binding factor beta interacts with Runx2 and is required for skeletal development. *Nature genetics* 32, 633-638, (2002).
224 Franceschi, R. T. & Xiao, G. Regulation of the osteoblast-specific transcription factor, Runx2: responsiveness to multiple signal transduction pathways. *J Cell Biochem* 88, 446-454, (2003).
225 Ziros, P. G. *et al.* The bone-specific transcriptional regulator Cbfa1 is a target of mechanical signals in osteoblastic cells. *J Biol Chem* 277, 23934-23941, (2002).
226 Marom, R., Shur, I., Solomon, R. & Benayahu, D. Characterization of adhesion and differentiation markers of osteogenic marrow stromal cells. *J Cell Physiol* 202, 41-48, (2005).
227 Lefebvre, V. & de Crombrugghe, B. Toward understanding SOX9 function in chondrocyte differentiation. *Matrix biology : journal of the International Society for Matrix Biology* 16, 529-540 (1998).
228 Lefebvre, V., Huang, W., Harley, V. R., Goodfellow, P. N. & de Crombrugghe, B. SOX9 is a potent activator of the chondrocyte-specific enhancer of the pro alpha1(II) collagen gene. *Molecular and cellular biology* 17, 2336-2346 (1997).
229 Zhao, Q., Eberspaecher, H., Lefebvre, V. & De Crombrugghe, B. Parallel expression of Sox9 and Col2a1 in cells undergoing chondrogenesis. *Developmental dynamics : an official publication of the American Association of Anatomists* 209, 377-386, (1997).
230 Ng, L. J. *et al.* SOX9 binds DNA, activates transcription, and coexpresses with type II collagen during chondrogenesis in the mouse. *Developmental biology* 183, 108-121, (1997).
231 Zhou, G. *et al.* Dominance of SOX9 function over RUNX2 during skeletogenesis. *Proc Natl Acad Sci U S A* 103, 19004-19009, (2006).
232 Furumatsu, T., Tsuda, M., Taniguchi, N., Tajima, Y. & Asahara, H. Smad3 induces chondrogenesis through the activation of SOX9 via CREB-binding protein/p300 recruitment. *J Biol Chem* 280, 8343-8350, (2005).
233 Tew, S. R. & Hardingham, T. E. Regulation of SOX9 mRNA in human articular chondrocytes involving p38 MAPK activation and mRNA stabilization. *J Biol Chem* 281, 39471-39479, (2006).
234 Gleghorn, L., Ramesar, R., Beighton, P. & Wallis, G. A mutation in the variable repeat region of the aggrecan gene (AGC1) causes a form of spondyloepiphyseal dysplasia associated with severe, premature osteoarthritis. *American journal of human genetics* 77, 484-490, (2005).
235 Kashiwagi, M., Tortorella, M., Nagase, H. & Brew, K. TIMP-3 is a potent inhibitor of aggrecanase 1 (ADAM-TS4) and aggrecanase 2 (ADAM-TS5). *J Biol Chem* 276, 12501-12504, (2001).
236 Sandy, J. D. & Verscharen, C. Analysis of aggrecan in human knee cartilage and synovial fluid indicates that aggrecanase (ADAMTS) activity is responsible for the catabolic turnover and loss of whole aggrecan whereas other protease activity is required for C-terminal processing in vivo. *The Biochemical journal* 358, 615-626 (2001).

237 Estes, B. T., Wu, A. W. & Guilak, F. Potent induction of chondrocytic differentiation of human adipose-derived adult stem cells by bone morphogenetic protein 6. *Arthritis Rheum* 54, 1222-1232, (2006).
238 Vandesompele, J. *et al.* Accurate normalization of real-time quantitative RT-PCR data by geometric averaging of multiple internal control genes. *Genome biology* 3, (2002).
239 Liu, T. M. *et al.* Identification of Common Pathways Mediating Differentiation of Bone Marrow- and Adipose Tissue-Derived Human Mesenchymal Stem Cells into Three Mesenchymal Lineages. *Stem Cells* 25, 750-760, (2007).
240 Hutmacher, D. W., Schantz, J. T., Lam, C. X., Tan, K. C. & Lim, T. C. State of the art and future directions of scaffold-based bone engineering from a biomaterials perspective. *Journal of tissue engineering and regenerative medicine* 1, 245-260, (2007).
241 Rosso, F., Giordano, A., Barbarisi, M. & Barbarisi, A. From cell-ECM interactions to tissue engineering. *J Cell Physiol* 199, 174-180, (2004).
242 McBride, S. H., Falls, T. & Knothe Tate, M. L. Modulation of stem cell shape and fate B: mechanical modulation of cell shape and gene expression. *Tissue engineering. Part A* 14, 1573-1580, (2008).
243 Erickson, I. E. *et al.* High Mesenchymal Stem Cell Seeding Densities in Hyaluronic Acid Hydrogels Produce Engineered Cartilage with Native Tissue Properties. *Acta Biomaterialia*, (2012).
244 Awad, H. A., Wickham, M. Q., Leddy, H. A., Gimble, J. M. & Guilak, F. Chondrogenic differentiation of adipose-derived adult stem cells in agarose, alginate, and gelatin scaffolds. *Biomaterials* 25, 3211-3222, (2004).
245 Hamilton, D. W., Riehle, M. O., Monaghan, W. & Curtis, A. S. Chondrocyte aggregation on micrometric surface topography: a time-lapse study. *Tissue Eng* 12, 189-199, (2006).
246 Zuyderhoff, E. M. & Dupont-Gillain, C. C. Nano-organized Collagen Layers Obtained by Adsorption on Phase-Separated Polymer Thin Films. *Langmuir : the ACS journal of surfaces and colloids* 28, 2007-2014, (2012).
247 Christensen, A. P. & Corey, D. P. TRP channels in mechanosensation: direct or indirect activation? *Nature reviews. Neuroscience* 8, 510-521, (2007).
248 Mehta, D. *et al.* RhoA Interaction with Inositol 1,4,5-Trisphosphate Receptor and Transient Receptor Potential Channel-1 Regulates Ca2+ Entry: ROLE IN SIGNALING INCREASED ENDOTHELIAL PERMEABILITY. *Journal of Biological Chemistry* 278, 33492-33500, (2003).
249 Barnes, W. G. *et al.* beta-Arrestin 1 and Galphaq/11 coordinately activate RhoA and stress fiber formation following receptor stimulation. *J Biol Chem* 280, 8041-8050, (2005).
250 Beech, D. J. TRPC1: store-operated channel and more. *Pflugers Archiv : European journal of physiology* 451, 53-60, (2005).
251 Zhang, Z. & Bourque, C. W. Amplification of transducer gain by angiotensin II-mediated enhancement of cortical actin density in osmosensory neurons. *The Journal of neuroscience : the official journal of the Society for Neuroscience* 28, 9536-9544, (2008).
252 Janson, I. A., Kong, Y. P. & Putnam, A. J. Nanotopographic substrates of poly (methyl methacrylate) do not strongly influence the osteogenic phenotype of mesenchymal stem cells in vitro. *Plos One* 9, (2014).
253 Xu, J. *et al.* Chondrogenic differentiation of human mesenchymal stem cells in three-dimensional alginate gels. *Tissue engineering. Part A* 14, 667-680, (2008).
254 Tacchetti, C. *et al.* Cell condensation in chondrogenic differentiation. *Exp Cell Res* 200, 26-33 (1992).

255 Shekaran, A. & Garcia, A. J. Nanoscale engineering of extracellular matrix-mimetic bioadhesive surfaces and implants for tissue engineering. *Bba-Gen Subjects* 1810, 350-360, (2011).
256 Bueno, E. M. & Glowacki, J. Cell-free and cell-based approaches for bone regeneration. *Nature reviews. Rheumatology* 5, 685-697, (2009).
257 Shekaran, A. & Garcia, A. J. Extracellular matrix-mimetic adhesive biomaterials for bone repair. *Journal of Biomedical Materials Research Part A* 96A, 261-272, (2011).
258 Pei, M., He, F. & Kish, V. L. Expansion on extracellular matrix deposited by human bone marrow stromal cells facilitates stem cell proliferation and tissue-specific lineage potential. *Tissue engineering. Part A* 17, 3067-3076, (2011).
259 Datta, N., Holtorf, H. L., Sikavitsas, V. I., Jansen, J. A. & Mikos, A. G. Effect of bone extracellular matrix synthesized in vitro on the osteoblastic differentiation of marrow stromal cells. *Biomaterials* 26, 971-977, (2005).
260 Chrzanowski, W. & Khademhosseini, A. Biologically inspired 'smart' materials. *Advanced drug delivery reviews* 65, 403-404, (2013).
261 Roque, A. I. *et al.* Reversible non-stick behaviour of a bacterial protein polymer provides a tuneable molecular mimic for cell and tissue engineering. *Adv Mater* 26, 2704-2709, 2616, (2014).
262 Gekle, M., Mildenberger, S., Freudinger, R. & Silbernagl, S. Functional characterization of albumin binding to the apical membrane of OK cells. *The American journal of physiology* 271, (1996).
263 Fosset, M., Chappelet-Tordo, D. & Lazdunski, M. Intestinal alkaline phosphatase. Physical properties and quaternary structure. *Biochemistry-Us* 13, 1783-1788 (1974).
264 Morton, R. K. The substrate specificity and inhibition of alkaline phosphatases of cow's milk and calf intestinal mucosa. *The Biochemical journal* 61, 232-240 (1955).
265 Zhao, C. *et al.* Effects of a lubricin-containing compound on the results of flexor tendon repair in a canine model in vivo. *The Journal of bone and joint surgery. American volume* 92, 1453-1461, (2010).
266 Doi, Y. & Abe, H. Structural effects on biodegradation of aliphatic polyesters. *Macromolecular Symposia* 118, 725-731, (1997).
267 Vroman, I. & Tighzert, L. Biodegradable polymers. *Materials* 2, 307-344 (2009).
268 Murray, E., Thompson, B. C., Sayyar, S. & Wallace, G. G. Enzymatic degradation of graphene/polycaprolactone materials for tissue engineering. *Polymer Degradation and Stability* 111, 71-77, (2015).
269 Nair, L. S. & Laurencin, C. T. Biodegradable polymers as biomaterials. *Progress in Polymer Science* 32, 762-798, (2007).
270 Bhavsar, M. D. & Amiji, M. M. Development of novel biodegradable polymeric nanoparticles-in-microsphere formulation for local plasmid DNA delivery in the gastrointestinal tract. *AAPS PharmSciTech* 9, 288-294, (2008).
271 Liu, H. W., Chen, C. H., Tsai, C. L. & Hsiue, G. H. Targeted delivery system for juxtacrine signaling growth factor based on rhBMP-2-mediated carrier-protein conjugation. *Bone* 39, 825-836, (2006).
272 Alberti, K. *et al.* Functional immobilization of signaling proteins enables control of stem cell fate. *Nature methods* 5, 645-650, (2008).
273 Klenkler, B. J. & Sheardown, H. Characterization of EGF coupling to aminated silicone rubber surfaces. *Biotechnology and bioengineering* 95, 1158-1166, (2006).

274 Ben-David, D. *et al.* Low dose BMP-2 treatment for bone repair using a PEGylated fibrinogen hydrogel matrix. *Biomaterials* 34, 2902-2910, (2013).
275 Mann, B. K., Schmedlen, R. H. & West, J. L. Tethered-TGF-beta increases extracellular matrix production of vascular smooth muscle cells. *Biomaterials* 22, 439-444 (2001).
276 Park, M. S. & Kim, J. K. Breath figure patterns prepared by spin coating in a dry environment. *Langmuir : the ACS journal of surfaces and colloids* 20, 5347-5352 (2004).
277 Wojciak-Stothard, B., Curtis, A., Monaghan, W., MacDonald, K. & Wilkinson, C. Guidance and activation of murine macrophages by nanometric scale topography. *Exp Cell Res* 223, 426-435, (1996).
278 Dalby, M. J. *et al.* Increasing fibroblast response to materials using nanotopography: morphological and genetic measurements of cell response to 13-nm-high polymer demixed islands. *Exp Cell Res* 276, 1-9, (2002).
279 Dalby, M. J. *et al.* Fibroblast reaction to island topography: changes in cytoskeleton and morphology with time. *Biomaterials* 24, 927-935 (2003).
280 Dalby, M. J., Riehle, M. O., Johnstone, H., Affrossman, S. & Curtis, A. S. Investigating the limits of filopodial sensing: a brief report using SEM to image the interaction between 10 nm high nano-topography and fibroblast filopodia. *Cell biology international* 28, 229-236, (2004).
281 Dalby, M. J. *et al.* Nanomechanotransduction and interphase nuclear organization influence on genomic control. *J Cell Biochem* 102, 1234-1244, (2007).
282 Geiger, B., Spatz, J. P. & Bershadsky, A. D. Environmental sensing through focal adhesions. *Nature reviews. Molecular cell biology* 10, 21-33, (2009).
283 DeLise, A. M., Fischer, L. & Tuan, R. S. Cellular interactions and signaling in cartilage development. *Osteoarthritis Cartilage* 8, 309-334, (2000).
284 Hersel, U., Dahmen, C. & Kessler, H. RGD modified polymers: biomaterials for stimulated cell adhesion and beyond. *Biomaterials* 24, 4385-4415 (2003).
285 Connelly, J. T., Garcia, A. J. & Levenston, M. E. Inhibition of in vitro chondrogenesis in RGD-modified three-dimensional alginate gels. *Biomaterials* 28, 1071-1083, (2007).
286 Kitaori, T. *et al.* Stromal cell-derived factor 1/CXCR4 signaling is critical for the recruitment of mesenchymal stem cells to the fracture site during skeletal repair in a mouse model. *Arthritis Rheum* 60, 813-823, (2009).
287 Boker, A. *et al.* Hierarchical nanoparticle assemblies formed by decorating breath figures. *Nature materials* 3, 302-306, (2004).
288 Eming, S. A., Krieg, T. & Davidson, J. M. Inflammation in wound repair: molecular and cellular mechanisms. *The Journal of investigative dermatology* 127, 514-525, (2007).
289 Neves, S. R. *et al.* Cell shape and negative links in regulatory motifs together control spatial information flow in signaling networks. *Cell* 133, 666-680, (2008).
290 McBride, S. H. & Knothe Tate, M. L. Modulation of stem cell shape and fate A: the role of density and seeding protocol on nucleus shape and gene expression. *Tissue engineering. Part A* 14, 1561-1572, (2008).
291 Schrobback, K., Klein, T. J. & Woodfield, T. B. The importance of connexin hemichannels during chondroprogenitor cell differentiation in hydrogel versus microtissue culture models. *Tissue engineering. Part A*, (2015).